Environmental Stress Cracking (ESC) and Slow Crack Growth (SCG) of PE-HD induced by external fluids

Umgebungsbedingter Spannungsriss und langsames Risswachstum in PE-HD induziert durch äußerliche Einwirkung verschiedener Fluide

Vom Fachbereich Material- und Geowissenschaften der Technischen Universität Darmstadt zur Erlangung des Grades eines Doktors der Ingenieurwissenschaften (Dr.-Ing.) genehmigte Dissertation von M. Sc. Markus Schilling aus Berlin

Darmstadt 2019

TECHNISCHE UNIVERSITÄT DARMSTADT

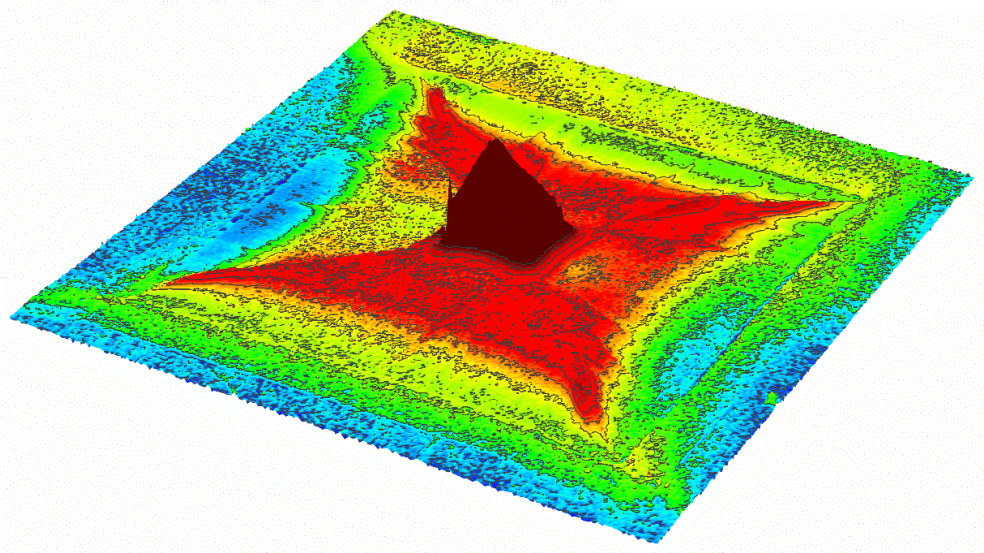

Environmental Stress Cracking (ESC) and Slow Crack Growth (SCG) of PE-HD induced by external fluids

Umgebungsbedingter Spannungsriss und langsames Risswachstum in PE-HD induziert durch äußerliche Einwirkung verschiedener Fluide

Approved doctoral thesis of M. Sc. Markus Schilling from Berlin

Genehmigte Dissertation von M. Sc. Markus Schilling aus Berlin

1. Written expertise / Gutachten:	Prof. Dr. Dr. h.c. Ralf Riedel
2. Written expertise / Gutachten:	Priv.-Doz. Dr. habil. Ingo Alig

Chairperson examination board / Vorsitzende*r der Prüfungskommission:

Date of Submission / Tag der Einreichung:	29. October 2019
Date of Examination / Tag der Prüfung:	11. March 2020

Schilling, Markus : Environmental Stress Cracking (ESC) and
Slow Crack Growth (SCG) of PE-HD induced by external fluids
Darmstadt, Technische Universität Darmstadt,
Jahr der Veröffentlichung der Dissertation auf TUprints: 2020,
URN: urn:nbn:de:tuda-tuprints-115443
URI: https://tuprints.ulb.tu-darmstadt.de/id/eprint/11544
Tag der mündlichen Prüfung: 11.03.2020

Declaration of Authorship

I hereby declare that this doctoral thesis submitted is my own unaided work and was compiled with the recorded sources only. All direct or indirect scientific sources used are acknowledged as references. This work was not previously presented to another examination board.

Erklärung zur Dissertation

Hiermit versichere ich, die vorliegende Dissertation ohne Hilfe Dritter und nur mit den angegebenen Quellen und Hilfsmitteln angefertigt zu haben. Alle Stellen, die aus wissenschaftlichen Fremdquellen entnommen wurden, sind als solche kenntlich gemacht. Diese Arbeit hat in gleicher oder ähnlicher Form noch keiner Prüfungsbehörde vorgelegen.

Darmstadt, 29. October 2019

Markus Schilling

This doctoral thesis is assigned to the department Dispersive Solids of the TU Darmstadt. The practical work of this thesis was performed at Federal Institute of Materials Research and Testing (BAM) in Berlin, Germany and at Fraunhofer Institute for Structural Durability and System Reliability LBF in Darmstadt, Germany in the frame of a joint project financially supported by AiF.

It comprises 96 figures, 14 tables, 73 equations and 223 literature references (including the appendix).

Die vorliegende Dissertationsschrift stammt aus dem Fachgebiet Disperse Feststoffe der TU Darmstadt. Die praktische Durchführung der Arbeit erfolgte an der Bundesanstalt für Materialforschung und -prüfung (BAM) in Berlin und am Fraunhofer-Institut für Betriebsfestigkeit und Systemzuverlässigkeit (LBF) in Darmstadt im Rahmen eines gemeinsamen von der AiF geförderten Forschungsprojektes.

Sie beinhaltet 96 Abbildungen, 14 Tabellen, 73 Gleichungen und 223 Literaturquellen (inklusive des Anhangs).

Parts of this thesis were already published in peer reviewed scientific journals:

(1) M. Schilling, M. Böhning, H. Oehler, I. Alig, U. Niebergall, Environmental stress cracking of polyethylene high density (PE-HD) induced by liquid media - Validation and verification of the full-notch creep test (FNCT), Mat. Sci. Eng. Tec., 48 (2017) 846-854.

(2) M. Schilling, U. Niebergall, M. Böhning, Full notch creep test (FNCT) of PE-HD – Characterization and differentiation of brittle and ductile fracture behavior during environmental stress cracking (ESC), Polym. Test., 64 (2017) 156-166.

(3) M. Schilling, U. Niebergall, I. Alig, H. Oehler, D. Lellinger, D. Meinel, M. Böhning, Crack propagation in PE-HD induced by environmental stress cracking (ESC) analyzed by several imaging techniques, Polym. Test., 70 (2018) 544-555.

Additionally, parts of the results of this thesis were taken into account in the latest revision of the FNCT standard ISO 16770:2019-09.

– This page is intentionally blank. –

Abstract

High-density polyethylene (PE-HD) is widely used as a packaging material. Typical applications are pipes and containers for storage and transport of dangerous goods. For these applications, the understanding of the craze-crack damage mechanisms slow crack growth (SCG) and environmental stress cracking (ESC) is of importance. Since these mechanisms are considered to be the major causes of failure, their understanding is essential for inspection and release of those materials.

A well-established test method for the assessment of these damage mechanisms is the full-notch creep test (FNCT). It is used in this study for a detailed investigation of crack propagation phenomena in PE-HD container materials under the influence of different fluids such as air, water and aqueous detergent solutions (Arkopal N 100) as well as biodiesel and diesel. Based on the results of the FNCT, a classification scheme of different fluids is proposed, which allows for an assignment of the respective damage mechanisms. Hereby, it is differentiated between (i) inert, (ii) purely surface-active and (iii) additionally sorptive, bulk-active fluids with respect to SCG. If the test fluid changes the intrinsic properties (at the surface or in the bulk), the damage mechanism is addressed to ESC behavior.

In FNCT investigations, stress, temperature and specimen geometry were varied systematically. In addition to the time to failure as common measure for the resistance of a PE-HD type against crack propagation, specimen elongation was considered in detail.

Several imaging techniques were applied for fracture surface analysis of specimens tested in FNCT to gain novel information on SCG and ESC behavior. From height profiles obtained by laser scanning microscopy (LSM) and information on surface structures from scanning electron microscopy (SEM), indicators for the differentiation of the crack propagation mechanisms could be derived. Based on the LSM data, an algorithm for the distinction between ductile shear deformation and brittle crack growth as dominating failure mechanism was developed. Imaging techniques were also used for determination of crack propagation rates, which were related to time-resolved FNCT elongation data. From the time-resolved determination of crack lengths of partly damaged FNCT specimens, an increasing length of craze zone with a progressively propagating crack was revealed for the first time. This relation of crack and craze zones was specified by fracture mechanical considerations.

Kurzzusammenfassung

Polyethylen hoher Dichte (PE-HD) wird als Werkstoff für Rohre und Behälter für den Transport und zur Lagerung von Gefahrgütern verwendet. Für die Beurteilung und technische Freigabe dieser Materialien ist das Verständnis der beiden Schädigungsmechanismen „langsames Risswachstum“ (engl.: „slow crack growth“, SCG) und „umgebungsbedingter Spannungsriss“ (engl.: „environmental stress cracking“, ESC) essentiell.

Eine etablierte Prüfmethode zur Bewertung dieser Schädigungsmechanismen ist der Full-Notch Creep Test (FNCT), der in dieser Arbeit zur systematischen Untersuchung des Risswachstums in PE-HD Behältermaterialien unter Einwirkung von Luft, Wasser und wässrigen Netzmittellösungen (Arkopal N 100) sowie Biodiesel und Diesel verwendet wird. Aus den Ergebnissen des FNCT wird ein Klassifikationsschema für Fluide vorgeschlagen, welches ebenfalls eine Zuordnung zu den Schädigungsmechanismen erlaubt. Hierbei wird in (i) inerte, (ii) rein oberflächen-aktive und (iii) zusätzliche sorptive, volumen-aktive Fluide hinsichtlich des langsamen Risswachstums (SCG) unterschieden. Wenn ein Fluid lokal die intrinsischen Materialeigenschaften des Polymers verändert, wird der Schädigungsmechanismus dem umgebungsbedingten Spannungsriss (ESC) zugeordnet.

Bei den FNCT-Untersuchungen wurden die mechanische Spannung, die Temperatur und die Prüfkörpergeometrie systematisch variiert. Zusätzlich zur Standzeit wurde die Prüfkörperdehnung zeitabhängig erfasst.

Aus einer erweiterten Bruchflächenanalyse konnten neuartige Informationen über SCG und ESC erhalten werden. Hierzu wurden verschiedene Bildgebungsverfahren verwendet. Insbesondere wurden mit Laserscanningmikroskopie (LSM) Höhenprofile und mit Rasterelektronenmikroskopie (REM) Oberflächeninformationen zur Charakterisierung der Rissfortschrittsmechanismen erhalten. Auf Basis der LSM wurde unter Zuhilfenahme von Höhenprofildaten ein Algorithmus zur Unterscheidung zwischen duktiler Scherverformung und sprödem Risswachstum als dominierende Schädigungsmechanismen entwickelt. Die aus den bildgebenden Verfahren ermittelten Rissfortschrittsraten konnten mit den Daten der während des FNCT erfassten Dehnung der Prüfkörper in Beziehung gesetzt werden. Weiterhin wurde mithilfe von zeitaufgelösten Risslängendaten erstmals eine direkte Korrelation der Risslänge zu vorgeschädigten, fibrillierten Bereichen (Crazes) im PE-HD Prüfkörper während des FNCT nachgewiesen. Demnach vergrößert sich die Craze-Länge linear mit zunehmender Risslänge. Dieser Zusammenhang zwischen Riss- und Craze-Längen wurde auf mathematisch, bruchmechanischer Grundlage bestätigt.

Acknowledgements

This thesis would not have been made possible without the persistent support of some people, I want to acknowledge gladly.

First, I would like to express my sincere thanks to Prof. Dr. Dr. Ralf Riedel, head of the division Disperse Feststoffe of the Institute of Materials Science of the TU Darmstadt, for his encouragement, his scientific supervision as well as helpful hints and fruitful discussions. Furthermore, Priv.-Doz. Dr. Ingo Alig from the division Plastics of Faunhofer Institute for Structural Durability and System Reliability LBF is gratefully acknowledged for his scientific expertise to help me making this thesis and our collaborative project successful. I also thank him for his supervision of my PhD thesis. I would also like to express my gratitude to my co-examiners Prof. Dr. Wolfgang Ensinger, head of the division Materialanalytik and dean of the department Material- und Geowissenschaften of the TU Darmstadt, and Prof. Dr. Bai-Xiang Xu, head of the division Mechanics of Functional Materials at the TU Darmstadt.

Moreover, I thank BAM and AiF for financial support of the project I was allowed to work on during my PhD. In this respect, Dr. Pedro Portella of BAM is acknowledged in the first place.

Being my supervisors at BAM, I am especially deeply grateful to Dr. Ute Niebergall and Dr. Martin Böhning for making this three years much, much more than a hard-working job. Without giving me the opportunity to work with them, I would not have finished the PhD procedure like this. I will never forget their relentless effort in trying to support me in every way possible. They were able to make me improve subject-specifically and personally in numerous discussions leading to scientific exchange and motivation.

Furthermore, I am grateful for the support of all colleagues from BAM of divisions 5.3 and 7.5. I am much obliged to Niklas Marschall for his time performing imaging measurements, implementing our computational algorithms for fracture surface depictions and the calculation of the criterion of brittleness. Oliver Schwarze and Nicolai Schmidt are also acknowledged for their support with specimen preparation. For providing their assistance in CT and SEM measurements, Dietmar Meinel and Christiane Weimann are kindly acknowledged.

Additionally, the author gives thanks to Harald Oehler and Dr. Dirk Lellinger from Faunhofer LBF for their help with the performance of charaterization methods and their scientific input, especially concerning the final report of our joint project. Moreover, the author is grateful to Peter Bisson and Dr. Iakovos Vittorias of LyondellBasell for kindly providing the PE-HD materials applied in this study and for important information. To me, it was an honor and delight to work and collaborate with all these people during the last years.

Certainly, such a work would also be impossible to create, if there was not the great private support I was glad to experience from my family and friends. Especially, I would like to mention my parents, who motivated and supported my massively to get better every day. Particularly since the finalization of this PhD thesis marks an important point in my life, a certain reminiscence is inevitable. Unconditioned and unquestioned encouragement and assistance by my parents during my entire life comes to my mind. I cannot express properly what that means to me and I am also deeply grateful to be allowed to receive such care. Furthermore, my grandparents are to be acknowledged for always motivating, supporting and keeping me going. With justification, they were always endeavored to teach me a good portion of modesty. I am obliged to be able to adopt this virtue, at least a bit. Last but not least, I deeply thank my wife-to-be, especially for being so patient with me over the last couple of years and just being at my side, going through tough times, always trying to achieve best possible results. She gives me reason to continue relentlessly, trying to get better further on.

Körper und Stimme leiht die Schrift
dem stummen Gedanken,
durch der Jahrhunderte Strom trägt ihn
das redende Blatt.

Friedrich Schiller (1759-1805), Der Spaziergang

Table of Contents

– This page is intentionally blank. –

1. Motivation

Polymers subjected to mechanical loads and environmental influences show a loss of their mechanical properties required for specific applications [1]. Accordingly, cracking and failure due to mechanical stresses additionally influenced by a fluid is an issue for the application of high-density polyethylene (PE-HD) components. Since PE-HD is frequently used in high-performance applications such as containers for the storage and transport of dangerous liquid and gaseous fluids [2], a high relevance in terms of safety is evident. Therefore, the understanding of corresponding damage mechanisms is necessary [3].

Ageing and failure of polymers can occur by chemical and physical mechanisms. Mechanical stress induced failure of polymers can be subdivided into mechanisms based on crack growth and shear deformation (SD). Crack growth damage mechanisms are also classified according to the times to failure which correspond to the applied mechanical loads. High mechanical loads that take effect on polyolefins in short times (sudden impact) result in rapid crack propagation (RCP). In contrast, slow crack growth (SCG) occurs at low overall mechanical stresses, which are typically well below the yield strengths of polymers [4, 5].

For PE-HD, slow crack growth (SCG) is of importance [4, 6, 7, 8] since it is considered to be the major failure mechanism in polyolefins and it is typically occurring suddenly and unexpectedly [9]. SCG is commonly discussed in terms of a craze-crack mechanism and comprises the three stages (i) crack initiation, (ii) crack propagation and (iii) residual fracture (final failure). Crack initiation is considered to emerge from a local stress concentration within the polymer. The local stress concentration results from inhomogeneities, surface scratches, notches, defects or other imperfections in the material. After a crack is initiated, the typical craze-crack mechanism starts after micro-voids (microcracks) developed in the plastic deformation zone at the crack tip. They grow to larger voids while fibrils are formed from highly orientated inter-void polymer material (craze) [10, 11]. Further crack growth occurs when the fibrils in the craze-zone fail. Depending on stress level and rate of loading, failure occurs due to chain scission, disentanglement or cavitation. For SCG, disentanglements are regarded as the dominant mechanism. Such failure results in fracture surfaces representing a macroscopic brittle behavior [5, 11, 12]. A major characteristic of the craze-crack mechanism is the significant generation of additional (internal) surface during crazing accompanied by a volume increase due to the formation of voids and fibrils [3]. Therefore, this process is influenced by the environment. External fluids are able to change the surface energy and Van der Waals forces between polymer chains. Thus, the energy required for the generation of additional surface can be reduced. In contrast, a volume-constant ductile SD does not create additional surface. Due to the influence of fluids, the damage process occurring to PE-HD is also commonly termed environmental stress cracking (ESC). Usually, ESC is supposed to result when environmental fluids significantly influence the course of damage to PE-HD, e.g. the time to failure t_f.

However, the terms SCG and ESC are frequently used ambiguously, and they are not properly defined to clearly describe damage mechanisms in PE-HD under the influence of mechanical stress and fluids. In this respect, a clarification of technical terms is required.

Furthermore, the distinct influence of different environmental fluids on PE-HD is not yet completely understood. Most publications only refer to detergents. Therefore, this systematic study assessing the influence of different fluids on SCG phenomena was performed and a categorization of fluids according to their damage effects to PE-HD is proposed.

Significant test methods are required to examine and quantify the SCG resistance of polyolefins, especially PE-HD. Two approaches are used for SCG testing: static and dynamic mechanical loading. In static tests, a specimen is subjected to a constant load and the time to failure t_f is taken as a

measure for the SCG/ESC resistance. Test conditions such as temperature, fluid and specimen geometry as well as the applied mechanical stress are selected to perform the experiments in acceptable times. Usually, a defined notch is introduced to the specimen for crack initiation. Such, a constant mechanical load results in progressive crack growth due to craze-crack mechanism and leads to characteristic fracture [8, 5, 13]. Using notched specimens, the effect of crack initiation can be neglected. This reduces test times and allows to focus on crack propagation [14, 15]. In alternative test methods, specimens are subjected to dynamic loads. In such fatigue tests, notched and unnotched specimens can be used to either consider crack propagation only or the entire damage process [16].

To evaluate the influence of different fluids on the SCG/ESC performance of several PE-HD types used as container materials, the full-notch creep test (FNCT) [13] was selected in this study. The FNCT is widely applied for PE pipe and container materials in Europe [17]. The geometry of FNCT specimens (according to ISO 16770 [13]) ensures plane strain conditions as encountered in most practical applications. Suitable mechanical load and temperature conditions lead to the occurrence of characteristic brittle failure due to crack growth induced by the craze-crack mechanisms SCG/ESC. The time to failure t_f is recorded to assess the SCG/ESC resistance. Additional to the standard procedure using detergent solutions, FNCT were conducted in several test fluids such as air, water and the organic liquids biodiesel and diesel. These test fluids were selected according to their surface activity and sorption behavior to PE-HD. Accordingly, they are classified as inert, surface-active and bulk-active. An enhanced FNCT fracture surface analysis was performed for evaluation of the influence of the fluids on SCG.

Moreover, based on the understanding of crack propagation, the established FNCT was assessed concerning significance and time efficiency. Therefore, the FNCT was performed using different specimen geometries, mechanical stresses and temperatures. Furthermore, data obtained from enhanced fracture surface analysis allow a classification of fracture surfaces in terms of SCG/ESC.

This thesis comprises five paragraphs. In the first two paragraphs, basics and experimental methods are described. The polyethylene (PE) materials, basics on stress cracking and concepts of fracture mechanics as well as the test methods and imaging techniques are explained. The third paragraph contains the description of materials and test fluids applied in this study and their characterizations are presented. In the results and discussion section, the data of mechanical tests and imaging analysis are depicted and interpreted. This paragraph is subdivided into a section on SCG phenomena in different fluids, the influence of physical properties and structure of PE-HD on SCG, crack growth analysis and consequences for stress crack testing using the FNCT. The latter relates to an improvement of the FNCT. Finally, conclusions are given.

2. Basics

This paragraph comprises the basics required to assess crack growth phenomena in PE-HD that are influenced by external fluids. It is subdivided into five sections and starts with the consideration of polymer basics.

Polymers are termed after the Greek words 'polus' ('many, much') and 'meros' ('parts') and refer to large macromolecules whose structures are composed of repeated subunits. The subunits derive from small molecules of low molecular mass known as monomers. Due to the concatenation of such monomers to polymer chains, high molecular masses (MM) are obtained. The properties of polymers are intricately related to their structure [18]. Historically, the term 'polymer' was introduced by Jöns Jacob Berzelius in 1833, however using a different from the modern definition by IUPAC [19]. The modern concept of polymers as covalently bonded macromolecular structures was proposed by Hermann Staudinger in 1920 [20, 21].

The macromolecules of polymers are long flexible chains with a backbone string of mostly carbon atoms. The intramolecular covalent bonds between carbon atoms are very strong. Between the macromolecules (intermolecular), weaker van der Waals and hydrogen bonds are formed. Since each carbon atom has four electrons to participate in covalent bonding, single, double and triple bonding is possible. In ethylene (C_2H_4), two carbon atoms are doubly bonded, and each is also singly bonded to two hydrogen atoms. An example of a triple bond can be found in acetylene (ethyne). Molecules having double and triple covalent bonds are denoted as unsaturated, because other groups of atoms may easily become attached to the original molecule. Such molecules may serve as monomers in polymerization processes.

2.1. Polyethylene (PE)

Polyolefins are a subset of polymers which contain chains of only saturated hydrocarbons (no carbon double bonds). Polyethylene (PE) is a polyolefin which is generated from the monomer ethylene. It is a thermoplastic polymer that can be produced in a wide range of mechanical properties (section 2.1.2) which leads to a variety of applications (section 2.1.3). Polyolefins represent the highest fraction of plastics in use with more than 40 % in Germany (2015). About 28 % thereof accounts for PE, which is thus the most used polymer [22]. Globally, the rapid growth in polymer production since the 1950s is extraordinary and surpassing most other materials [23, 24].

2.1.1. Polymerization, Structure and Additives

A polymerization is required to obtain a polymer. Formally, this process begins when an active monomer is formed by the reaction of an initiator or radical species (R·) to a doubly bonded monomer, such as ethylene (Figure 1, a). In such a radical polymerization of ethylene, its π bond is broken by the radical species R· and a new σ bond is formed. The remaining unpaired electron represents the new propagating center. The polymer chain is then created by the sequential addition of monomers to the active initiator-mer center (Figure 1, b). The active site (unpaired electron) is transferred to each successive monomer end when it is linked to the chain (Figure 1, c). The higher the number of repeating units in a single macromolecule represented by n_{mer}, the longer is the polymer chain.

a) b) c)

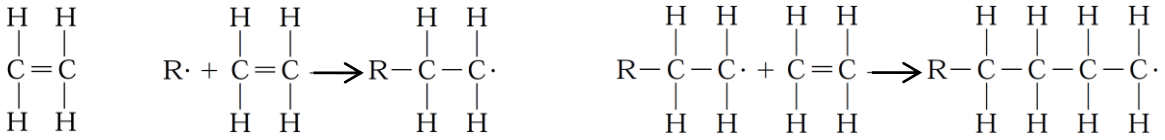

Figure 1: Formal polymerization process schematically depicted for initiator R· and ethylene; a) ethylene monomer, b) reaction of initiator R· to ethylene, c) transfer of active site to successive monomer end (after [18]).

The result of this chain-growth polymerization is polyethylene (PE). This process can be divided into the three stages chain initiation (Figure 1, b), chain propagation (Figure 1, c) and chain termination. There are several mechanisms to initiate a polymerization. The free radical mechanism uses the incorporation of free radicals as initiator or catalyst species (R·). Such free radicals are reactive atoms or molecules having unpaired electrons. A major issue of free radical initiated polymerization is a lack of control, especially effecting high degrees of branching. Additionally, chain termination occurs randomly when two chains collide, which leads to the impossibility to control the length of individual polymer chains. An improved polymerization method allowing a higher degree of control involves special catalysts, which were introduced by Karl Ziegler and Giulio Natta (Ziegler-Natta catalysts) [25, 26, 27]. Other forms of chain-growth polymerization include cationic and anionic polymerization.

Furthermore, a step-growth polymerization leads to polymers created by the stepwise reaction of functional monomer groups usually containing nitrogen or oxygen. Most step-growth reactions are classified as condensation polymerizations. Therein, two or more molecules combine into a larger molecule denoted as condensate, which is commonly accompanied by a release of low-molecular side products (e.g. water and ammonia) [28].

Polymer chain

The angle between single bonded carbon atoms along a PE chain is close to 109°. The C–C bond length is about 0.154 nm. PE is denoted as homopolymer when all repeating units along the chain are of the same type. In contrast, polymer chains composing two or more different mer units are termed copolymers. Usually, both polymer types are likely to occur in polymer synthesis. When a monomer bonds with two other units forming the two-dimensional chainlike molecular structure, it is denoted as bifunctional. Accordingly, trifunctional monomers have three active bonds resulting in a three-dimensional molecular network structure [18].

Cross-linking and chain-branching

Besides forming a linear chain (Figure 2, a), polymers can be joined by other chains at several points along their length to produce a cross-linked structure (Figure 2, b). Chemical cross-linking leads to thermosetting polymers, in which cross-linking agents are normally activated by heat (e.g. epoxy resins). Another possibility of polymer structure is chain branching, which occurs when a secondary chain initiates from a point in the main chain (Figure 2, c) [28]. Chain branches are smaller than the main chain. They are differentiated according to their length in small chain branches (SCB) and long chain branches (LCB).

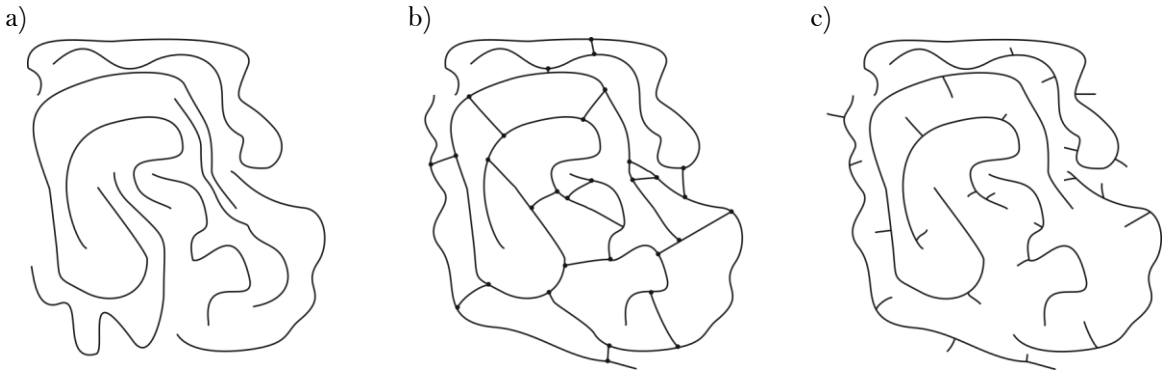

Figure 2: Schematic diagram of a linear (a), cross-linked (b) and branched (c) polymer (inspired by [28, 29]).

During the polymerization of PE, chain branches are likely to be formed. These branches are also termed 'comonomers'. They may be comprised of a random number of carbon atoms. The number of branches (comonomers) and their lengths directly affect the density of the polymer [30, 31]. Therefore, a controlled adjustment of comonomers in polymerization is desirable. The production of PE is usually realized by high-pressure or low-pressure polymerization.

PE production processes

When high-pressure polymerization (1000 to 3000 bar) is applied, the occurrence of a high number of side chains is common. Therefore, low-density PE (PE-LD) is generated by a free radical reaction in high-pressure polymerization. PE-LD mainly contains long chain branches (LCB) with a number of 20 to 30 branches per 1000 carbon atoms. The portion of branches per 1000 carbon atoms is denoted as branching degree. The branching degree influences the crystallinity of a polymer, because it determines the volume of randomly organized molecules within the amorphous regions [31]. Thus, a high branching degree results in a low crystallinity. A main chain is often no longer definable unambiguously and PE-LD is also termed branched PE [30]. Polymer chains with many branches are sterically-constrained and unable to pack as closely as chains with a higher degree of linearity. Consequently, intermolecular forces (e.g. van der Waals forces) are reduced resulting in lower density and a decrease in mechanical properties [31]. Typically, PE-LD has a density of about 0.915 g/cm³ to 0.935 g/cm³ and a crystallinity of 40 % to 50 %. The average molar mass of PE-LD can be up to 600 kg/mol and it depends on the conversion rate during polymerization [30].

Applying low-pressure polymerization, linear PE is produced, which includes high-density PE (PE-HD), medium-density PE (PE-MD) and linear low-density PE (PE-LLD). Using a copolymerization process of ethylene and α-polyolefins such as butene-1 or 1-hexene, short chain branches (SCB) with lengths of two to five carbon atoms can be obtained. Therefrom, PE-LLD is produced that exhibits a high fraction of comonomers. Due to an increase of comonomer fraction, the branching degree rises, and density is decreased below a typical value of 0.915 g/cm³. Medium-density PE (PE-MD) can be generated by blending PE-LD and PE-HD compounds or by direct copolymerization of PE-LLD [30].

High-density polyethylene (PE-HD)

The linear PE-HD is a homopolymer that possesses low fractions of comonomers. Its linear arrangement leads to a high packing density and a high crystallinity of approx. 60 % to 80 %. Commonly, the density of PE-HD averages 0.942 g/cm³ to 0.965 g/cm³. The number of short branches has an average of less than two branches per 1000 carbon atoms (low branch degree). PE-HD is mainly produced using three different processes and catalyst systems: (1) Ziegler-Natta

polymerization applying titanium halide, titanium ester and aluminum alkyl catalysts, (2) the Phillips process using chromium oxide catalysts and (3) gas phase polymerization with other metallocene catalysts. Usually, two or more of these polymerization processes are combined and conducted in sequence, resulting in loop or cascade processes [32]. Due to the structural appearance of the catalyst systems, the sequence of monomers incorporated in the polymer chain can be directly controlled. The Ziegler-Natta polymerization is operated at pressures of one bar to 50 bar; Phillips polymerization at 30 bar to 40 bar. Regarding the procedural perspective, polymer properties such as average molecular mass (section 2.1.2), MMD and the number and length of branches can be adjusted within narrow limits by the application of different polymerization processes. Process parameters such as temperature, pressure, catalysts, catalyst ratio and the concentration of inhibitors are varied [31].

Applying special catalysts to a low-pressure polymerization, PE types with higher molecular masses can be produced. These are denoted as high molecular weight PE (PE-HMW) and ultra-high molecular weight PE (PE-UHMW). Their molecular masses are approx. 500 to 1000 kg/mol (PE-HMW) and 3000 to 6000 kg/mol (PE-UHMW). Thus, they are much higher than that of PE-HD with approx. 200 to 500 kg/mol [30]. Additionally, cross-linking of PE can be realized by shaping and finalization or a subsequent process. Radical spots in the polymer chain are thereby interconnected to form a network.

The range of properties and applications of PE can be varied and enhanced by adjusting polymer density, molecular mass, cross-linking and copolymerization.

Additives

PE is exposed to environmental influences (e.g. weathering) which leads to a gradual deterioration in performance. Such degradation can be initiated by different impurities or chemical compounds being inherent and production-based unavoidable. To uphold the properties required for application, additives are incorporated into PE to inhibit or retard the destructive processes. For instance, UV stabilization can be provided to PE materials by the addition of agents that absorb the harmful part of solar radiation and disperse the absorbed energy in the form of heat. Further stabilization is maintained by quenching the excited states of chromophors that initiate photodegradation, by quenching of singlet oxygen, by the inhibition of the radical processes using antioxidants or by hydroperoxide decomposition. Finally, the practical applicability of a polymer (PE) depends on the amount and chemical structure of each component of the stabilizer mixture [33].

A typical method to analyze the additive system in a polymer is liquid chromatography (LC or high-pressure liquid chromatography, HPLC) [34, 35]. Besides stabilizing a polymer against long-term environmental degradation, additives are integrated to enhance its processability. Therefore, properties such as melt viscosity and flowability are customized by additive-controlled adjustments of cross-linking efficiency [36].

2.1.2. Properties

Major aspects governing the mechanical properties of PE are the molecular mass, polymer density and crystallinity. These properties may further influence each other. A variation of these structural properties significantly affects macroscopic mechanical properties of final polymer products (section 2.1.3) such as strength, toughness and resistance to degradation and stress cracking (section 2.3). It has to be noted that observed properties may also depend on the test procedures and conditions used (section 2.5) [31].

Molecular mass

Since not all chains grow to the same length during polymerization, each polymer contains molecular chains of varying lengths. This results in a distribution of chain lengths and molecular masses. The terms 'molecular mass', 'molar mass' and 'molecular weight' are frequently used in literature denoting the same property. The mass (length) distribution of polymer chains is important and it determines the properties of the polymer. Historically, the molecular mass distribution (MMD) was ascertained by fractionation procedures. Therefore, different types of average molecular mass are quoted. The commonest are the number average M_n and the weight average M_w defined as (Eq. 1 and 2) [18, 28]:

$$M_n = \overline{M_n} = \frac{\sum_i M_i N_i}{\sum_i N_i} = \sum_i x_i M_i \quad (1)$$

$$M_w = \overline{M_w} = \frac{\sum_i M_i^2 N_i}{\sum_i M_i N_i} = \sum_i w_i M_i \quad (2)$$

with M_i: mean molecular weight of size range i, N_i: number of chains per size, x_i: fraction of the total number of chains within the corresponding size range, w_i: weight fraction of molecules within the same size interval.

M_w is always higher than M_n, as the former is strongly influenced by the relatively small number of very long molecules. The ratio of the two averages gives an idea of the width of MMD and is denoted as polydispersity D_{pol} (Eq. 3) [28]:

$$D_{pol} = \frac{\overline{M_w}}{\overline{M_n}} \quad (3).$$

An alternative expression of the average polymer chain size is the degree of polymerization n, which represents the average number of mer units in a chain. The number-average (n_n) and the weight-average (n_w) are obtained by (Eq. 4 and 5):

$$n_n = \frac{\overline{M_n}}{\bar{m}} \quad (4)$$

$$n_w = \frac{\overline{M_w}}{\bar{m}} \quad (5)$$

including $\bar{m}$: mer molecular weight. For a copolymer with two or more different mer units, $\bar{m}$ is derived from (Eq. 6):

$$\bar{m} = \sum_i f_i m_i \quad (6)$$

with f_i and m_i being the chain fraction and molecular mass of mer i [18].

The MMD is especially important in determining the flow properties of a polymer. Additionally, it affects polymer characteristics such as the mechanical properties indirectly by influencing the final physical state. There are also direct correlations of MM to viscoelastic behavior and brittle strength [28].

Orientation and crystallinity

Regarding the arrangement of molecular chains, the two separate aspects molecular orientation and crystallinity have to be considered. These two properties may be considered as one and the same in semi-crystalline polymers (PE). After cooling from the melt, many polymers form a disordered structure denoted as the amorphous state. Some of these may have comparatively high moduli at room temperature; others have a low modulus. These two types of polymers are therefore denoted as

glassy and rubber-like, respectively. Their mechanical behavior depends on the application temperature relative to the glass-rubber transition temperature (T_g). Usually, amorphous polymers are modeled as random molecule tangles. However, a preferred separation distance between molecular chains indicates a not completely random packing. Stretching of an amorphous polymer leads to an alignment of the molecules along the stretch direction. Such a structure is regarded as an amorphous oriented skein. When stretching results in molecular orientation and regions of three-dimensional order, the structure is commonly termed crystalline due to a dense chain arrangement. However, the exact appearance of crystalline structure may vary. Many polymers crystallize when they are cooled slowly from the melt. Although they might possess isotropic bulk mechanical properties, they might not be adjusted into a strong adequate sequence, but they show a spherulitic structure.

Prerequisites for the crystallization of polymers are a regular structure, a temperature below the crystal melting point and sufficient time available for the long molecules to become ordered in the solid state [28]. Besides slow cooling from the melt, conditions for crystallization can also be created by applying tempering processes to a polymer which was already completely solidified.

The structure of the crystalline regions of polymers can be deduced from wide-angle X-ray diffraction patterns of highly stretched specimens (section 3.1.8), which was first implemented in 1939 [37]. Diffraction patterns of PE commonly show diffuse scattering attributed to amorphous regions in addition to discrete reflections from crystallites. Polymers exhibiting such structures are termed semi-crystalline. Crystallinity in semi-crystalline polymers can vary from a few to over 90 per cent. In semi-crystalline polymers, the molecular chains alternate between regions of order (chain folding to form crystallites) and disorder (amorphous regions). Kinetic factors determine the growth rate of crystallization and the morphology. Since the free energy barrier associated to nucleation of crystallites is supposed to be energetic in origin, the growth rate of crystallization is a function of the supercooling degree. Supercooling is the temperature difference between the crystallization temperature and the melting point [38]. Resulting from the assumption that the free energy barrier for nucleation is predominantly entropic, chain folding is supposed to cause a lamellar morphology in semi-crystalline polymers [39]. Hence, chain folding and threading of molecules through crystalline regions occur in such polymers. Therefore, spherulites (diameter about 1 µm to 10 µm) are formed. Their formation starts at a nucleation center and they grow circularly outwards until they impinge upon neighboring spherulites. Dominant lamellae represent the main direction of spherulitic growth. Texture is formed by secondary lamellae twisted around them. Intervening spaces are filled by subsidiary lamellae. Orientation through plastic deformation (e.g. by drawing) destroys the spherulitic structures.

The fraction of crystalline structures in a semi-crystalline polymer is represented by the degree of crystallinity [28]. This is expressed as the ratio of crystalline to amorphous phases. The value describing the degree of crystallinity is henceforth simply referred to as 'crystallinity'.

At room temperature, the crystalline regions of PE determine the strength and the stiffness, whereas the amorphous regions account for the toughness and the time-dependent behavior. A semi-crystalline polymer can be schematically regarded as a compound structure consisting of crystalline, inter-crystalline and amorphous regions (Fig. 3). Crystalline regions are composed of lamellae. Within such crystal lamellae, mainly linear unbranched chain segments are packed and develop a robust orthorhombic lattice. Crystalline regions are pervaded by amorphous regions, in which disordered molecules can be found (Fig. 3).

a) b)

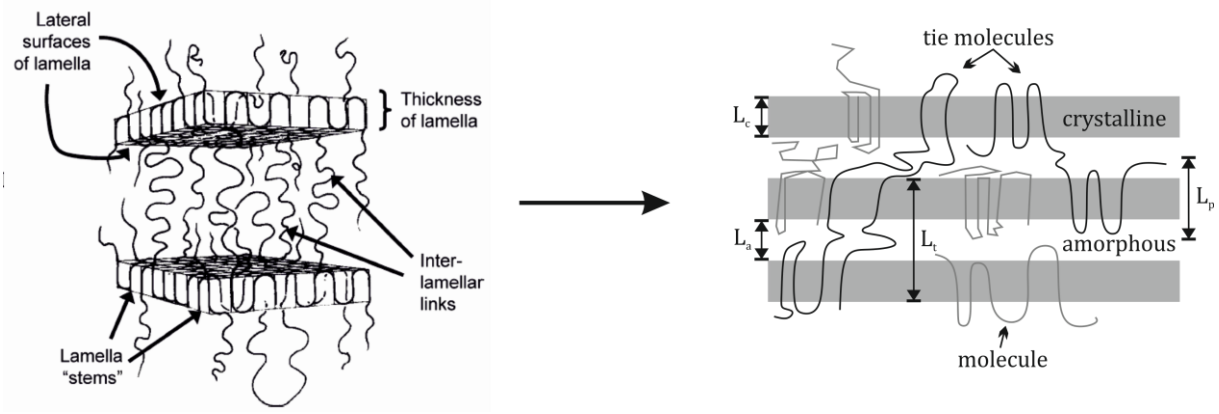

Figure 3: Schematic illustration of the lamellar structure of a semi-crystalline polymer (PE) with crystalline lamellar and amorphous regions; a) overview adapted from [5, 40], b) characteristic values L_p: long period of lamellar structure, L_c: thickness of lamella (crystalline region), L_a: thickness of amorphous region, L_t: minimal length of a tie molecule, modified, adapted from [30].

Typically, the amorphous regions have a thickness L_a of about one to ten nm, whereas lamellar thickness L_c and the long period L_p are in the size range of five to 45 nm [41]. The length of lamellae can be up to one µm. The layer in between (rigid) crystalline and amorphous phases reaches a thickness of about three µm [30]. In contrast to the crystalline lamellar region, no strict arrangement of polymer chains but mainly molecule loops or branch points can be found.

Some special polymer chains are able to interconnect at least two crystalline regions by pervading single amorphous phases entirely (Fig. 3, b). These molecules are denoted as 'tie molecules' and represent an inter-crystalline physical linkage. Due to their ability to constrain the deformation, tie molecules are crucial for the mechanical behavior of PE, especially with respect to stress cracking resistance. The strength of the entire polymer is determined by intermolecular forces, bonds, length and entanglement degree of tie molecules. The number of tie molecules in a polymer is assigned to the molecular mass since the probability for the formation of tie molecules is increased with the existence of longer polymer chains. By increasing branch density, the long period L_p is decreased, which results in a higher probability for the formation of tie molecules [42]. Moreover, branches may impede the movement of tie molecules and strengthen them. The higher the number of tie molecules, the lower is the disentanglement stress influencing every single tie molecule. Low lamellar thicknesses of crystalline regions (L_c, Fig. 3 b) result in low resistance against the movement of tie molecules through crystallites. At higher L_c, this resistance is increased, but the number of tie molecules is reduced. Thus, there is an optimum condition for the formation of tie molecules that leads to an increased polymer strength. This is supposed to be reached when the distance between branches is equivalent to the lamellar thickness L_c [30]. In consequence of the physical interconnection maintained by tie molecules, disentanglement processes within the polymer are hindered resulting in an increased stress cracking resistance.

Furthermore, an increase in PE-HD crystallinity leads to a higher Young's modulus, yield stress and crystallite melting temperature [29]. Concurrently, the impact toughness is supposed to be decreased with increased crystallinity [30].

Mechanical behavior

Characteristic mechanical properties of polymers strongly depend on the ambient (application, test) conditions including temperature, mechanical stress, strain and load rate. Usually, polymers are denoted as viscoelastic materials, which emphasizes their intermediate position between viscous liquids and elastic solids.

At low temperatures or high frequencies of measurement, a polymer may behave glass-like with a high Young's modulus of about 1 GPa to 10 GPa and it may break or flow at strains higher than 5 %. At high temperatures or low frequencies, the same polymer can be rubber-like with a modulus of 1 MPa to 10 MPa and withstand very large extension of about 100 %. Still at higher temperatures, permanent deformation may occur under load and the polymer behaves like a highly viscous liquid. In between these conditions at an intermediate temperature or frequency, the glass transition range can be noticed. Therein, a polymer behaves neither glassy nor rubber-like, but it is viscoelastic and shows an intermediate modulus. In this region, the change of mechanical properties is typically accompanied by a change in the volume coefficient of expansion. This is used to define the glass transition temperature (T_g). T_g is crucial since it denotes the temperature of a significant change in the overall mechanical behavior of polymers.

The different features of mechanical behavior such as creep and recovery, brittle fracture, necking and cold drawing can be displayed by a single polymer type at appropriately varied temperatures. At temperatures well below T_g, the load rises linearly to the breaking point with increasing elongation, and brittle fracture occurs at low strains (up to approx. 10 %, Fig. 4, curve 1). At high temperatures (Fig. 4, curve 4), the polymer is rubber-like and the load exhibits a nearly sigmoidal relationship to the elongation. In this case, fracture occurs at very high strains (approx. 300-1000 %). In an intermediate temperature range below T_g (Fig. 4, curve 2), the load-deformation relationship shows a load maximum (yield point) before failure. At slightly higher temperatures below T_g, necking and cold drawing can be observed (Fig. 4, curve 3). The load-elongation curve shows a yield point and a subsequent decrease in conventional stress. With increasing strain, the load falls to a constant level, at which deformations in the order of 300 % to 1000 % can be obtained. After formation of a neck, the load begins to rise again, and final failure occurs [28]. Such typical mechanical behavior (Fig. 4) can also be achieved by considering different polymers (e.g. amorphous compared to semi-crystalline polymers).

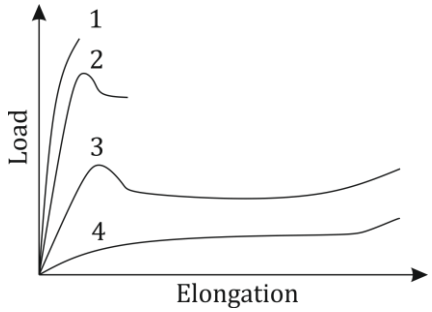

Figure 4: Schematic load-elongation curves for a polymer depending on the temperature; 1: brittle failure, 2: ductile failure, 3: cold drawing, 4: rubber-like behavior; after [28].

The mechanical behavior of polymers is concerned with their deformations that occur under load. In specific cases, such deformations depend on the geometrical shape of test specimens or the way the load is applied. Neglecting such parameters, generalized equations termed constitutive relations are commonly used. They relate stress and strain for a particular type of material. Hooke's law relates the stress σ to the strain ε for the uniaxial deformation of an ideal elastic isotropic solid and provides the Young's modulus E (Eq. 7) [28]:

$$\sigma = E\varepsilon \Rightarrow E = \frac{\sigma}{\varepsilon} \quad (7).$$

According to Hooke's law, stress is exactly proportional to strain. This is not always true for polymers but applies as an acceptable approximation for very small strains in many cases: The constitutive relations are non-linear. Since non-linearity is not related to recoverability, polymers may be able to recover from strains beyond the proportionality limit without any permanent deformation. Hence, the definitions of stress and strain in Hooke's law are only valid for small deformations.

Thermal properties

The melting temperature T_m and the glass transition temperature (region) T_g depend on molecular mass and crystallinity of PE. Commonly, melting occurs between 105°C and 136°C. This temperature range is also suggested to be the processing temperature of usual commercial PE types, especially for PE-HD container materials. The glass transition temperature T_g of PE is supposed to be in the range of -120°C to -110°C, which is attributed to the γ-relaxation. At about -30°C to -10°C, the β-relaxation can be identified. The γ-relaxation characterizes the activation to overcome van der Waals interactions of CH_2-molecules within the main chain, whereas the β-relaxation is assigned to the activation to overcome van der Waals interactions of CH_2- and CH_3-molecules commonly occurring in chain branches [43]. Furthermore, the lower transition temperature is attributed to the free amorphous phases. In contrast, the upper transition temperature is accredited to constrained amorphous regions that are influenced by crystalline phases (inter-crystalline layer, rigid amorphous phase). Below T_g, the amorphous phase is stiff. Above T_g, the Young's modulus is decreased, and the amorphous phase softens. Within this soft region, deformation of the amorphous phase is restricted by entanglements representing a physical network. Accordingly, the α-transition at about 40°C to 60°C is related to the start of chain movement in the crystalline and rigid amorphous phases. Crystalline regions and tie molecules are considered as deformation barriers until they melt entirely at temperatures of approx. 110°C to 120°C, which is characterized by the α'-transition [30]. Due to the increase of the mobility of atoms and polymer chains at higher temperatures, there is a correlation of temperature to test speeds and to time intervals. As a result of higher temperatures and enhanced polymer chain mobility, disentanglement occurs at lower stresses. At higher strain rates, polymer chains have less time to reduce stresses (e.g. by disentangling) and chain bonds may break at lower stresses. This leads to macroscopic brittle failure (section 2.3).

Chemical properties

PE is chemically relatively non-reactive to most acids, alkalis or aqueous solutions. However, it is susceptible to oxidizing agents, which cause a reduction in mechanical properties in consequence of the loss of electrons and the subsequent decrease of saturated hydrocarbon bonds. Oxidation of PE starts to occur at temperatures above 40°C. Since the energy of UV radiation is sufficient to break chemical bonds of PE and form free radicals, this oxidation onset temperature can be further reduced. Oxidation effects lead to polymer chain scission. Halogens are also able to attack PE chemically by forcing a substitution reaction to occur, which leads to embrittlement, discoloration and other losses in mechanical performance [31]. In order to retard or inhibit oxidation and time-dependent degradation, PE is stabilized by additives. It has to be noted that stabilizers preventing one special chemical attack may facilitate another. Hence, additives have to be well-matched concerning application.

2.1.3. Application

The application fields of PE comprise almost all relevant industrial and business sectors such as packing, building and construction, automotive, electric and electronic, household, leisure, sports and agriculture. Typically, PE-LD and PE-LLD are used as bags, small bottles, food packaging films or agricultural films. PE-HD and PE-MD are predominantly applied in market sectors such as houseware, toys and bottles. Moreover, PE-HD is utilized in high-performance applications such as pipes and the storage and transport of dangerous gaseous and liquid goods [24]. Therefore, the resistance of PE-HD against environmental influences, destabilization, degradation and failure is of extraordinary relevance in terms of safety. PE-HD is the main polymer used for applications that require outstanding chemical and physical properties with chemical stability and long-term resistance against degradation and stress cracking. Nowadays, the development of increasingly resistant PE-HD resins is in focus. The aim is to achieve excellent combinations of stress cracking resistance (section 2.3), strength, toughness and stiffness while maintaining appropriate processing properties.

Furthermore, sustainable dealing with polymer waste after application (e.g. by recycling) is considered a relevant issue [22, 23, 24, 44, 45]. On that account, understanding of damage processes is crucial to enhance the performance of PE-HD and avoid waste.

2.2. Solubility and diffusion of fluids in PE-HD

Since the interaction of PE-HD and sorptive fluids with respect to mechanical properties is examined in this study, characteristics and related processes such as solubility and diffusion have to be considered. Their basic concepts are signified in this chapter.

2.2.1. Solubility

Solubility is the property of a solid, liquid or gaseous chemical substance termed solute to dissolve in a solid, liquid or gaseous solvent. In contrast, insolubility denotes the inability of a specific species to dissolve in another. Physical and chemical properties of the solute and the solvent as well as environmental conditions such as temperature, pressure and the presence of other chemicals within the mixture determine the solubility of a substance. Commonly, the saturation concentration is considered as a measure with respect to the solubility of a substance in a specific solvent. The saturation concentration designates a situation, at which adding of more solute does not increase the concentration of the solution, which might be accompanied by the precipitation of the excess amount of solute [46].

Solutions can be classified according to the phases involved. The solvent could be a liquid comprising a pure substance or a mixture. When it is dissolved in another liquid, the result may simply be termed liquid solution. When one or more solutes forming a unique solid phase, in which components are compatible, are dissolved within a solvent, the solution might be termed solid solution. Solid solutions are usually accomplished in metals [18]. The solution of a liquid in a gas is rarely denoted as solution but addressed as vapor-liquid equilibrium instead. Dissolving a liquid in a solid phase, a liquid-solid solution is formed, e.g. when liquids are absorbed by a solid polymer as regarded in this study.

Serving as a simplistic rule, a solute will dissolve best in a solvent that has a similar chemical structure. Hence, the overall solvation capacity of a solvent primarily depends on its polarity [47]. For instance, a polar (hydrophilic) solute is very soluble in highly polar water, less soluble in fairly

polar methanol, and practically insoluble in non-polar solvents. The solubility is favored by the entropy of mixture (ΔS) and depends on the enthalpy of dissolution (ΔH) and the hydrophobic effect. The free enthalpy of dissolution ('Gibbs free energy') depends on the temperature and is given by (Eq. 8) [48]:

$$\Delta G = \Delta H - T\Delta S \quad (8).$$

To describe the solubility mathematically, a solubility coefficient can be used following Henry's law. Henry's law states that the amount of dissolved gas is proportional to its partial pressure in the gas phase [49]. The proportionality factor is termed Henry's law constant or Henry solubility and defined by the concentration (Eq. 9) [50, 51]:

$$H^{cp} = \frac{C_a}{p} \quad (9)$$

with H^{cp}: Henry solubility (coefficient), C_a: concentration of a species in the aqueous phase, p: partial pressure of that species in the gas phase under equilibrium conditions. Analogously and based on the same effect, another constant termed Henry's law volatility constant K_H is defined by (Eq. 10) [49, 52]:

$$K_H^{pc} = \frac{p}{C_a} = \frac{1}{H^{cp}} \quad (10).$$

Hence, for a polymer subjected to diffusion by a foreign gaseous or liquid species, equation 11 is valid:

$$C(x) = S(c,p)\, p(x) \quad (11)$$

with: C: concentration of foreign species, p: (external) pressure, S: solubility coefficient within the bulk material, x: distance covered by foreign species within the bulk material. For small solubility values, the concentration- and pressure-dependence of the solubility coefficient disappears and comparison of equations 9, 10 and 11 leads to (Eq. 12) [48, 50]:

$$S = H^{cp} = \frac{1}{K_H^{pc}} \quad (12).$$

Furthermore, the solubility of a liquid species in a polymer depends on the temperature (Eq. 8). Accordingly, a higher temperature leads to a higher solubility, as especially shown by Böhning et al. for biodiesel and diesel dissolving in PE-HD at three different temperatures [53]. With increasing temperature, the final equilibrium concentration of solute (biodiesel, diesel) in PE-HD was increased. This also denotes an increase in solubility. The solubility is closely related to the phenomenon of diffusion.

2.2.2. Diffusion

The term diffusion designates a process by which matter is transported from one part of a system to another resulting from random molecular motions. Such mass transfer can occur ordinarily on a microscopic level either within a solid, a liquid or a gas. When atoms of the same type diffuse, the process is termed self-diffusion. If atoms or molecules of different species diffuse into another material, the process will be denoted as interdiffusion or impurity diffusion. From a macroscopic perspective, interdiffusion may be discerned by changes in concentration of one fluid in another substance over time [18]. As diffusion is the stepwise migration of atoms or molecules, an empty adjacent site or free volume (space to move in) has to be available and the species has to have enough energy to move. The fraction of moving atoms or molecules increases with temperature since more

energy for atom/molecule movement is allocated at higher temperatures. The motion of atoms and molecules proceeding during the diffusion process is random. As a single molecule has no preferred direction of motion, this motion can be described in terms of the 'random walk' picture. Nevertheless, a definite fraction of molecules moves from regions of higher concentration to sections of lower concentration on the average, simply because there are more molecules available for motion in regions of higher concentrations. Thus, a diffusion process leads to a concentration equilibrium as a result of random molecular motions after a certain time. Consequently, diffusion is time-dependent (diffusion coefficient D = f(t)) [48]. The rate of mass transfer can be expressed as a diffusion flux J_{df}, which is defined as the mass M (number of atoms/molecules) diffusing through and perpendicular to a unit cross-sectional area A per unit of time t (Eq. 13):

$J_{df} = \frac{M}{At}$ or in differential form: $J_{df} = \frac{1}{A}\frac{dM}{dt}$ (13).

When the diffusion flux does not change with time, the process is denoted as steady-state diffusion. From the contemplation of the concentration of moving species through the unit cross-sectional area A covering a distance x, the occurrence of a concentration gradient becomes apparent (Eq. 14):

$$concentration\ gradient = \frac{dC}{dx} \quad (14)$$

with C: concentration of diffusing (moving) species [18]. The similarity of diffusion to heat transfer by conduction was first used by Fick to describe diffusion quantitatively. Diffusion in isotropic substances is mathematically based on the proportionality of the transfer rate of diffusing substances through the unit area of a section to the concentration gradient (Eq. 14) measured normal to the section regarded (Eq. 15):

$$J_{df} = -D\frac{\partial C}{\partial x} \quad (15)$$

attributing the diffusion coefficient D. D is considered to be a measure for the mobility of diffusing species within a certain substance. It might be taken as a constant but may also vary markedly on concentration. The negative sign (Eq. 15) indicates diffusion occurring in the direction opposite to that of increasing concentration. Equation 15 is known as first Fick's law and mathematically consistent only for an isotropic fluid. In an anisotropic substance, the diffusion properties may depend on the direction in which they are measured [48]. Thus far, steady-state diffusion was considered. However, most practical diffusion situations comprise nonsteady-state diffusion processes. In such cases, the diffusion flux J_{df} and the concentration gradient vary with time, which results in a net accumulation or depletion of the diffusing species. Then, the partial differential equation known as Fick's second law has to be applied (Eq. 16) [18]:

$$\frac{dC}{dt} = D\left(\frac{\partial^2 C}{\partial x^2} + \frac{\partial^2 C}{\partial y^2} + \frac{\partial^2 C}{\partial z^2}\right) \quad (16)$$

which can be used, if D is constant and which is reduced to (Eq. 17)

$$\frac{dC}{dt} = D\frac{\partial^2 C}{\partial x^2} \quad (17)$$

if diffusion can be considered one-dimensional. Strictly, these considerations are only valid for isotropic materials. However, due to similarities in the equation forms, certain anisotropic situations can be reduced to corresponding isotropic materials. Whether this is possible in a given case depends on boundary conditions. When the material is infinite or when it is bounded by planes perpendicular to the axes of diffusion, e.g. in specimens with distinct geometries, equations for isotropic are applicable to anisotropic materials [48].

Influences on diffusion coefficient D

The diffusion coefficient D is influenced by several factors. The magnitude of D indicates the rate at which atoms or molecules diffuse. Thereby, D is influenced by the diffusing species as well as the host material. Considering the order of magnitude of D, a contrast between rates of diffusion by different processes such as self-diffusion or interdiffusion is perceptible.

Furthermore, temperature has a strong influence on diffusion rates and the coefficient D, which are related according to (Eq. 18):

$$D = D_0 \, exp\left(-\frac{Q_d}{RT}\right) \tag{18}$$

with D_0: temperature-independent preexponential, Q_d: activation energy for diffusion, R: universal gas constant, T: absolute temperature. The activation energy is considered to be the energy required to produce the diffusive motion of one mole of atoms or molecules. The larger the activation energy, the more difficult it is to induce an atom/molecule motion. Hence, a large activation energy results in small diffusion coefficients. The logarithmized equation 18 assumes the form of an equation of a straight line with the variables ln D (log D) and 1/T (T: absolute temperature). Accordingly, Q_d and D_0 are determined experimentally by considering the slope and the intercept of the straight line obtained from the plot of ln D (log D) versus the reciprocal of the absolute temperature T. This approach indicates Arrhenius behavior of the temperature dependency of the diffusion process [18].

Diffusion in polymers

In polymers, the diffusive motion of small foreign molecules (e.g. O_2, H_2O, CO_2) between the polymer chains is regarded rather than the diffusive motion of atoms within the chain structure. Additionally, the absorption and permeability characteristics of a polymer are related to the degree to which foreign substances (fluids) diffuse into the material. The penetration of such species can lead to swelling and is often associated with a diminution of the mechanical and physical properties of polymers [18].

Diffusion rates are higher through amorphous than through crystalline regions since amorphous structures exhibit a higher amount of free volume. The diffusion mechanism is considered as a diffusive movement from one part of free volume to another in an adjacent amorphous region. Foreign species (fluids) might be absorbed until the free volume in the amorphous regions of a polymer is stowed. Due to concurrent swelling of the polymer, the available free volume might be additionally increased. At the point in time when the same amounts of foreign species are absorbed and desorbed, the system has reach a diffusive equilibrium. The higher the degree of crystallinity of a polymer resulting in a lower amount of free volume available, the less it might be subjected to absorption and swelling.

The properties of diffusing molecules affect the diffusion rate. Smaller molecules diffuse faster than larger molecules [50, 51]. Furthermore, the polarity configuration of the diffusing substance and of the polymer plays a decisive role [18].

According to Crank [48], polymer diffusion behavior cannot be described by a concentration-dependent Fick's law with constant boundary conditions, when the polymer is extensively swollen. Commonly, this is the case in polymers with a high amorphous fraction exhibiting a 'non-Fickian' diffusion behavior. Moreover, properties of an amorphous polymer are time-dependent. Consequently, deviations from Fickian behavior are associated with the finite rates at which polymer structures change in response to the sorption or desorption. Non-Fickian effects are directly related to changes of the polymer and to the corresponding influence on solubility and diffusional mobility [48]. When the temperature or the penetrant concentration is increased, the relaxation that

is connected to structural changes within the polymer decreases. Therefore, a sorption process is influenced by the segmental motions which occur at the same rate or slower than the diffusion process. Hence, the relative rates of diffusion and polymer relaxation are of major importance concerning diffusion [54]. All mathematical models deal with the combination of penetrant diffusion and polymer relaxation that proceeds at different relative rates according to experimental conditions [48].

2.3. Mechanical failure

The superordinate term 'stress cracking' (SC) denotes the phenomenon of cracking and failure of polymer materials that are subjected to external or internal mechanical stresses. The associated failure modes slow crack growth (SCG) and rapid crack propagation (RCP) are assigned to be the major causes for life span reduction in application. Therefore, the understanding of these crack growth mechanisms is important. Furthermore, the possibility to precisely evaluate, rank and tailor the resistance of materials against these damage mechanisms is relevant [3]. In this study, damage effects that are attributed to the field of slow crack growth (SCG) are referred to by investigating the semi-crystalline polyolefin PE-HD (section 2.1) which is exposed to static external mechanical stresses and environmental influences.

It has to be noted that the designation of damage mechanisms is ambiguous. The term 'slow crack growth' (SCG) is used to denominate a fundamental mechanism of crack propagation, especially in distinction to rapid crack propagation (RCP). In contrast to SCG, RCP results from shock stresses (sudden impact). Coincidentally, the term 'slow crack growth (SCG)' is also used to differentiate (section 2.3.6) the damage process from the 'environmental stress cracking (ESC)'. SCG and ESC are both assigned to the fundamental mechanism of slow crack propagation. If the fundamental mechanism of slow crack propagation is to be addressed, 'SCG/ESC' will be termed pairwise in this study. For segregated contemplation and denotation, the terms SCG and ESC are used separately.

2.3.1. First considerations of slow crack growth

The terms SCG and ESC are used to describe mechanisms that lead to brittle failure of polymers associated with small deformation or flow of material.

Historically, such phenomena were first a concern of amorphous polymers known since the 1950s. Later, a different type of brittle failure was observed for PE. Initially, only ductile failure associated with substantial deformation by necking and yielding phenomena was regarded as relevant for PE (sections 2.1.2 and 2.5.1) [9]. This was assumed to be in contrast to instantaneous impact fracture (RCP), which represents a failure mechanism typically resulting in brittle fracture of polymers. However, it was revealed that brittle failure in PE might also result from long-term static loading at low stress-levels (SCG). Such a damage mechanism leading to brittle failure is significantly accelerated in liquids or gases [5, 14]. A differentiation between the subordinated terms 'SCG' and 'ESC' is given in section 2.3.6 in combination with a description of their differences. Based on the results obtained from the investigations in this study, a clarification of these terms is proposed (section 5.1).

Since PE-HD is applied in fields that require long service times (section 2.1.3), the understanding of the relation between polymer structures and mechanical properties is crucial for the tailoring of PE-HD products. With such insights, new and improved test methods can be designed that allow for a prediction and a ranking of PE-HD types in terms of SCG/ESC performance.

Naturally, brittle failure of polymers involves the propagation of a crack through the material. Material toughness is typically defined as the amount of energy that is absorbed in a mechanical test. Fracture mechanics defines 'toughness' as the resistance to crack propagation as measured in a dedicated test [55]. In polymers, the resistance to crack growth is governed by local plasticity that is reflected in the micro-deformation mechanisms. Polymers fail either through deformation without change of volume and creation of internal surfaces (shear, section 2.3.3), or by deformation accompanied by volume increase (crazing, section 2.3.2) [56]. In this context, shear is identical with flow of the continuum. This flow involves elongational or shear deformation in rheological terms and occurs at the macroscopic yield point associated with the engineering yield strength (yield stress). The phenomenon of shearing usually occurs in macroscopic tensile tests as localized shear bands or homogeneous shear flow [3].

In contrast, crazes emerge, propagate and fail while turning into a crack, which is denoted as craze-crack mechanism. This craze-crack mechanism in PE-HD leads to SCG and ESC (section 2.3.6). Crazing was first mentioned and described morphologically in 1973 [57] by transmission electron microscopy (TEM) on thin films [58, 59]. During the typical damage process by the craze-crack mechanism, the actual stress acting on a PE material is constantly increased. As a result, the craze-crack mechanism commonly transitions into shear deformation when a certain stress value is reached (sections 5.1 and 5.3.3).

2.3.2. Crazing, craze-crack transition

In SCG/ESC mechanisms, crazes are initiated in the PE-HD material when the external stress causes microscopic voids to open at local stress concentrations. The latter result from inhomogeneities in the molecular network, defects, scratches, pre-created notches or an enrichment of pigments. The probability of such micro-voids (microcracks) to occur depends on the local stress situation. Following craze nucleation mechanism models, plane strain conditions are considered more likely to lead to the emergence of micro-voids than plane stress [60, 61]. Emanating from such micro-voids, larger voids grow in a plane perpendicular to the highest principal stress (zone of plastic deformation). As a consequence, fibrils are formed from the highly orientated inter-void material. This stage is denoted as craze. When fibrils start to fail by breaking or disentangling of polymer chains due to the high local stress, a craze-crack transition occurs, and macroscopic failure is initiated. Hence, crack growth results from recurring failure of fibrils in the craze-zone. 50 % of the craze volume is assumed to be drawn material (fibrils) and 50 % is void. In contrast to cracks, crazes have load bearing capacities [9]. This condition is illustrated exemplary for a pre-formed notch of a typical FNCT specimen (Figure 5). When the depicted part is considered as the tip of the initial notch in a specimen equal to a pre-formed crack, the indicated crack opening distance (COD) is equivalent to the crack tip opening distance (CTOD) of classic models (section 2.3.5) [11]. The macroscopic stress required for crazes to propagate is denoted as 'craze stress' σ_c.

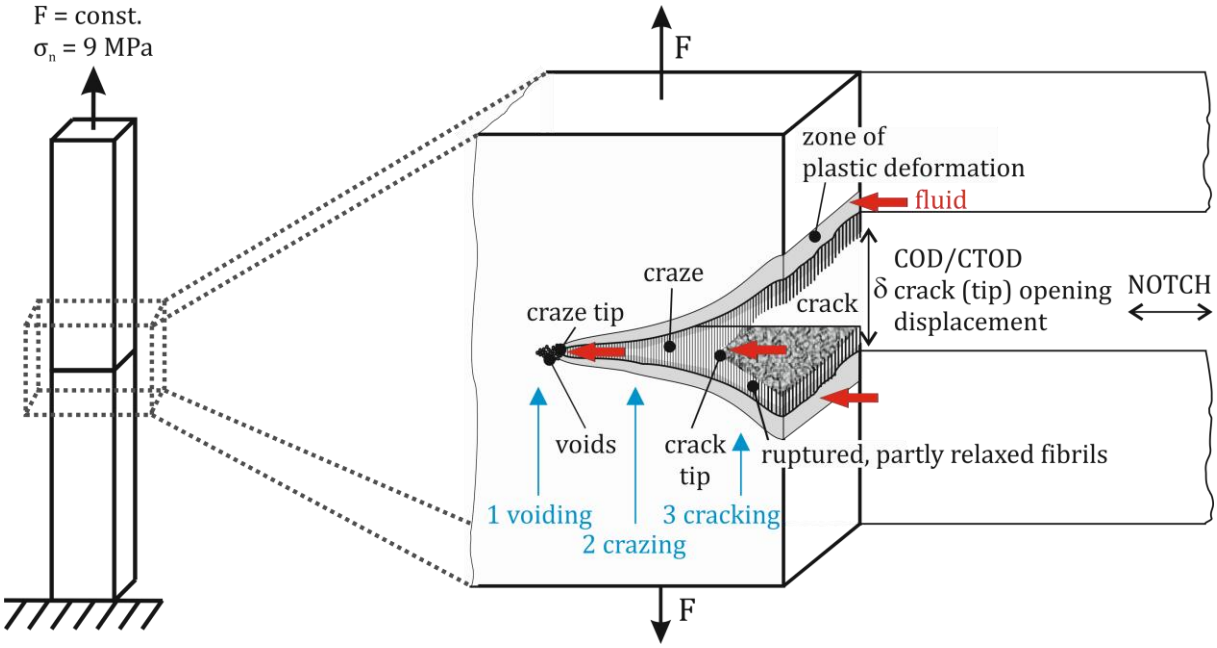

Figure 5: Schematic representation of craze and crack zone formed at the tip of a notch in an FNCT specimen (inspired by [10, 62]), referring to both, SCG and ESC; red arrows denote a potential fluid attack during ESC.

The mechanism of craze propagation, the craze-crack transition and the craze stress are based on the idea that the tendency to create new internal surfaces favors the predominance of crazing [60, 63]. Hence, the creation of new internal surfaces is necessary to induce cracks. The respective energy E_{is} required therefor is the determining factor and it is considered to consist of two contributions (Eq. 19) [3]:

$$E_{is}(\gamma, v_e) = \gamma + \frac{1}{4} v_e U d_{end} \tag{19}$$

with γ: surface energy as the van der Waals cohesive energy between molecules, v_e: effective entanglement density (entanglements that are able to convey load), d_{end}: end-to-end distance between effective entanglements and U: required energy to fracture covalent chain bonds. The term $\frac{1}{4} v_e U d_{end}$ describes the contribution of covalent load bearing bonds crossing the created internal surface. Using the factor of $\frac{1}{4}$, the two surfaces created in the free volume and the fact, that one effective entanglement involves two molecular branches for load transfer, are recognized. A dependence of E_{is} on v_e is implied, which reveals the possibility to enhance E_{is} and inhibit crack propagation by increasing the effective entanglement density.

The craze stress σ_c can be deduced from the growth rate of a craze while respecting its microstructure. For amorphous and semi-crystalline polymers, the craze tip is considered to be transformed into fibrils driven by the surface energy and by a Taylor meniscus instability [58, 60, 64, 65]. Since the material is drawn into craze fibrils, the craze stress σ_c was found to be proportional to the square root of the surface energy (Eq. 20) [3]:

$$\sigma_c \propto \sqrt{\sigma_y E_{is}(\gamma, v_e)} \tag{20}$$

including a strong strain rate dependence of the yield stress σ_y, whereas the strain rate dependence of the craze stress is weak.

Additionally, the craze microstructure, i.e. the fibril diameter D_{fibril}, is directly related to the surface energy (Eq. 21) [60]:

$$D_{fibril} \propto \frac{E_{is}}{\sigma_c} \quad (21).$$

Hence, the surface energy γ is significant for craze and crack propagation (craze-crack transition). Based on a fracture mechanics approach, the craze-crack transition can be described by calculating a critical stress intensity or the strain energy release rate of the mechanically anisotropic fibrillar network within a craze. The stress transfer by the network of crossing tie fibrils is essential to generate a stress concentration at the craze-crack interface fibril. The higher the number of effectively entangled (or cross linked) polymer chains which cross the fracture interface (tie molecules, 2.1.1), the more resistant the polymer will be. A proportionality between the effective entanglement density and the number of effectively load bearing chains can be assumed. Consequently, for amorphous and semi-crystalline polymers, craze propagation and craze-crack transition are considered to rely primarily on the effective entanglement density and the toughness of entanglements during loading [3].

2.3.3. Shearing, yield strength

Shearing is a plastic deformation mechanism characterized by a flow of continuum that prevents the creation of internal surfaces. Shearing is more effective than crazing in energy dissipation since the entire volume of the plastically deforming material is participating. The creation of internal surfaces is prevented by maximizing E_{is} and facilitating the flow by lowering the resistance to macroscopic flow (yield stress).

For amorphous and semi-crystalline polymers, the yield stress as well as its temperature and strain rate dependency are described by an activated flow and the activation enthalpy ΔH in an Eyring thermally activate flow process (Eyring Eq. 22) [28]:

$$\dot{\varepsilon} = \dot{\varepsilon}_0 e^{-\left(\frac{\Delta H}{RT}\right)} \sin h\left(\frac{v\sigma_y}{RT}\right) \quad (22)$$

with $\dot{\varepsilon}$: strain rate, $\dot{\varepsilon}_0$: start value of strain rate, ΔH: activation enthalpy, v: activation volume for shear flow und a shear stress σ_y, R: gas constant, T: absolute temperature (thermodynamic temperature).

2.3.4. Fracture behavior in slow crack growth

Damage to PE-HD will occur either due to craze-crack failure or due to fracture of the plastically yielded zone after shear deformation. Depending on whether the yield stress or the craze stress is lower, the prevailing micro-deformation mechanism shifts from crazing to shear deformation or vice versa. Crazing is associated with brittle failure and shearing with ductile failure. Thus, transitions in these deformation mechanisms may also be denoted as brittle-ductile fracture transitions. Furthermore, the occurrence of brittle fracture is a safe indicator that craze-crack mechanisms such as SCG and ESC participated in the damage process (section 2.3.6).

There are two possibilities to create internal surfaces in crazing mechanism:

(1) At low temperatures and high strain rates, the characteristic time for disentangling a polymer chain is long and internal surface will be created when the chains break. In this regard, both terms in equation 19 contribute to the surface energy E_{is}.

(2) At elevated temperatures (with respect to T_g) and low strain rates, chain relaxation becomes faster compared to the timescale of deformation processes. Additional internal surfaces will predominantly be formed by intermolecular separation and chain disentanglement. The surface energy is then dominated by the van der Waals contribution γ (Eq. 19) [3].

Since the brittle-ductile transition at elevated temperatures is related to molecular disentanglement phenomena, an increased resistance to crazing and cracking is supposed to be found with increased molecular mass (higher transition temperature and more tie molecules, section 2.1). Longer molecular relaxation times shift the disentanglement transition towards higher temperatures, loading times and lower strain rates. Due to the inherent time dependency, the SCG/ESC mechanisms are dominant at long-time intervals.

Therefore, predominantly brittle failure due to SCG/ESC only occurs, if the external macroscopic stress is appropriate. Qian et. al supposed that predominantly ductile failure results as soon as the external stress becomes much higher than about one-half the yield strength [66]. At that point, a brittle-ductile transition due to a transition from the craze-crack to the shear deformation mechanism occurs. Consequently, tests to examine SCG/ESC behavior have to be performed at low external stresses. In this respect, Qian et al. recommended to apply stresses lower than one-half of the yield strength. However, the results obtained in this study indicate a direct relation of the brittle-ductile transition to the yield strength (sections 5.3.2 and 5.3.3).

It has to be noted that rapid crack propagation (RCP) also leads to brittle failure generated by shock stress (e.g. in Charpy impact tests) [53, 67] and smooth, flat fracture surfaces are obtained. Therefore, they are termed truly brittle fracture surfaces. In differentiation to this, fracture surfaces that result from slow crack growth mechanisms should be termed brittle-like or pseudo-brittle. They might expose macroscopically brittle surfaces but are not truly brittle compared to RCP. This can be concluded from the occurrence of microscopic fibrillar structures that are noticed on SCG/ESC fracture surfaces obtained by scanning electron microscopy (SEM). Such fibrillar structures indicate a microscopically ductile failure (section 5.1.3). In contrast, RCP fracture surfaces also exhibit flat and brittle features on this smaller, microscopic length scale. In this study, mainly SCG/ESC phenomena are addressed that may result in macroscopically brittle and microscopically ductile fracture. Therefore, SCG/ESC fracture behavior is referred to as 'brittle' for the sake of simplicity. If the microscopically occurring brittle fracture behavior resulting from RCP is especially intended to be addressed, it is henceforth referred to as 'truly brittle' fracture. From these considerations, an assignment of damage mechanisms and fracture surface appearances becomes evident: RCP leads to truly brittle, SCG leads to brittle and shear deformation (SD) results in (macroscopically) ductile fracture surfaces.

In SCG/ESC test methods (section 2.5), only one of the damage periods, crack initiation or crack propagation, is commonly in focus. To examine crack propagation caused by the craze-crack mechanism, a defined imperfection (notch) is usually introduced into the specimen to cause crack initiation prior to loading. Therefore, the contribution of crack initiation (e.g. to the failure time) is deliberately omitted in such tests. The force applied takes effect perpendicularly to the direction of the notch. However, cracks propagate within the notch plane. Due to a reduction of the residual fracture surface area and an associated increase of the local mechanical stress, brittle as well as ductile fracture behavior occurs during a test (first brittle, then ductile behavior) [62, 68]. Hence, a distinct fracture surface exhibits characteristic features of craze-crack mechanism (macroscopically brittle) as well as shear deformation (final failure, macroscopically ductile). Therefore, the overall classification of a fracture surface is essentially ascribed to the failure mode (craze-crack or shearing) which dominated under the given conditions and predominantly led to fracture of the material [11].

In practical testing, conditions have to be selected that lead to predominantly brittle fracture surfaces of specimens on a macroscopic length scale since their occurrence is the prerequisite to consider the

test as representative for SCG/ESC. In this respect, the initial stress applied to a specimen is crucial. In FNCT, the integral transition from predominantly brittle to ductile fracture surfaces can be determined by a plot of actual initial stress applied σ_L over a broad range vs. time to failure t_f (Fig. 6) [13].

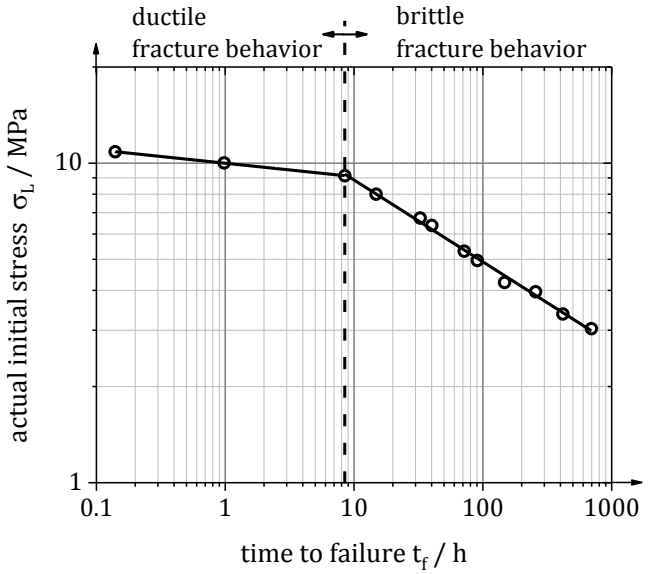

Figure 6: Typical stress-time to failure curve of a PE-HD container material over a broad range of actual stresses applied, according to ISO 16770 [13].

SCG/ESC behavior with typical brittle fracture surfaces is attributed to the strong decreasing linear part at lower stresses and higher failure times (Fig. 6) in the double-logarithmic depiction of time to failure t_f and initial stress applied σ_L. Due to a significant t_f difference at higher/lower σ_L, the transition point ('knee' in the curve) can usually be identified easily.

2.3.5. Time laws of crack growth

Crazing and the subsequent craze-crack transition are functions of stress, temperature (sections 2.3.2 and 2.3.3) and time [9]. The time-dependent behavior of SCG/ESC is described by Brown and Lu [11] with respect to the crack tip opening displacement (CTOD) δ as depicted in figure 7. According to this model, the steep increase in CTOD at the beginning of SCG/ESC is due to the initial craze formation at the tip of the defect (e.g. notch, scratch), the quick growth to an initial value δ_0 and a plastic deformation in the adjacent zone of the material when the specimen is loaded. The CTOD increases further due to crazing with a constant rate $\dot{\delta}$ until fracture of the crazes is initiated at the time t_B with a corresponding displacement δ_B. At this point, crazes start to break, and the growing crack is formed (craze-crack transition). This leads to a slight, continuous increase of the slope of the CTOD vs. time curve. The acceleration for $t > t_B$ is ascribed to the increase of stress intensity during crack growth and $\ddot{\delta}$ in this range is regarded as a measure for the slow crack growth. The results of FNCT elongation measurements and crack growth rates obtained in this study reveal that such a change in the slope of the constant craze-crack growth region at t_B was not confirmed (cf. sections 3.2.2, Fig. 26 b, c and 5.3.1, Fig. 64). To a greater degree, crazes and cracks are indicated to propagate concurrently after the first crazes were formed in region I (section 5.3.2).

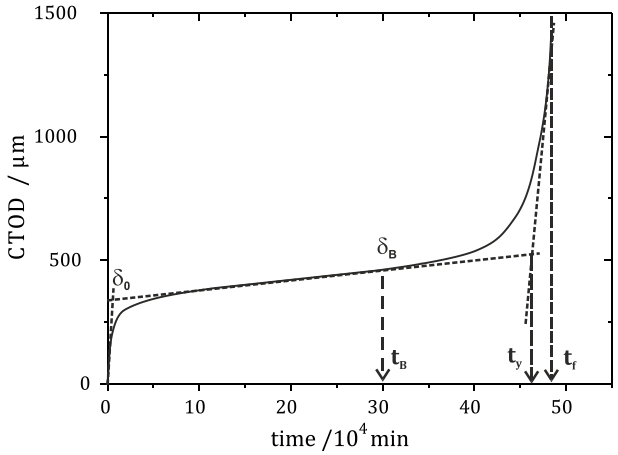

Figure 7: Behavior of time-dependent crack tip opening displacement (CTOD), after [11, 62].

The drastic increase of $\dot{\delta}$ when the total failure at t_f is approached is usually attributed to a transition to ductile behavior since the local stress (true stress) at the decreasing residual cross-sectional area exceeds by far that of the brittle range and leads to yielding (section 2.3.3) over the remaining cross-section at t_y. This often results in the formation of an elevated ligament in the center of the fracture surface.

Hence, the resistance to SCG and ESC is essentially determined by the mechanical strength of the fibrils in the craze zone. Mainly two mechanisms can be related to the rupture of these fibrils (section 2.3.4): (a) breaking of covalent bonds of a stretched polymer chain or (b) disentanglement of polymer chains. For non-crosslinked materials such as PE-HD, mechanism (a) is only applicable to tie molecules anchored in crystal lamellae on opposite sides of the growing crack, while (b) introduces a significant time-dependence due to the relation to chain mobility on segmental and longer length scales. The latter is therefore determined by the length of the chain molecules, i.e. the molecular weight of the polymer or the fraction of long chains in the molecular weight distribution, and the molecular architecture, i.e. long and short chain branches (LCB, SCB) [69, 70, 71, 72, 73].

Generally, a low concentration of tie-molecules makes the disentanglement of polymer chains the dominating mechanism that determines the strength and the time-dependent behavior of the fibrils in the craze-zone [5]. It has to be noted that chemical variations of polyethylene, i.e. molecular weight distribution and short chain branching (by introducing comonomers), affect all determining factors at the same time such as crystal size, tie molecules and overall morphology as well as the formation of entanglements and chain mobility for their release [62].

2.3.6. Slow Crack Growth and Environmental Stress Cracking

In this section, a differentiation between the related phenomena SCG and ESC is given in dependence on the type of polymer and environmental influences.

Failure due to slow crack growth phenomena (SCG/ESC) is commonly observed for PE-HD pipes but it is also relevant for other critical high-performance applications such as geosynthetic barriers (geomembranes, GBR-P) and containers. Failure of components in such fields of application is typically a safety relevant issue.

SCG occurs, if a surrounding fluid does not or only slightly affect the failure mechanism. If the fluid has a significant influence on the course of failure, e.g. on the time to failure t_f, it should be termed ESC. Therefore, SCG behavior can be regarded as an intrinsic property of a polymer, whereas for ESC behavior, the influence of the fluid in contact is essential. The molecular and morphological

origins of the resistance of a polymer to SCG and ESC are essentially the same. Hence, it can be expected that a polymer with a good resistance to SCG also exhibits a good ESC resistance. In scientific literature, the term 'stress corrosion' is also used for polymers in analogy to damage mechanisms obtained in metals or inorganic glasses. However, this seems misleading because the regarded failure mechanism in polymers does not involve any chemical degradation but only physical interactions.

ESC in PE-HD and other polymers

In amorphous glassy polymers, such as polystyrene (PS) and poly(methyl methacrylate) (PMMA), the molded-in internal stress is often sufficient to induce SCG/ESC failure without any external load. Therefore, SCG/ESC failure often occurs spontaneously in such glassy materials without having shown any pre-damage [14]. Internal stresses that lead to ESC in such polymers are often caused by diffusion-controlled sorption and swelling phenomena in the amorphous polymer matrix with limited molecular mobility in the glassy state.

In semi-crystalline polymers above T_g such as PE-HD, the crack growth at a certain stress level primarily depends on the strength of the fibrils in the craze zone. At this point, the influence of an external fluid (environment) may take effect. This can reduce the surface energy of the PE-HD. As a consequence, the energy required to create new (internal) surfaces is reduced (section 2.3.2). Therefore, the craze-crack mechanism may be facilitated. Due to an enhanced porosity in the craze region (free volume), a fluid can furthermore easily penetrate and at least partially plasticize the fibrillary structures. This influence is also indicated by red arrows in figure 5 (section 2.3.2) . Since the fluid enhances molecular mobility, a premature breakdown of the fibrils leads to a significantly accelerated crack growth [17]. The plasticization is a purely physical phenomenon affecting the intermolecular van der Waals interaction between the polymer chains. No chemical modification or degradation is involved in the failure mechanism itself, although a pre-existing chemical and structural damage may have a distinct influence on the fracture behavior. Since the ambient fluid has a significant effect on the stress cracking behavior, it is appropriate to denominate this phenomenon explicitly as environmental stress cracking (ESC).

Many different liquids lead to an acceleration of the SCG/ESC mechanism, especially alcohols and surfactants. As consequences for PE in practical applications, two aspects are of primary importance: (1) the design of fast and efficient test procedures for SCG and (2) the demand for test compatibility with various liquids and chemicals considering ESC.

One of the most important critical and demanding applications of PE-HD with respect to long-term performance and reliability is pipes, for which stress cracking (mainly SCG) is a major concern. Traditionally, PE-HD pipes are assessed by hydrostatic pressure tests in water at elevated temperatures (ISO 1167-1 [74], ISO 1167-2 [75], ISO 9080 [76]). In these tests, specimens without notch are used, i.e. crack initiation contributes massively to the test duration. Therefore, test times often exceed 1000 h considerably. This is awkward in the development process of novel optimized materials. The observed acceleration of SCG by some liquid environments was utilized to design more efficient test procedures as alternatives to the hydrostatic pressure test. In order to provide a sound basis for reproducibility, well-defined and pre-conditioned ('ripened') aqueous nonionic surfactant (detergent) solutions are specified in the corresponding standards [7, 13, 77].

These test procedures are based on ESC but explicitly address the SCG behavior (section 2.5.4). Although both failure mechanisms are closely related, this is an important difference. As a 'neutral' acceleration of SCG is intended to assess an intrinsic PE-HD property, the liquid is not in the focus of the test. It is only used to ensure identical and reproducible accelerated test conditions. At the same time, the ranking of different PE-HD materials is supposed to be retained (i.e. 'neutral'

acceleration), independent of the exact type of fluid (surfactant, detergent) applied. It has to be noted that this is not always achieved (section 2.3.7).

Another relevant question in terms of the ESC failure mechanism is the extent of the accelerating influence of different liquids on the stress cracking. Thereby, the applications in which the PE-HD material may get in contact with such liquids are clearly focused, as e.g. in packaging, containers for liquids, pipes and geosynthetic barriers.

The strength of crazes is significantly influenced by a fluid in contact. In addition to the effects caused by the reduction of surface energy (section 2.3.2), it is assumed that the disentanglement of polymer chains is facilitated by an increase in molecular mobility due to the plasticizing effect of the fluid. Such a plasticization is based on the reduction of the cohesive energy of the amorphous polymer matrix. The direct interaction of polymer chains is partially replaced by interactions with the plasticizer, which can be an additive or a penetrant. Crystalline regions have to be regarded impermeable and are therefore not directly reached and affected by liquids [8].

2.3.7. Influence and categorization of fluids

Especially regarding the differentiation of SCG and ESC, the influence of environmental fluids on these damage mechanisms is considered in detail and fluids are categorized. First efforts in the categorization of fluids according to their influence on SCG were made by Ayyer et. al., when air and water were denominated 'inert' [78]. Previously, fluids such as air and water were simply referred to as 'non-aggressive environments' [9].

Based on the results obtained from the systematic assessment of the influence of different fluids on SCG phenomena in this study, an enhanced and profound fluid categorization is proposed (section 5.1). Therein, air is considered to be inert leading to pure SCG. Water might not have an influence on the failure mechanism or the brittle-ductile transition, but a reduction of the time to failure t_f compared to air independent of the PE-HD type is observed. Thus, water is referred to as a neutrally accelerating fluid (Fig. 56). For surface-active irregular accelerating liquids such as surfactants (detergents), the mechanism is changed to ESC because the liquid plays a decisive role. Thereby, a significant acceleration of failure (reduction of time to failure t_f) is observed and the brittle-ductile transition region (with respect to stress) as well as the ranking of different PE-HD types may change. Frequently, aqueous surfactant solutions are used as standard test fluids (section 2.5.4) with the intention to address SCG. However, considering the actual failure mechanism, ESC occurs in these cases. Furthermore, such surfactants are regarded as the most aggressive liquids causing accelerated crack growth [9, 14, 79].

Special attention has to be paid to liquids which lead to a mass uptake by the polymer ('sorptive, bulk-active' fluids). Since liquids affect the crack growth, a differentiation has to be made whether the liquid is absorbed by the bulk material (amorphous fractions in semi-crystalline polymers such as PE) to a significant extent. Important parameters in this respect are the equilibrium concentration (saturation) of the plasticizing agent under the given conditions and its rate of sorption determined by its diffusivity (section 2.2.2). In this context, surface-active liquids (e.g. detergents) are often considered to interact only at the surface, i.e. at the surface of the fibrillary crazes. Sorptive liquids are able to additionally influence the bulk material. Therefore, a distinction between surface-active and sorptive, bulk-active liquids is suggested (section 5.1.3). For the latter, a pre-saturation of the bulk and its potential effect on the ESC behavior has to be taken into account when considering the performance of materials. In case of a pre-saturated bulk, sorptive liquids may already have an effect on the early stages of ESC, e.g. the formation of voids and crazes. The effective concentration of the absorbed liquid within the polymer depends on the overall exposure time and the limiting saturation

concentration, mainly determined by the chemical nature of the liquid and the polymer (e.g. polarity and molecular weight) [53, 67].

The categorization of fluids in this study only refers to SCG/ESC mechanisms which represent pure physical phenomena. It is especially not meant to consider chemical effects. The fluids presented may also affect PE-HD chemically, but not within the regarded timescales, which are too low to make chemical effects evolve. Therefore, long-term chemical influences of fluids are not in the focus. Furthermore, common stabilized PE-HD materials commercially available are used in this study to reliably exclude interfering influences by long-term chemical degradation phenomena and to ensure a high practical relevance (section 4.1).

2.4. Fracture mechanics

In this chapter, the basic concepts of fracture mechanics that are relevant in this study are presented briefly.

Mechanical properties of polymers are heavily affected by temperature, strain rate and the applied load during testing. Accordingly, the load-elongation curve at a constant strain rate changes with increasing temperature (Fig. 4). Factors influencing the transition from brittle to ductile fracture behavior as well as factors that are further involved in necking and cold-drawing have to be considered. Ductile and brittle behavior may be defined from the stress-strain curve (Fig. 4). Brittle behavior is designated, when a specimen fails at its maximum load at comparatively low strains (about < 10%, Fig. 4, curve 1). In contrast, ductile behavior exhibits a peak of load followed by failure at a lower stress (Fig. 4, curve 2, also curves 3 and 4 after necking, cold-drawing and homogeneous deformation).

However, the differentiation between ductile and brittle failure is also manifested in two other different ways: the energy dissipated in fracture and the nature of the fracture surface. The former is an important consideration for practical applications and the basis of impact tests (e.g. Charpy test). Using the appearance of the fracture surface as an indication for the distinction between brittle and ductile failure is also common practice. Although this approach is empirical, it represents a powerful tool in the fracture surfaces analysis and fracture mechanics [28].

2.4.1. Griffith fracture theory

The understanding of fracture behavior of brittle materials originates in research on the brittle fracture of glasses by Griffith [80]. His fracture theory represents the first consideration of linear elastic fracture mechanics (LEFM) that has been applied to the fracture of all common materials. It is appropriable for fracture processes that include localized plastic deformations at a crack tip and which do not lead to general yielding within a specimen.

According to the theory, fracture was anticipated to produce new surface area in a specimen. Therefore, it was assumed that the increase in energy required to create this new surface has to be balanced by a decrease in elastically stored energy. Furthermore, it was proposed that the elastically stored energy is not distributed uniformly throughout the specimen but concentrated locally around small cracks. As a consequence, fracture occurs due to spreading of cracks that originate in defects (section 2.3). Crack growth is associated with an amount of work dW raised on the system by external forces and with a change in the elastically stored energy dU. The difference of these energy values is available for the creation of new surfaces. Hence, the condition for the growth of a crack by a length dc is (Eq. 23):

$$\frac{dW}{dc} - \frac{dU}{dc} \geq \gamma \frac{dA}{dc} \quad (23)$$

with γ: free energy per unit area of surface (section 2.3.2), dA: associated increment of surface. Without a change in the overall extension ε during crack propagation, dW = 0 and

$$\left(\frac{dU}{dc}\right)_{\varepsilon} \geq \gamma \frac{dA}{dc} \quad (24).$$

The change in elastically stored energy (dU) can be calculated by using a solution obtained for a plate pierced by a small elliptical crack that is stressed perpendicularly to its major axis. As a result, the fracture stress σ_B of the material is defined in terms of the crack length 2c by (Eq. 25):

$$\sigma_B = \left(\frac{2\gamma E^*}{\pi c}\right)^{\frac{1}{2}} \quad (25)$$

with E*: 'reduced modulus' equal to Young's modulus E for a thin sheet in plane stress and equal to $\frac{E}{(1-\upsilon^2)}$ with υ: ratio of Poisson for a thick sheet in plane strain [28]. Typical experiments for the fracture mechanical analysis of crack propagation involve the determination of the specimen deflection or load for a given crack length correlated to the surface energy γ [81, 82, 83].

2.4.2. Irwin model

Due to the Irwin model, the fracture mechanical issue of crack propagation can be addressed by a stress field near an idealized crack length 2c [84]. Hence, applied stresses and crack propagation are directly correlated. In the Irwin model approach, stress fields in the crack region are identical in shape for all types of loading situation normal to the crack. Stress intensity is determined by the constant for given loads and geometry K_I, which is termed stress intensity factor. The superscript I indicates a loading condition normal to the crack.

For crack opening mode I and an infinite sheet with a central crack of length 2c subjected to a uniform stress σ, the relation of K_I is:

$$K_I = \sigma(\pi c)^{1/2} \quad (26).$$

When the external stress σ reaches the fracture stress σ_B, K_I has the critical value (Eq. 27):

$$K_{IC} = \sigma_B(\pi c)^{1/2} \quad (27).$$

K_{IC} is the critical stress intensity factor defining the stress field at fracture. Incorporating the Griffith formulation (Eq. 25) and defining the fracture stress, equation 27 can be expressed as (Eq. 28):

$$\sigma_B = \left(\frac{{K_{IC}}^2}{\pi c}\right)^{\frac{1}{2}} \quad (28).$$

2.4.3. Dugdale plastic zone model

A large discrepancy between theoretical and experimental values for surface energies γ led to the proposal to include a term into the surface energy arising from the plastic work when deforming a material as a crack propagates [82, 85, 86]. Therefore, it was suggested to describe the fracture of polymers by the surface work parameter J (termed 'surface work parameter' to differentiate it from the true surface energy). Additionally, a generalized theory of fracture combining viscoelastic and plastic deformation was proposed by Andrews [87]. The largest contribution to the surface energy

of polymers was concluded to emerge from a viscous flow process, which is related to interference bands on the fracture surface. Energy is required to align polymer chains ahead of a crack and subsequent crack growth leaves a highly oriented layer of polymer material on the fracture surface. Following these ideas, a small wedge of porous material forming at a crack tip was found which is denoted as craze. A craze is formed under plane strain conditions (section 2.5.4). Hence, the polymer is not free to contract laterally and its density is reduced [28, 57, 88, 89]. The craze profile in polymers was found to be similar to the Dugdale plastic zone model for metals [90]. Since practically the stress at a crack tip cannot be infinite, two alternative results are possible. On the one hand, a zone in which shear yielding of the polymer occurs could be present for plane stress conditions in thin and plane strain conditions in thick sheets. On the other hand, for plane strain conditions in thick sheets, the stress singularity at the crack tip can be released by the formation of a craze. This exhibits a line zone in contrast to oval (plane stress) or kidney-shaped (plane strain) shear yield zones [90]. A constant stress σ_c identified as the craze stress is assumed, which is not the yield stress (Fig. 8). Accordingly, shear yielding and crazing are different in nature and they respond differently to changes in polymer structure.

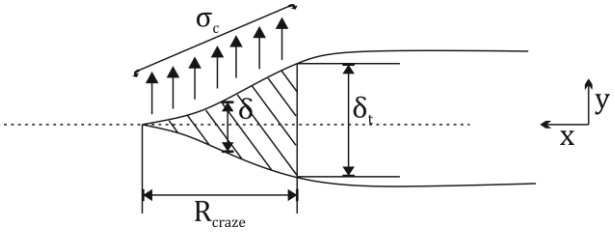

Figure 8: Dugdale plastic zone model for a craze (according to [28, 90]); σ_c: craze stress, R_{craze}: length of craze zone, δ: separation distance between upper and lower craze surface, δ_t: crack opening displacement (COD).

Applying the Dugdale plastic zone model for a craze (Fig. 8), the length of the craze for a loaded crack on the point of propagation can be derived from (Eq. 29) [91]:

$$R_{craze} = \frac{\pi}{8}\frac{K_{IC}^2}{\sigma_c^2} \tag{29}$$

with R_{craze}: length of the craze zone, σ_c: craze stress, K_{IC}: critical stress intensity factor. The corresponding crack opening displacement (COD) δ_t is the value of the separation distance δ between the upper and lower surface at the crack tip and (Eq. 30):

$$\delta_t = \frac{8\sigma_c R_{craze}}{\pi E^*} = \frac{K_{IC}^2}{\sigma_c E^*} \tag{30}$$

with E^*: 'reduced modulus' equal to Young's modulus. Thus, the fracture toughness of the polymer is related to the parameters δ_t and σ_c.

Following this approach, a deeper understanding of the brittle-ductile transition in polymers can be generated concerning the competing effects of yielding and crazing. Both are activated processes with different temperature and strain rate dependencies. According to external conditions, either one process is the dominating effect during fracture. The crack travels a line of zero shear stress but maximum triaxial stress within the plane. Such stress fields favor crazing and the craze length is determined solely by the requirement for the craze to grow in order to cancel the stress singularity at the crack tip (Eq. 29) [28].

Since extensive yielding should not occur during failure processes including crazing, brittle fracture is a prerequisite for respective analysis. Furthermore, presented models are directly applicable to polymers commonly exhibiting brittle failure. Practically, such fracture occurs under plane strain

conditions for specimens of minimum thickness or within small specimen regions. Appropriate conditions can be assumed in dedicated test methods (e.g. full-notch creep test, section 2.5.4).

When large-scale yielding occurs at the crack tip, the fracture mechanical description of polymers has to be extended by the J-integral, which is based on Griffith and Irwin theories.

The J-integral approach was introduced for semi-crystalline polymers defining a quantity [92], which describes the flow of energy into the crack tip region [28, 93]. Hence, polymers exhibiting ductile fracture behavior can be described applying J-integral. However, if brittle fracture is ensured to occur in plane strain conditions, the J-integral approach will provide equivalent results compared to Griffith and Irwin models for amorphous and semi-crystalline polymers [94, 95, 96]. Therefore, the application of the J-integral is redundant in this study.

2.5. Test methods addressing crack growth

Several mechanical test methods were developed over the last decades to gain information about SCG and ESC. Some methods only aim at obtaining values of failure time for practical reasons, such as in quality control purposes. Others are especially designed to provide a deeper understanding of failure mechanisms. Furthermore, due to their setup, some tests primarily address the crack initiation whereas others focus the crack propagation (craze-crack mechanism). Accordingly, results obtained from such tests (e.g. time to failure values) have to be rated with respect to the phenomena they were aiming at (crack initiation or propagation).

A selection of test methods most frequently used is given. The compilation ranges from simple bending tests across insertion methods to tests of notched specimens under constant tensile load. Since they were applied in this study, the Bell telephone test (BTT) and the full-notch creep test (FNCT) are especially considered (sections 2.5.1 and 2.5.4).

2.5.1. Bell Telephone Test

When the consideration of stress cracking phenomena (section 2.3.1) first arose, the simple bent strip method was introduced by DeCoste, Malm and Wallder in the early 1950s [97]. Originally, it was used to investigate failure of PE that occurred during cable sheaths production. It was developed further on at the Bell Telephone Laboratories into the Bell Telephone test (BTT) [98]. In 1970, this was turned into ASTM D1693, which is still in use [99, 100].

For BTT, a PE-HD test strip (nominal dimensions of 38 mm x 13 mm) is cut from a pressed sheet (Fig. 9 a). A controlled imperfection is introduced centrally into one surface of each specimen with a razor blade. Afterwards, 10 specimens are clamped into an especially designed stainless steel specimen holder (Fig. 9 b). The assembled holder is introduced in a test tube filled with fluid (Fig. 9 c). Damage of specimens is defined as the first visible crack that appears and it is evaluated by optical analysis with the eye. Cracks are supposed to develop at the controlled imperfection and run perpendicularly to the outer edge of the specimen. When damage is induced in at least half of the total number of specimens, the test time is recorded [99, 100]. This time to damage is used as a measure of ESC resistance (ESCR).

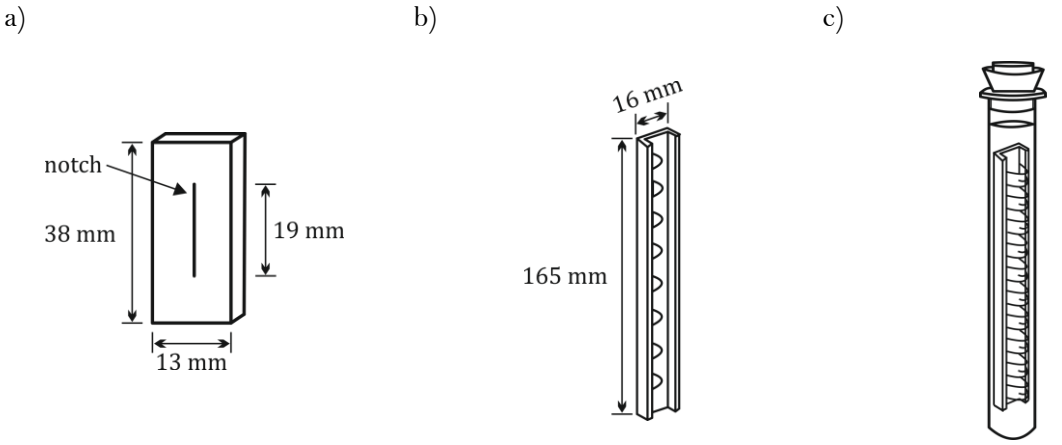

Figure 9: Schematic depiction of BTT equipment; a) test specimen, b) specimen holder, c) test assembly (after ASTM D1693 [99]).

BTT is intended to be used for quality control purposes and not for direct application to engineering problems. It is supposed to be a quick and easy-to-apply test method to compare PE materials concerning their ESCR. However, the distribution of BTT failure times for nominally identical test specimens under controlled conditions was shown to be approximated by a log-normal distribution. Hence, due care should be taken with its results [77].

It has to be noted that BTT is supposed to predominantly address crack initiation during ESC. Although crazing and a coherence to craze-crack mechanism (section 2.3) is indicated in the ASTM, crack growth is not focused explicitly. Moreover, applied stress decreases with time due to relaxation processes within the polymer since no stress (force) adapting device is part of the BTT setup. Hence, constant force conditions are not ensured. Therefore, BTT seems to be unsuitable for describing ESC crack growth but it is capable of providing information on crack initiation [101].

2.5.2. Bending Tests with defined curvature

BTT was soon improved especially in terms of reproducibility by introducing a precisely defined imposed curvature of test pieces. Some methods use test strips which are fastened to constant radius jigs. After fluid exposure, crazing is examined. In other methods, constant radius patterns are applied, and tensile strength and elongation of specimens are measured after the test. Besides constant radius patterns of different radii, patterns with a radius varying over its length (multi-radius patterns) are applied. Parabolic and elliptical patterns are used to measure the critical crazing strain. However, a constant radius is favored over multi-radius patterns because it allows for more exact measurements of physical properties after fluid exposure [77].

Alternatively, a three-point loading test is applied. The loading jig is arranged in such way that the central loading bar is tilted relatively to the plane of the outer two bars. The device commonly incorporates ten test pieces [77]. Such a test setting results in a range of strains being applied to the test pieces. Hence, each jig represents a multi-strain exposure unit. The test pieces are allowed to recover after fluid exposure. The flexural strength is measured afterwards to characterize degradation.

Two approaches of the development of defined curvature methods are noticeable: (1) the detection of degradation prior to the occurrence of cracks by measurements of physical property changes and (2) the determination of critical strain from exposures over a range of strains [77]. Methods addressing both approaches are defined in ISO 22088-3 [102].

2.5.3. Insertion test methods

Ball or pin impression of ISO 22088-4 [103] are also common methods to apply strain to fluid-immersed test specimens in order to investigate their ESC behavior. An oversized ball or pin is impressed into a prefabricated hole (specified diameter) within a test piece. Concurrently, the specimen is brought in contact with an external fluid. The applied constant strain generates micro-cracks that develop into visible macro-cracks. After a preselected time period, the specimen is evaluated by visual examination and by measurement of its tensile and flexural properties. Hence, the ball or pin impression methods predominantly address crack initiation.

Constant test conditions such as the conditioning time, the temperature and the state of the fluid provide a high test reproducibility. Using balls or pins of progressively larger diameter leads to higher stresses and a reduction of test times. The possibility of using especially prepared specimens as well as product parts is advantageous.

2.5.4. Constant Tensile Load Tests

Several constant tensile load test methods have been developed to investigate the SCG/ESC behavior of polymers. They mainly differ in terms of geometry of specimens and notches and they are predominantly performed in creep test configuration under uniaxial constant load. Test conditions are selected such that brittle fracture characteristic for SCG/ESC (section 2.3) is obtained subsequent to crack initiation, i.e. crack propagation is the dominating effect to be addressed with respect to the time to failure t_f. An overview of the most important methods is given.

Pennsylvania Edge Notched Tensile Test

The Pennsylvania edge notched tensile test (PENT) for PE pipe and fitting resins and products is defined in ISO 16241 [104] and ASTM F1473 [105]. It is performed in air (inert fluid). Therefore, the PENT procedure addresses the SCG behavior of a PE material (section 2.3.6).

PENT specimens are prepared from compression molded sheets. Specimens are notched and exposed to a constant tensile stress at an elevated temperature. The specimen geometry is represented by a bar of (10 x 25 x 50) mm^3 (Fig. 10) [104]. The specimen has three notches, which are the main and two side notches [105]. The latter have a depth of 1 mm but they are allowed to be modified in dependence on a varying specimen thickness. The main notch is 3.5 mm deep. Notches are introduced by pressing a razor blade into the specimen with a speed of less than 0.25 mm/min. It is important to have the side notches coplanar to the main notch (Fig. 10).

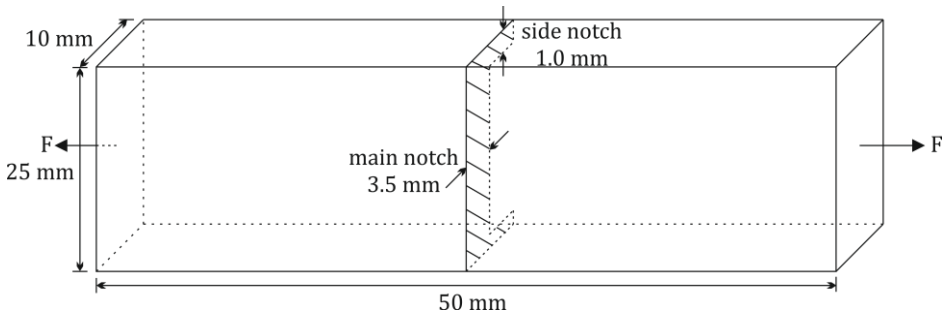

Figure 10: Representative geometry of compression-molded PENT specimen (according to [105]).

PENT is performed at 80°C and a constant load of 2.4 MPa for PE materials. Time to failure is recorded as a measure of SCG resistance (SCGR). It may also be performed at lower temperatures

and higher stresses, but the preclusion of ductile and the induction of brittle fracture has to be maintained. Furthermore, PENT can also be aborted prior to failure, e.g. in quality control processes, after a required test time is reached. This method is commonly applied for tests of compression-molded specimens, but specimens cut from products may also be used. This is advantageous concerning material evaluation close to actual application conditions.

The time to failure depends on temperature, stress, specimen geometry and notch depth. To obtain comparable results, these parameters have to be selected equally in several test series. An increase in temperature, stress and notch depth leads to a decrease in time to failure.

Notched Constant Tensile Load Test

The notched constant tensile load test (NCTL) formulated in ASTM D5397 [106] is a method for the ESCR evaluation of polyolefin materials such as PE. According to the ASTM standard, it is supposed to provide data from which the susceptibility of polyolefin geomembrane sheets to stress cracking under constant tensile loads and accelerated environmental conditions can be evaluated. Therefore, NCTL addresses the evaluation of ESC behavior [106].

In NCTL, a dumbbell-shaped specimen (Fig. 11) is cut from a polyolefin sheet, it is notched and subjected to a constant tensile load in the presence of a surface-active agent and an elevated temperature. The time to failure of the test specimen is recorded. A notch is introduced at one surface of the specimen (Fig. 11). Hence, this method can be regarded as similar to a single-notch creep test (SNCT). The depth of the notch results in a residual ligament thickness of 80% of the nominal specimen thickness t_n of 2 mm.

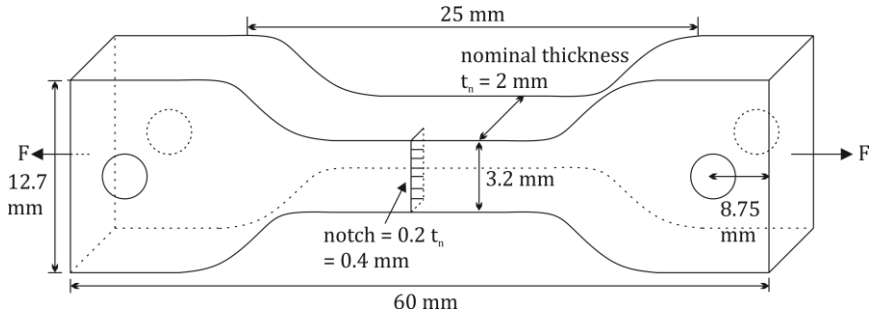

Figure 11: Schematic representation of NCTL specimen according to [106].

Specimens are loaded in a stress cracking apparatus that attributes creep test configuration at a stress of various portions of their room temperature yield stress values. The applied stress levels range from 20% to 65% of the yield stress at maximum increments of 5%. For PE, the test is performed at 50°C in a fluid bath completely immersing the specimen. A conditioning time of at least 30 minutes is used. The test apparatus consists of a temperature-controlled fluid container, in which the surface-active solution is constantly agitated to provide a uniform concentration throughout the bath. The mechanical load is applied by attaching an appropriate weight for each individual specimen to a lever construction [106]. The time to failure associated with a specified tensile load level provides data to assess and compare different polyolefin materials concerning their ESC behavior. The method is supposed to be an index test to grade polyolefin materials with respect to ESC sensitivity.

Full-Notch Creep Test

The full-notch creep test (FNCT) was originally developed by Nishio and Iimura in the 1980s [107]. It was initially applied as an industrial tool to analyze stress cracking parameters. Later, it was used

in the process of product development and it was introduced as a test method in terms of quality control [108]. Finally, the FNCT was standardized in ISO 16770 [13] and it is nowadays widely applied to polyolefin materials to assess their SCG/ESC resistance. The FNCT is especially used for scientific analysis, development, approval and certification of PE-HD materials. By selecting an appropriate fluid, the FNCT device and procedure can address SCG and ESC.

When the FNCT was developed for the assessment of SCG resistance (SCGR) of PE-HD, quality of the available resins allowed for testing in air and water within reasonable timescales. However, the advent of high-performance PE-HD materials led to test times longer than 1,000 h and an acceleration was sought by using surfactant solutions (detergents). They were found to be most prominent cracking agents for PE [14, 109] (section 2.3.7). Hence, they were defined as model fluids for the assessment of PE-HD in terms of SCG. Following the rigorous definition (section 2.3.6), this changed the damage mechanism to ESC. Since the physico-chemical properties that determine crack growth are similar to a certain extent, this is usually accepted to be representative for SCG as well.

In FNCT, a test specimen is subjected to a static tensile load in a temperature-controlled environment. A specimen has the shape of a square-section bar with central coplanar notches in each face, i.e. a circumferential notch is cut centrally into the lateral surfaces (Fig. 12). Since the occurrence of brittle fracture is a prerequisite to address SCG/ESC behavior (section 2.3.4), the specimen geometry is such that plane strain conditions are obtained. Brittle fracture occurs after a certain exposure time under appropriate tensile load and temperature conditions. Plain strain conditions are sought to be obtained as they lead to the occurrence of micro-voids that turn into crazes and cracks (craze-crack mechanism) as in SCG/ESC mechanisms [28]. Furthermore, they usually correspond to the conditions under which PE is used in engineering applications [110]. Final failure occurs to the FNCT specimen after a transition from craze-crack mechanism to shear deformation that naturally appears due to an increase in actual stress (sections 2.3.4 and 5.1.1). Since the craze-crack mechanism is however the dominating effect, the recorded time to failure t_f is utilized as a measure of the resistance against SCG and ESC.

Due to introduction of a notch, crack initiation is disregarded but crack propagation and the final failure are in focus in FNCT.

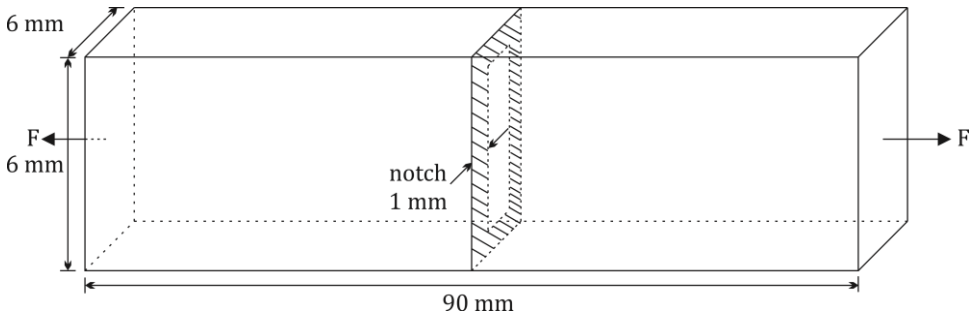

Figure 12: Schematic depiction of FNCT specimen for PE-HD container materials according to ISO 16770 [13].

FNCT specimens (Fig. 12) are prepared by cutting from compression-molded sheets (section 4.1). Molding, cooling and annealing conditions are given in ISO 1872-2 [111], ISO 293 [112], ISO 17855-2 [113] and ISO 16770 [13]. Notches are introduced by a razor blade. Cutting, notching and specimen storage prior to the test are realized at (23 ± 2)°C. A conditioning time of (10 ± 2) h has to be applied prior to loading, when the specimen is clamped in the FNCT apparatus and exposed to the test environment and temperature.

According to specimen C in ISO 16770 [13], FNCT specimen dimensions of (90.0 x 6.0 x 6.0) mm^3 are used for PE-HD blow molding and container materials (Fig. 12). The circumferential notch has a depth of d_{notch} = 1.0 mm. Molded specimens of PE-HD container materials are to be tested at 50°C and a nominal stress σ_n of 9.0 MPa. A detergent (surfactant) is to be applied as test fluid. Typically, Arkopal N 100 is used. Arkopal N 100 is a nonylphenoxy-(ethyleneoxy)-ethanol and commonly applied as a 2 wt% aqueous solution (section 4.2.1).

2.5.5. Alternative Mechanical Test Methods

High-performance PE-HD materials are increasingly resistant to SCG and ESC. This entails long test times within development and quality control processes when conventional mechanical test methods are applied. Therefore, time- and cost-effective test methods were sought within the last decades. In this respect, established methods such as the FNCT were modified by introducing new detergents, by applying higher temperatures and by adjusting mechanical stresses to reduce test times. However, this might be questionable since SCG/ESC could not be the dominating mechanisms and the results might not be comparable anymore (section 5.4).

Besides the approach of improving established methods, alternative test methods were developed. Therein, dynamical mechanical loading is typically favored over static tensile loading to reduce test times. Material rankings obtained by dynamic test methods are usually considered to correlate well to traditional static loading methods such as the FNCT [114]. Two alternative SCG test methods mainly applied to PE-HD pipe grades are presented subsequently.

Cracked Round Bar Test

The cracked round bar test (CRB) [114] was developed to determine the SCG behavior of PE-HD and was turned into ISO 18489 recently [115]. CRB specimens are cylindrical bars with dimensions of 80 mm to 100 mm in length and diameters of 14 mm (Fig. 13). A notch with a depth of 1.5 mm is introduced centrally perpendicular to the specimen axis.

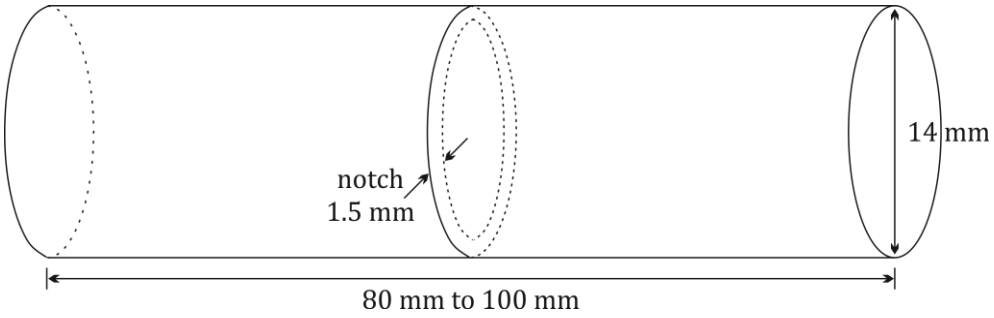

Figure 13: Configuration of CRB test specimen according to [115].

CRB is a cyclic tensile test which involves a constant stress range. The circumferential notch in the center of the specimen enables stress-initiated crack propagation. Crack initiation is neglected due to the introduction of a notch prior to the test. The number of cycles until final failure is recorded as a function of the stress range related to the initial crack length and is taken as a measure of SCGR. Due to high constraints and low plastic deformations along the crack tip, the specimen geometry ensures short test times. The cyclic load follows a sinusoidal waveform. The maximum load, the load ratio and the load-cycle frequency are preset parameters. Their values are based on polymer density. CRB is performed in air and addresses SCG. Typically, CRB is performed at room temperature but testing at an elevated temperature is permitted according to ISO 18489. When an elevated

temperature is used, a conditioning time of at least 2 h is indispensable [115]. CRB conditions are selected appropriately to obtain brittle fracture since this is the prerequisite to address SCG.

Kratochvilla, Frank and Pinter evaluated the usability of CRB to describe the SCG behavior of pressure pipes [116] by comparing results to established classical methods such as the notched pipe test (NPT) [117], double-notch creep test (based on FNCT in accordance with [13]) and instrumented Charpy impact test [118, 119]. For PE pipes, a linear correlation of the results of CRB to the afore-mentioned methods was found in terms of the rankings of PE 100 types. These results denote the CRB as an alternative SCG test method with the advantage of lower test times and temperatures used. Moreover, the results of two independent Round Robin tests certify a high reproducibly and reliability to the CRB in terms of material ranking by SCGR [120]. It has to be noted that any influence of fluids (ESC) is unconsidered in CRB. Thus, CRB is capable of providing information on material rankings concerning SCG only. Therefore, it might be predestinated for PE pipe material testing.

Strain Hardening Test

The strain hardening test (SHT) was also developed as a fast and efficient SCG test method for PE-HD pipe materials [121]. It was turned into ISO 18488 [122] most recently.

SHT is a tensile test performed at 80 °C in air. The test specimen is extended along its major axis at a constant speed of 10 mm/min until failure or until its strain reaches 1200%. The elongation is determined by an optical extensometer. A specimen (Fig. 14) of 0.3 mm or 1.0 mm thickness is punched out of a molded sheet after an annealing process. It has a typical tensile specimen shape (ISO 527-2 [123]) with a minimum overall length of 70 mm and a gauge length of 12.5 mm (according to [121] and [122]).

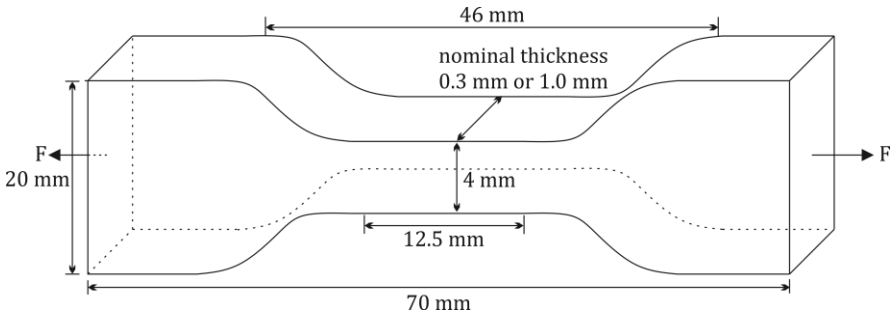

Figure 14: Schematic depiction of SHT specimen according to [122].

For SHT analysis, the draw ratio λ_d is calculated based on gauge length L and it is expressed as a dimensionless ratio (Eq. 31):

$$\lambda_d = \frac{\Delta L}{L_0} + 1 \qquad (31)$$

L_0 is the initial distance between the gauge marks and ΔL is the increase in specimen length. Above the natural draw ratio (NDR, $8 < \lambda_d < 12$), the Neo-Hookean constitutive model (proposed in [122] and [124]) is used to fit and extrapolate the data of the strain hardening part in the stress-strain curve. Therefrom, the strain hardening modulus $\langle G_p \rangle$ as the average difference quotient is calculated (Eq. 32):

$$\langle G_p \rangle = \frac{1}{N} \sum_{i=1}^{N} \frac{\sigma_{i+1} - \sigma_i}{\lambda_{d\,i+1} - \lambda_{d\,i}} \qquad (32)$$

with σ: true stress and λ_d: true strain. $<G_p>$ incorporates all N difference quotients between the onset of the strain hardening part and below the maximum elongation of the stress-strain curve obtained by SHT. $<G_p>$ represents the intrinsic strain hardening and is supposed to be a measure of the SCGR [3, 121].

This correlation implies that the strain hardening response is determined by the same molecular configurations that govern the SCGR as measured in a classical SCG test such as the FNCT [101]. A possible reason for that can be found in the SCGR being proportional to the magnitude of craze stress which is mainly determined by the effective entanglement density of a polymer. Hence, evaluating the effective entanglement density or the amount of load bearing chains (number of tie molecules) is supposed to be the best measure of the intrinsic SCGR of a polymer. Slender molecular backbones and lower chain stiffness favor high entanglement densities and a high SCGR [3]. Stress-strain data were interpreted thermodynamically first in 1968, when the enthalpic yield processes were separated from the entropic network response of strain hardening [125]. Furthermore, the strain hardening part was considered as a purely entropic response of the entanglement network. Consequently, the strain hardening modulus was considered to be proportional to the node density of a polymer. According to an Eyring thermally activated flow process (section 2.3.3), the resistance to failure of a stretched fibril within a craze is proportional to the square of the number of loaded chains and the effective entanglement density. Because $<G_p>$ reflects the effective density of the polymer molecular network (v_e), the critical strain energy release rate is also proportional to G_p^2 with

$$G_p = v_e RT = A\Sigma_e RT \qquad (33)$$

G_p: strain hardening modulus in the solid state, R: universal gas constant, T: temperature, A: constant, Σ_e: amount of load bearing chains. Equation 33 represents the basic assumption for the hypothesis that $<G_p>$ is a valid measure to predict SCGR [3]. For polymers with a high crystallinity such as PE-HD that have strong secondary interactions [61, 126], the strain hardening response exceeds the (rheological) entanglement density.

For amorphous polymers, a linear scaling of $<G_p>$ with the yield stress was found based on theoretical considerations [127] and experimental investigations [128]. The dependency of $<G_p>$ on the yield behavior of a polymer is of major importance, because it implies that the strain hardening contains enthalpic contributions. Therefore, strain hardening scales with the amount of secondary interactions, at least at temperatures far below the glass transition temperature region (T_g) and far below α'-transition for semi-crystalline polymers. The enthalpic effect leads to an overestimation of $<G_p>$ on the one hand but it is time dependent on the other. This is contrary to the entropic part. Hence, longer load times result in disappearance of the enthalpic contributions and $<G_p>$ tends towards its entropic value with decreasing strain rate. Since long-term SCGR and long loading times are to be addressed, strain hardening measurements are supposed to reflect the entropic network contributions and avoid the enthalpic part. Therefore, yield stress and strain rate have to be low [3]. Moreover, the strain hardening becomes independent of strain rate at higher temperatures [129], which indicates an overcome of enthalpic effects. Thus, strain hardening measurements are suggested to be performed at the α-transition temperature of PE to eliminate enthalpic contributions [121]. Consequently, a minor stress is necessary to overcome the crystal coherence [3].

SHT can be applied as an alternative approach for material ranking concerning the intrinsic SCGR, which is confirmed by several studies [8, 121, 130, 131]. The simple procedure, the absence of surfactants and notches and the short test times compared to classical SCG test methods are advantageous [101]. However, the influence of environmental fluids causing ESC is unconsidered in SHT.

3. Experimental

3.1. Methods for material and fluid characterization

In this chapter, the methods are introduced that were applied to characterize the PE-HD materials and fluids in terms of their physical and chemical properties relevant for this study. Especially, data obtained from these characterizations are used for the evaluation of the structure to property relations with respect to SCG/ESC.

3.1.1. Densitometry

The mechanical properties of PE-HD are decisively affected by the degree of crystallinity and the morphology, which are indicated by the polymer density [28, 132]. Therefore, the density of applied PE-HD materials (section 4.1) was determined in accordance with ISO 1183-1 [167]. Specimens were weighed in air and n-heptane (density $\rho_{n\text{-heptane}}$: 0.681 g/cm³) at 23°C applying Archimedes' principle. The analytical balance (MC 410 S, Sartorius, Göttingen, Germany) was equipped with a density determination kit.

Density data were obtained using designated density specimens, FNCT specimens and granules. The density specimens with dimensions of (20.0±2.0 x 20±2.0 x 2.0±0.5) mm³ and a mass of about 1.0 g met the requirements of ISO 1183-1. They had a cavity-free surface to prevent the formation of air bubbles in n-heptane. Density specimens were cut from sheets of 2.0±0.5 mm thickness (section 4.1).

3.1.2. Surface tensiometry

The surface tension of test fluids was determined using the tensiometer K11 MK3 of Krüss GmbH (Hamburg, Germany). Since the surface tension is supposed to correlate to the energy required to create new internal surfaces within a PE-HD material (section 2.3.2, especially Eq. 19), it is considered to have a decisive influence on SCG. The creation of new internal surfaces is part of the craze-crack mechanism. Due to the attractive forces between molecules (cohesion), a characteristic energy is required to change the size of an interface or surface. The interfacial or surface tension is considered as the force that has to be spent to increase the interface or surface area by a specific amount. The term 'surface tension' is used for a liquid bordering to a gaseous phase. The term 'interfacial tension' refers to an interface between two liquids or a liquid and a solid.

The tensiometer determines the surface tension with a measuring probe which is suspended from a force sensor. This probe is a ring or a plate consisting of a material with optimum wetting properties and a high surface energy. Therefore, a platinum-iridium alloy is used for the ring and the plate is made of roughened platinum. During the measurement, the liquid is brought into contact with the probe by adjusting the height of a sample vessel. A force acts on the balance as soon as the probe touches the liquid surface. Using the value of wetted length of the probe, the measured force can be utilized to calculate the surface tension.

Ring method

The ring method (also described in ASTM D971 [133] for two liquids) was developed by Lecomte du Noüy [134]. The test liquid in the sample vessel is raised until contact with the ring surface is realized. The sample vessel is subsequently lowered, which stretches the liquid film lamella created beneath the ring (Fig. 15 a). When this lamella is stretched, a maximum force occurs which is

recorded (Fig. 15 b). At this maximum, the force vector is parallel to the direction of motion and the measured force correlates to the surface tension. The contact angle θ is 0° for a material with optimum wetting properties such as platinum and iridium.

a) b)

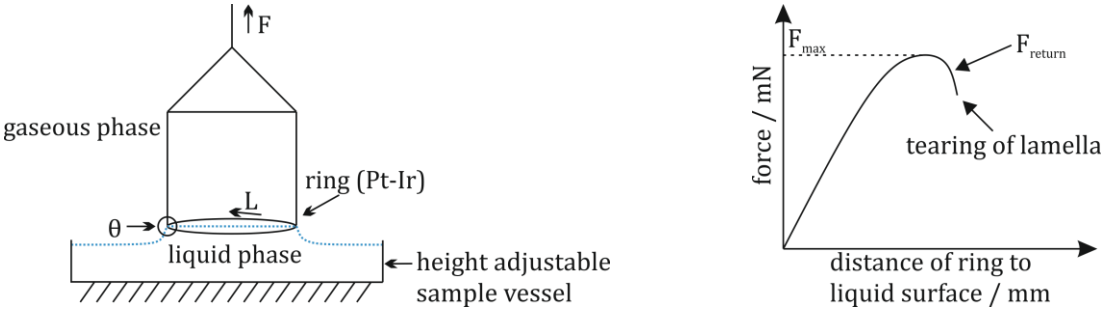

Figure 15: Schematic depiction of the ring method (a) and schematic plot of force vs. distance of the ring to the liquid surface (b).

Practically, the distance between the ring and the liquid surface is increased until the region of maximum force has been covered (Fig. 15 b). Afterwards, the sample vessel is moved down, passing through the maximum of the force for a second time. The maximum force is then determined precisely considering the first as well as the return movement. Tearing of the lamella is avoided during the measurement. The surface tension is calculated according to (Eq. 34):

$$\gamma = \frac{F_{max} - F_V}{L \cos\theta} \qquad (34)$$

with γ: surface tension, F_{max}: maximum force measured, F_V: weight force of raised volume of liquid, L: wetted length, θ: contact angle. The contact angle θ decreases with increasing strain of the liquid lamella and reaches a value of 0°, which results in cos θ = 1.

Correction of ring method measurements

The results of the ring method are influenced by two effects: (1) The weight force of the liquid uplifted underneath the ring (F_V) increases the value detected by the force sensor and has to be subtracted. (2) The flexion of the lamella is higher on the inner than on the outer side of the ring. Hence, the force maximum (at θ = 0°) is not reached at the same time on the inner and the outer side of the ring. Therefore, values obtained by the ring method were corrected according to a method introduced by Huh and Mason [135]. Permitting the highest range of validity, the Huh and Mason correction method provides an accuracy of measuring values of ± 0.19 %. The correction was performed automatically in the tensiometer software.

Plate method

According to the Wilhelmy plate method, the test liquid vessel moved upward at a constant speed to partly immerse the plate (Fig. 16) [136].

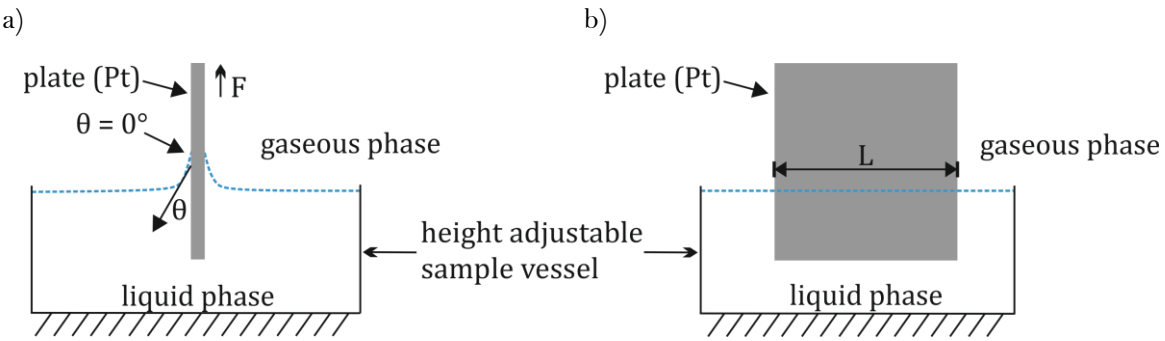

Figure 16: Schematic image of Wilhelmy plate method; plate immersed in liquid during measurements, a) front view, b) side view.

The microbalance sensor measured the force applied to the moving plate. Using algorithms based on the Wilhelmy plate method, the force value and the advancing dynamic contact angle, the surface tension was calculated according to (Eq. 35):

$$\gamma = \frac{F}{L \cos\theta} \qquad (35)$$

with γ: surface tension, F: measured force, L: wetted length, θ: contact angle. The speed of the vessel platform was set to a constant value to maintain a steady motion during the experiment. When the plate moved upwards, the contact angle θ reached 0°, which leads to cos θ = 1. Then, the measured force and the plate length have to be considered only. Due to the plate method setup, no corrections of measured values are necessary.

In this study, surface tension of water, biodiesel, diesel, Arkopal, NB, NBA and NBL was obtained by using the ring and the plate method at 23°C and 50°C.

3.1.3. Gravimetry

To characterize the sorption and desorption behavior, the mass uptake of PE-HD was determined gravimetrically by immersion in diesel, biodiesel, Arkopal, NB, NBA and NBL at 60°C. Due to its high polarity and surface tension, water is expected not to be absorbed by PE-HD. Arkopal is an aqueous solution (2 wt% aq., section 4.2.1) and expected to be absorbed only slightly. Nevertheless, its sorption behavior was determined as well. Specimens applied for gravimetric analysis were round discs milled from sheets (section 4.1). They had a diameter of 80.0±3.0 mm, a thickness of 2.0±0.2 mm and a central hole with a diameter of 10.0±1.0 mm (Fig. 17 a, b). The central hole allowed for fixing the discs on a vertical glass shaft with glass spacers separating the specimens (Fig. 17 c).

a) b) c)

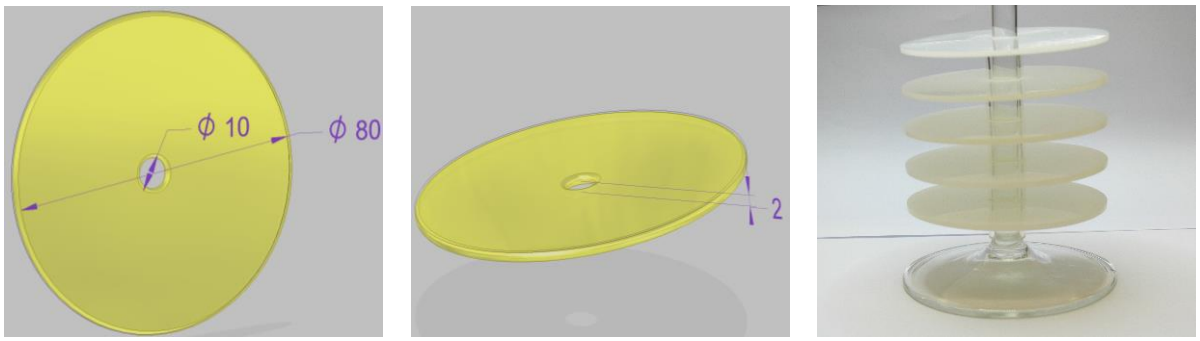

Figure 17: Specimens used for gravimetric analysis, a), b) schematic representations, c) depiction of 5 individual specimens attached to a glass shaft.

Such attached specimens (Fig. 17 c) were immersed in glass jars (height: approx. 20 cm, inner diameter: approx. 10 cm) filled with the test liquid and closed with a PTFE sealed glass lid. The jars were placed in temperature-controlled water baths at 60°C. A temperature of 60°C was selected to induce an accelerated diffusion (section 2.2.2) leading to a faster saturation of the specimens to test within practical timescales (in accordance with [53]). The final equilibrium concentration (saturation) obtained for biodiesel and diesel at 60°C is slightly higher compared to 50°C but sorption effects that depend on the fluids are equivalently evident (section 2.2.1) [53]. The size of specimens was selected to approximate plane sheet geometry but maintain mechanical stability. Considering plane sheet geometry, the polymer in which diffusion occurs is defined only by the two parallel opposing surface planes and fluxes through the edges can be neglected (section 2.2.2). Thus, diffusive transport can be considered as restricted to one dimension [48, 53].

Five identical discs were placed in each jar. To measure the mass uptake, specimens were removed from the jar, dried carefully by a tissue paper, weighed and re-immersed in the jar within less than five minutes. Such procedures were performed at preselected time intervals.

The concentrations C of penetrants are given as mass fractions w by (Eq. 36):

$$C = w = \frac{m - m_0}{m_0} \tag{36}$$

m_0: initial mass of the specimen prior to immersion, m: current mass of specimen measured after certain time intervals.

For the calculation of diffusion coefficients, equation 37 was used, which is derived from Fick's second law and which is based on plane sheet geometry [48, 53]:

$$\frac{M_t}{M_\infty} = 1 - \frac{8}{\pi^2} \sum_{i=0}^{\infty} \frac{1}{(2i+1)} exp\left\{-\frac{D(2i+1)^2 \pi^2 t}{l^2}\right\} \tag{37}$$

M_t: time-dependent mass uptake ($M_t = m(t) - m_0$), M_∞: equilibrium mass uptake ($M_\infty = m(t \to \infty) - m_0$), D: diffusion coefficient, t: time, l: doubled specimen thickness h ($l = 2h$) because diffusion occurs from both sides of the specimen. Diffusion coefficients were obtained by nonlinear curve fitting (included module of Origin software, OriginLab Corporation, Northampton, MA, USA) the mass uptake curves using the first ten terms of the infinite sum in equation 37.

Desorption behavior was determined by measuring the mass loss of the specimens after they had reached their equilibrium mass uptake. Therefore, they were kept at a constant temperature of 60°C suspended freely in an oven with circulating air (UT 6200 of Heraeus Instruments, Heraeus Holding GmbH, Hanau, Germany).

Moreover, sorption procedure was applied for the preparation of saturated specimens for subsequent FNCT (section 3.2.2). Therefore, FNCT specimens were immersed in sorptive liquids diesel and biodiesel until they reached the equilibrium mass uptake. The mass uptake of these specimens was measured on a regular basis. When they reached the equilibrium mass uptake, they were immediately tested in FNCT.

3.1.4. Spectrophotometry and colorimetry

The fracture surfaces of FNCT specimens tested in sorptive fluids exhibited a characteristic coloration. UV/visible spectrophotometry was applied to characterize the color of such surfaces objectively by distinct spectrophotometric values.

Therefore, a visible light reflectance spectrophotometer (CM-2600d of Konica Minolta, Konica Minolta Business Solutions Deutschland GmbH, Langenhagen, Germany) was used in a wavelength range of 360 nm to 740 nm with a wavelength pitch of 10 nm. After illuminating the fracture surface uniformly with white light, the light reflected at an angle of 8° to the normal of the surface was measured. Three pulsed xenon lamps served as light sources and reflectance was measured by a silicon photodiode array detector (dual 40 elements). Prior to all measurements, a calibration of the maximum white level (100% reflectance) and minimum reflectance (zero level) was performed by using the white calibration plate CM-A145 and the zero calibration box CM-A32 included in the spectrophotometer package.

Since FNCT fracture surfaces had to be analyzed omitting interfering light from the environment and all specimens had to be placed equally, a special jig was designed and constructed (design / constructional drawing given in appendix A2 Fig. A2.86). Spectrophotometry was performed to selected FNCT fracture surfaces which showed characteristic colors for distinct systems of PE-HD types and fluids.

Additionally, biodiesel and diesel were characterized by spectrophotometry. Biodiesel and diesel samples were prepared in three aging conditions: (1) unaged (0 a), (2) aged at 50°C for 0.5 a and (3) aged at 50°C for 1.5 a. The spectrophotometry of liquids was performed applying a Varian Cary 300 Scan UV/Vis spectrophotometer (Agilent Technologies Inc., Santa Clara, CA, USA). Liquids were filled in a quartz glass cuvette. An air-filled quartz glass cuvette was used as reference. A base line correction was performed using two air-filled cuvettes prior to the measurements of liquids. The measurements were conducted in a wavelength range of 300 nm to 700 nm with scanning intervals of 1 nm and a signal/noise ratio of 3000 counts.

For FNCT specimens, the measurements were performed in reflection R_{coeff} mode. In contrast, liquids were measured in transmittance T_{meas} mode. To obtain comparable results in terms of wavelength-dependent peak and shoulder positions, the absorbance A_{cal} was calculated in both cases.

For reflection mode measurements, wavelength-dependent spectral reflection data R_{coeff} can be obtained including (SCI) and excluding (SCE) the specular component (gloss). The SCI mode addresses the color change of the entire light reflected from the specimen surface. In SCE mode, only the diffusive fraction of the reflected light is measured. The SCE value is strongly influenced by the surface structure since diffusive and specular fractions vary significantly with surface roughness. However, the sum of the two is considered to be constant. Hence, the SCI mode is independent of the fracture surface texture (gloss) and only sensitive to color changes due to the absorbance of the specimen. Therefore, SCI data were considered in this study. The error values result from the standard deviation of a six-fold reproduction.

For the liquids, the absorbance A_{cal} was obtained directly from the instrument. Using the measured transmittance T_{meas}, the absorbance A_{cal} is defined by (Eq. 38) [137]:

$$A_{cal} = -log\left(\frac{I_0}{I}\right) = -\log\left(T_{meas}\right) \quad (38)$$

with I_0: incident irradiation intensity, I: measured irradiation intensity in transmittance mode.

Due to the conditions in the spectrophotometer, the transmittance T_{meas} of the sample depends on the molar concentration, the light path length and the molar absorptivity of the measured liquid at a specific wavelength. Hence, these parameters are included in the value of A_{cal} in addition to scattering effects (Fig. 45) [138, 139].

The absorbance A_{cal} of FNCT fracture surfaces was calculated from the obtained reflectance R_{coeff} (Fig. 44). For this purpose, the Kubelka-Munk function was used, which is especially capable of describing matte (opaque) and bright colors such as obtained in this study (Eq. 39) [140, 141, 142, 143]:

$$F\left(R_{coeff}\right) = \frac{K}{S_{coeff}} = \frac{(1-R)^2}{2\,R} \approx A_{cal} \quad (39)$$

with $F(R_{coeff})$: Kubelka-Munk function, R_{coeff}: reflectance, K: absorption coefficient, S_{coeff}: scattering coefficient. Absorption and scattering are included in the Kubelka-Munk function (Eq. 39). Therefore, absorbance A_{cal} data obtained from UV/Vis spectrophotometry in transmittance mode for liquids can be compared to reflectance mode measurements of FNCT fracture surfaces.

3.1.5. Gel permeation chromatography

Gel permeation chromatography (GPC) is an established method to characterize the molecular mass (MM) and molecular mass distribution (MMD) of polymers [144, 145, 146]. Since the fractionation of the polymer sample achieved in GPC columns is related to its MMD, M_n and M_w can be calculated from GPC data (Eq. 1 and 2). It has to be noted that the hydrodynamic volume of the polymer (dimensions of polymer bundle) that depends on the solvent used is basically determined by GPC. To obtain the molar mass of the polymer from the retention time in the GPC column, a calibration with standards is essential that have a narrowly distributed molar mass. Due to practical reasons, polystyrene is usually applied as such a standard. Therefore, the obtained MM and MMD values are related to the polystyrene calibration, which is sufficiently exact [29, 147].

In this study, MMD of applied PE-HD types (section 4.1) was determined by a high-temperature GPC device (PL 220 of Agilent Technologies, Santa Clara, CA, USA) equipped with IR4 infrared detectors (Polymer Characterization, S.A., Valencia, Spain). Prior to PE-HD testing, a calibration with polystyrene standards was performed. PE-HD samples were prepared from sheets and as-received granules by dissolving them for two hours in 1,2,4-trichlorobenzene (TCB) with 2 g/l butylated hydroxytoluene (BHT, concentration approx. 1 mg/ml at 150°C). 200 µl of PE-HD solution were measured at 150°C and a flow rate of 1 ml/min.

3.1.6. Differential Scanning Calorimetry

Differential scanning calorimetry (DSC) allows for analyzing the molecular polymer structure since the peaks in DSC curves correspond to endothermic and exothermic events that are associated with structural changes [148]. DSC monitors the amount of heat required to increase the temperature of a specimen relatively to a reference. Therefore, enthalpic changes are measured. If a specimen

undergoes an endothermic phase transition (e.g. melting), heat will be absorbed. An exothermic event (e.g. crystallization) requires less heat to increase the total temperature. Thus, transitions such as melting, crystallization and the glass transition can be studied [145, 148].

In DSC, the heat flow difference of the specimen and the reference is measured as a function of temperature or time during heating or cooling with a constant rate (10 K/min). Accordingly, thermal transitions in the specimen are identified by DSC graphs due to enthalpic changes (ΔH) that depend on temperature changes. For polymers, exothermic behavior (crystallization) results in an increase of the heat flow curve (concave peak) and endothermic events (melting) lead to a decreasing (convex peak) heat flow curve (Fig. 18).

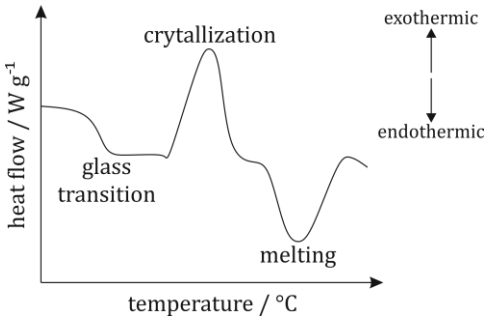

Figure 18: Schematic DSC curve exhibiting thermal events recorded in a polymer, after [145, 146].

The enthalpy of crystallization and melting processes is proportional to the area of corresponding peaks. Since smaller crystals have a lower and larger crystals have a higher melting temperature, the crystal size distribution is described by the DSC curve. The crystallinity of a polymer $X_{c,\,DSC}$ is calculated using the melting enthalpy ΔH_m of the specimen (Eq. 40) [145]:

$$X_{c,DSC}[\%] = \frac{(\Delta H_a - \Delta H_m)}{(\Delta H_a - \Delta H_c)} 100 \qquad (40)$$

ΔH_m: melting enthalpy of the specimen, ΔH_a: melting enthalpy of an amorphous standard (100% amorphous), ΔH_c: melting enthalpy of a (hypothetic) crystalline standard (100% crystalline).

Using the melting enthalpy of a single crystal (ΔH_m^0), crystallization $X_{c,\,DSC}$ can be estimated from (Eq. 41):

$$X_{c,DSC}[\%] = \frac{(\Delta H_m)}{(\Delta H_m^0)} 100 \qquad (41).$$

Since ΔH_m^0 is scarcely temperature dependent, a constant value of $\Delta H_m^0 = 290\ \mathrm{J/g}$ is used for PE-HD [146, 149].

In this study, a DSC 823e (Mettler Toledo, Gießen, Germany) was applied. Specimens were cooled down to -50°C with a cooling rate of 5 K/min and subsequently heated to a temperature of 160°C with a heating rate of 10 K/min (first heating). To perform the second heating period, specimens were cooled again to -30°C (cooling rate of 10 K/min) and reheated with a heating rate of 10 K/min to a temperature of 160°C. DSC specimens were prepared from sheets of 1 mm thickness (section 4.1).

3.1.7. Dynamic mechanical analysis

Dynamic mechanical analysis (DMA) is used to gain information about first (major), secondary and tertiary transitions in polymers [150]. In DMA, an oscillating force is applied to a specimen and the material response is analyzed. Material properties such as the tendency to flow (viscosity) and the stiffness (modulus) can be determined from the phase lag and the specimen recovery. These properties are related to the ability to lose energy as heat (damping) and the ability to recover from deformation (elasticity). In polymers, information on property changes is obtained by the relaxation of chains or changes in the free volume that occur during DMA [150]. Polymers show viscoelastic behavior. Therefore, stress (load) leads to elastic and plastic response. Although one effect could be dominating, DMA is capable of evaluating both of these mechanical property changes.

The stress (or strain) is applied to the specimen at a specific frequency ω. Stress σ and strain ε curves have sinusoidal shape with the amplitudes σ_0 and ε_0 (Fig. 19). Accordingly, time dependent σ and ε can be described as (Eq. 42 and 43) [145, 150]:

$$\sigma(t) = \sigma_0 \sin \omega t \tag{42}$$

$$\varepsilon(t) = \varepsilon_0 \sin(\omega t - \delta) \tag{43}$$

with σ: stress, σ_0: stress at time t = 0, ω: frequency, t: time, ε: strain, ε_0: strain at t = 0, δ: phase angle.

The stress and strain curves differ by the phase angle δ (Eq. 43 and Fig. 19).

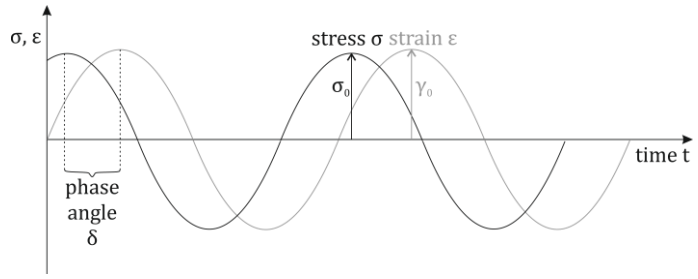

Figure 19: Schematic representation of periodic sinusoidal applied stress curve with strain curve exhibiting a difference of phase angle δ, after [145, 146, 150].

Stress and strain are related by the complex modulus G* which consists of an elastic storage (G', real part of complex) and an imaginary loss (G") modulus (Eq. 44):

$$G^* = G' + iG'' \tag{44}.$$

G' is a measure of the ability of a material to store energy (for a perfectly viscous fluid, G' = 0). G" represents a measure of the ability to dissipate energy (for a completely elastic material, G" = 0). The ratio of these two moduli is denoted as damping and represented by the value of tan δ (Eq. 45):

$$tan(\delta) = \frac{G''}{G'} \tag{45}.$$

Using storage and loss modulus (G' and G"), the complex compliance (J*) and the complex viscosity (η*) can be calculated [145, 150].

DMA can be performed in a range of test modes such as shear, bend, torsion, compression and tension mode [28]. Furthermore, DMA is advantageous due to the capability of measuring a material response over a range of temperatures (temperature sweep) and frequencies (frequency sweep) in a single experiment [145].

In this study, temperature-dependent DMA was performed in shear mode (rheometer of type Ares of TA Instruments, New Castle, Delaware, USA) in a temperature range of -115°C to +120°C. All measurements were conducted using a frequency of 1 Hz and a deflection of 0.05%. DMA specimens were cut from sheets of 1.0±0.3 mm thickness (section 4.1). Specimen dimensions are given in figure 20 and table 1. Three DMA measurements were performed for each PE-HD type.

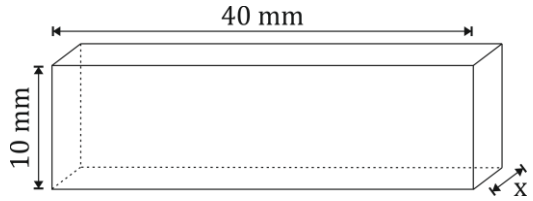

Figure 20: Schematic depiction of DMA specimen with dimensions.

Table 1: Thicknesses of DMA specimens.

PE-HD type (section 4.1)	specimen thickness x (Fig. 20) / mm
AGUV	1.23
AGBD	1.10
AQ149	1.26
5021DX	1.18
5831D	1.05

3.1.8. X-ray diffraction

X-ray diffraction (XRD) is a technique to evaluate the structure of crystals [147]. Diffraction occurs when a wave encounters a series of regularly spaced obstacles, which are able to scatter the wave and which have spacings that are comparable in magnitude to the wavelength. Hence, diffraction results from specific phase relationships established between several scattered waves.

X-ray wavelengths usually meet the order of atomic spacings in solids and are scattered by the electrons of atoms or ions lying within the beam path. Constructive interference has to occur for X-ray diffraction by a periodic arrangement of atoms (Fig, 21).

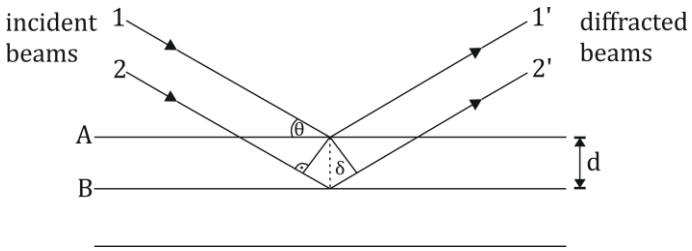

Figure 21: Geometry scheme for interference of an X-ray wave scattered by two planes of atoms separated by spacing d (Bragg's law), after [147].

Parallel planes of atoms (A and B in Fig. 21) are separated by the interplanar spacings d. When parallel, monochromatic and coherent X-ray beams of wavelength λ incide on these planes at an angle θ, several rays (1 and 2 in Fig. 21) are scattered by the atoms. The interplanar spacing d gives

rise to different path lengths of X-rays that are scattered from different planes. Constructive interference (1' and 2') occurs at an angle θ to the planes, if path length difference δ is equal to an integer (n) of wavelengths. The condition for diffraction is given by Bragg's law (Eq. 46) [145, 147, 151]:

$$n\lambda = 2dsin\Theta \tag{46}$$

with n: order of reflection, which is any integer consistent with sin θ not exceeding unity. If Bragg's law is unsatisfied, interference will be nonconstructive and result in a very low-intensity diffracted beam. Therefore, X-ray spectra can be obtained by plotting the measured scatter intensity in dependence on diffraction angle θ. The location and the shape of peaks in these spectra provide information on the crystal structures. Perfect crystals exhibit sharp, imperfect crystals show broadened peaks. Completely amorphous materials exhibit no peaks. The diffuse spectra of semi-crystalline PE-HD consist of broadened peaks due to the presence of an amorphous phase [152].

Two different types of X-ray scattering techniques are distinguished. When the experiment is performed using a scattering angle of 6° and higher, the technique is termed wide angle X-ray scattering (WAXS) [153]. WAXS spectra provide information on the overall crystallinity $X_{c,XRD}$, which is calculated by integrating the peak area and subtracting the scattering area of the amorphous phase [145]. The WAXS crystallinity $X_{c,XRD}$ may differ from the crystallinity obtained from DSC analysis, because structural characteristics affect the measurement parameters differently.

In contrast, small angle X-ray scattering (SAXS) is performed with scattering angles θ lower than 6°. Usually, SAXS experiments start from diffraction angles less than 1° [154, 155]. Since structures of a size between 1 nm and 100 nm can be depicted, the fine molecular structures such as the lamella structure of PE are analyzed with this technique. Furthermore, the periodic structure within a material can be obtained by SAXS. The thickness of the periodic structure is denoted as long period L_p. In PE, L_p equals the thickness of the sum of a crystalline lamella and an amorphous layer. To obtain L_p, Bragg's law is modified by considering small diffraction angles (sin θ = θ = ϵ) and it simplifies to (Eq. 47) [145]:

$$L_p\epsilon = n\lambda \tag{47}$$

with L_p: long period, ϵ: Bragg angle of intensity maximum, n: level of scattering, λ: wavelength of X-rays.

Since L_p was found to be proportional to the polymer crystallinity $X_{c,SAXS}$ and since L_p consists of one crystalline and one amorphous layer, lamella thickness of a polymer can be calculated. In turn, $X_{c,SAXS}$ can also be obtained from lamella thickness measurements (Eq. 48):

$$lamella\ thickness = X_{c,SAXS}\,[\%]\,L_p \Rightarrow X_{c,SAXS}[\%] = \frac{lamella\ thickness}{L} \tag{48}.$$

In SAXS, using the scattering vector q as the difference of the wave numbers of incident and scattered wave ($q = k_f - k_i$) and using the assumption for small angles $|k_f| \approx |k_i| = \frac{2\pi}{\lambda}$, Bragg's law can be considered as (Eq. 49):

$$|q| = \frac{4\pi}{\lambda} sin(\Theta) \tag{49}$$

with q: scattering vector, λ: wavelength, θ: scattering angle. The scattering cross-section per volume element is applied for further analysis, which is defined in one dimension (z-direction) for an isotropic two-phase system according to (Eq. 50):

$$\sum q = \frac{2}{4\pi q^2} r_e^2 (2\pi)^2 \int_{-\infty}^{\infty} exp(-iqr)\, K(z) dz \quad (50)$$

with the correlation function K(z). r_e is the classic electron radius obtained from the vacuum permeability ('magnetic constant') μ_0, the electric charge of an electron e, the mass of an electron m_e and equation 51:

$$r_e = \frac{\mu_0 e^2}{4\pi m_e} \approx 2.818 \cdot 10^{-15} m \quad (51).$$

Applying Fourier transform, the correlation function K(z) can be derived from $\sum q$ (Eq. 50) by (Eq. 52):

$$K(z) = \frac{1}{r_e^2 (2\pi)^3} \int_{q=0}^{\infty} 4\pi q^2\, \Sigma q \cos(qz)\; dq \quad (52).$$

From the characteristic K(z), the long period L_p (Eq. 47) can be determined graphically [146].

In this study, X-ray scattering experiments (XRD) were performed (D8 Advance, Bruker, Billerica Massachusetts, USA) ranging 2θ scattering angles from 3° to 50°. The diffractometer was equipped either with a molecular-metrology setup (WAXS) consisting of a copper anode (focus point, 40 kV, 55 mA) and a 2D detector (q-range: 0.08 to 2.80 nm^{-1}) or a slid-collimated Kratky-compact camera (SAXS, copper anode with 40 KV, 40 mA, line focus, point detector, q-range of 0.13 to 5.40 nm^{-1}).

3.2. Characterization of slow crack growth phenomena

This chapter comprises the mechanical test methods Bell telephone test (BTT) and full-notch creep test (FNCT) used to assess the SCG/ESC behavior of PE-HD. The FNCT (section 2.5.4) was the main mechanical test method applied in this study. Additional extensive fracture surface analysis was performed on FNCT specimens.

3.2.1. Bell Telephone Test

To analyze the crack initiation behavior of PE-HD materials, a classic Bell telephone test (BTT) was performed according to ASTM D1693 [99] and ISO 13274 [100] (section 2.5.1). In addition to standard and organic test fluids also applied in FNCT (sections 4.2.1 and 4.2.3), preselected fluids of different chemical categories (section 4.2.4) were used in BTT.

In accordance with ASTM D1693, test specimens had dimensions of 38.0 ± 2.5 mm by 13.0 ± 0.8 mm. They were cut from sheets of 1.9 ± 0.1 mm thickness. A controlled imperfection with a depth of 0.35 mm was introduced centrally by a razor blade to one surface of every specimen (Fig. 22 b). Such prepared specimens were bent notched surface up in a clamp, which was closed smoothly. Subsequently, 10 specimens were attached to each specimen holder. Specimen holders were made of stainless steel with an overall length of 165.0 ± 1.0 mm. They were manufactured to meet the dimensional requirements of ASTM D1693 [99] (Fig. 22 a). Specimen holders comprising 10 specimens each were introduced to (borosilicate) test tubes of 200 mm length, which contained the test fluids. Due care was taken for all specimens to be completely immersed by the fluids. Such prepared test tubes were closed by a silicone stopper identified suitable for such application according to ASTM D1693. All test tubes were stored in a water bath at a temperature of 50°C (Fig. 22 c). Specimens were evaluated once a day and failure time was recorded for any specimen individually.

a) b)

c) d)

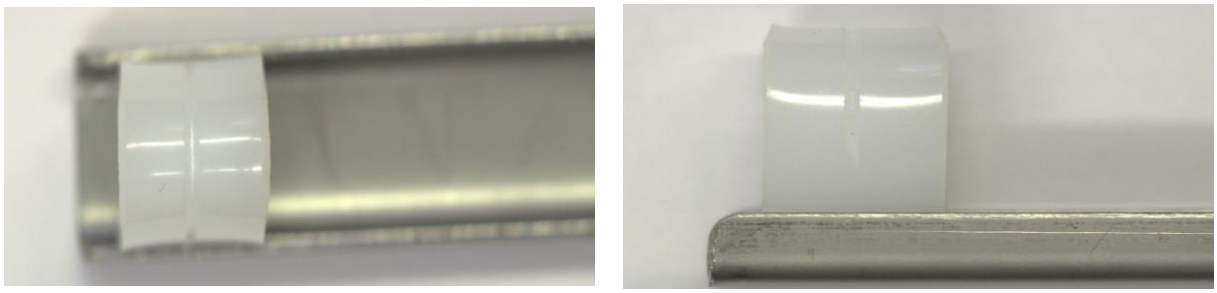

e) f)

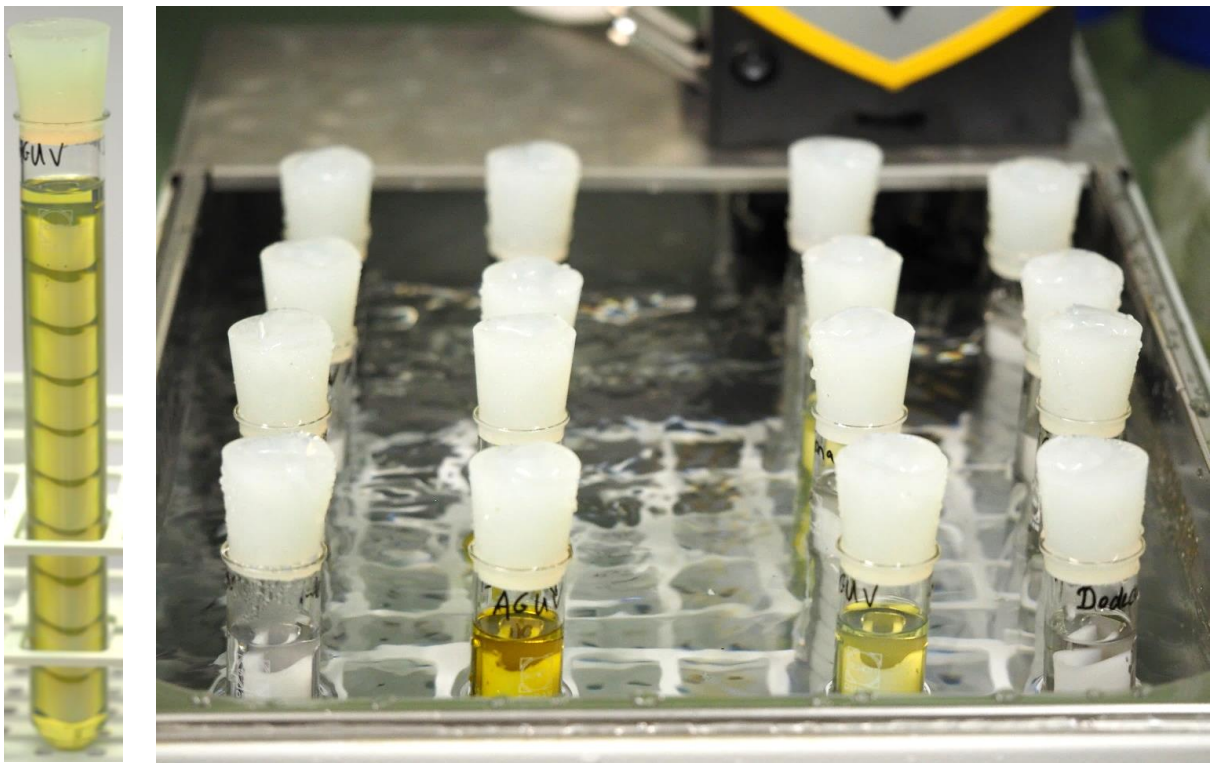

Figure 22: Depictions of the implementation of BTT; a) specimen holder, b) single specimen, c), d) single specimen assembled in specimen holder, e) entirely assembled specimen holder introduced into single test tube filled with liquid (biodiesel), f) filled test tubes in constantly stirred water bath (50°C).

According to ASTM D1693 [99] and ISO 13274 [100], BTT is to be finished when (i) ≥ 50% of the total number of specimens failed or (ii) after 1000 hours. A specimen was considered as 'failed', when it showed any damage (e.g. microcracks). To gather further information, BTT was terminated not until after 21000 hours and the first failure occurred to any specimen was additionally recorded.

3.2.2. Full-Notch creep test

Full-notch creep test (FNCT) experiments were performed in a variety of procedures based on ISO 16770 (section 2.5.4). Test parameters such as fluid, temperature, load and specimen geometry were varied. Moreover, pre-saturated specimens were used to evaluate the influence of sorptive fluids on crack growth. Saturation conditions were selected in accordance with the results of sorption and desorption experiments (sections 3.1.3 and 4.3.4).

FNCT device

FNCT were performed applying a novel FNCT device (IPT Institut für Prüftechnik Gerätebau, Todtenweis, Germany), which consisted of 12 individually controlled sub-stations. The FNCT principle according to ISO 16770 [13] was maintained. However, in contrast to conventional devices, electric stepping motors and stress gauges were used instead of a usual lever-arm construction to apply constant forces (Fig. 23).

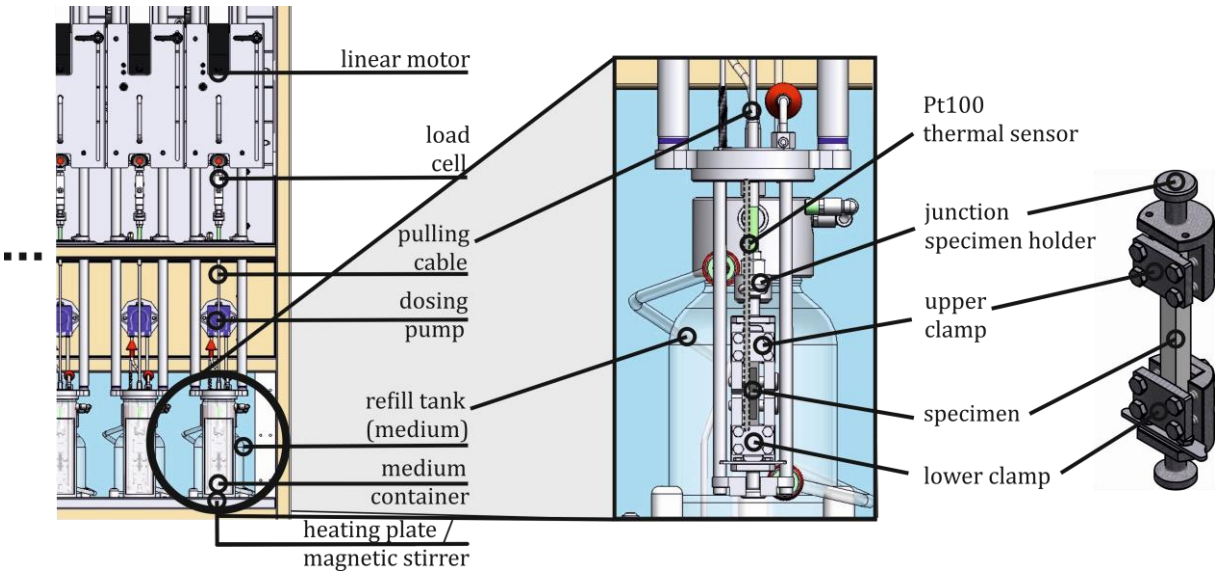

Figure 23: Schematic depiction of FNCT device applied in this study with specimen and specimen holder (after depictions of IPT Gerätebau, Todtenweis, Germany).

In addition to the mandatory measurement of time to failure t_f, the time-dependent elongation d of specimens was continuously recorded. In conventional FNCT devices, constant loading is usually realized by applying a preselected weight to a lever arm with a typical arm ratio between 4:1 and 10:1. However, ISO 16770 allows alternative constant load application with an accuracy of ± 1% [13], which is ensured by the linear stepping motor of the device used (Fig. 23).

In this FNCT device, specimens were immersed in separate temperature-controlled fluid baths (Fig. 24). To ensure a high accuracy of temperature measurement, Pt100 thermistors were located within the fluid container close to the specimen (Fig. 23). Temperature was transferred by a heated plate under each container, which was regulated on the basis of measurement data obtained from the thermistor. The algorithm of the regulation software was such, that overshooting was completely avoided. Selected temperature values were approached smoothly and kept constant. The fluid was constantly stirred at low speeds to ensure homogeneous immersion and a constant temperature throughout the entire fluid bath.

a)

b)

c)

Figure 24: Fluid containers of FNCT device, a) individual container with quartz glass window, b) individual container without window, c) 5 sub-stations, closed fluid containers during measurement.

Initially, two different fluid container types were available: one including and one excluding a quartz glass window (Fig. 24 a, b). Due to its low thermal conductivity, an FNCT in air was impossible to perform by using such container types. When a temperature change (heat uptake) of the air was measured, the heated plate would already have been overpowered. Furthermore, constant temperature values within the container could not be ensured. Therefore, a novel fluid container type for FCNT in air was especially designed, constructed (design / constructional drawing given in appendix A2 Fig. A2.87) and applied in this study (appendix A3 Fig. A3.88). Such double-walled containers comprised air in the internal space and distilled water in the shell. The water was heated and stirred. Therefore, a constant temperature was ensured within the test chamber.

In order to ensure a well-defined, comparable and reproducible starting point for all FNCT, a pre-load of 30 N was applied smoothly with a rate of 1 N/s after specimen clamping and immersion. The pre-load was upheld for 30 s. The elongation measurement started right thereafter. In view of typically applied forces of approx. 130 to 160 N (corresponding to stresses specified for PE-HD in ISO 16770), this still represented an appropriate considerably low stress level. For starting the measurement, the specimen jig had to be in a tensioned state. Hence, such an initial pre-loading step was procedure-based inevitable. The algorithm of force adjustment included an adaption according to the reaction of the specimen. The preselected force value was approached with a certain velocity, which was reduced smoothly before the nominal force value was reached. If necessary, the velocity was increased again to reach the nominal force within an acceptable timescale, but overshooting was always prevented.

FNCT procedures

Since SCG/ESC of PE-HD were addressed in this study, different FNCT procedures were performed and compared. For all procedures, the FNCT specimens were cut from sheets of 6.0±0.2 mm thickness. They were notched by a razor blade {(43.00 x 22.00 x 0.13) mm^3} employing a semiautomatic notching device with a defined duct following ISO 16770 [13], ISO 13274 [100] and ISO 11542 [156]. Specimens were clamped using a jig to ensure equal clamping for every specimen.

Standard FNCT procedure

Following the standard procedure for PE-HD container materials according to ISO 16770 (section 2.5.4), the FNCT was performed at 50°C and a nominal (reference) stress σ_n of 9.00 MPa [13, 181, 157, 158]. To obtain the characteristic time to failure t_f* for a distinct combination of PE-HD type and fluid, five individual measurements were performed with different nominal load levels (stresses): 8.25 MPa, 8.75 MPa, 9.00 MPa, 9.25 MPa, 9.75 MPa. To have an indication about the nominal force F that was to apply for each distinct specimen, F was calculated for each FNCT experiment by relating the nominal stress to the nominal cross-section after notching (Fig. 25, Eq. 53). This is assumed by measuring the actual specimen dimensions with a caliper (edge lengths a and b) and subtracting the nominal notch depth d_{notch} (Eq. 53):

$$F = \sigma_n(A_{tfs} - A_n) = \sigma_n\,(a - 2d_{notch})(b - 2d_{notch}) \qquad (53).$$

However, the exact determination of the notch depth d_{notch} and the actual initial cross-section (ligament area) A_L is performed by light microscopy (section 3.3.1) of the fracture surface after the test (Fig. 25). This allows for the calculation of the exact initial stress σ_L for each specimen, which was used for further analysis (Eq. 54):

$$\sigma_L = \frac{F}{A_L} \qquad (54).$$

a) b)

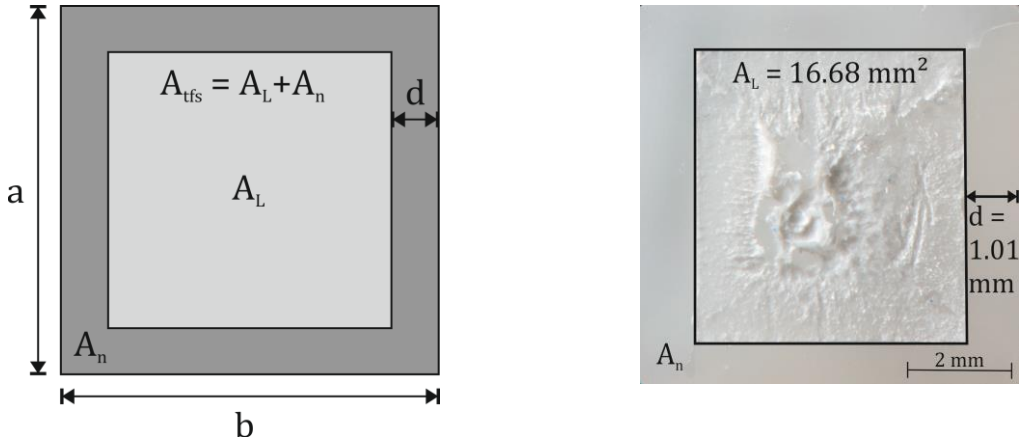

Figure 25: a) Schematic projection of the initial residual cross-section after notching, A_L: ligament area, d = d_{notch}: notch depth, A_n: notch area, A_{tfs}: area of total fracture surface, a, b: length and width (edge lengths) of FNCT specimen; b) example of exact determination of d and A_L employing light microscopy measurement tools.

The time to failure t_f* is then determined by interpolation to the reference stress value σ_n of 9 MPa using a linear regression of the five individual time to failure t_f values in a double logarithmic plot of single t_f against the actual initial stress σ_L (exemplary depicted in Fig. 26 a). Using this interpolation method, a t_f* can effectively be obtained, which exactly refers to the nominal (reference) stress. Otherwise, this nominal reference value would not be accessible. Therefore, this analysis procedure is supposed to lead to very precise and reproducible results.

Analysis procedure

FNCT analysis usually comprises the determination and comparison of time to failure t_f* values of different PE-HD types in various liquids. The main source of uncertainty within the measurement procedure is the determination of the actual initial cross-sectional area (ligament area) A_L of the FNCT specimen and thus the actual initial stress σ_L (Eq. 54). Therefore, the interpolation procedure based on 5 individual t_f values according to ISO 16770 is commonly maintained (Fig. 26 a). Single FNCT t_f have to be regarded with due care.

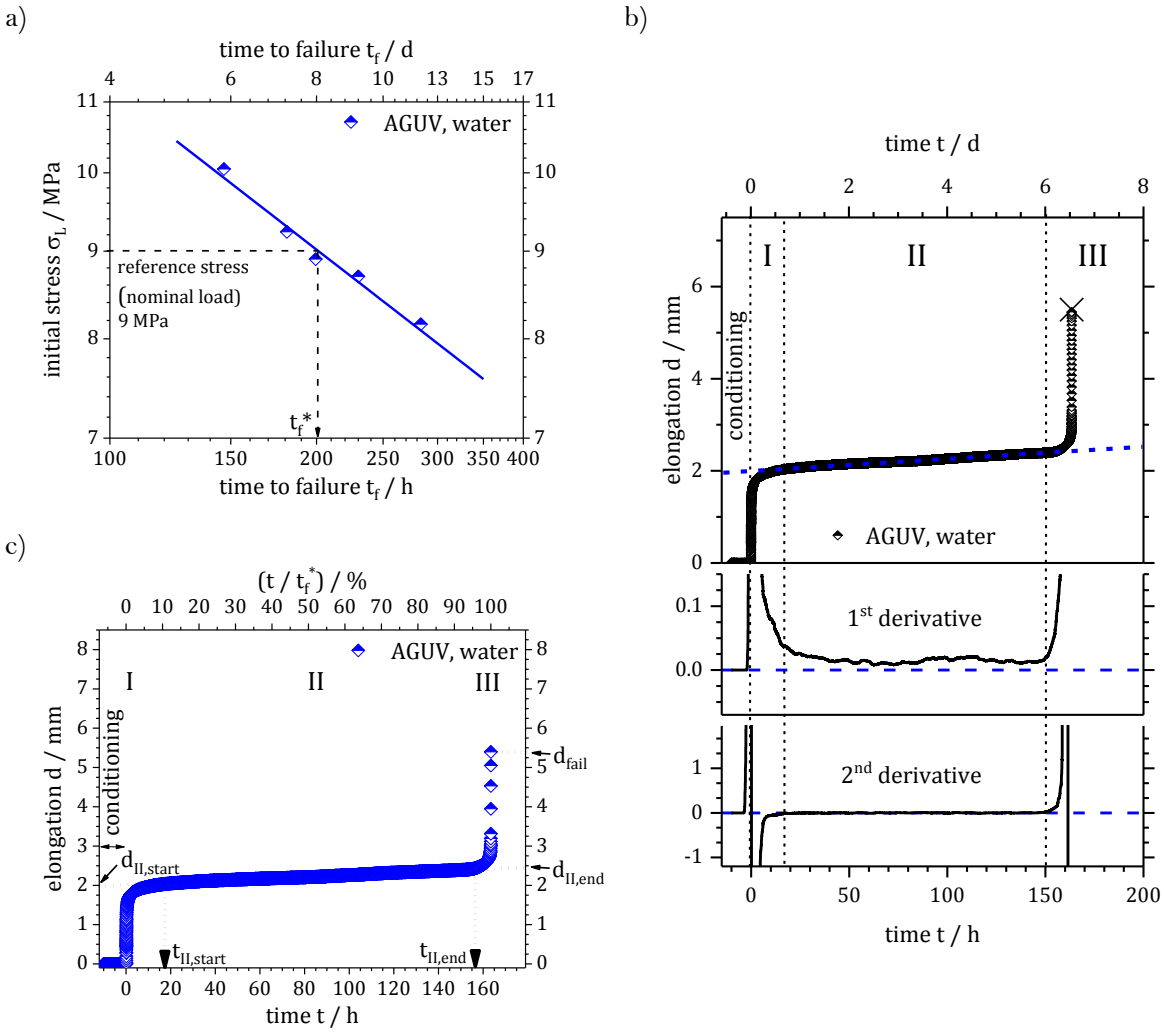

Figure 26: a) Time to failure t_f* obtained by linear regression from 5 single FNCT (double-logarithmic representation); b), c) typical elongation-time curves.

In figure 26 a, a typical FNCT analysis of the PE-HD type 'Lupolen 4261 AG UV 60005' (Tab. 3 in section 4.1) tested in water at 50°C and σ_n = 9 MPa is depicted. In this example, t_f* has a value of approx. 200 hours. It has to be noted that error bars might not be noticeable due to their small size.

In addition to the t_f-values, the specimen elongation was measured, which provides an indirect information on crack growth during SCG and ESC in the FNCT. Figures 26 b and c show exemplary time-dependent elongation curves in the course of an FNCT.

Three regions can be identified in a typical FNCT elongation curve. The overall appearance seems to be similar to the time-dependent crack tip opening displacement (CTOD) described by Brown and Lu [11] (section 2.3.5). However, no indication was found for a change in the slope of the constant crack growth region. In region I, the elongation increases fast, which is attributed to the initial craze

formation together with relaxation and orientation of the polymer chains immediately after applying the load. The second region (region II) represents constant crack growth, in which the elongation increases linearly with time [159]. When the third region (region III) starts, failure is inevitable and the elongation increases severely due to a prevailing ductile deformation. Investigations are usually focused on the second region, which reflects SCG/ESC induced crack growth and predominantly determines the time to failure t_f. For the distinction between the different regions, the first and second derivatives of the elongation-time curve are taken into account. The region of constant crack growth (region II) is characterized by a constant value in the first derivative. Start and end points are defined by the zero-crossings of the second derivative (Fig. 26 b).

In figure 26 c, characteristic values obtained from elongation measurements are defined such as the elongation values at the start and the end of region II, $d_{II,start}$ (at time $t_{II,start}$) and $d_{II,end}$ (at time $t_{II,end}$), as well as the elongation at failure d_{fail}. Moreover, the time-dependent course of the elongation in the FNCT is related to its percental equivalent considering the overall time to failure t_f^* (t/t_f^*, Fig. 26 c).

Geometry variation

To examine the influence of the specimen geometry on FNCT, geometry and notch configurations were varied (Fig. 27). In addition, an improvement of the FNCT concerning the time to failure t_f was evaluated. In this respect, a PE-HD type-independent test acceleration with a significant reduction of t_f was sought.

FNCT specimen

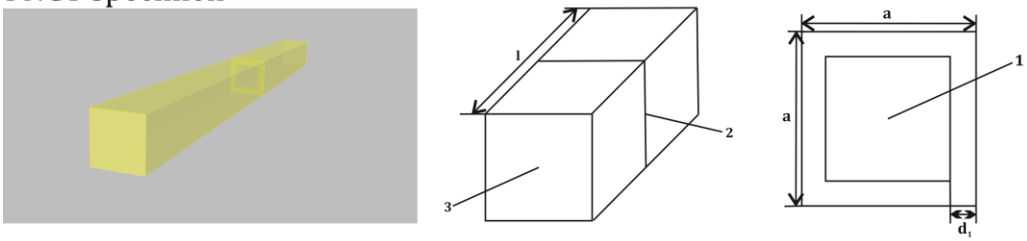

l: specimen length
2: notch (circumferential)
3: total cross section A_{tfs}

a: width of cross section incl. notch
d_{notch}: notch depth = d_1
1: residual fracture surface A_L

DNCT specimen

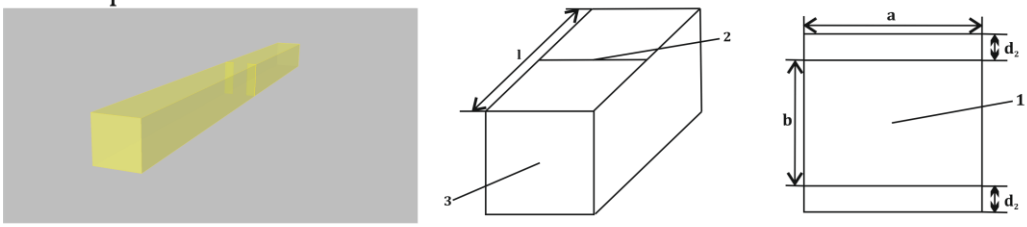

l: specimen length
2: notch (doubled, also on opposite site)
3: total cross section A_{tfs}

a: width of cross section incl. notch
b: width of cross section excl. notch
d_{notch}: notch depth = d_2
1: residual fracture surface A_L

RNCT specimen

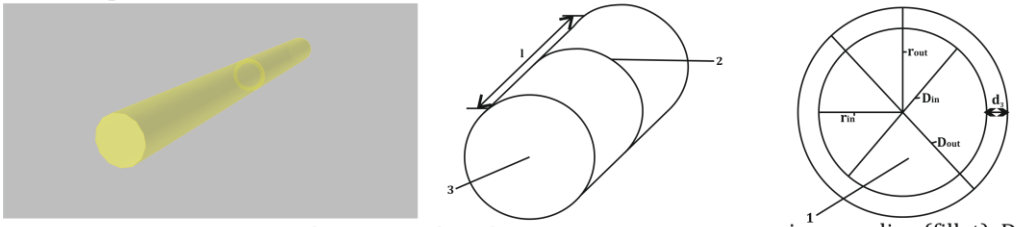

l: specimen length
2: notch (circumferential)
3: total cross section A_{tfs}

r_{in}: inner radius (fillet), D_{in}: inner diameter
r_{out}: outer radius, D_{out}: outer diameter
d_{notch}: notch depth = d_3
1: residual fracture surface A_L

Figure 27: Schematic representation of specimen geometry and notch types applied in this study.

In addition to full notches, double notches were utilized, i.e. two notches were generated on opposing sides of the specimen (Double Notch Creep Test, henceforth referred to as 'DNCT'). Specimen dimensions were the same as for FNCT, but the notch depth was adapted to 1.67 mm to realize a double-notched specimen with the same nominal initial cross-section.

Moreover, cylindrical specimens were tested. Therefore, specimens were lathed, and notches were introduced with a razor blade. Based on FNCT specimen geometry (section 2.5.4 and Fig. 27), the cylindrical specimens had a length of 90.0 ± 0.2 mm and a diameter of 6.0 ± 0.2 mm (Round Notch Creep Test, referred to as 'RNCT'). The notch depth was adapted to 0.74 mm. All other test parameters were the same for FNCT, DNCT and RNCT. Geometry variation measurements were performed using AGUV and 5021DX in air, Arkopal, biodiesel and diesel.

Temperature variation

Temperature-dependent FNCT were performed for all PE-HD types in the test fluids water, Arkopal, biodiesel and diesel. For standard FNCT specimens and procedures, the test temperatures were varied: 30°C, 40°C, 60°C and 70°C were used in addition to the usual temperature of 50°C. However, instead of five, only one specimen was tested at each temperature with a nominal stress of 9.00 MPa. Therefore, the time to failure values t_f (except for 50°C) result from only one measurement per temperature. Significant effects of the test temperature can nevertheless be recognized unrestrictedly.

Stress variation

In order to study the transition from brittle to ductile fracture behavior (brittle/ductile transition, section 2.3.4), the initial nominal stress σ_n was varied for AGUV and 5021DX in air, water, Arkopal, biodiesel and diesel. Again, only one specimen per stress value σ_n was tested at 50°C. The obtained time to failure values t_f were related to the actual initial stresses σ_L calculated from the A_L values measured by light microscopy after the test for each specimen (Eq. 54). The region of brittle/ductile transition is supposed to be determined from the change in slope in the curve of σ_L vs. t_f (Fig. 6 in section 2.3.4 and [13]).

Partially damaged specimens

For a detailed investigation of crack propagation by several imaging techniques (section 3.3), partially damaged specimens were studied. Therefore, standard FNCT were initially performed, but specimens were removed prior to failure after preselected time periods. Thus, the progress in crack growth for several stages could be analyzed. The nominal stress σ_n applied was 9 MPa and test temperature was 50°C for all specimens. The time intervals for removal of the specimens were defined percentagewise relative to the overall t_f* (Tab. 2). t_f* was previously determined by a standard FNCT procedure. AGUV was used for all specimens in Arkopal (section 4.2.1), diesel and biodiesel (section 4.2.3).

Table 2: Loading time stages on percentage basis of t_f* and distinct loading time values of AGUV in Arkopal, biodiesel and diesel.

relative loading time / %	loading time AGUV, Arkopal / h	loading time AGUV, biodiesel / h	loading time AGUV, diesel / h
0.00*	0.00*	0.00*	0.00*
0.20	0,10	0.02	0.02
1.00	0,60	0.10	0.08
2.00	1,10	0.20	0.17
5.00	2.80	0.50	0.41
15.00	8.50	1.50	1.24
25.00	14.20	2.50	2.07
33.00	18.70	3.30	2.74
40.00	22.60	4.00	3.32
50.00	28.30	5.00	4.15
60.00	34.00	6.00	4.98
66.00	37.40	6.60	5.47
75.00	42.50	7.50	6.22
85.00	48.10	8.50	7.05
97.00	54.90	9.70	8.05
98.50	55.80	9.85	8.17
100.00	56.60	10.00	8.30

* specimen notched only, no loading / test fluid exposure

3.3. Fracture surface analysis

For the analysis of SCG/ESC induced fracture surfaces and crack propagation, several imaging techniques such as light microscopy (LM), laser scanning microscopy (LSM), scanning acoustic microscopy (SAM), industrial computed tomography scanning (CT) and scanning electron microscopy (SEM) were used.

In order to analyze crack propagation, partially damaged FNCT specimens were prepared for both destructive (LM, LSM, SEM) and non-destructive (SAM, CT) imaging techniques. LM, LSM and SEM can only be used for analysis of freely accessible fracture surfaces. Therefore, the residual undamaged part of partially damaged specimens was broken by a hammer strike after immersion in liquid nitrogen (cryo-fracture) to get free surfaces for further analysis. Because cryo-failed areas and fracture surfaces parts of ESC crack growth exhibit different shapes, crack growth damaged and undamaged areas could be determined.

To compare crack growth data from different imaging analysis techniques, an average crack length c was defined. Therefore, the values of damaged (A_d) and undamaged (A_{ud}) areas were assumed to be quadratic. Based thereon, average crack lengths c were calculated (Eq. 56, Fig. 28).

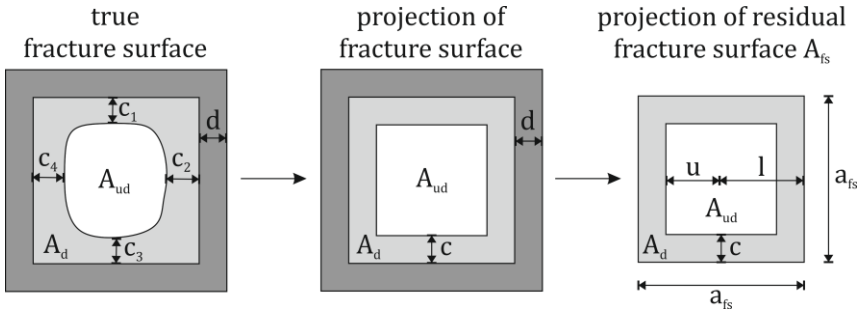

Figure 28: Schematic projection of true fracture surface area (left) and its idealization (center, right) to calculate an average crack length c; A_d: damaged area, A_{ud}: undamaged area, c: average crack length, c_1 to c_4: several arbitrary crack lengths, d = d_{notch}: notch depth, a_{fs}: width and length of residual fracture surface, u: half side length of undamaged area, l: half side length of ligament area A_L.

Considering geometric proportions schematically depicted in figure 28, the average crack length c can either be derived from:

(i) the numerical determination of single crack length values using

$$c = \bar{c} = \frac{1}{n}\sum_i^n c_i \qquad (55)$$

or (ii) the numerical determination of A_{ud} and A_d with conversion into quadratic areas using

$$c = l - u = \frac{\sqrt{A_L}}{2} - \frac{\sqrt{A_{ud}}}{2} = \frac{1}{2}\left(\sqrt{A_{ud} + A_d} - \sqrt{A_{ud}}\right) \qquad (56).$$

These two methods of imaging data analysis were used: (i) for industrial micro computed X-ray tomography scanning (section 3.3.4) and (ii) for light microscopy (section 3.3.1), laser scanning microscopy (section 3.3.2) and scanning acoustic microscopy (section 3.3.3).

3.3.1. Light microscopy

Light microscopy (LM using AxioCam ICc 3 on a Stemi 2000-C microscope, Carl Zeiss AG, Oberkochen, Germany) was employed to determine the actual ligament area A_L (using onboard software AxioVision 4.9) of each individual specimen. Therefrom, the actual initial stress in the FNCT was calculated and used to obtain the overall time to failure t_f^* (section 3.2.2, Eq. 54).

LM was also applied for analysis of the fracture surfaces after FNCT failure. This allows a classification into brittle or ductile fracture. As described in chapter 0, the determination of damaged (A_d) and undamaged (A_{ud}) areas of partially damaged specimens was possible from LM images. From A_d and A_{ud}, average crack lengths c were calculated (Eq. 56).

3.3.2. Laser scanning microscopy

A more detailed fracture surface analysis of FNCT specimens was achieved by laser scanning microscopy (LSM). Therefore, a VK-X 100 LSM (Keyence GmbH, Neu-Isenburg, Germany) was employed, which comprises a semiconductor laser with a wavelength of 658 nm and a maximum output power of 0.95 mW. Detailed high-contrast achromatic (65536 gray shades) laser pictures as well as height information of the investigated surfaces (images of 1407 x 1343 pixels) were obtained. In LSM, the microscope head (Fig. 29) was operated mechanically with a height increment of 12 µm. Within each height step, the specimen surface was scanned optically by the laser and the height value of the highest reflected intensity was identified as focus (Fig. 29). Therefore, height information with a minimum (optical) height resolution of 5 nm could be obtained. The point of laser light has a diameter of 0.2 µm, which represents the lateral scanning resolution.

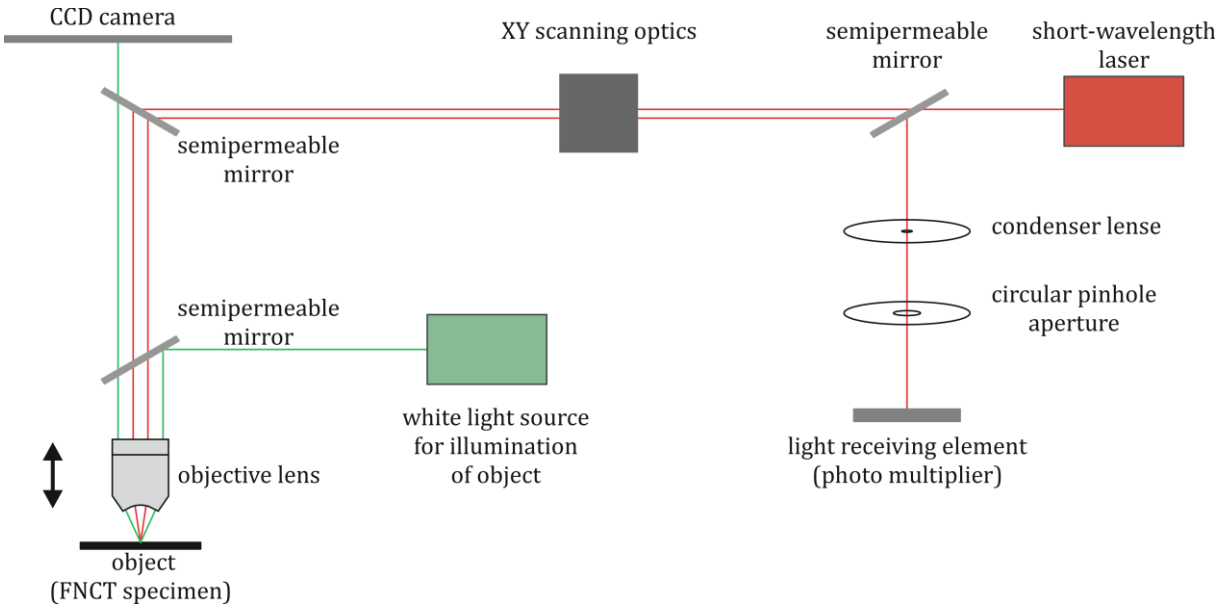

Figure 29: Scheme of functional elements in the microscope head of an LSM (after depictions by Keyence GmbH).

Similar to LM (section 3.3.1), LSM was applied for fracture surface analysis for classification into brittle and ductile failure as well as for determination of damaged and undamaged areas of partially damaged specimens. Consistently, the average crack lengths c for every stage of partial damage were calculated.

Origin software (OriginLab Corporation, Northampton, MA, USA) was used to create a 3D depiction of height information (in pixels) obtained from LSM using a custom-made algorithm. In order to relate height data to the level of fracture plane, a virtual coplanarity at the height of the notch was constructed by averaging single height values of 500 by 100 data points in the notch area A_n (Fig. 25). This average height value was set as reference of the coplanarity and used as zero level scale for all height data. After transformation of pixel based into metric data using the conversion factor given in the LSM software, data were gridded applying Renka-Cline interpolation method [160] (included in Origin software) and plotted as a 3D surface image. Top view height images (2D depictions) were obtained by changing the perspective.

3.3.3. Scanning acoustic microscopy

The scanning acoustic microscope (SAM) operates by focusing a short acoustic pulse of high frequency onto or into a sample (Fig. 30). Distilled water acts as a coupling liquid between the ultrasonic transducer and the sample. The incident ultrasonic wave is partially reflected by the sample surface and partially transmitted into the sample. The transmitted wave can be reflected by internal boundaries, absorbed by the polymer or scattered by inclusions or inhomogeneities.

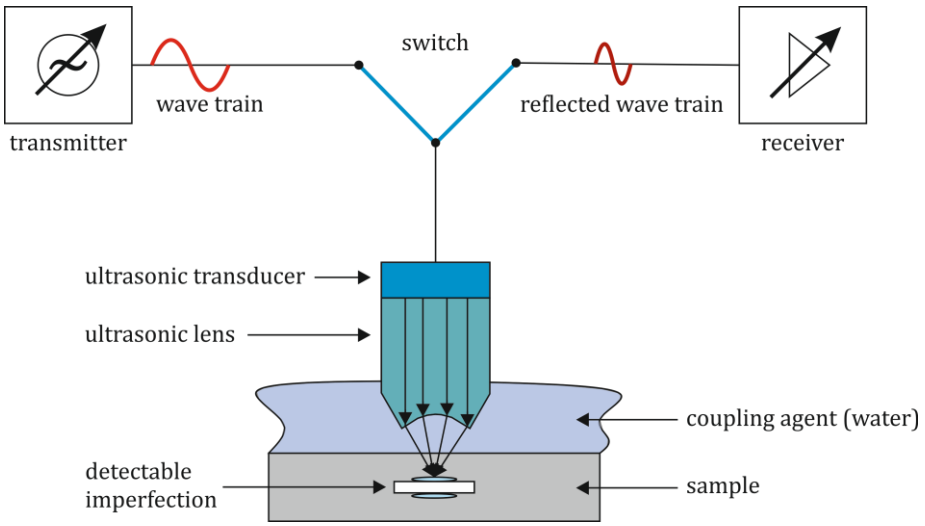

Figure 30: Schematic principle of a scanning acoustic microscope.

The acoustic contrast at an interface between two materials is related to the difference of their acoustic impedances Z_i. Z_i is defined as the product of sound velocity c_i and density ρ_i of the corresponding material (Eq. 57):

$$Z_i = c_i \rho_i \qquad (57).$$

For perpendicular incidence, the reflected fraction of the amplitude is described by the acoustic reflection coefficient $r_{acoustic}$ (Eq. 58):

$$r_{acoustic} = \frac{Z_2 - Z_1}{Z_1 + Z_2} \qquad (58)$$

with Z_1 and Z_2: acoustic impedances of the two materials. Reflections occur, if the impedances are different. Due to the large differences in density and sound velocity, the reflections on interfaces between water, air and polymer can be clearly distinguished [161].

a) b)

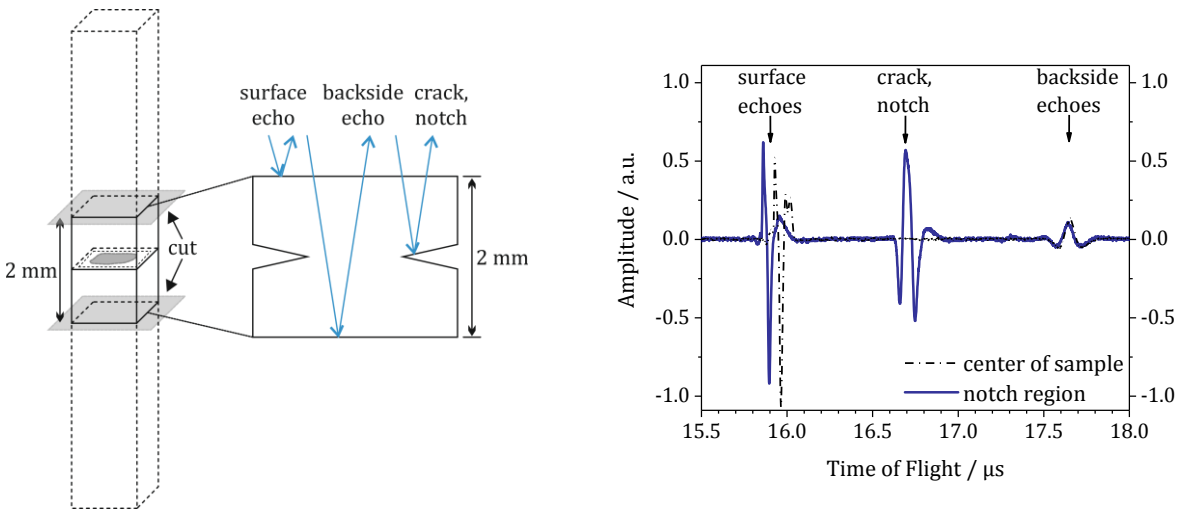

Figure 31: a) Schematic depiction of FNCT sample preparation for SAM and expected echoes, b) two echo trains from the center (dashed line) and the notched region (solid line) of an FNCT specimen.

Two reflected ultrasonic signals (echo trains from different positions) are given exemplary in figure 31 b. One represents the echo train from the center of the sample, which is partially reflected at the surface and the backside of the specimen (dashed line, also Fig. 31 a). The other depicts a signal from the notched region, which is partially reflected at the surface and the notch (and the backside of the specimen to a small extent). The time-of-flight (TOF) difference between surface and backside echo amounts to approx. 1.6 µs. This value corresponds to a specimen height of 2 mm. From TOF and the ultrasonic pathway (double of the sample length), a sound velocity of 2340 m/s is obtained. This is in accordance with typical sound velocity values for PE-HD [162, 163]. The echo attributed to the crack or notch is detected approx. 0.8 µs later than the surface echo (Fig. 31 a). Thus, the presence of a crack or notch is indicated by the occurrence of an echo in the TOF region between surface and backside echo. To distinguish the occurrence of an echo from noise signals, a signal amplitude significantly higher than the noise was used as criterion. A_{ud} (Fig. 28) was determined by the number of spots without signal between surface and backside echo. Since in both cases a signal between surface and backside echo is detected, the differentiation between notch and crack is challenging. Therefore, an average crack length was determined by subtracting the average edge length of the undamaged area A_{ud} and the average notch length d from the edge length of the total cross section of the sample (A_{tfs}, Fig. 25) using equation 59:

$$c = \frac{\sqrt{ab} - \sqrt{A_{ud}}}{2} - d \qquad \text{(assumption: all areas are quadratic, Fig. 28)} \qquad (59).$$

The total cross section of the sample was determined by a caliper (edge lengths a and b, Fig. 25). Moreover, from the TOF of the signals, information from the depth of the crack in the specimen as well as its surface structure (profiling from the echos) can be evaluated [164, 165]. Therefrom, three-dimensional images can be obtained.

In this study, the scanning acoustic microscope (type "Evolution II" of PVA TePla Analytical Systems GmbH, Westhausen, Germany) was operated in reflection mode, using an ultrasonic transducer with a nominal frequency of 30 MHz. The spatial resolution at 30 MHz was 20 µm. The SAM measurements were performed at Fraunhofer Institute for Structural Durability and System Reliability LBF in Darmstadt.

Partially damaged FNCT specimens (section 3.2.2), were cut to thin slides of 2 mm height with cuts 1 mm laterally above and below the notch (Fig. 31 a). The cutting surfaces were turned to provide flat surfaces. The such prepared SAM specimens were attached straightened and entirely immersed by the coupling liquid (distilled water) in SAM. AGUV specimens partially damaged in Arkopal were analyzed for the loading time stages given in table 2, except for 0.2%, 1% and 2% (section 3.2.2).

3.3.4. Industrial micro computed X-ray tomography scanning

A custom-built X-ray micro computed tomography (CT) system at BAM (Bundesanstalt für Materialforschung und -prüfung, Berlin, Germany) was used for all CT measurements. The system consisted of a manipulator, a 225 kV X-ray tube (X-Ray WorX GmbH, Garbsen, Germany) and a 2048x2048 pixel flat panel detector (Perkin Elmer Inc., Waltham, Massachusetts, USA). FNCT specimens were placed on a rotating table, which was located between X-ray tube and detector (Fig. 32).

a) b)

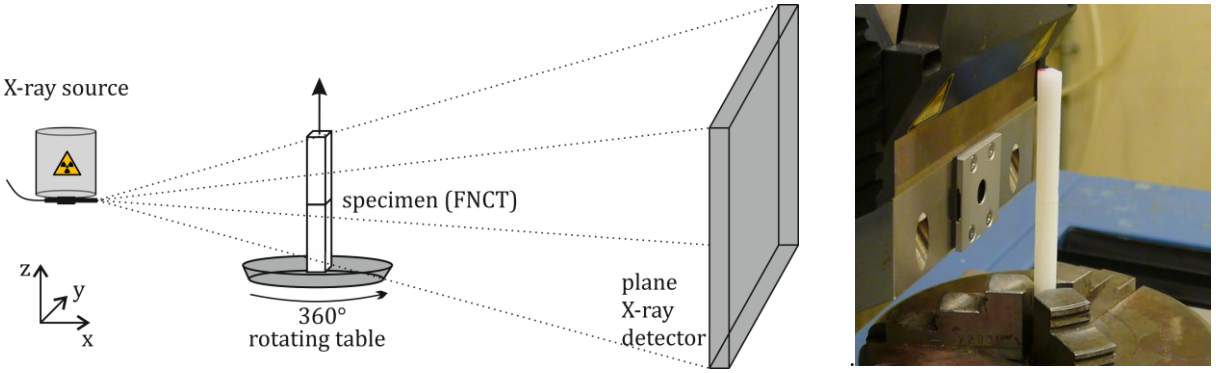

Figure 32: FNCT specimen attached to the CT system, positioned in front of the X-ray tube for CT measurement, a) schematic depiction, b) image from inside the CT system.

During rotation of the specimen by 360 degrees in its horizontal plane, 3000 continuously radiographed pictures with equidistant rotation increments were taken, i.e. a single image was produced every 0.12 degrees of rotation. From this projection images, a volume based (3D) data set is reconstructed using the cone-beam algorithm of Feldkamp [166]. Therein, every volume element (voxel) has a size of (5.4 x 5.4 x 5.4) mm^3 and represents the X-ray attenuation coefficient within the voxel volume by a corresponding grey value. Because of the low attenuation of the PE-HD specimen, a low energy of 60 kV was selected for all measurements. The exposure time for each projection image was 6 seconds.

The reconstructed three-dimensional CT data were evaluated with VGStudio 3.0 (Volume Graphics GmbH, Heidelberg, Germany), a software which was especially developed for analysis and visualization of CT data.

No initial preparation of the specimens was necessary for CT measurements, since the CT device was able to accommodate the entire specimen (Fig. 32 b). In contrast to the other imaging techniques, the partially damaged specimens were replaced to the FNCT device after each CT scan for continued exposure. Four stages of damage of one and the same specimen after 0%, 33%, 66% and 97% t_f* of loading in the FNCT in Arkopal, biodiesel and diesel, respectively, (Table 2) were investigated.

The analysis of crack growth in CT experiments was not based on averaged crack lengths obtained from the evaluation of surface areas as for LM, LSM and SAM. Instead, the individual crack lengths

were obtained directly by tools of the visualization software. The determination of the average crack length is based on averaging of 25 single crack length measurements in each edge direction according to equation 55 (section 3.3 and Fig. 28). Thus, 100 crack length measurements for all circumferential notches, every specimen and stage of damage (n = 100 in Eq. 55) were conducted.

3.3.5. Scanning electron microscopy

Surface structure analysis was performed employing the scanning electron microscope (SEM) EVO MA10 (Carl Zeiss Microscopy GmbH, Jena, Germany), which was equipped with a tungsten cathode and a secondary electron detector. Prior to SEM analysis, specimens were gold sputtered in a SCD 050 sputter coater (Leica Microsystems, formerly Bal-Tec Balzers, Wetzlar, Germany) for 100 s at a current of 40 mA and room temperature to reach a layer thickness of approx. 25 nm. SEM micrographs were obtained using an acceleration voltage of 10 kV, a working distance of 20 mm (overview image) as well as 4.5 mm (detailed imaging with a higher depth of focus) and Zeiss Smart SEM (UI) software.

4. Materials and test fluids

In this paragraph, the PE-HD materials, the general specimen preparation (section 4.1) and the test fluids (section 4.2) used in this study are presented. The description of PE-HD materials and test fluids includes their characterization (section 4.3).

4.1. Polymers and specimen preparation

Five different commercially available PE-HD resins were selected to cover a range of materials practically applied for packaging and transport of dangerous goods. PE-HD types with unimodal as well as trimodal molecular mass distributions (MMD) were used. The investigated materials (Tab. 3) were kindly provided by LyondellBasell (Basell Polyolefine GmbH, Frankfurt/Main, Germany). According to data sheets, the values of density, melting temperature, melt flow rate (MFR) and tensile modulus were determined by ISO 1183-1 [167], ISO 1133-1 [168], ISO 3146 [169] and ISO 527-1/-2 [170, 123], respectively.

Table 3: Investigated PE-HD types; data were obtained from LyondellBasell data sheets [171, 172, 173, 174, 175].

Name	density / g cm^{-3}	melting temperature / °C	melt flow rate (MFR) (190°C, 21.6 kg) / g (10 min)$^{-1}$	tensile modulus (23°C) / MPa	comonomer / catalyst	polymerization process
Lupolen 4261 **AG UV** 60005	0.945	130	6	850	**hexene** / chromium based	**gas phase**
Lupolen 4261 **AG BD**	0.945	131	6	900	**hexene** / chromium based	**gas phase**
Lupolen 4261 **A Q149**	0.945	130	6	850	**hexene** / chromium based	**loop process** (no additives)
Lupolen **5021 DX**	0.950	131	22	1000	**hexene** / chromium based	**loop process**
Hostalen ACP **5831 D**	0.958	180 to 210	22	1350	**butene**, Ziegler based	**advanced cascade process (ACP)**

henceforth referred to as **AGUV**, **AGBD**, **AQ149**, **5021DX** and **5831D**.

The PE-HD resins AGUV and AGBD with monomodal MMD are designed to meet the requirements of high-performance applications. They are produced by gas phase polymerization applying chromium-based catalysts and 1-hexene comonomers. They contain antioxidants, light

stabilizers and further additives to be resistant to UV radiation and heat. AGBD is particularly conceptualized to exhibit an enhanced long-term stability in biodiesel applications. AGUV and AGBD are resins with an outstanding SCG/ESC resistance (SCGR/ESCR), chemical resistance and high impact resistance. Their main applications are containers for dangerous goods packaging.

Since AQ149 is also derived from the Lupolen 4261 product family using 1-hexene comonomers, it is supposed to have properties comparable to AGUV and AGBD. Different from the latter, AQ149 is however produced in a chromium-based catalyst loop process and it is delivered as powder and without any additives.

5021DX is also obtained from a loop polymerization process using chromium-based catalysts and 1-hexene comonomers but it exhibits a broad monomodal MMD. It is typically utilized for small blow molding and conventional packaging applications such as for consumer goods, surfactants and engineering parts. It exhibits a high chemical and SCG/ESC resistance as well as good flowability and organoleptic properties.

The PE-HD resin 5831D with a broad trimodal MMD is prepared in an advanced cascade process (ACP) using Ziegler-based catalysts and 1-butene comonomers. It is designed to combine a high stiffness with a high SCGR/ESCR. Its usual applications are components in the field of small blow molding such as thin-wall packaging, consumer goods and toys.

Due to the different polymerization processes and comonomer types, different groups of PE-HD resins are obtained: (1) AGUV, AGBD, AQ149 and 5021DX contain 1-hexene comonomers whereas 5831D contains 1-butene comonomers. (2) AGUV and AGBD are produced by gas phase polymerization, AQ149 and 5021DX by a loop polymerization process and 5831D by an advanced cascade process (ACP). These groupings are reflected in the structure and morphological properties (cf. section 4.3).

Furthermore, AGUV, AGBD, 5021DX and 5831D were obtained as pellets. In contrast, AQ149 was available as powder. Hence, it was not subjected to an additional extrusion process for granulation. Although all these materials (Tab. 3) are ascribed to PE-HD resins, they are henceforth occasionally referred to as 'different materials', which is based on their differences concerning polymerization process and comonomer type.

With the selection of these commercially available PE-HD types including different additive packages, a high practical relevance is ensured. Furthermore, AQ149 is considered as a non-stabilized PE-HD resin since it does not contain any stabilizing additives. The incorporation of additives in PE-HD resins usually aims for an enhanced processability and long-term stabilization, i.e. against chemical ageing (section 2.1.1). Due to the specimen preparation using a heated press and the consideration of crack propagation in this study, additives of the PE-HD types can be neglected. The test durations obtained in this study are short (< 1 year). Hence, long-term damage effects such as chemical ageing and degradation are not addressed explicitly. Therefore, the additives of the PE-HD types just allow for an unaffected assessment of physical effects (sorption, SCG, ESC) since they are supposed to exclude chemical contributions to damage (section 2.3.7). In turn, the additives do not contribute to the test results. However, in non-stabilized PE-HD types (no additives), damage effects may be superimposed and a clear distinction between physical and chemical effects may be aggravated.

General specimen preparation

A general specimen preparation was applied prior to additional preparation processes, which were necessary to obtain special specimens for different test procedures. Using as received granules and powder, molded sheets were prepared in a heated press equipped with a crimping tool (hydraulic

press type KHL 100 of Bucher-Guyer AG, Niederweningen, Zürich, CH) under conditions according to ISO 293 [112], ISO 17855-1 [176], ISO 17855-2 [113] and ISO 16770 [13]. Sheets were pressed for 5 minutes at a temperature of 180°C and a pressure of 5 MPa. The cooling rate was 15 K/min, sheets were removed below 40°C and subsequently annealed for 3 h at 100°C. The crimping tool of the heated press combines the advantages of obtaining sheets with low internal stresses (low crystallite orientations) and the same thicknesses. Overrun material is expelled during pressing process and not subjected to pressure during cooling. Specimens were cut from sheets according to the required dimensions. Therefore, sheet thickness was varied according to application. For FNCT, sheets of 6.0±0.2 mm thickness were prepared. Further details of preparation processes are qualified in the test method descriptions.

4.2. Test Fluids

Test fluids including their preparations are presented in this section. They are categorized according to their natural classifications (sections 4.2.1 to 4.2.3) and in terms of their SCG/ESC influence on PE-HD. Fluids used in Bell telephone test (section 3.2.1) are additionally introduced (section 4.2.4).

4.2.1. Detergents and surfactants

In this study, a 2 wt% aqueous solution of the surfactant Arkopal N 100 is used for ESC analysis. Arkopal N 100 is specified and recommended in ISO 16770 [13]. It is also termed 'detergent' due to its cleaning properties in dilute solutions that result from its amphiphilic character of being partly hydrophilic (polar) and partly hydrophobic (non-polar). According to ISO 16770, the 2 wt% aqueous Arkopal N 100 solution was prepared using distilled water and it was aged for two weeks at 50°C prior to usage. Arkopal N 100 is a 4-nonylphenyl-polyethylene glycol with an average molecular weight of 680 g/mol (Fig. 33) [177].

The 2 wt% aqueous Arkopal N 100 solution is henceforth simply referred to as '***Arkopal***'.

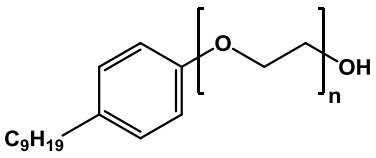

Figure 33: Chemical structure of Arkopal N 100 (4-nonylphenyl-polyethylene glycol); the average molecular weight of 680 g/mol corresponds to n ≈ 10…11; for Arkopal N 100, the value of n = 10.

Since the bulk absorption of the surface-active agent Arkopal by PE-HD is practically negligible (section 4.3.4), another model fluid is required to evaluate ESC effects influenced by absorption. Therefore, n-butyl acetate (Fig. 34) was used purely and in several solutions. ***N-butyl acetate (NB)*** is an ester (Fig. 34) and a colorless liquid at room temperature [100, 178].

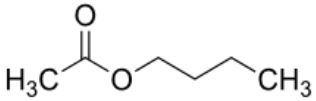

Figure 34: Chemical structure of n-butyl acetate (NB).

Although n-butyl acetate (NB) is usually applied in stacking or insertion tests [100], it was applied in FNCT in this study in three different modifications (Tab. 4).

Table 4: Modifications of n-butyl acetate (NB) used in this study.

Modification	Denotation	Annotation
N-butyl acetate	***NB***	pure liquid
2 wt% of NB in a 2 wt% aqueous solution of Arkopal N 100	***NBA***	aqueous solution including detergent
2 wt-% of NB in a 5 wt-% aqueous solution of Lutensol	***NBL***	aqueous solution including detergent

Lutensol (fatty alcohol polyglycol ether) is a non-ionic surfactant and usually used as NBL in stacking tests of PE-HD applied for transport and packaging of dangerous goods [179].

4.2.2. Air and Water

The natural fluids air and water [180] were applied as test fluids. Air represents an inert fluid and water is considered as a liquid which neutrally accelerates slow crack growth. Data obtained in air are typically used as a reference for all other fluids [181]. In this study, distilled water was utilized.

4.2.3. Organic Liquids

Due to practical relevance and topicality, the organic liquids diesel and biodiesel were selected as test fluids. Diesel is a common fuel, which is derived from naturally occurring and mined petroleum oil by a specific fractional distillation. Therefore, it is a complex mixture of apolar paraffinic, cyclo-paraffinic, aromatic and olefin hydrocarbons, which is additived to meet the requirements of engines concerning efficiency and environmental friendliness. To be distinguished from alternative diesel fuel, petroleum-derived diesel is usually referred to as 'petrodiesel' in the open scientific literature [182]. It is simply termed 'diesel' in this study. Diesel (Cas No. 68334-30-5) is a yellow liquid with a flash point > 56°C (at normal pressure, determined in accordance with ISO 3679 [183]) [184].

Biodiesel is a renewable, alternative diesel fuel and defined as the mono-alkyl esters of vegetable oils or animal fats (fatty acid methyl esters, FAME) [185]. It is produced by transesterification of parent oil or fat to achieve a viscosity close to that of diesel but exhibiting higher polarity [53]. Since it is mainly used in Europe, rapeseed methyl ester (RME) was applied as biodiesel in this study. Under normal conditions, RME-biodiesel (EINECS No. 273-606-8) is a liquid colored bright yellow to brown with a flash point > 150°C (ISO 3679) [183].

Diesel was obtained from a local filling station, complying with the specifications in EN 590 [186]. Especially pure biodiesel without additives (RME) was provided by ASG (ASG Analytik-Service Gesellschaft mbH, Neusäß, Germany) in fatty acid methyl ester (FAME) quality (EN 14214 [187]).

4.2.4. Fluids for Bell telephone test

In addition to the fluids applied in FNCT, a variation of liquids was used only in BTT (Tab. 5). In BTT, all liquids were especially evaluated concerning their capability of crack initiation. These fluids were selected to cover a broad range of chemical categories. Accordingly, they were selected due to similar chain lengths but different moieties.

All fluids were obtained from Sigma-Aldrich (Sigma-Aldrich Chemie GmbH, Munich, Germany).

Table 5: Fluids of different chemical classes applied in BTT; data obtained from data sheets [188, 189, 190, 191, 192].

Name	CAS No.	chemical category	chemical formula
dodecane	112-40-3	alkane hydrocarbon	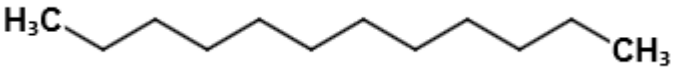
1-nonanol	143-08-8	fatty alcohol	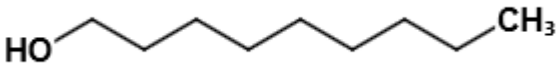
2-nonanone	821-55-6	alkanon	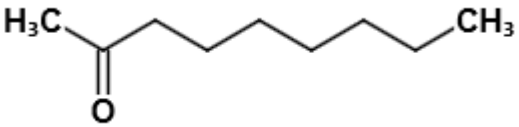
nonanal	124-19-6	alkyl aldehyde	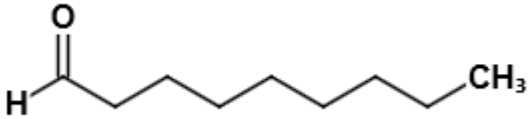
2-nonyl acetate	143-13-5	acetate	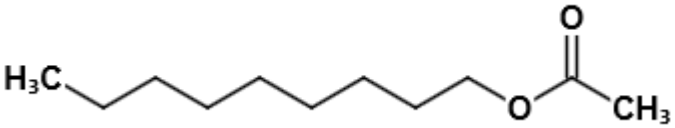

4.3. Characterization results

This chapter comprises the characterization results of PE-HD types and test fluids in terms of selected physical and chemical properties.

4.3.1. Molecular mass and crystallinity

GPC, DSC, DMA and XRD (sections 3.1.5 to 3.1.8) results presented in this section were also part of the Master thesis of P. Pip and performed at Fraunhofer LBF in Darmstadt, Germany [146, 193].

The molecular mass distribution (MMD) obtained from GPC of granules is depicted in figure 35 a. 5021DX exhibits a medium molecular mass (MM) M_w compared to the other PE-HD types but it has the narrowest MMD. AGUV and AGBD show similar MMD broader than that of 5021DX. The MMD of AQ149 is similar to AGUV and AGBD but AQ149 shows the lowest M_w. 5831D has the broadest MMD with a MM slightly higher than AQ149 but lower than the other PE-HD types. The MMD of 5831D might be fitted mathematically by three Gauss distribution functions, which is according to expectation since 5831D is a trimodal PE-HD type (section 4.1). Due to this trimodality, the polydispersity D_{pol} of 5831D obtained by the ratio of M_n and M_w (Eq. 1, 2 and 3) has to be taken with due care and may be considered as an estimation (Tab. 6).

a) b)

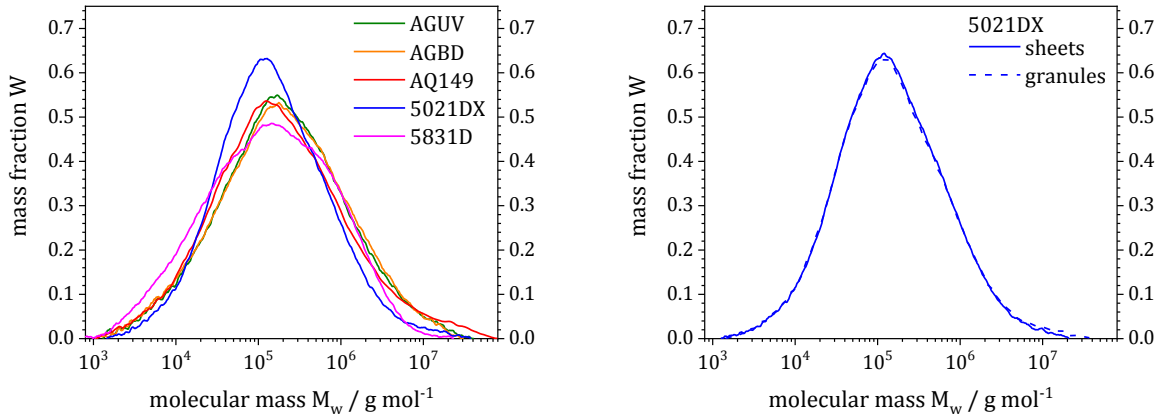

Figure 35: Molecular mass distribution obtained from GPC of a) granules and b) granules and a sheet of 5021DX.

M_n, M_w and D_{pol} data determined by GPC are presented in table 6. The comparison of MMD obtained from GPC of granules and sheets of 5021DX (Fig. 35 b, Tab. 6) reveals that the MMD is recurred within an allowable tolerance after standard sheet preparation by a heated press (section 4.1), i.e. there is no significant change in MM after thermal processing. The MMD of granules and sheets of the other PE-HD types are also equal.

Table 6: $\overline{M_n}$, $\overline{M_w}$ and D_{pol} obtained from MMD.

PE-HD type	$\overline{M_n}$ / 10^4 g mol^{-1}	$\overline{M_w}$ / 10^5 g mol^{-1}	D_{pol}
AGUV	4.62	8.57	18.6
AGBD	4.53	8.31	18.5
AQ149	5.02	4.61	9.2
5021DX	5.07	5.51	10.9
5021DX (sheet)	4.25	11.4	26.9
5831D	3.14	5.19	(16.5)

The temperature-dependent heat flow curves of AGUV and AGBD obtained from DSC of sheets (Fig. 36) have an almost identical shape for the first (Fig. 36 a, b) and second (Fig. 36 c, d) heating cycle. Therefrom, an equal crystallinity can be assumed. Crystallinity values are given in figure 36 and table 7. The courses of the first heating DSC curves of 5021DX and AQ149 are similar but exhibit larger melting peaks compared to AGUV and AGBD. This is attributed to a higher crystallinity, which might result from different polymerization processes since AGUV and AGBD are produced by a gas phase and AQ149 as well as 5021DX by a loop process. The comonomers used for all these PE-HD types were hexenes (Tab. 3). 5831D has the largest melting peak which confirms the highest crystallinity. 5831D also shows the highest melting temperature T_m. The differences between 5831D and the other PE-HD types are assumed to result from different comonomer types (butene vs. hexene) and polymerization processes (ACP for 5831D only vs. gas phase and loop process). A higher amount of comonomers as well as shorter chain lengths of incorporated comonomers are accepted to result in a higher crystallinity, a higher melting temperature and a higher density of PE [194, 195, 196, 197]. This is due to a facilitated convergency of the polymer chains with a lower amount and length of chain branches. Accordingly, 5831D with the comonomer 1-butene exhibits higher values in crystallinity, melting temperature (Fig. 36, Tab. 7) and density (section 4.3.2) than the other PE-HD types that contain 1-hexene comonomers.

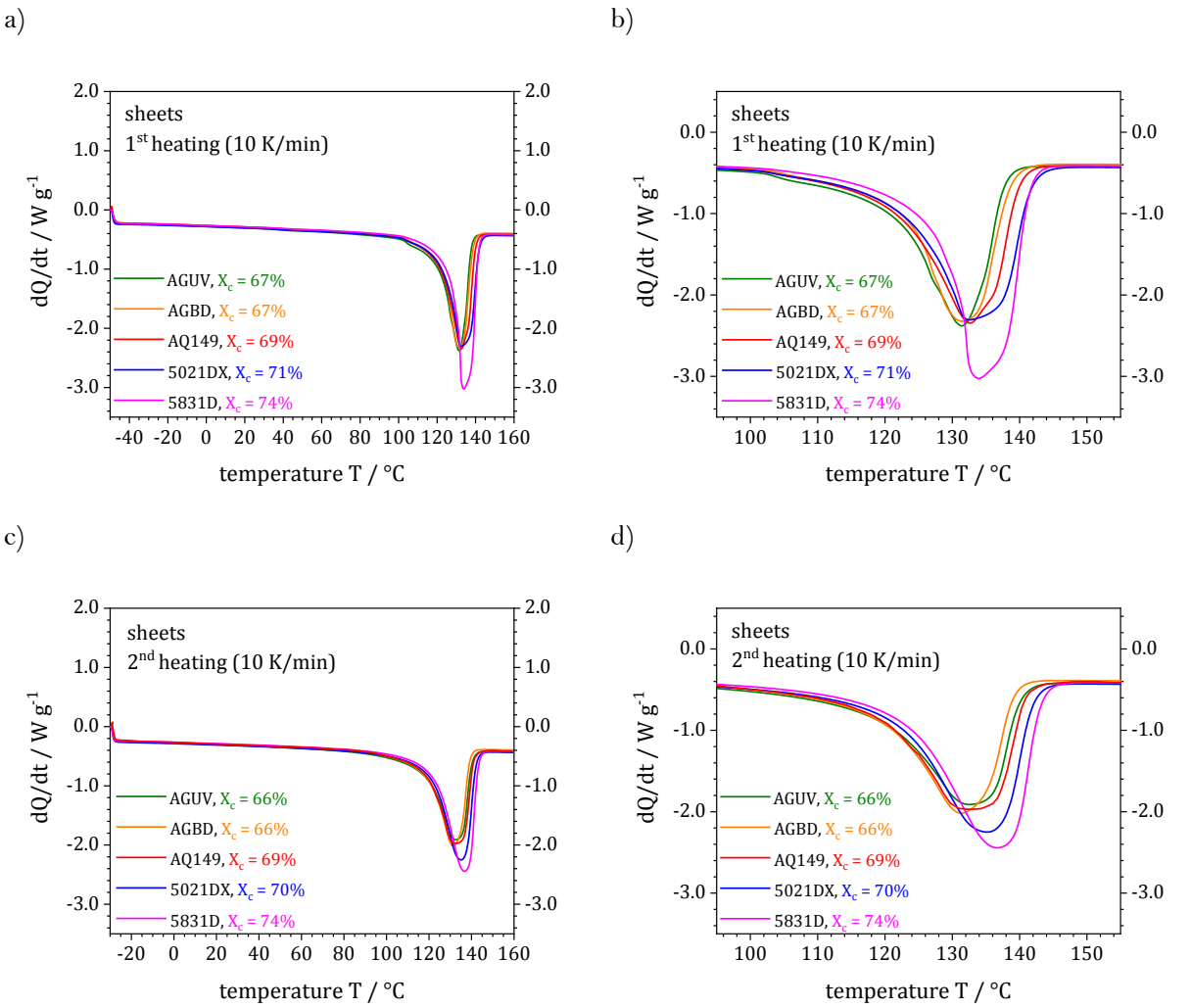

Figure 36: DSC data of the first and second heating in a temperature range of -50°C to 160°C (a) and -30°C to 160°C (c) with a heating rate of 10 K/min for 1 mm thick specimens, b), d) extracted data in the melting temperature range (95°C to 155°C).

After the second heating (Fig. 36 c, d), the courses of AGUV, AGBD and AQ149 as well as 5021DX and 5831D tend to assimilate, respectively. However, differences between melting temperature and crystallinity obtained after first and second heating are low. Hence, the specimen preparation process using a heated press and including tempering (section 4.1) does not change the melting temperature and the crystallinity significantly (Tab. 7).

Table 7: Melting temperature T_m and crystallinity values $X_{c,\,DSC}$ obtained from DSC.

PE-HD type	melting temperature T_m (1st heating) / °C	crystallinity $X_{c,\,DSC}$ (1st heating) / %	melting temperature T_m (2nd heating) / °C	crystallinity $X_{c,\,DSC}$ (2nd heating) / %
AGUV	131	67	133	66
AGBD	131	67	131	66
AQ149	133	69	132	69
5021DX	132	71	135	70
5831D	134	74	137	74

WAXS spectra are depicted in figure 37 a and b. The peak and background areas were determined between $2\theta = 20°$ and $2\theta = 25°$ in all spectra (Fig. 37 b). The peaks at $2\theta \approx 21.6°$ and $2\theta \approx 23.9°$ are ascribed to the diffraction of the (110)-plain and (200)-plain of the polymer crystals, respectively. The ratio of the sum of these two peaks to the total area represent the crystallinity $X_{c,\,XRD}$ given in table 8.

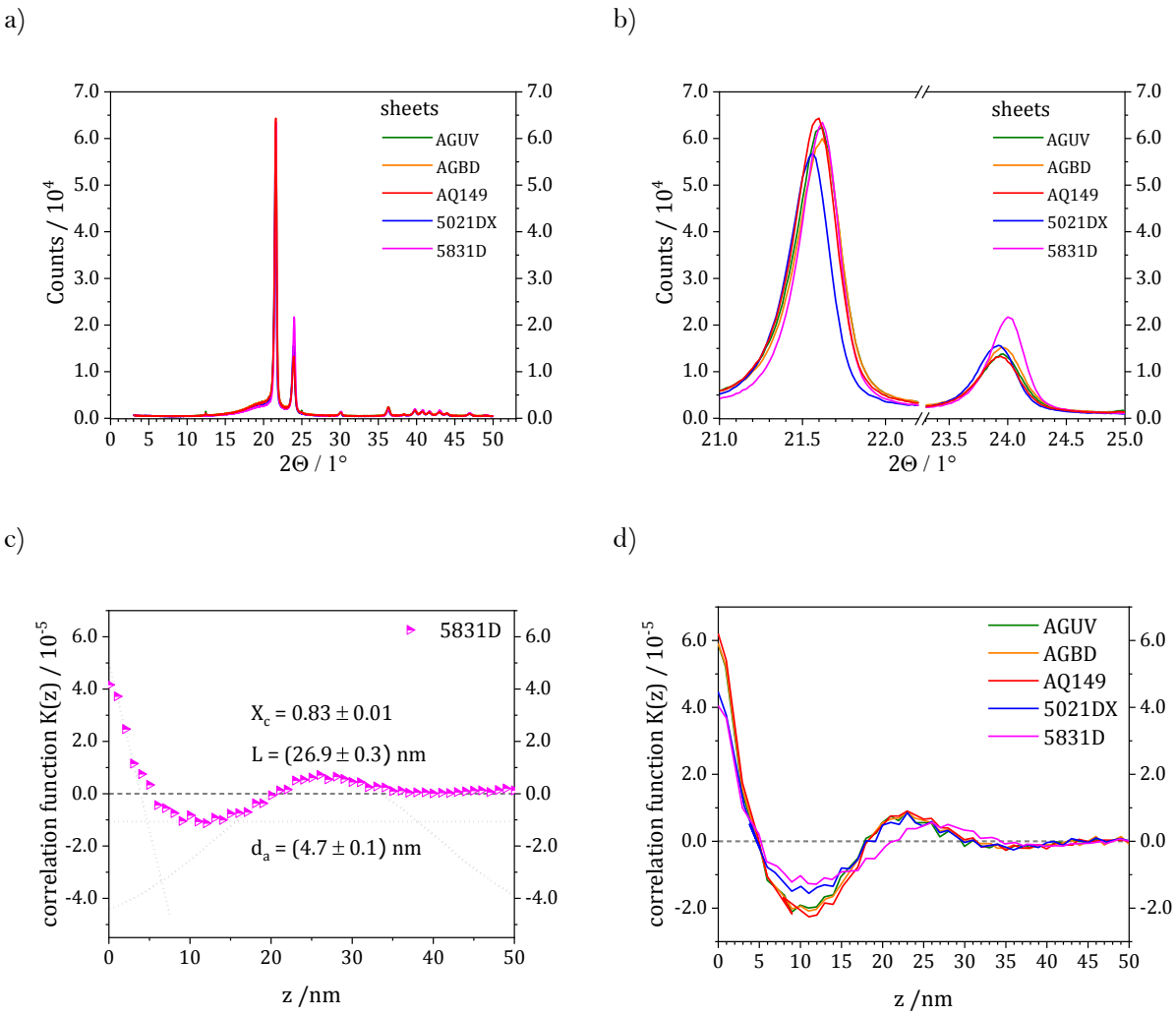

Figure 37: WAXS (a, b) and SAXS (c, d) data; a) in the entire 2θ-range, b) focusing on Bragg peaks, c) exemplary analysis of correlation function, d) correlation functions of all PE-HD types.

As expected, the DSC and XRD crystallinity values of all PE-HD types differ quantitatively but are similar qualitatively by showing the same ranking of PE-HD types (Tab. 8). $X_{c,\,XRD}$ values of AGUV and AGBD are equal. AQ149 and 5021DX exhibit slightly higher, whereas 5831D shows the highest crystallinity $X_{c,\,XRD}$. These differences are ascribed to different polymerization processes and comonomer types (Tab. 3).

Table 8: Crystallinity values $X_{c,\,DSC}$ and $X_{c,\,XRD}$ obtained from DSC and XRD.

PE-HD type	**crystallinity (first heating) $X_{c,\,DSC}$ / %**	**crystallinity $X_{c,\,XRD}$ / %**
AGUV	67	44
AGBD	67	44
AQ149	69	45
5021DX	71	46
5831D	74	50

Furthermore, SAXS correlation function data are depicted in figure 37 d. The analysis of a correlation function is illustrated exemplary for 5831D in figure 37 c. The local maximum of the correlation function provides a value of the long period L_p. Moreover, the slope between $z \approx 0$ and $z \approx 5$ was fitted linearly. From the intersection of this linear curve and the tangent to the local minimum of the correlation curve at $z \approx 10$ (black dotted lines in Fig. 37 c), a value of the thickness of the amorphous region L_a can be derived (section 3.1.8 and [198]), when a crystallinity of > 50% is presumed. This is reasonable because a crystallinity of > 50% was obtained by calorimetric analysis ($X_{c,\,DSC}$, Tab. 7). If the specimen crystallinity was < 50%, the thickness of the crystalline instead of the amorphous region would have been determined by this analysis procedure.

The long period L_p as well as the thicknesses of crystalline L_c and amorphous L_a regions are given in table 9. Additionally, the characteristic L_a/L_c and L_a/L_p ratios as well as the crystallinity $X_{c,\,SAXS}$ are indicated. $X_{c,\,SAXS}$ values result from the L_a/L_p ratios [198].

Table 9: Long period L_p, thicknesses of the amorphous L_a as well as crystalline L_c regions and crystallinity $X_{c,\,SAXS}$ obtained from SAXS.

PE-HD type	long period L_p / nm	amorphous regions L_a / nm	crystalline regions L_c / nm	ratio L_a/L_c	ratio L_a/L_p	crystallinity $X_{c,\,SAXS}$ / %
AGUV	23.7 ± 0.3	4.8 ± 0.1	18.9 ± 0.2	0.254	0.203	80.0 ± 1.0
AGBD	23.2 ± 0.2	5.6 ± 0.6	17.6 ± 0.3	0.318	0.241	76.0 ± 3.0
AQ149	23.5 ± 0.3	6.4 ± 0.8	17.1 ± 0.5	0.372	0.272	73.0 ± 4.0
5021DX	23.6 ± 0.4	5.0 ± 0.2	18.6 ± 0.2	0.269	0.212	79.0 ± 1.0
5831D	26.9 ± 0.3	4.7 ± 0.1	22.2 ± 0.2	0.212	0.175	83.0 ± 1.0

The long periods L_p of AGUV, AGBD, AQ149 and 5021DX are almost equal. 5831D shows the highest L_p and crystallinity $X_{c,\,SAXS}$. These results are qualitatively comparable to $X_{c,\,DSC}$ and $X_{c,\,XRD}$ (Tab. 8). Again, this can be assumed to result from the different comonomers of the PE-HD types: Since AGUV, AGBD, AQ149 and 5021DX contain 1-hexene comonomers, their long periods L_P and crystallinities $X_{c,\,SAXS}$ are similar. In contrast, 5831D with 1-butene comonomers exhibits higher values of L_P and a higher amount of crystalline parts.

Furthermore, the lower molecular mass M_w of 5021DX and 5831D compared to the other PE-HD types (Fig. 35 a) indicates the presence of shorter polymer chains. Therefrom, a lower number of tie molecules is assumed to occur in 5021DX and 5831D.

In figure 38, the temperature-dependent dynamic storage moduli G' and loss moduli G" (Fig. 38 a) as well as dissipation factors tan δ (Fig. 38 b) obtained from DMA in shear mode (section 3.1.7) are depicted. The decrease in G' and G" above 90°C is ascribed to the melting of crystalline phase. Below this temperature, three relaxation regions are identified at approx. -120°C, between -100°C and 20°C and at approx. 45°C. In the temperature range between -100°C and 20°C, the G"-curves of AGUV and AGBD are almost equal and show a relaxation maximum at approx. -35°C (Fig. 38 a, c). Those of 5021DX and 5831D are similar but exhibit a relaxation shift to higher temperatures of approx. -20°C. AQ149 shows the same relaxation shift accompanied by a relaxation shoulder broadening. It also exhibits the most pronounced G" curve differences compared to the other PE-HD types (Fig. 38 c). The similarities of AGUV and AGBD as well as 5021DX and 5831D curves in addition to their relaxation maxima grouping between approx. -60°C and -20°C (Fig. 38 a, c) might

be explained by the different molecular masses and crystallinities: AGUV and AGBD have the same crystallinity and similar MMD. 5021DX and 5831D exhibit higher crystallinity values than AGUV and AGBD and they are likely to have a lower number of tie molecules which is indicated by a lower MM.

Hence, these differences in melting behavior might result from different polymerization processes and comonomers of the PE-HD types (Tab. 3). Especially, the trimodal MMD of 5831D (Fig. 35 a) is significant in this regard. Differences of AGUV and AGBD to AQ149 in the temperature range of -80°C and 0°C are ascribed to different polymer production processes (synthesis and subsequent granulation) since AQ149 was applied as powder (section 4.1). AGUV and AGBD underwent an additional extrusion process during granulation in contrast to AQ149.

Therefore, similar molecular structures but differences in comonomer contents and the number of tie molecules may result in different mechanical properties between (i) AGUV/AGBD, (ii) AQ149 and (iii) 5021DX/5831D.

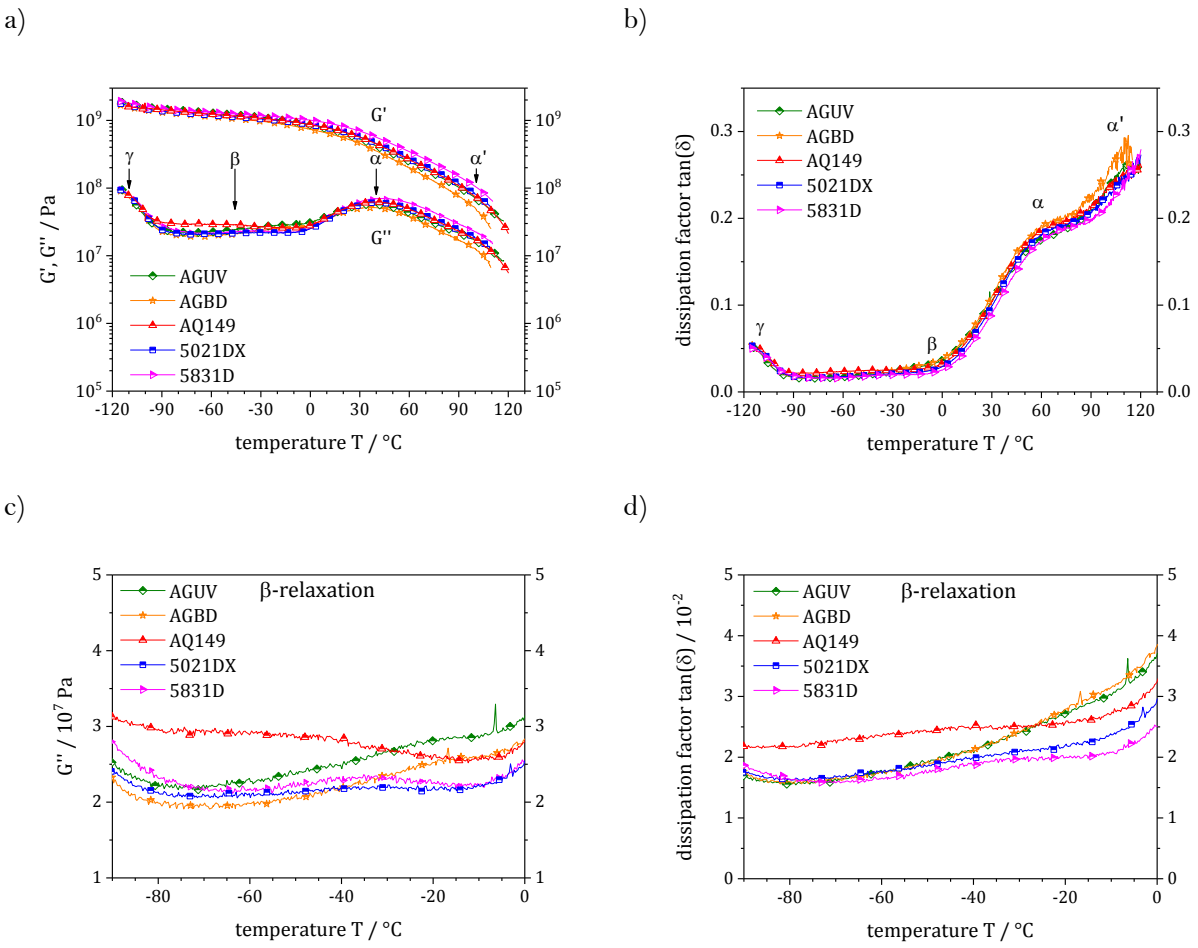

Figure 38: DMA data, a) temperature-dependent shear moduli G‘ and G“ and b) dissipation factors tan δ with a detailed consideration of c) G“ and d) tan δ within the temperature region of β-relaxation (-90°C to 0°C).

Relaxations can be characterized by shoulders in the tan δ curves (Fig. 38 b). The exact assignment of different relaxation processes in PE-HD to corresponding temperature regions is under constant discussion in the scientific literature. Typically, the α-relaxation is distinguished between α and α’ with $T_{\alpha'} > T_{\alpha}$ (Fig. 38 b) since the occurrence of two different relaxation processes is assumed. The γ-relaxation is ascribed to the amorphous phase and due to a localized crankshaft motion [199]. This

crankshaft motion is supposed to be a rotation of neighboring CH_2-groups about their interconnection axis which is associated with a stress reduction. The γ-relaxation of AQ149 is most pronounced. The other PE-HD types behave similar to each other with less pronounced γ-relaxations. This indicates a lower branching degree of AQ149 leading to a lower steric hindrance of the rotational relaxation.

The β-relaxation is also attributed to the amorphous phase, in which polymer chains become mobile. Accordingly, the β-relaxation depends on crystallinity and the degree of branching [200]. Due to the high crystallinity of examined PE-HD types, the β-relaxation is barely noticeable in tan δ curves (Fig. 38 b). In the temperature region between -30°C and 0°C, the dissipation factors within the two groups AGUV/AGBD and 5021DX/5831D are similar, respectively (Fig. 38 d). However, the AGUV/AGBD curves exhibit higher tan δ values, which indicate more prominent β-peaks and correspond to the slightly lower crystallinity values (Tab. 8). The tan δ curve of AQ149 shows a shoulder and is generally shifted to higher values (Fig. 38 d). Although AQ149 exhibits a higher crystallinity than AGUV and AGBD, β-relaxation is most pronounced in AQ149. A possible reason can be found in the lower branching degree of AQ149 compared to all other PE-HD types.

The α-relaxation is supposed to occur in the crystalline phase and is observable at crystallinities of $> 55\%$ [200]. The primary mechanism of α-relaxation is an interlamellar shear process, which is influenced by crystallinity and lamella thickness. The α-relaxation temperatures obtained for the different PE-HD types in the tan δ curves indicate a linear relation between crystallinity and α-relaxation.

The α'-relaxation is attributed to the interfacial region of the amorphous and crystalline phase ('rigid amorphous phase'). This interface process is supposed to be an interlamellar slip process ('grain boundary phenomenon') [201]. Therefore, it is very sensitive to the orientations of lamellae in the adjacent crystalline phases and is shifted towards the melting region with increasing crystallinity [202].

4.3.2. Density

The results of density measurements (section 3.1.1) are illustrated in figure 39. Density values of density samples, FNCT samples, granules and data sheet values obtained from the manufacturer are compared (Fig. 39 a). Additionally, densities of biodiesel and diesel pre-saturated and unsaturated FNCT specimens are shown comparatively (Fig. 39 b).

a) b)

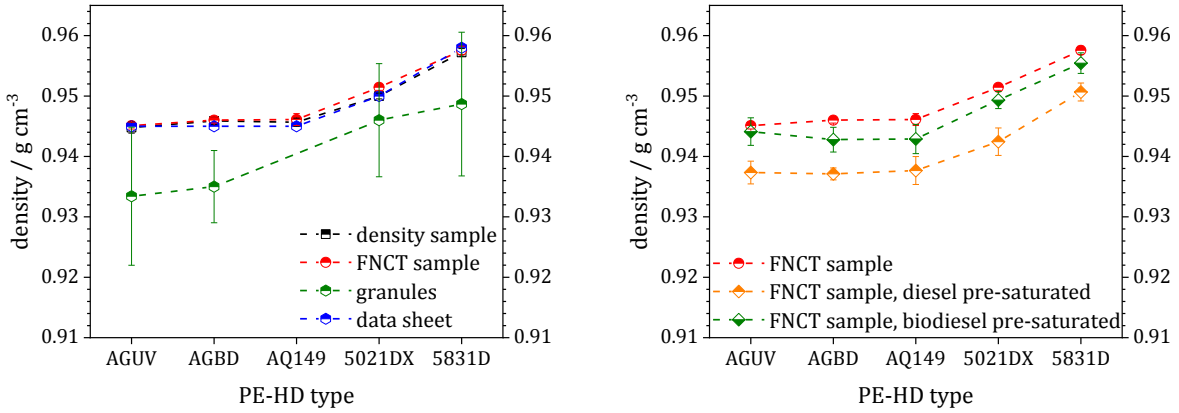

Figure 39: Density of a) different specimen types, b) FNCT specimens in dependence on sorption conditions.

Almost identical density values were obtained for density samples, FNCT samples and data sheets (Fig. 39 a). By reproducing data sheet values, the measurement method was additionally proven to be adequate. In turn, data sheet values are confirmed. The equality of density values obtained from density and FNCT specimens substantiate that no significant changes are introduced during FNCT specimen preparation. According to expectation, the density values of granules are the lowest. Due to the specimen preparation process including melting and recrystallization of the polymer induced by heating, cooling and subsequent tempering (annealing), the specimen crystallinity is increased. This leads to a higher density. Since AQ149 was received as powder (section 4.1), no granule density data could be obtained. Because the density values were determined by gravimetry, the error values of granule measurements (standard deviation) are higher due to their small size and weight (Fig. 39 a). AGUV, AGBD and AQ149 have the same density. 5021DX shows a higher density followed by 5831D. Hence, the density values correlate qualitatively to the crystallinities of PE-HD types (section 4.3.1) [203, 204]. The distribution of crystallinities of the PE-HD types results from the comonomer types and polymerization processes (section 4.3.1).

Furthermore, a decrease in density of pre-saturated FNCT specimens is revealed (Fig. 39 b). The densities of all PE-HD types are reduced by about the same factor after pre-saturation. FNCT specimens pre-saturated in diesel exhibit the lowest density followed by specimens pre-saturated in biodiesel and the unsaturated (Fig. 39 b). The reason for the decrease in density can be found in the swelling of FNCT specimens by diesel and biodiesel and the corresponding densities of mixture. The density values of diesel ($\rho_{diesel} \approx 0.84$ g/cm³ [184]) and biodiesel ($\rho_{biodiesel} \approx 0.88$ g/cm³ [185]) are lower than the densities of the PE-HD types. Therefore, the densities of the mixtures of PE-HD types and diesel or biodiesel are also lower than the density of pure PE-HD. Since the density of diesel is lower compared to biodiesel, the decrease in density of pre-saturated FNCT specimens is more pronounced in diesel than in biodiesel. In turn, the decrease in density is already an indication of the occurrence of PE-HD swelling by diesel and biodiesel (section 4.3.4). This is associated with a slight increase in volume of the FNCT specimens.

4.3.3. Surface tension of liquids

To characterize the interaction of liquids to their environment, surface tensions were measured (section 3.1.2) at 23°C and 50°C applying both, ring and plate method (Tab. 10, Fig. 41). The small error values represent the standard deviation of a ten-fold determination of surface tension for each liquid. Density values of the fluids used in ring method were received from data sheets (Tab. 10). The densities of aqueous solutions (Arkopal, NBA and NBL, section 4.2.1, Tab. 4) were calculated according to the individual densities of involved components by considering their fractions. Due to marginal differences in densities related to the test temperature, the same density values of liquids were applied for measurements at 23°C and 50°C.

Table 10: Surface tension and density values [177, 178, 180, 184, 185] of liquids.

liquid	**density (23°C, 50°C) / g cm^{-3}**	**surface tension ring method (23°C) / mN m^{-1}**	**surface tension plate method (23°C) / mN m^{-1}**	**surface tension ring method (50°C) / mN m^{-1}**	**surface tension plate method (50°C) / mN m^{-1}**
water (pure)	0.9982	70.6 ± 0.1	71.6 ± 0.2	66.6 ± 0.2	68.2 ± 0.1
Arkopal (aq.)	0.9982	31.7 ± 0.0	32.0 ± 0.1	30.1 ± 0.1	30.3 ± 0.2
NBA (aq.)	0.9964	31.4 ± 0.0	31.8 ± 0.1	30.1 ± 0.0	30.5 ± 0.2
NBL (aq.)	0.9945	30.8 ± 0.1	31.1 ± 0.0	29.1 ± 0.0	29.8 ± 0.2
biodiesel (pure)	0.8800	30.8 ± 0.0	31.3 ± 0.1	28.9 ± 0.1	29.4 ± 0.2
diesel (pure)	0.8367	27.5 ± 0.0	27.7 ± 0.1	25.8 ± 0.1	26.1 ± 0.1
NB (pure)	0.8820	24.5 ± 0.0	24.4 ± 0.0	21.9 ± 0.0	22.0 ± 0.2

The surface tension values obtained by ring and by plate method show no decisive differences. Therefore, the values are assumed to be very exact.

The surface tension indicates the interaction of a liquid to its environment. It characterizes the tendency of a liquid to shrink into the minimum surface area in a gaseous surrounding and the ability of a liquid to wet its solid environment. Hence, the surface tension is closely related to the wetting ability of a liquid. Likewise, the solid surface tension quantifies the wetting characteristics of a solid material. Both parameters influence the interfacial tension between a liquid and a solid. The wetting of a solid surface by a liquid as well as the conditions associated with that wetting in terms of interfacial tensions and energies are usually considered with respect to the contact angle between the solid and the liquid (Fig. 40).

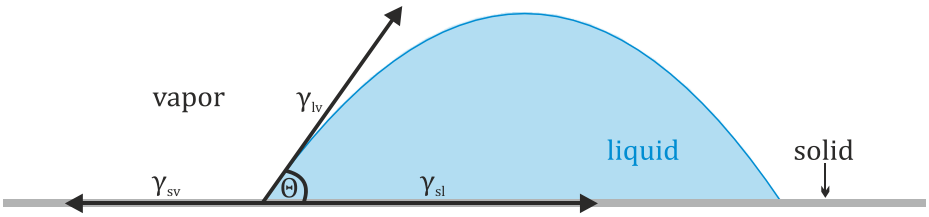

Figure 40: Schematic illustration of the contact angle formed by a sessile liquid drop including surface tensions γ_{sv}, γ_{sl} and γ_{lv}, after [209].

This contact angle is determined by a combination of the interfacial tensions of liquid, solid and vapor (external forces). In a specific environment, the contact angle is supposed to be characteristic for a given solid-liquid system [205]. As first described by Young in 1805 [206], the contact angle between a liquid and a solid surface is defined by the mechanical equilibrium of the three participating interfacial tensions (Young's Eq. 60):

$$\gamma_{sv} = \gamma_{sl} + \gamma_{lv} \cos(\Theta) \qquad (60)$$

with: γ_{sv}, γ_{sl} and γ_{lv} representing the solid-vapor, solid-liquid and liquid-vapor interfacial tensions, respectively, and θ is the contact angle. In this Young's equation, only two quantities are easily measurable, which are θ and γ_{lv}. To determine γ_{sv} and γ_{sl}, additional relations were established by Zisman et al. [207] and Neumann et al. [208]. Finally, according to Kwok and Neumann, the solid-liquid interfacial tension γ_{sl} only depends on the liquid-vapor γ_{lv} and solid-vapor γ_{sv} surface tensions [209]. Therefore, the solid-liquid interfacial tension γ_{sl} is a function of liquid-vapor γ_{lv} and solid-vapor γ_{sv} surface tensions [209]:

$$\gamma_{sl} = f(\gamma_{lv}, \gamma_{sv}) \Rightarrow \gamma_{sl} \propto \gamma_{lv} \qquad (61).$$

Especially, the solid-liquid interfacial tension γ_{sl} is directly related to the liquid-vapor surface tension γ_{lv}. Therefore, γ_{lv} is an indicator for γ_{sl}: a lower γ_{lv} denotes a lower γ_{sl}.

Furthermore, the numerical value of the interfacial tension γ_{sl} of a polymer was found by Mondal et al. [210] to be similar to the interfacial energy. This interfacial energy ('surface energy') is one essential parameter in regard to the formation of new internal surfaces during the liquid-influenced craze-crack mechanism of PE-HD (Eq. 19). Therefore, the surface tension of liquids is directly related to SCG and ESC. Hence, differences in surface tension between the liquids are in the focus (Fig. 41) to assess their influence on γ_{sl} and thus the ESC mechanism.

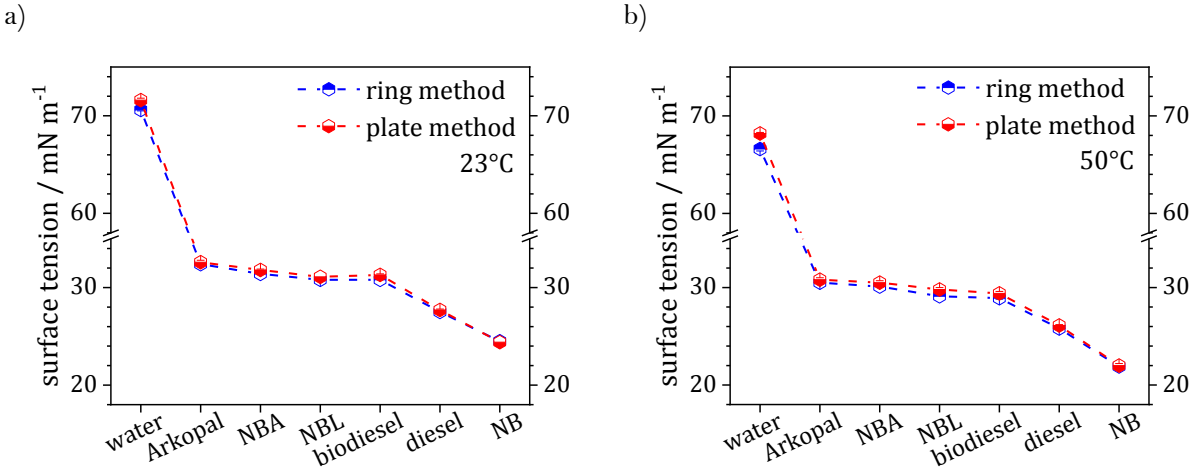

Figure 41: Surface tension values for all liquids obtained from tensiometer measurements at a) 23°C and b) 50°C.

Water exhibits the highest surface tension (Fig. 41). The surface tensions of all other liquids are lower by a factor of at least 0.5. Especially, the surface tension of Arkopal is lower compared to water. Diesel shows a lower surface tension than biodiesel, both exhibiting values moderately lower than Arkopal. The surface tension of NB is the overall lowest, whereas NBA and NBL show values similar to Arkopal and biodiesel.

The similarity in surface tension of Arkopal and NBA is remarkable, since the NB fraction within the solution of NBA seems not to affect the surface tension significantly. The n-butyl acetate may

evaporate during the measurement (section 4.3.4). Therefore, NBA is considered as an unstable solution. Consequently, the measured remaining solution was Arkopal (Fig. 43 b).

Furthermore, an increase in temperature from 23°C to 50°C leads to a decrease in surface tension. However, the quantitative reductions are marginal and qualitative differences in surface tension between all liquids are reproduced at higher temperatures (Fig. 41 a, b). The surface tension differences between the density-independent plate method and the density-dependent ring method (section 3.1.2) remain similar in 50°C measurements compared to 23°C.

4.3.4. Sorption and desorption behavior

The gravimetric analysis of the sorption and desorption behavior performed in this study (section 3.1.3) allowed for the determination of the relative mass uptake of liquids by PE-HD (Fig. 42 a-c, 43 b). From sorption curves of concentration C vs. time t, diffusion coefficients (section 2.2.2) were calculated for biodiesel and diesel (Fig. 43 a).

Besides the assessment of the time-dependent sorption degree, gravimetric analysis enabled to ensure that specimens had reached their concentration equilibrium (saturation) when saturated FNCT specimens were tested.

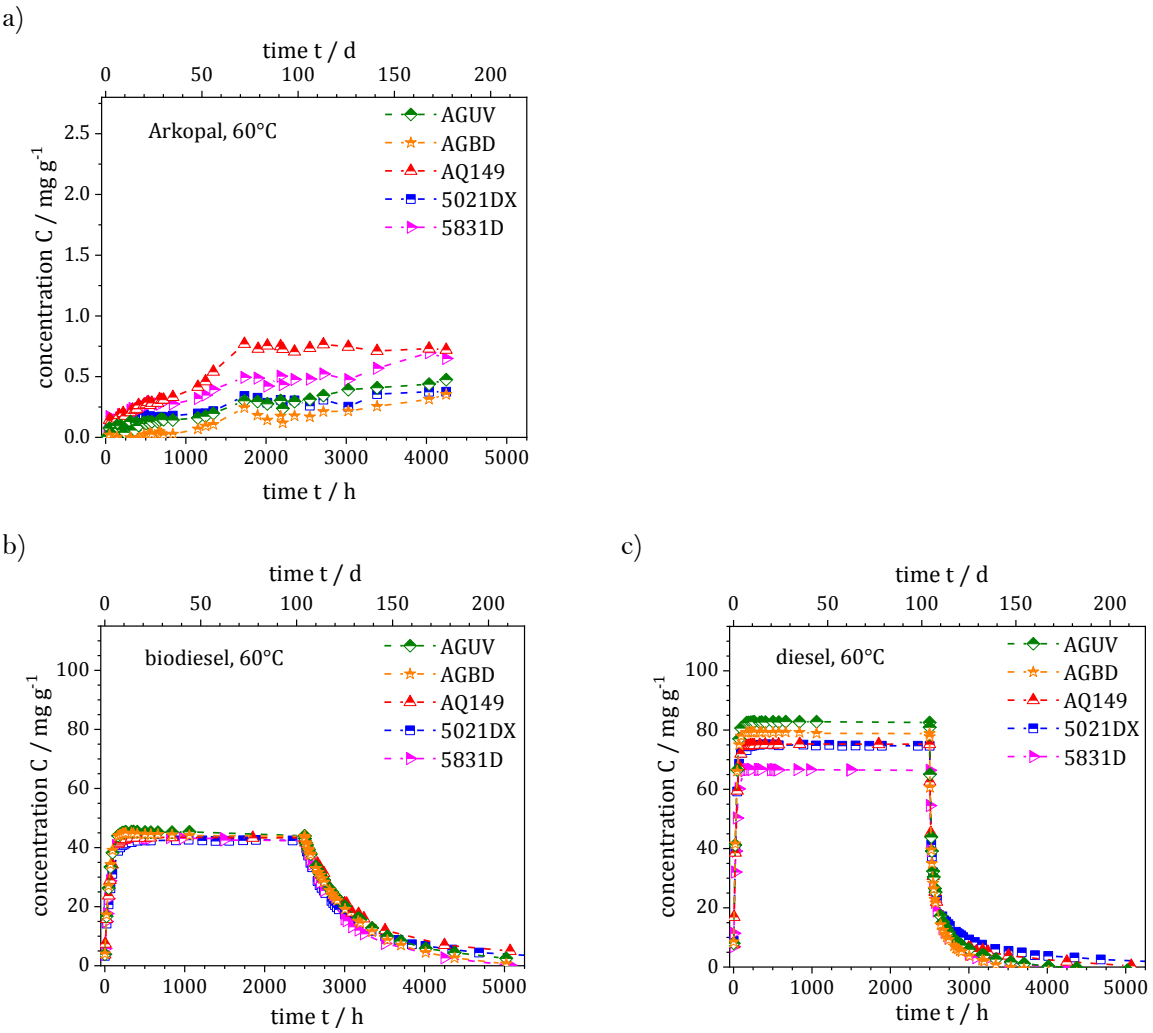

Figure 42: Sorption / desorption behavior obtained by gravimetric analysis at an exposure temperature of 60 °C for a) Arkopal, b) biodiesel and c) diesel.

a)

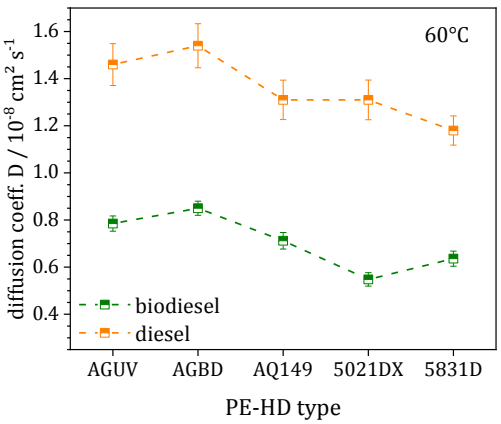

b)

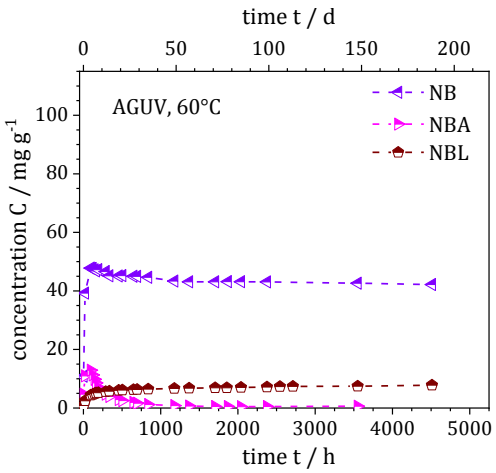

Figure 43: a) Diffusion coefficients D for biodiesel and diesel, b) sorption behavior obtained by gravimetric analysis for AGUV in NB, NBA (†unstable solution/emulsion) and NBL at an exposure temperature of 60 °C.

The results reveal, that the value of equilibrium concentration and the time to reach this value depend on the liquid (Fig. 42 a-c, 43 b). Diesel exhibits the highest value of equilibrium concentration with approx. 0.083 g/g (8.3%), followed by NB / biodiesel with approx. 0.045 g/g (4.5%). The Arkopal solution shows the lowest equilibrium concentration with a value of approx. 0.0005 g/g (0.05%). Due to the high fraction of water (98 wt%) within the Arkopal solution and the high polarity of water, this is according to the expectation that water is not absorbed by a polyolefin such as PE. Therefore, the Arkopal solution is to be considered as a non-sorptive, bulk-inactive fluid (Fig. 42 a, [157]). The equilibrium concentration of NBL (Fig. 43 b) has a value of approx. 0.01 g/g (1.0%). For NBA, the liquid concentration C is increased in the beginning of the test, but it is decreased after some time without reaching an equilibrium concentration > 0%. Hence, PE-HD was desorbing during further exposition by NBA. Since NBA was comprised of a sorptive (NB) and a non-sorptive fraction (Arkopal solution), the sorptive part was evaporated during the measurement. As a consequence, NBA has to be considered as an unstable solution which is reduced to an Arkopal solution by evaporation of NB after a distinct time.

In biodiesel, AGUV shows the highest maximum mass uptake, followed by AGBD, 5831D, AQ149 and 5021DX (Fig. 42 b). The scatter of the maximum mass uptake values depending on the PE-HD type in biodiesel is low. In diesel, the PE-HD type ranking in terms of mass uptake is AGUV, AGBD, AQ149, 5021DX and 5831D (Fig. 42 c). The differences in maximum mass uptake are more pronounced, ranging from approx. 0.067 g/g (5831D) to 0.083 g/g (AGUV). Concerning the maximum mass uptake in Arkopal solution, two groups of PE-HD types can be noticed (Fig. 42 a): AQ149 and 5831D exhibit higher, AGUV, AGBD and 5021DX lower values of maximum mass uptake. However, the overall mass uptake is much lower than in biodiesel and diesel. The mass uptake tends to correlate with the crystallinity and the density of PE-HD types that are governed by the polymerization processes and comonomers used (e.g. 1-hexene, 1-butene, section 4.3.1). This seems reasonable since liquids are preferentially absorbed in the amorphous parts of PE-HD [53, 211]. Hence, the lower the crystallinity of a PE-HD type, the more amorphous fractions are present, and the more liquid can be absorbed.

According to diffusion coefficients D, diesel is absorbed faster than biodiesel (Fig. 43 a). The diffusion coefficients D (at 60°C) vary in a small range depending on the PE-HD type: from $5.48 \cdot 10^{-9}$ $cm^2 s^{-1}$ to $8.5 \cdot 10^{-9}$ $cm^2 s^{-1}$ for Biodiesel and from $1.18 \cdot 10^{-8}$ $cm^2 s^{-1}$ to $1.54 \cdot 10^{-8}$ $cm^2 s^{-1}$ for Diesel. From these data, pre-saturation and conditioning times of FNCT specimens were calculated. Thus, a saturation time of approx. three weeks is required to receive saturated FNCT specimens with

dimensions of (6 x 6 x 90) mm³ (section 2.5.4). It has to be noted that due to the inherent properties of the diffusion process, a concentration gradient of diffusing species is formed from the outer rim to the center of the specimen during diffusion (section 2.2.2).

The results from desorption experiments show the reversibility of the sorption process. After a certain desorption time, the initial mass of every specimen is reached again. However, the time needed to complete desorption is longer than the time to reach saturation with approx. 9 weeks for diesel and approx. 15 weeks for biodiesel at 60°C. The difference in desorption time (desorption kinetics) between diesel and biodiesel is ascribed to the different volatility of the two penetrants. During desorption, a thin penetrant film was observed visually on the surface of biodiesel-soaked specimens. Such a film was not present on diesel-soaked specimens. The formation of such a liquid film on the surface reduces the effective concentration gradient [211], which determines the diffusive mass transfer of the penetrant. As a result, the desorption of biodiesel is further decelerated compared to diesel, especially more than expected from the different diffusion coefficients. Furthermore, the biodiesel film was most pronounced on the surface of AQ149 specimens, which explains the slower desorption process compared to all other PE-HD types.

4.3.5. Colorimetry

UV/Vis spectrophotometry was performed in reflection and transmission mode (section 3.1.4) to evaluate colored fracture surfaces after failure of specimens in FNCT (Fig. 44) as well as biodiesel and diesel in several aging conditions (Fig. 45). The absorbance A_{cal} data are compared. These were calculated from reflected and transmitted data. For FNCT specimen measurements, the surface of a genuine specimen was used as reference (Fig. 44).

a) b)

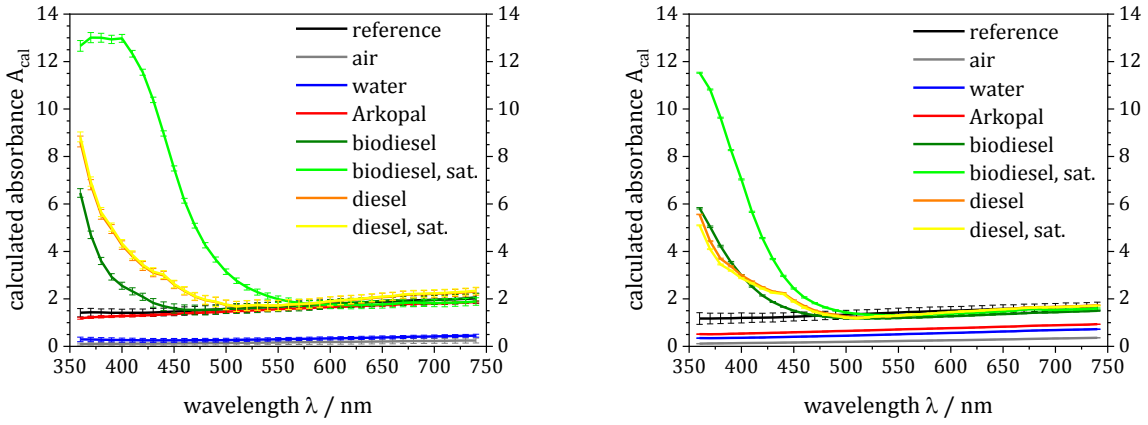

Figure 44: Calculated absorbance A_{cal} in dependence on wavelength λ (Kubelka-Munk function) for a) AGUV and b) 5021DX.

The curve shapes of wavelength-dependent calculated absorbance A_{cal} obtained from AGUV fracture surfaces are similar for all liquids compared to 5021DX (Fig. 44 a, b). Fracture surfaces obtained from FNCT in sorptive liquids biodiesel and diesel exhibit a distinctly higher absorbance in the wavelength region between approx. 350 nm to 500 nm. This wavelength region is attributed to partly UV, blue and bright green colors. Hence, an increased absorbance A_{cal} of fracture surfaces in this wavelength region indicates a coloration in yellowish and reddish tones. The more yellow, red and the darker the fracture surfaces appear, the more irradiation is absorbed in the wavelength

region between 350 nm to 500 nm. Furthermore, a significant difference between pre-saturated and non-saturated specimens becomes apparent for biodiesel. In diesel, there is no such difference.

FNCT specimens tested in Arkopal exhibit a higher A_{cal} for AGUV compared to 5021DX. This trend of higher absorbance and darker fracture surfaces of AGUV is confirmed in biodiesel and diesel, but not as significant as in Arkopal. The lower crystallinity of AGUV compared to 5021DX facilitates a higher absorption of (sorptive) liquids in AGUV (sections 4.3.1 and 4.3.3). This can also be seen in UV/Vis spectrophotometric A_{cal} data (Fig. 44).

To confirm the recognition of biodiesel and diesel being the causes for the coloration of FNCT fracture surfaces, biodiesel and diesel were analyzed in detail by UV/Vis spectrophotometry as well (Fig. 45).

a) b)

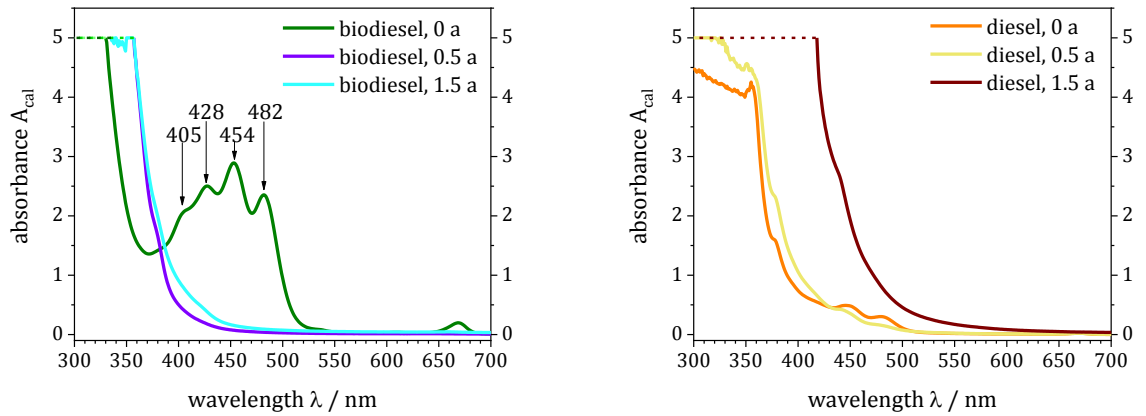

Figure 45: Calculated absorbance A_{cal} in dependence on wavelength λ for pure a) biodiesel and b) diesel after different times of ageing at 50°C.

A_{cal} obtained from UV/Vis spectrophotometry of biodiesel and diesel aged at 50°C for different time periods exhibits higher values in the same wavelength region as FNCT fracture surfaces of approx. 350 nm to 500 nm (Fig. 45 a, b, compared to Fig. 44). Accordingly, these liquids naturally exhibit a yellowish coloration. In unaged biodiesel, four distinct absorbance peaks are revealed at wavelengths of 405 nm, 428 nm, 454 nm and 482 nm, which disappear after ageing processes (0.5 and 1.5 years). Additionally, the absorbance bands of aged biodiesels (at approx. 380 nm to 400 nm) are shifted to lower wavelength values compared to unaged biodiesel (at approx. 500 nm). Thus, aged biodiesel exhibits a brighter yellowish color compared to unaged biodiesel.

In contrast, no such prominent absorbance peaks are unveiled in unaged diesel. The absorbance curves of aged diesel are shifted to higher wavelength values compared to unaged diesel (Fig. 45 b). Consequently, aged diesel exhibits darker red colors compared to unaged diesel.

It has to be noted that the detector used for the UV/Vis spectrophotometry of the liquids was capable of collecting A_{cal} data up to a value of 5. Hence, A_{cal} values higher than 5 have to be considered as total absorbance.

Moreover, no deliberately (pre)aged biodiesel or diesel was used for FNCT in this study.

5. Results and discussion

This paragraph is subdivided into four sections dealing with (i) the influences of different liquids and air (section 5.1), (ii) the influences of PE-HD structure on SCG/ESC (section 5.2) and (iii) the crack growth analysis (section 5.3). Finally, (iv) the consequences for stress crack testing using FNCT are presented (section 5.4).

To investigate the influence of different fluids on slow crack growth (section 5.1), classic FNCT time to failure and enhanced fracture surface analysis are used. The fracture surface analysis comprises micrographs obtained by LM, LSM and SEM (section 3.3). Especially, LSM and SEM allow for an advanced inspection of FNCT fracture surfaces. Characteristic features for the craze-crack mechanisms were found for different fluids. Furthermore, FNCT elongation data were found to provide a qualitative differentiation between fluid-dependent effects and to correlate to t_f* as well as to fracture surface appearances. Moreover, a blunting effect during crack initiation induced by sorptive liquids is described by the additional application of Bell Telephone Test (BTT) time to failure data.

The influence of the physical properties and the structure of PE-HD types (section 4.1) on slow crack growth is considered briefly (section 5.2). Therefore, FNCT t_f* were related to measured data of density, molecular mass (MM), crystallinity and α relaxation temperature (section 4.3) that were governed by the polymerization processes (e.g. reactor type, nucleation agent) and the chemical structure (e.g. comonomer type) of the PE-HD types.

Based on an enhanced crack growth analysis employing LM, LSM, SAM, CT and SEM imaging techniques, time-dependent crack lengths and crack growth rates were determined for FNCT in different environmental fluids (section 5.3). Therefrom, a direct correlation of craze and crack lengths was found. This correlation was indicated by fracture mechanics and verified experimentally in this study. Moreover, craze and crack lengths were related to FNCT elongation and the yield strength of PE-HD types.

Finally, stress-dependent FNCT with subsequent fracture surface analysis were performed to assess the transition from predominantly brittle to ductile failure behavior and the validity of the FNCT (section 5.4). Furthermore, the influence of test temperature on FNCT was studied. Stress- and temperature-dependent FNCT time to failure data were combined with fracture surface appearances. Therefrom, an empirical criterion to differentiate between predominantly brittle and ductile fracture surfaces was developed. This criterion is advantageous for practical testing in quality control processes.

5.1. Slow crack growth phenomena in different fluids

This section deals with slow crack growth phenomena under the influence of different fluids including air as reference. Therefore, 'classic' FNCT analysis using the time to failure (t_f*) in different fluids as an essential characteristic as well as elongation data and enhanced fracture surface analysis are included. Based on the results, a novel scheme of slow crack growth damaging processes on PE-HD for different classes of fluids (air, water, detergents, sorptive liquids) is proposed (section 5.1.4).

5.1.1. Air, water and detergent solution

The FNCT t_f* in air, water and a 2wt% aqueous solution of the detergent Arkopal are illustrated for different PE-HD types in figure 46.

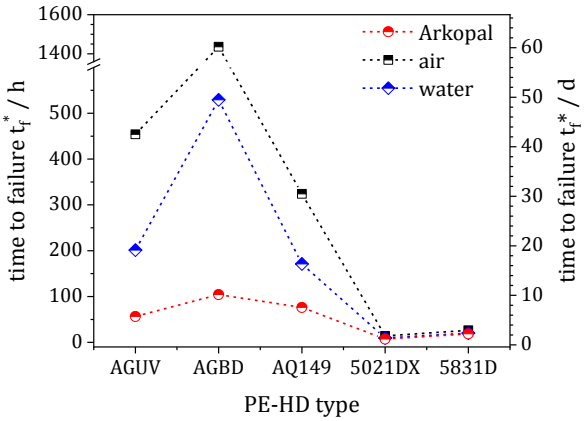

Figure 46: FNCT t_f* of different PE-HD types tested in air, water and the detergent Arkopal.

For all PE-HD types, the t_f* obtained in air are always larger than that in water and the detergent solution, which is smaller than that in water ($t_{f,\,air}$* > $t_{f,\,water}$* > $t_{f,\,detergent}$*, Fig. 46). Therefore, air is regarded as an inert fluid and t_f* results obtained in other fluids are referred to the t_f* of air. The failure mechanism in air is assumed to be pure SCG.

Water leads to a moderate reduction of FNCT t_f*, which is similar for all PE-HD types with a factor of approx. 0.5 compared to air. Hence, water is considered as a surface-active fluid, which accelerates crack growth neutrally concerning the ranking of different PE-HD types. Consequently, water leads to an accelerated SCG. The acceleration of SCG induced by a liquid is based on a reduction of interfacial tension that significantly facilitates the creation of additional internal surfaces during the craze-crack mechanism (cf. sections 2.3.2, 2.3.6 and 2.3.7). A detailed consideration of the damage mechanisms in this respect is given in section 5.1.3. Therein, the influences of all different fluids on SCG in PE-HD are discussed thoroughly.

The t_f* reduction by the detergent solution Arkopal is significantly higher and different for different PE-HD types (irregular). Although the PE-HD type ranking is qualitatively unchanged compared to air and water, the t_f* reduction is different. For instance, the t_f* reduction factor for AGUV is 1/8, whereas it is 1/14 for AGBD compared to air. Hence, the detergent has a distinct influence on the damage mechanism and is thus classified as a surface-active fluid, which accelerated crack growth irregularly in terms of the differences of PE-HD types in the ranking. According to definition (sections 2.3.6 and 2.3.7), such a surface-active fluid leads to ESC. How far a detergent can be considered to be 'neutral' in the sense of swelling and cohesion will be discussed below. Furthermore, the influences on SCG of physical and structural properties of the PE-HD types, such as crystallinity, density and molecular mass, that might also be relevant for their ranking are dealt with in section 5.2.

Fluid-dependent differences in fracture behavior are also apparent in LM and LSM fracture surfaces depicted exemplary for AGUV in figure 47.

a) Air, σ_L = 9.0 MPa

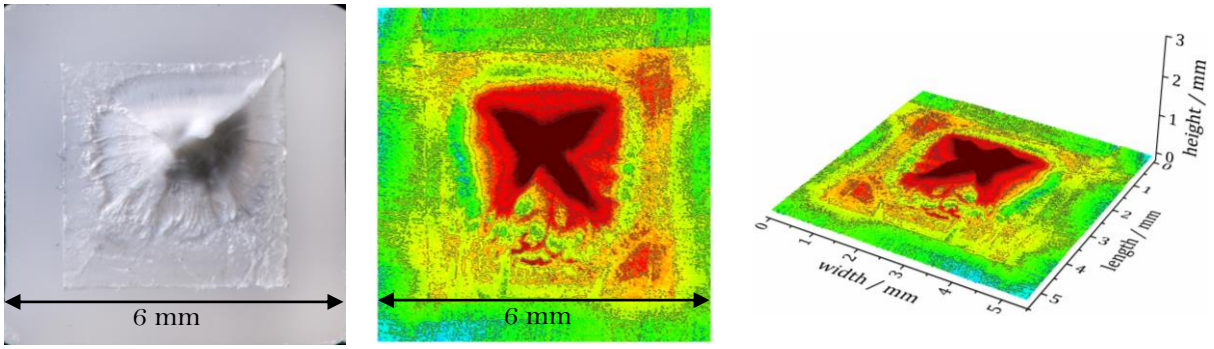

b) Water, σ_L = 8.9 MPa

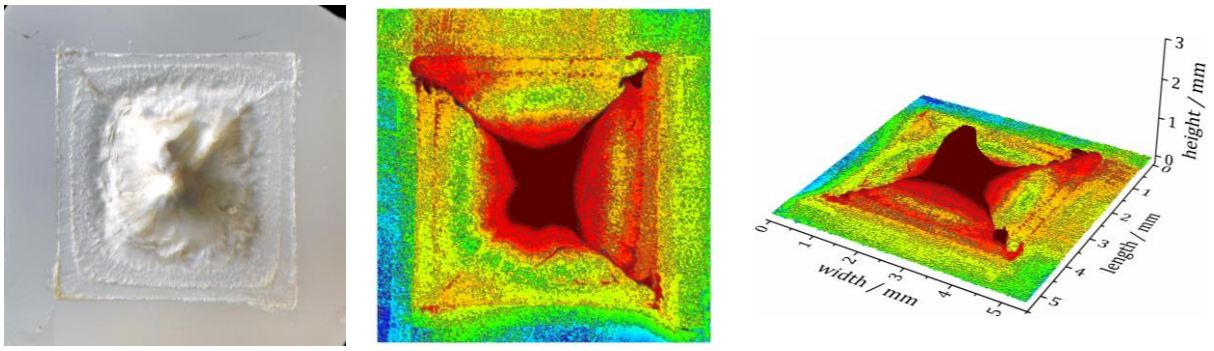

c) Arkopal, σ_L = 8.9 MPa

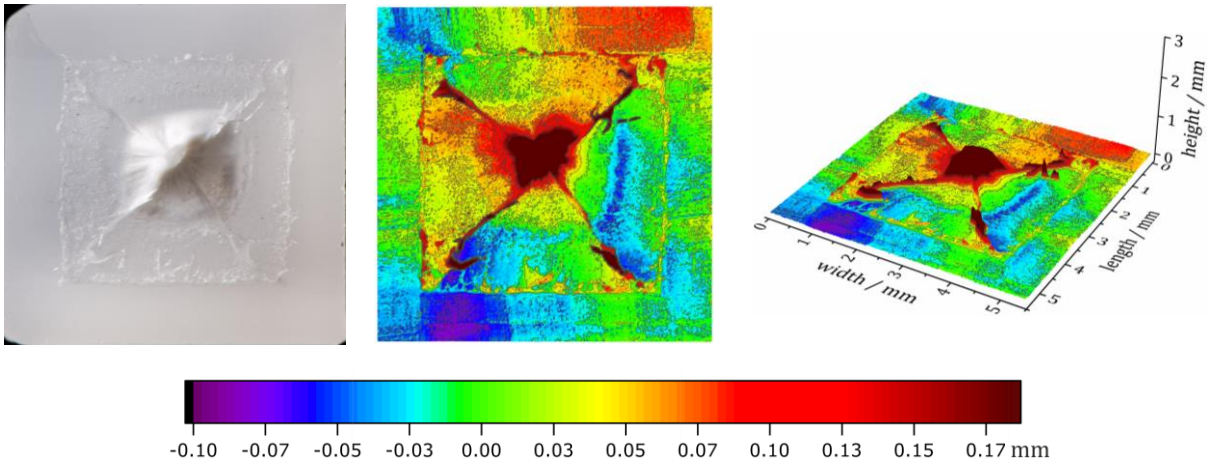

Figure 47: LM and LSM (2D and 3D) fracture surfaces for air (a), water (b) and Arkopal (c) of AGUV FNCT specimens tested at 50°C.

Fracture surfaces in air and water are almost equal and exhibit typical SCG signature (section 2.3.4): a brittle and smooth area beginning at the notch surrounds a high and rough ligament, which peaks in the center of the fracture surface (Fig. 47 a, b). The central ligament results from the increased true mechanical stress due to the decreasing residual, non-fractured area at constant force in the specimen center during FNCT and represents a globally ductile fracture behavior (sections 2.3.4 and 5.4). Especially from 2D and 3D LSM height data, differences of fracture surfaces are clearly indicated by the color codes. The color code is selected in a small height range of -0.10 mm to +0.17 mm. Despite the differences in t_f*, which have the same trend for different PE-HD types, the FNCT fracture surfaces in air and water are equal (Fig. 47 a, b). Both exhibit flat surface areas ascribed to brittle fracture behavior surrounding rougher areas with central ligaments

attributed to ductile failure in equal shares. Due to this similarity of fracture surfaces, the assignment of the ***inert fluid*** air and the ***surface-active, neutrally crack growth accelerating fluid*** water to an SCG mechanism seems to be plausible.

Fracture surfaces of FNCT in Arkopal differ to those obtained in air and water. Although also showing central ligaments typical for FNCT, brittle fracture surfaces in Arkopal exhibit a rather uniformly distributed roughness in contrast to air and water (Fig. 47 c). Additionally, the maximum height and the base area of the central ligament are smaller. These differences in fracture surface appearance and the significant t_f^* reduction lead to the assignment of such detergent solutions to an ESC-type mechanism. Because the detergent is surface-active, the acceleration of crack growth and the irregular PE-HD type ranking can be explained. Therefore, the Arkopal solution is denoted as a ***surface-active, irregularly crack growth accelerating liquid*** which leads to ESC in PE-HD.

Due to the same origins of SCG and ESC (craze-crack mechanisms, cf. sections 2.3.5 and 2.3.6), a qualitative rating in terms of the resistance of different PE-HD types against SCG/ESC (SCGR/ESCR) is commonly accepted, as far as predominantly brittle fracture surfaces are obtained in FNCT (section 2.3.4) [4, 9, 13]. Therefore, a detergent (Arkopal) is usually accepted to be used in FNCT to rank different PE-HD types. However, distinct peculiarities of their SCG and ESC behavior (quantitative evaluation) may be disregarded. Thus, an FNCT in fluids such as air and water is needed to test the intrinsic properties of PE-HD types in terms of their SCG resistance. Likewise, ESC inducing test fluids (e.g. surface-active detergents) have to be selected to distinctly evaluate ESC behavior. In both cases, a fracture surface analysis is expedient [157, 181].

5.1.2. Sorptive fluids (biodiesel and diesel)

In biodiesel and diesel, t_f^* are reduced strongly compared to the detergent, air and water (Fig. 48 a). Since detergents (Arkopal solution) are typically used in FNCT, Arkopal is taken as reference fluid in figures 48 a and b.

a) b)

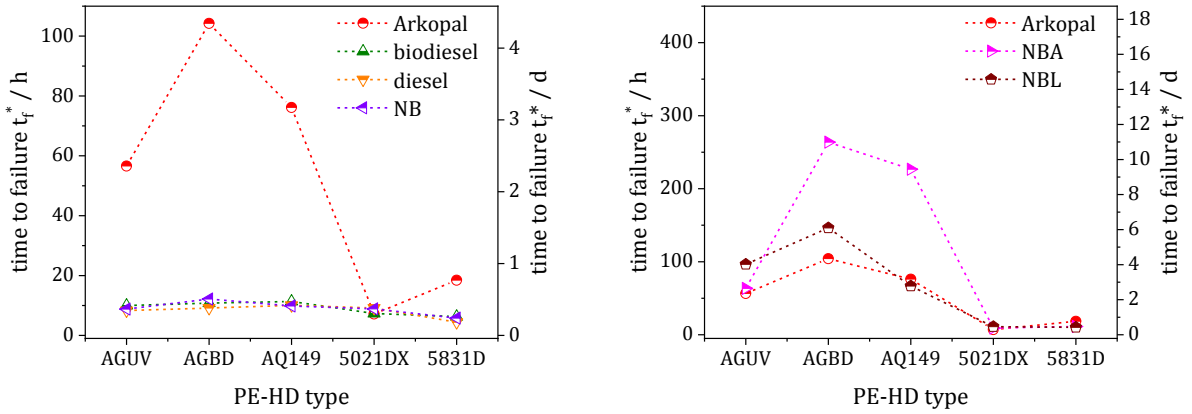

Figure 48: FNCT t_f^* values for different PE-HD types in a) Arkopal, biodiesel, diesel, NB and b) aqueous solutions Arkopal, NBA (†unstable solution), NBL.

Remarkably, the t_f^* differences between the PE-HD types occurring in air, water and detergent seem to disappear almost entirely in diesel, biodiesel and NB (Fig. 48 a). Additional to this t_f^* reduction, the rankings of PE-HD types are changed in biodiesel, diesel and NB. Due to the very short t_f^* in diesel, biodiesel and NB (approx. 10 hours), small variations in absolute t_f^* values however lead to large relative t_f^* differences that just facilitate a ranking of PE-HD types. Therefore, the extent of

differences in the PE-HD type ranking in biodiesel, diesel and NB is insignificant within the range of tolerance due to the small absolute t_f* differences.

Altogether, the times to failure of the test fluids are ranked $t_{f,\ air}$* > $t_{f,\ water}$* > $t_{f,\ detergent}$* > $t_{f,\ biodiesel}$* > $t_{f,\ diesel}$* with small differences in the PE-HD type ranking in biodiesel and diesel compared to detergent, air and water. Furthermore, diesel reduces t_f* more severe than biodiesel (Fig. 48 a). Therefore, a higher damage effect of diesel compared to biodiesel is expected. Furthermore, t_f* in NB has similar values as in biodiesel and diesel for all PE-HD types (maximum t_f* is about 10 hours). Their ranking is: $t_{f,\ diesel}$* < $t_{f,\ NB}$* < $t_{f,\ biodiesel}$*.

In comparison to Arkopal, NBA and NBL, t_f* is significantly reduced in NB (Fig. 48 b). The t_f* values in NBL are almost equal to t_f* in Arkopal. Similarly, t_f* in NBA are equal to t_f* in Arkopal for AGUV, 5021DX and 5831D. For AGBD and AQ149, NBA reduces t_f* by a factor of approx. 0.4 compared to Arkopal.

Since the liquids biodiesel, diesel and NB are absorbed by PE-HD to a significant extent (section 4.3.4), they are referred to as ***sorptive and bulk-active fluids*** (section 2.3.7). Since NBA and NBL comprise a sorptive (NB) and a purely surface-active (Arkopal, Lutensol) fluid component, they exhibit an intermediate position between detergent and NB in terms of sorption behavior (Fig. 43 b) and FNCT t_f* (Fig. 48 c). In NBA, the sorptive component NB is evaporated due to its volatile nature. Therefrom, an unstable solution results, which is confirmed by its sorption behavior (Fig. 43 b). Hence, no constant saturation of the FNCT specimen is expected for NBA, and the pure detergent (Arkopal solution) remains when NB is entirely evaporated. Accordingly, t_f* in NBA is similar to t_f* in Arkopal (Fig. 48 c). Although NBL is a stable solution (Fig. 43 b), the small amount of sorptive component (NB) seems not to be sufficient to lead to lower t_f*. Thus, the t_f* in NBL is also similar to that of Arkopal since the detergent Lutensol is the dominant component for crack growth within NBL. This is also confirmed by its sorption behavior, which exhibits a moderate absorption by PE-HD compared to NB (Fig. 43 b).

Based on the results of FNCT t_f* obtained for the different PE-HD types tested in different fluids, a categorization of fluids in terms of their influence on SCG is given in table 11. This categorization is also incorporated in the detailed consideration of SCG damage mechanisms of PE-HD (section 5.1.3 and scheme in Fig. 56 in section 5.1.4).

Table 11: Categorization of test fluids according to their effects on FNCT t_f*.

fluid category	**test fluid**	**characteristic**
inert	air	gas
surface-active, neutrally accelerating	water	pure liquid
surface-active, irregularly accelerating	detergent solution, Arkopal, NBA, NBL	aqueous solution of detergent
sorptive, bulk-active	biodiesel, diesel, NB	pure liquid

The effects of sorptive, bulk-active fluids to PE-HD can also be found in LM and LSM fracture images, which are depicted exemplary for AGUV in figure 49.

a) Biodiesel, σ_L = 8.9 MPa

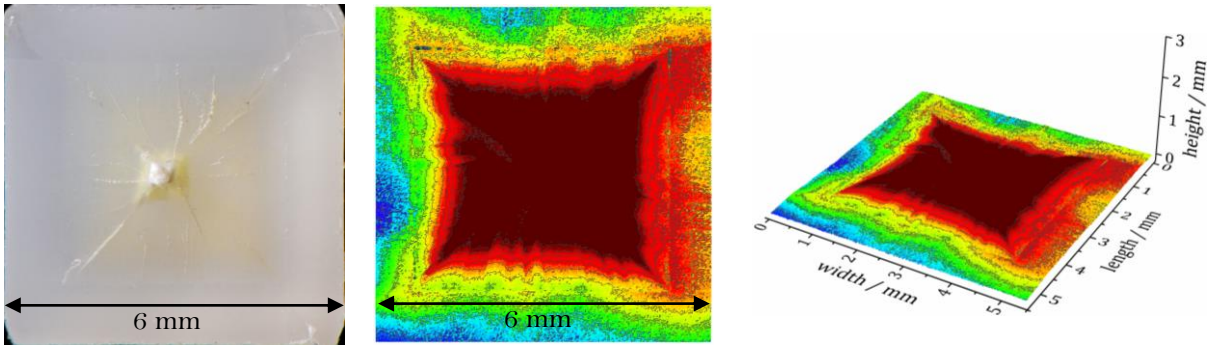

b) Diesel, σ_L = 9.1 MPa

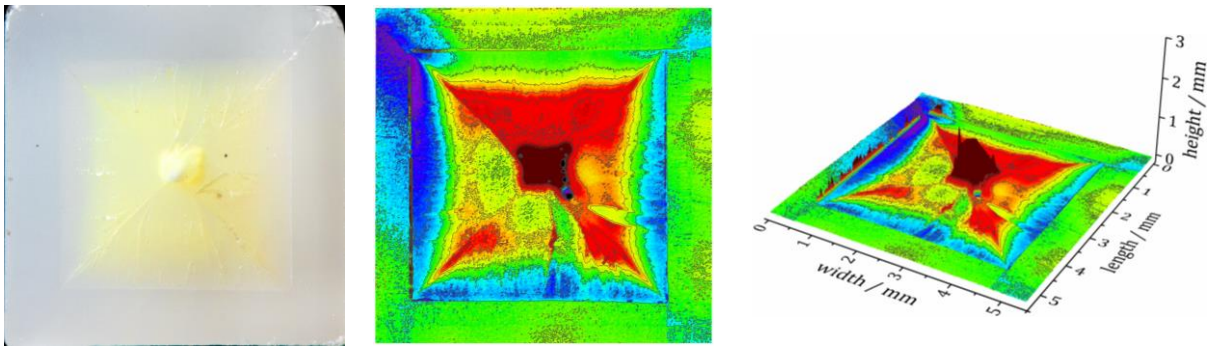

c) NB, σ_L = 9.1 MPa

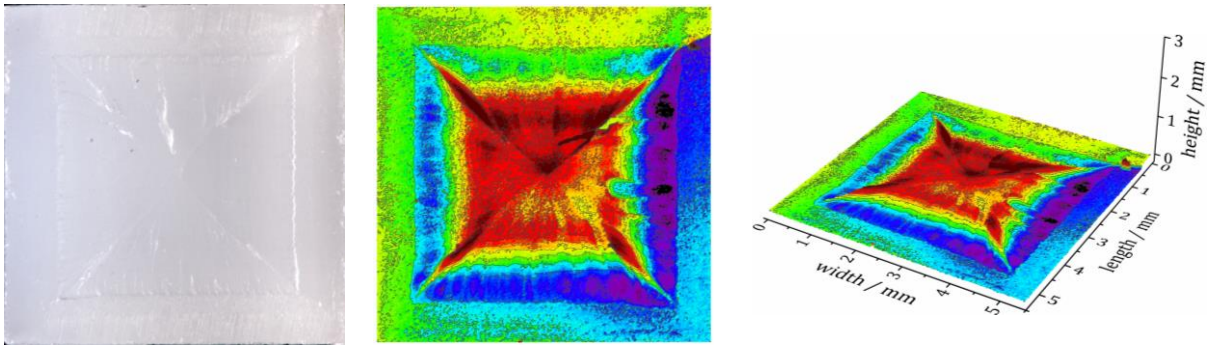

d) NBA, σ_L = 9.1 MPa

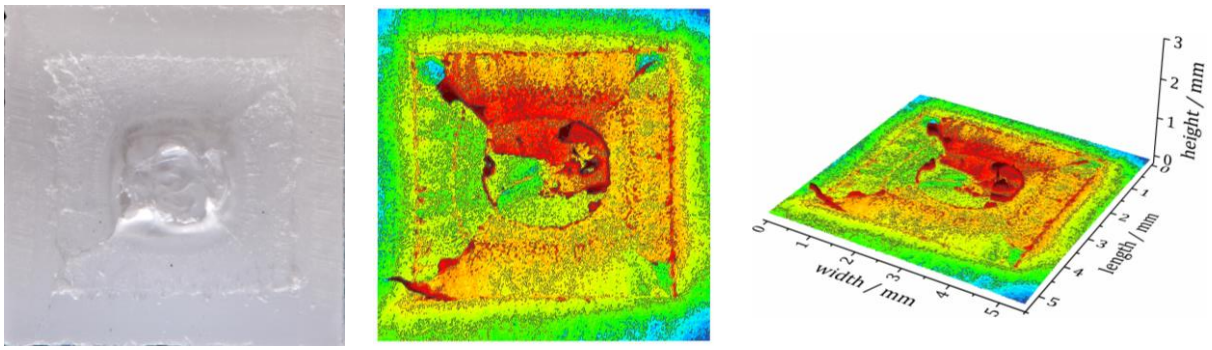

e) NBL, σ_L = 9.0 MPa

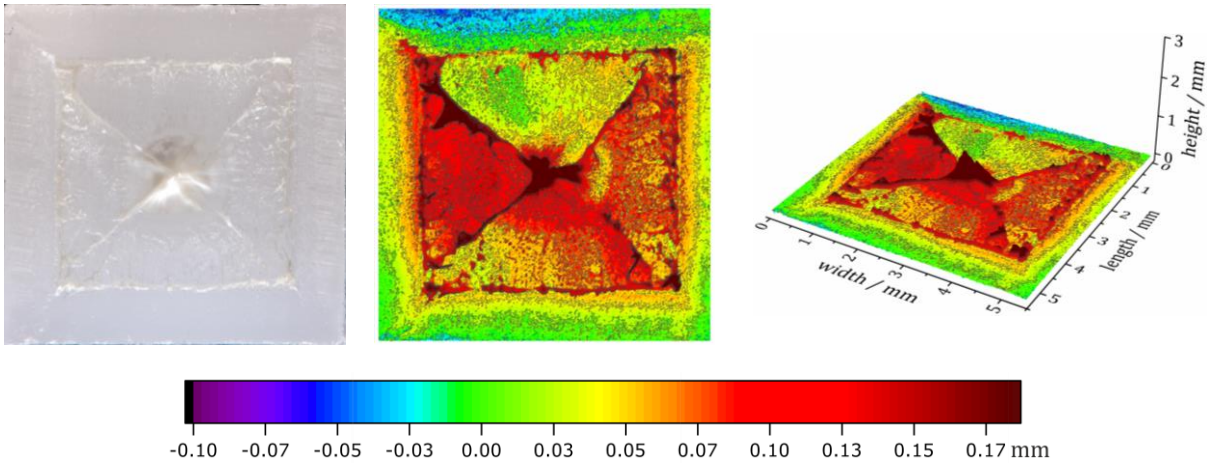

Figure 49: LM and LSM fracture surfaces for biodiesel (a), diesel (b), NB (c), NBA (d) and NBL (e) of AGUV FNCT specimens tested at 50°C.

Biodiesel, diesel and NB fracture surfaces (Fig. 49 a, b, c) show a high, but uniformly distributed surface roughness with a moderate maximum height and a large base area of the central ligament. In relation to the height of the notch area (zero level), biodiesel, diesel and NB fracture surfaces have an overlying pillow-like structure. The appearance of such a pillow-like structure is considered as typical for FNCT fracture surfaces resulting from crack growth in sorptive, bulk-active fluids.

The intermediate position of NBA and NBL in between NB and Arkopal in terms of sorption (more similar to Arkopal) is also displayed by the fracture surfaces: a pillow-like structure is signified but not as pronounced as in biodiesel, diesel and NB. NBA fracture surfaces show a less prominent peculiarity of the pillow-like structure compared to NBL since the latter is a slightly more sorptive and bulk-active liquid. However, the overall fracture surface appearance in both, NBA and NBL, is similar to air, water and detergent (Fig. 47). The fracture surface analysis is useful to differentiate between fracture and damage mechanisms.

Influence of sorptive, bulk-active liquids in detail

FNCT experiments with differently sorption-conditioned PE-HD specimens were performed to analyze the influence of the sorptive, bulk-active liquids biodiesel and diesel in more detail (Fig. 50). Three different sorption conditions were addressed by (1) performing standard FNCT applying a conditioning time of 10 h, (2) using pre-saturated specimens and a conditioning time of 10 h and (3) applying non-saturated specimens without conditioning (sections 3.2.2 and 4.3.4).

a) b)

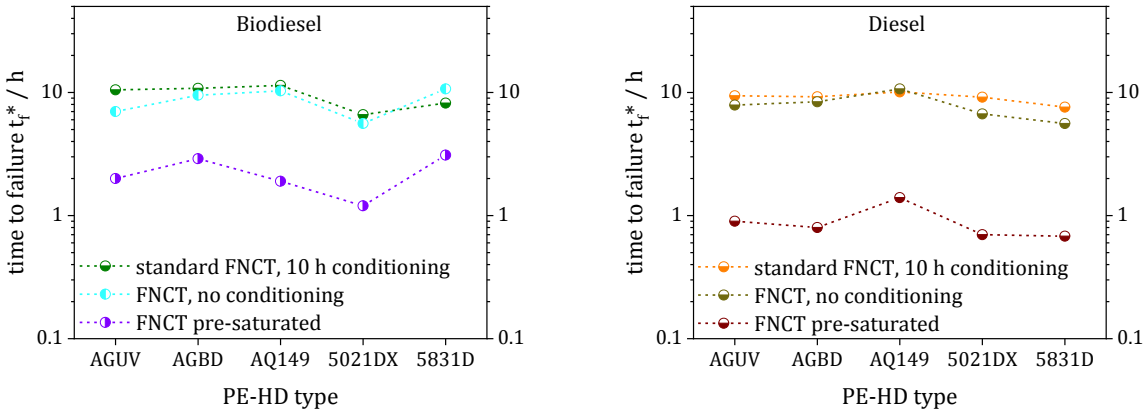

Figure 50: FNCT t_f^* of specimens tested in biodiesel (a) and diesel (b) in dependence on sorption condition.

For all PE-HD specimens pre-saturated in biodiesel and diesel, the t_f^* values are significantly reduced to approx. one to three hours (Fig. 50 a, b). This was expected due to a higher sorption degree compared to non-saturated specimens. The fluid-dependent rankings are reproduced ($t_{f,\ diesel}^* < t_{f,\ biodiesel}^*$, Fig. 48 a). Unexpectedly, t_f^* of non-saturated and unconditioned specimens is lower than t_f^* obtained from standard FNCT including 10 h conditioning.

The results of these FNCT experiments (Fig. 50) confirm the correlation of sorption to t_f* depending on the PE-HD types since t_f* is reduced for pre-saturated specimens. Hence, crack growth is further accelerated with increased liquid uptake by a specimen. This effect could be expected since the absorption of a liquid by PE-HD leads to a reduction of Van der Waals forces between polymer chains (due to a separation of chains) and a facilitated disentanglement that results in an accelerated craze-crack mechanism (more details are given in section 5.1.3).

However, an FNCT in a bulk-active liquid (biodiesel, diesel) using neither pre-saturated specimens nor a conditioning time leads to lower t_f* than a standard FNCT including a conditioning of 10 h. Since a sorptive liquid is already partly absorbed by the specimen during conditioning, the liquid mass uptake of a conditioned specimen is higher than that of an unconditioned specimen. After 10 h of conditioning at 50°C, the average concentration of biodiesel and diesel in PE-HD (AGUV) FNCT specimens is already approx. 0.5% and 1.2%, respectively (Fig. B1.89 in appendix B1). Furthermore, partly saturated specimens exhibit a sorption gradient with a higher sorption degree on the outer rim compared to the center of the bulk material (sections 2.2.2 and 4.3.4). This is also in contrast to completely saturated FNCT specimens, which show no sorption degree but have reached the maximum liquid uptake all over the entire specimen. Since unconditioned specimens result in lower t_f* than partly saturated specimens, a nonzero value of liquid uptake is assumed, at which a maximum t_f* is obtained. Evidently, a small amount of liquid absorbed by PE-HD leads to a blunting of the crack tip: The crack tip is compressed, and crack growth is decelerated [212]. When the absorbed liquid exceeds a certain amount in PE-HD (higher concentration), the enhanced crazing and disentanglement effects due to swelling and plasticization will become dominant again, and t_f* is reduced.

Features typical for biodiesel and diesel recur in LM and LSM fracture surfaces of FNCT specimens tested in dependence on their sorption condition (Fig. 51).

a) Biodiesel, standard conditioning of 10 h, σ_L = 8.9 MPa

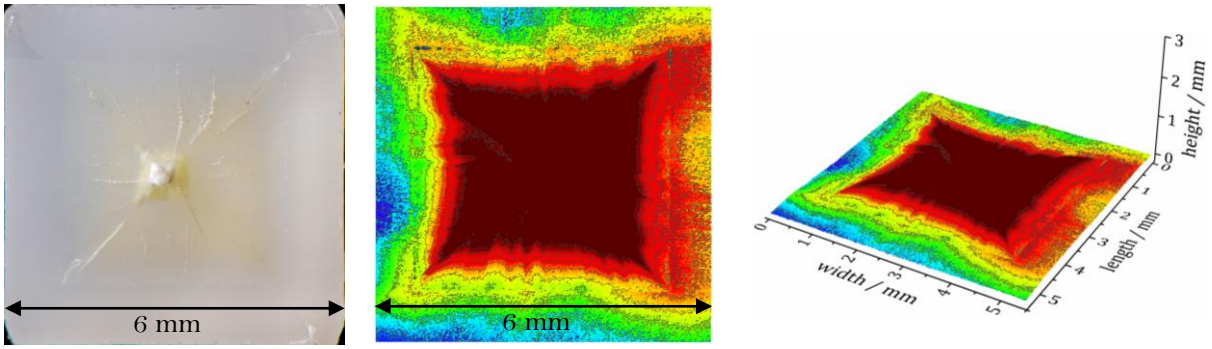

b) Biodiesel, pre-saturated specimen, σ_L = 9.1 MPa

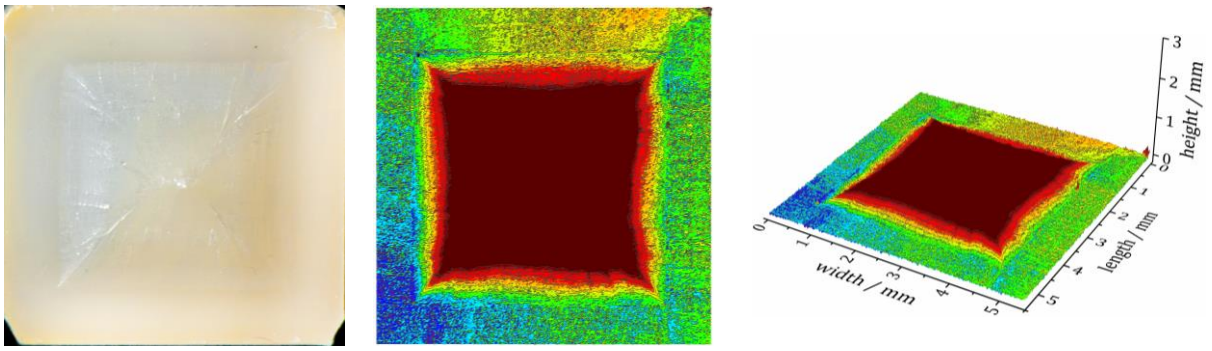

c) Biodiesel, no conditioning, σ_L = 8.8 MPa

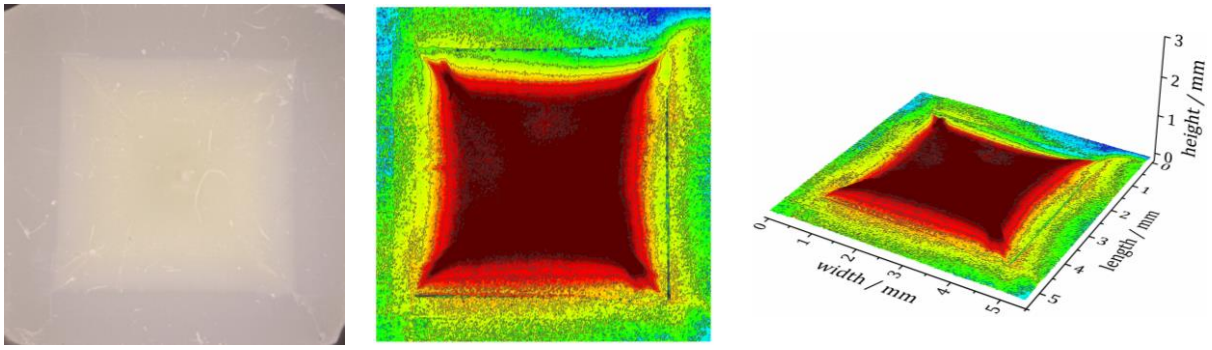

d) Diesel, standard conditioning of 10 h, σ_L = 9.1 MPa

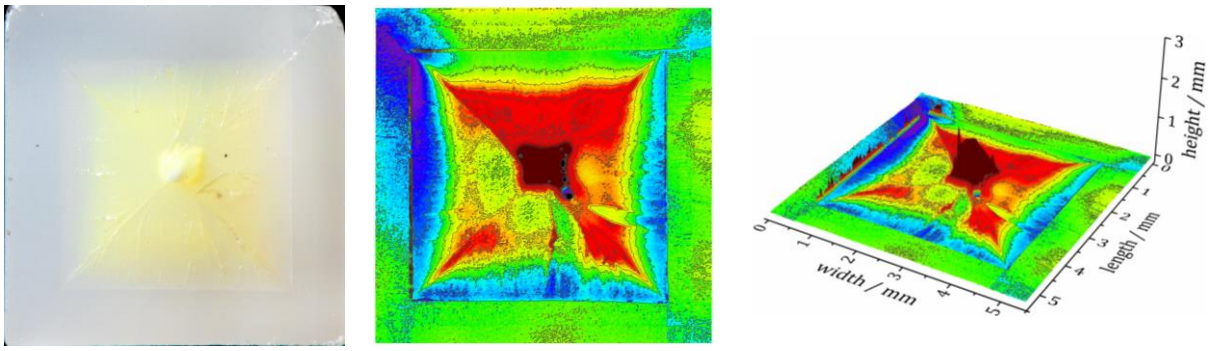

e) Diesel, pre-saturated specimen, σ_L = 8.7 MPa

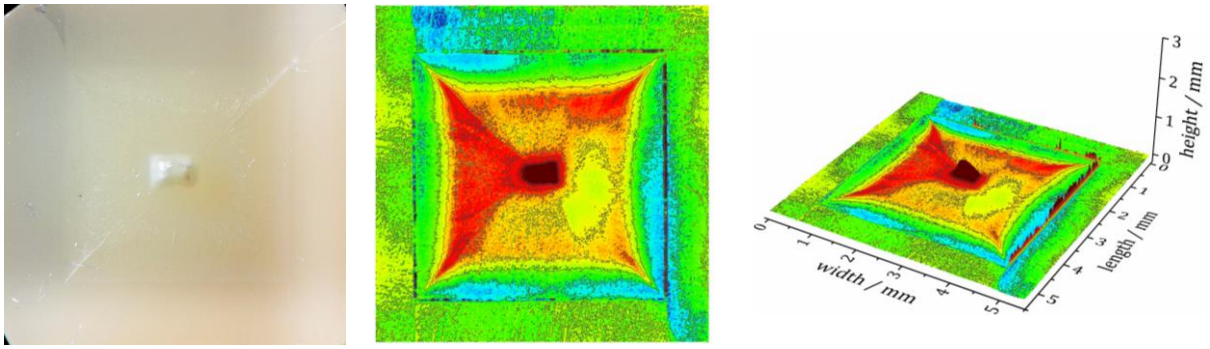

f) Diesel, no conditioning, σ_L = 9.0 MPa

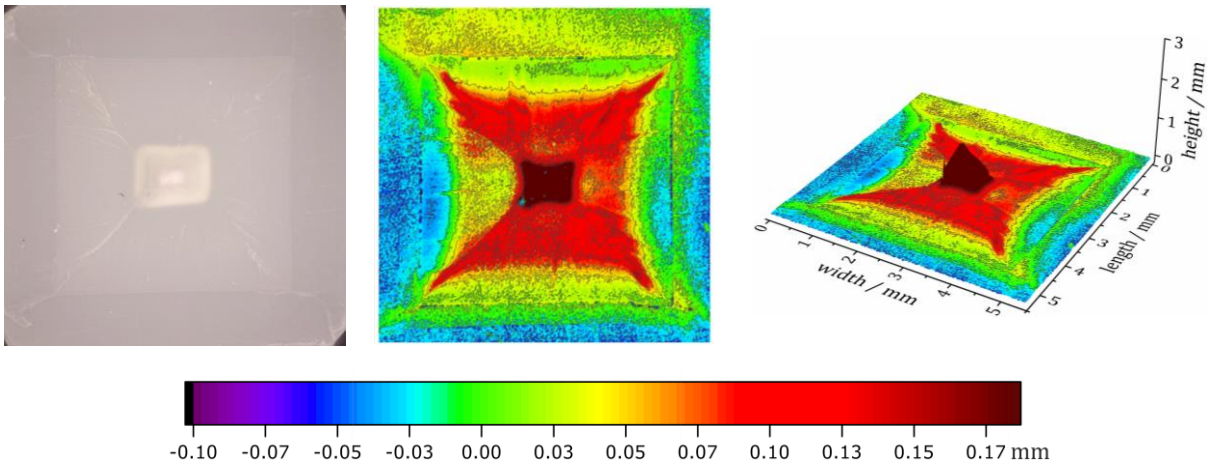

Figure 51: LM and LSM fracture surfaces of AGUV FNCT specimens tested in biodiesel and diesel in dependence on sorption condition.

The LM and LSM fracture surfaces show pillow-like structures, which are more pronounced in biodiesel than in diesel (Fig. 51). Diesel fracture surfaces exhibit a more prominent central peak with a lower base area compared to biodiesel fracture surfaces (Fig. 51 d, e, f). In terms of sorption condition, there are minor differences concerning the roughness distribution and the height of the central ligaments and pillow-like structures. In biodiesel, the surface roughness and the maximum height of fracture surfaces of pre-saturated specimens is higher compared to partially saturated specimens (Fig. 51 a, b, c). Differences in surface roughness and the central ligament between standard (Fig. 51 a) and non-conditioned (Fig. 51 c) specimens is barely identifiable. However, the sizes of the crack growth areas in between the notch and pillow-like areas on the fracture surfaces correlate to t_f*. Accordingly, fracture surfaces of pre-saturated specimens with the lowest t_f* exhibit the smallest crack growth area followed by non-conditioned (medium t_f*) and 10 h conditioned specimens (highest t_f*). The larger t_f*, the larger crack growth areas can be noticed that surround the pillow-like structures (Fig. 51 a to c). In this respect, diesel fracture surfaces are similar to biodiesel fracture surfaces (Fig. 51 d to f). This was expected since the fundamental damage mechanism (accelerated ESC) is the same in diesel and biodiesel. The slight differences in crack growth areas depending on the sorption conditions indicate only minor differences in the manifestation of the damage mechanism (sections 5.3.2 and 5.3.3).

Crack initiation / blunting effect

The blunting effect of sorptive liquids is confirmed by the results of Bell Telephone tests (BTT). In FNCT, a notch is deliberately introduced to start crack growth. Hence, crack propagation and final failure are focused rather than crack initiation in FNCT. In contrast, BTT is intended to explicitly address crack initiation (section 2.5.1). The imperfection introduced to BTT specimens prior to the test is perpendicular to the direction of crack growth and only cracks initiated during the test contribute to the results. Furthermore, the first cracks that occur (to ≥ 50% of all specimens) instead of complete specimen failure are taken as a measure of damage (section 3.2.1).

In the literature, the differentiation between the FNCT predominantly addressing crack growth and the BTT mainly focusing on crack initiation is not made unambiguously. Instead, both test methods are usually simply considered to address the SCG mechanism occurring to PE-HD [9, 14, 213]. However, since they provide information on different damage phases of SCG, FNCT and BTT are no competing but complementary test methods.

BTT results for AGUV and 5021DX are illustrated in figure 52.

a) b)

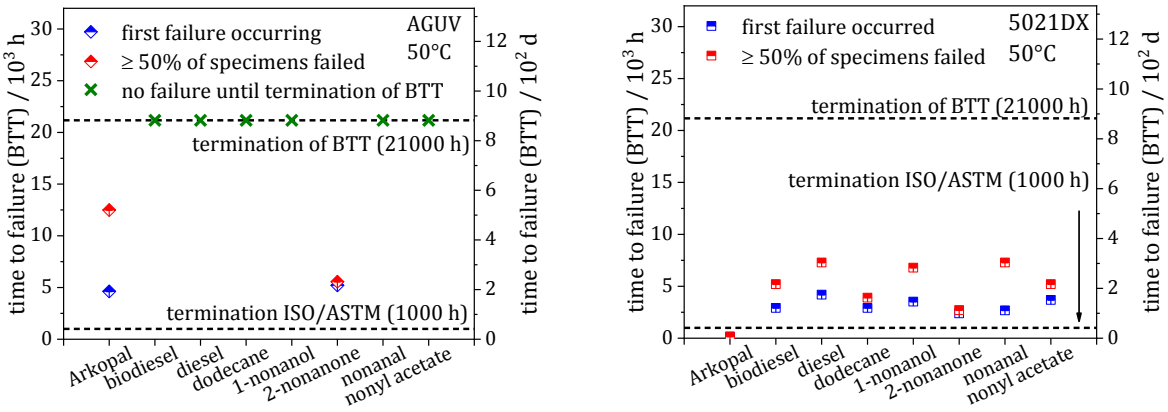

Figure 52: BTT time to failure of a) AGUV and b) 5021DX (according to ISO 13274 [100] and ASTM D1593 [99]).

For AGUV, cracks were only recognized in Arkopal solution and in the pure liquid 2-nonanone until the final termination of the test after 21000 h (Fig. 52 a). The first failure in Arkopal occurred after approx. 5000 h and ≥ 50% of specimens failed after approx. 12500 h. Hence, more than the doubled time was further required to induce failure in ≥ 50% of specimens after the first failure occurred. In 2-nonanone, the first failure occurred after approx. 5200 h and ≥ 50% of specimens failed after approx. 5600 h. Thus, crack initiation was most severe in 2-nonanone and Arkopal for AGUV. However, AGUV successfully passed the BTT in all test fluids according to the standards [99, 100] since a time to failure > 1000 h was obtained in any case.

For 5021DX, all test liquids led to failure within the regarded timeframe of 21000 h. Arkopal led to the most severe crack initiation since ≥ 50% of 5021DX specimens failed after approx. 160 h. 2-nonanone also evoked massive damage to 5021DX, especially exhibiting a small time differential between first failure and failure of ≥ 50% of specimens. The latest failure was reached in diesel, nonanal and 1-nonanol followed by biodiesel, nonyl acetate and dodecane.

As a result, crack initiation is most severe in surface-active fluids such as surfactants since Arkopal solution and 2-nonanone led to the most significant damage to AGUV and 5021DX in BTT (Fig. 52). In contrast, sorptive bulk-active liquids such as biodiesel and diesel exhibited longer BTT

failure times. In FNCT, the force applied to specimens is automatically kept constant and the effective stresses are increased as a result of the continuous reduction of the ligament area A_L during the test. Due to its implementation (section 3.2.1), an adaption of the applied force is impossible in BTT. Owing to relaxation processes within the PE-HD, effective stresses in BTT specimens are reduced during the test. An enhanced polymer chain mobility resulting from swelling by sorptive liquids leads to an even faster relaxation. Therefore, the blunting effect impedes crack initiation significantly when emerging microcracks are compressed immediately in the early stages of crack initiation. These differences concerning the influence of liquids on crack initiation and crack propagation were unveiled by BTT and FNCT.

The FNCT time to failure ranking of different PE-HD types recurred in BTT. Hence, a PE-HD type which exhibits a good resistance to crack growth in a distinct fluid tested in FNCT is also better performing in BTT. However, if the influence of different fluids on crack initiation and crack propagation in a certain PE-HD type is to be addressed separately, FNCT and BTT should be performed complementarily. Evidentially, there are especially different influences of sorptive liquids on crack initiation and crack propagation.

Coloration

Another apparent effect induced by sorptive, bulk-active liquids is the coloration of FNCT fracture surfaces revealed by LM of standard and pre-saturated AGUV specimens (Fig. 53). It has to be noted that a typical ductile fracture behavior is illustrated in figure 53 c, which results from an FNCT in air using completely saturated specimens. Such a result is unevaluable in terms of t_f* analysis but only used to show the coloration effect of sorptive, bulk-active fluids in this case.

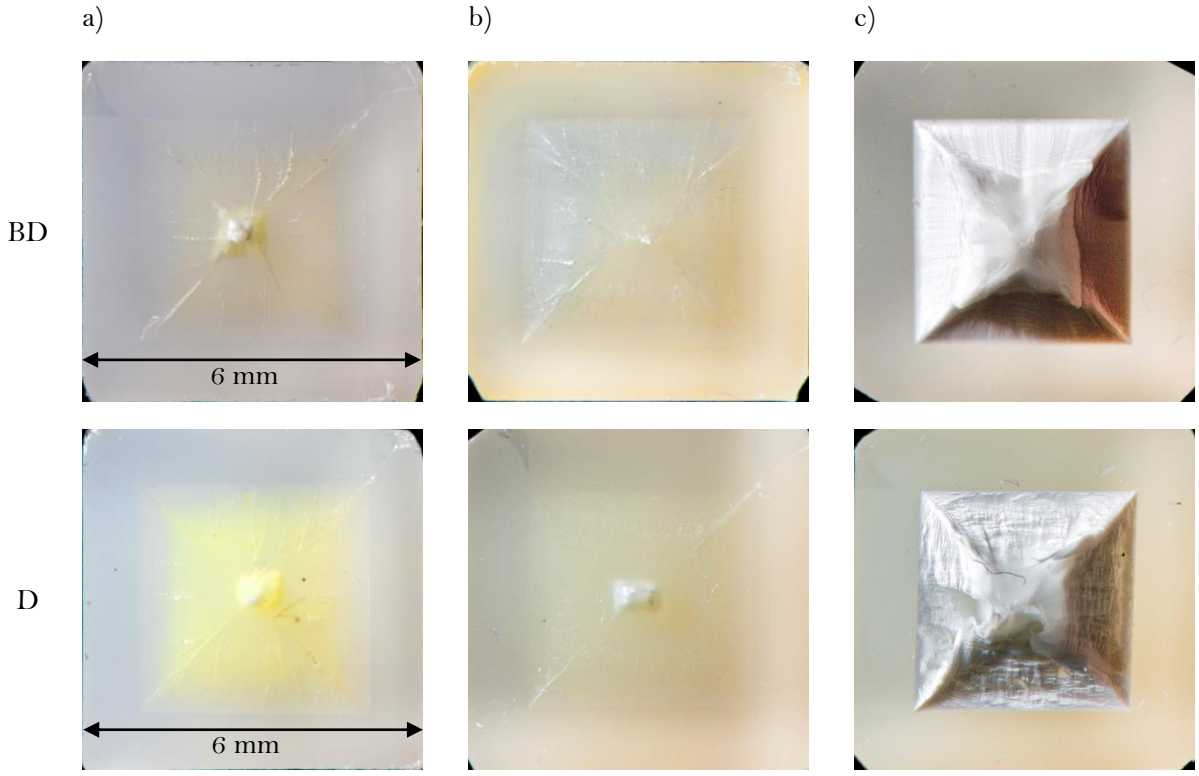

Figure 53: LM fracture surfaces of standard and pre-saturated AGUV FNCT specimens in biodiesel (BD) and diesel (D); a) standard FNCT, b) pre-saturated specimen, c) pre-saturated specimen tested in air.

As a result of a standard FNCT in a sorptive liquid, the fracture surface A_L (Fig. 25) excluding the notch area is colored similarly to the color of the liquid. This is a yellowish color for diesel and biodiesel (Fig. 53 a). If a pre-saturated specimen is tested within the liquid, the entire specimen will be colored due to a complete saturation and persistent liquid exposition (Fig. 53 b). In contrast, testing a pre-saturated specimen in air leads to a desorption and discoloration of the fracture surface A_L. Hence, the fracture surface (A_L) adopts its original color and the notch area exhibits a yellowish coloration (Fig. 53 c).

Since biodiesel and diesel are absorbed by PE-HD to a certain extent (section 4.3.4), a characteristic yellow coloration of partly and completely saturated FNCT specimens is consistent. Due to crazing, which comprises the formation of voids and fibrils, a higher amount of empty space is available in the craze zone to be filled with the sorptive liquid. Vice versa, the open structure in the craze zone also facilitates desorption in the absence of a surrounding sorptive liquid. Therefore, the absorption and diffusion of sorptive liquids (biodiesel, diesel) is facilitated and accelerated by crazing. It is concluded that the craze-crack mechanism in a sorptive liquid is a self-enhancing, crack growth accelerating process. This also results in lower t_f* values compared to non-sorptive, only surface-active fluids such as detergents (Fig. 48 a).

To objectify the color perception, (partly) saturated FNCT specimens as well as the liquids biodiesel and diesel were analyzed by UV/Vis spectrophotometry (section 3.1.4). For colored biodiesel and diesel specimens, a higher absorbance in the wavelength region between 350 nm and 500 nm compared to the other fluids is noticed. This wavelength region is attributed to the purple / blue region in the visible part of the electromagnetic spectrum. The complementary color yellow becomes dominant on the fracture surface since parts of the purple / blue spectral fractions are absorbed. In biodiesel, an even higher absorption is revealed for pre-saturated compared to non-saturated specimens. In diesel, the absorption in pre-saturated and non-saturated specimens is equal.

From the UV/Vis spectra of biodiesel and diesel (section 4.3.5), characteristic peaks are obtained in the same wavelength region as for FNCT specimens tested in biodiesel and diesel (about 350 nm to 500 nm). Distinct peaks are pronounced in biodiesel at wavelengths of approx. 405 nm, 428 nm, 454 nm and 482 nm. In the spectra obtained from biodiesel and diesel aged for 0.5 years and 1.5 years at a temperature of 50°C, no such peaks but characteristic absorption shoulders are obtained. In diesel, the absorption shoulders are shifted to higher wavelengths with increasing ageing time. This turns the liquid into a darker red color when it is aged. The disappearance of characteristic peaks in biodiesel after ageing indicates a chemical reaction, which is assigned to oxidative ageing [214, 215]. According to Munack et. al. [215], the peaks obtained from biodiesel spectra in the wavelength region between 400 nm and 480 nm are ascribed to the dye of carotenoids. Carotenoids are supposed to be contained in unrefined RME (section 4.2.3) and expected to be degraded during refining process. However, at least small fractions of carotenoids (in the magnitude of ppm) might have remained in the biodiesel. These are indicated by UV/Vis spectrophotometry. Due to the change in the spectra, the effect of oxidative ageing is assumed to be more prominent in biodiesel than in diesel. This is plausible since diesel does not contain carotenoids.

Non-aged diesel and biodiesel were used for specimen pre-saturation and FNCT in this study. An ageing time of 0.5 years was not reached during any tests. However, a slight oxidation effect might explain the differences in the absorbance spectra of pre-saturated and non-saturated biodiesel specimens. This effect cannot be recognized in diesel, since this is less sensitive to ageing oxidation than biodiesel.

5.1.3. Detailed consideration of fluid influences and fracture behavior

The reason for the t_f* reduction in FNCT caused by different fluids can be found in their ability to reduce the energy E_{is} that is required to create new internal surfaces. New internal surfaces are naturally created during crazing (section 2.3.2). Therefore, E_{is} is a determining factor for crazes to occur and for a crack to propagate during the craze-crack mechanism. As suggested by equation 19, E_{is} comprises two contributions: (1) the surface energy as the van der Waals cohesive energy between molecules and (2) the contribution of covalent load bearing bonds crossing the created (internal) surface. Contribution (2) becomes especially essential after the formation of crazes when fibrils fail and the resulting crack propagates through the material.

The first contribution is crucial for the formation of crazes and results from the energetic conditions at the surface of PE-HD. In the bulk material, each polymer chain is pulled equally in every direction by neighboring polymer chains of the same type, which results in a zero net force (van der Waals forces) that leads to coherence. The molecules at the surface do not have neighboring polymer chains in all directions to provide a balanced net force but they are exposed to environmental molecules. Therefore, they are prone to interact with different molecules such as surrounding fluids. At this point, an environmental fluid takes its effect. It leads to a reduction of interfacial energy of the fluid and the PE-HD. Thus, the energy required for the formation of crazes is also reduced (section 4.3.3) which facilitates the craze-crack mechanism. Accordingly, fluid-dependent FNCT t_f* correlate to the fluid surface tensions (Fig. 41 in section 4.3.3). To ensure a high precision, fluid-dependent surface tension values were double-determined by ring and by plate method. Besides room temperature, a temperature of 50°C was used to meet the FNCT conditions. Despite small differences in the absolute values, the qualitative ranking and fluid-dependent differences of surface tensions were reproduced in all tests. Water exhibits the highest surface tension. The surface tension of all other liquids is lower by a factor of at least 0.5. Arkopal shows a distinctly reduced surface tension compared to water, which explains the reduction of t_f* in FNCT. Since the sorption of the surface-active liquids water and Arkopal is very low (section 4.3.4), their reduction of the interfacial energy E_{is} is the dominating effect resulting in a faster crack propagation by craze-crack mechanism. Due to the significant differences in surface tensions between water and Arkopal, which lead to large differences in their reduction of E_{is}, the proposed mechanism change from SCG to ESC is substantiated (section 5.1.1).

Compared to surface-active liquids, t_f* are further reduced in the sorptive, bulk-active liquids biodiesel, NB and diesel, although their surface tension values are similar to that of the surface-active liquids. The fluid-dependent ranking of sorptive liquids is $t_{f,\,diesel}$* < $t_{f,\,NB}$* < $t_{f,\,biodiesel}$* (< $t_{f,\,NBL}$*) and it correlates to the sorption behavior (liquid uptake) of PE-HD types. Therefore, besides the surface tension, the plasticization of PE-HD by liquids plays a decisive role in t_f* reduction (section 5.1.2).

Liquids absorbed by PE-HD influence the interaction energy between polymer chains by swelling and plasticization effects. The higher the amount of absorbed liquid, the more severe is the ESC damage and the lower is t_f* (Fig. 42, 43 and 48). During sorption, the free volume in between polymer chains is filled with liquid. Due to the specimen swelling induced by the liquid, the free volume is additionally increased to a characteristic degree (saturation). As a consequence of swelling, (partly entangled) polymer chains are driven apart and bonding forces between the chains (e.g. van der Waals forces) are reduced. Instead of having strong bonding forces to neighboring polymer chains, a distinct chain interacts with liquid molecules. This is termed secondary interaction. In this way, a transition to crazing of polymer chains (formation of fibrils) is facilitated. Additionally, the enclosed liquid surrounding the polymer chains promotes their disentanglement due to lower interchain bonding forces. Therefore, the ESC induced crack propagation is further facilitated.

The fracture surface analysis unveils fluid-dependent differences in the appearance of FNCT fracture surfaces (Fig. 49). Air, water and Arkopal fracture surfaces exhibit typical central ligaments.

However, the surface roughness and maximum ligament heights of air and water differ compared to Arkopal. In addition to t_f^* reduction effects, the occurrence of different damage mechanisms (SCG/ESC) depending on the FNCT fluids is confirmed.

a) Air, σ_L = 9.0 MPa

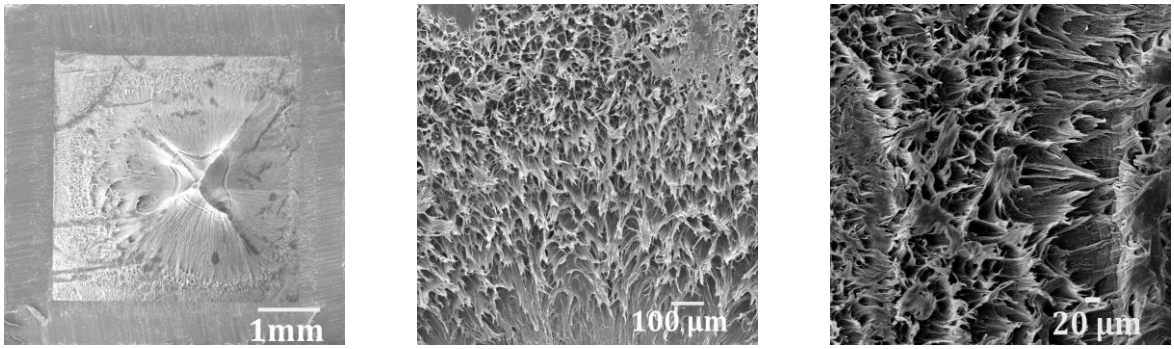

b) Water, σ_L = 8.9 MPa

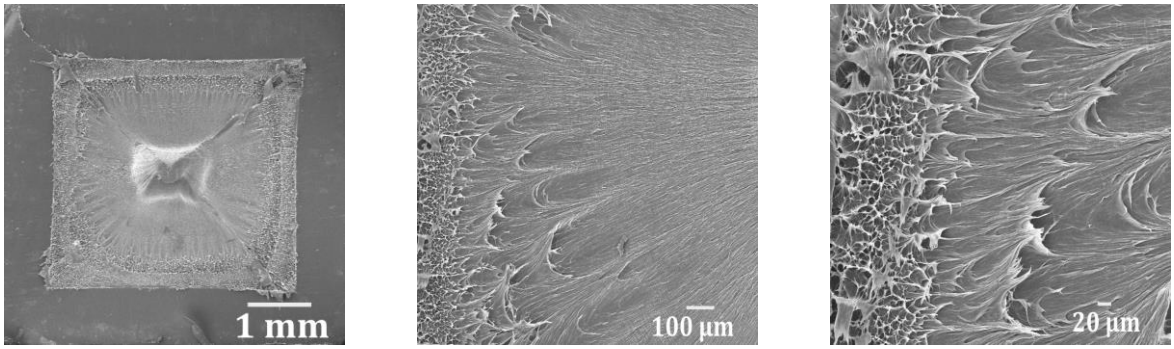

c) Arkopal, σ_L = 8.9 MPa

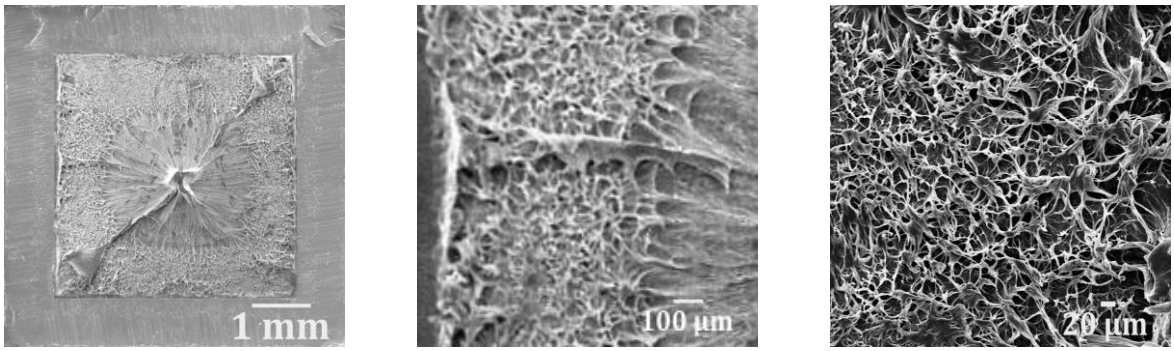

d) Biodiesel, σ_L = 8.9 MPa

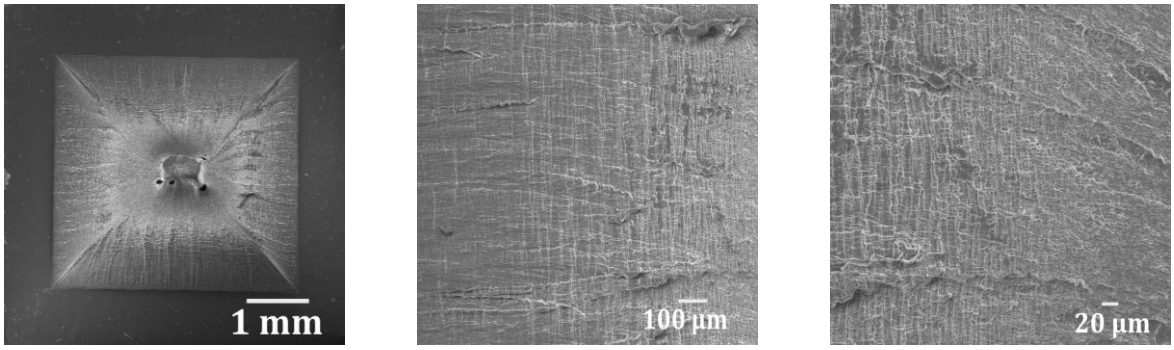

e) Diesel, σ_L = 9.1 MPa

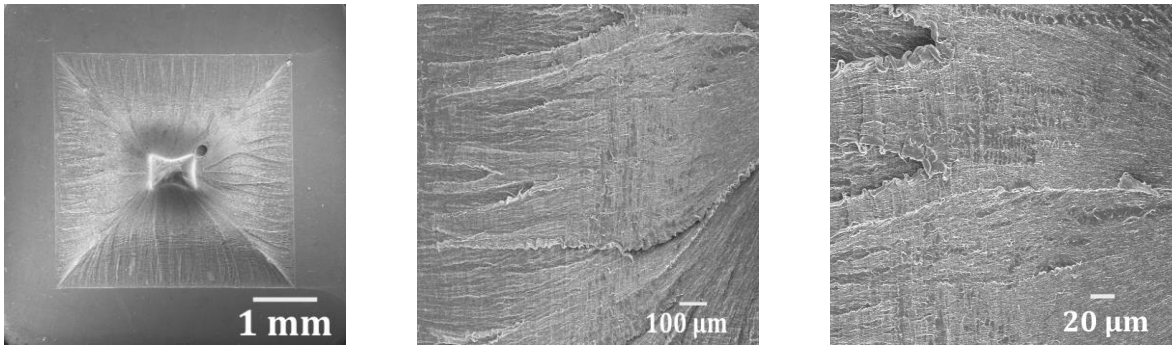

f) NB, σ_L = 9.1 MPa

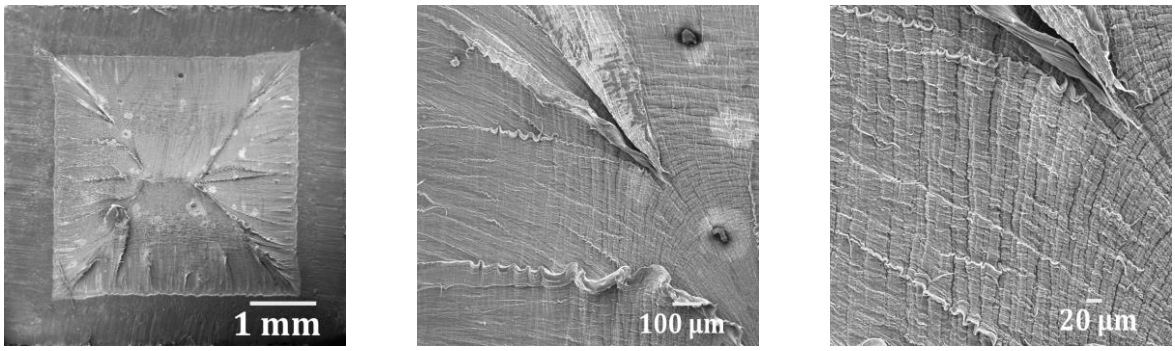

g) NBA, σ_L = 9.1 MPa

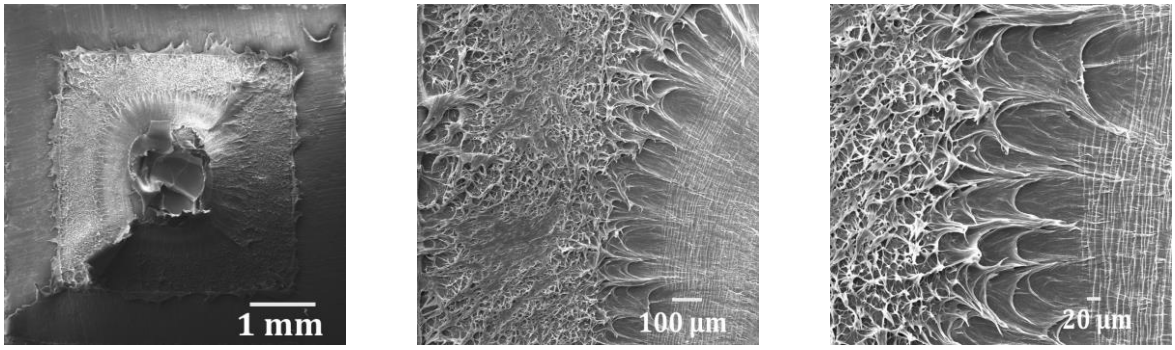

h) NBL, σ_L = 9.0 MPa

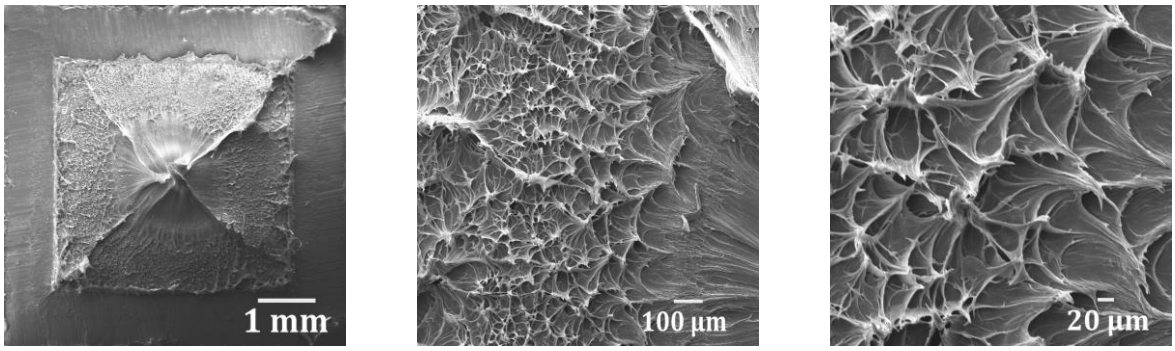

Figure 54: SEM fracture surfaces for fluid variation of AGUV FNCT specimens measured at 50°C.

Nevertheless, all these fracture surfaces exhibit a predominantly brittle fracture surface. In the sorptive, bulk-active fluids biodiesel, diesel and NB, a characteristic pillow-like structure is apparent on FNCT fracture surfaces. Due to moderate maximum heights of the central ligaments and a low surface roughness, such smooth fracture surfaces can also be considered as predominantly brittle. NBA and NBL fracture surfaces can be considered as brittle as well but they adopt an intermediate position concerning their appearance between surface-active (detergents) and sorptive, bulk-active fluids (NB).

To enable an assessment of fracture surfaces in terms of fluid-dependent damage mechanisms in more detail on a smaller length scale, SEM micrographs were obtained which are depicted in figure 54 (FNCT of AGUV at 50°C).

Different surface structures can be identified for brittle and ductile fracture behavior from SEM micrographs. Brittle parts of a fracture surface exhibit a lawn-like structure, such as in air, water and Arkopal (Fig. 54 a, b, c). Thus, a lawn-like surface structure is to be considered as typical for SCG/ESC induced brittle fracture. Such brittle fracture surfaces have to be differentiated from truly brittle surfaces resulting from rapid crack propagation (RCP) induced by a sudden impact of high stresses (shock stresses, section 2.3). Therefore, brittle SCG/ESC fracture surfaces can also be termed globally pseudo-brittle. However, they show a locally ductile behavior on the smaller microscopic scale of the SEM. Due to crazing and the increased true stress, a sort of tensile test is performed in every fibril during FNCT. Therefore, the formation of such locally ductile but globally brittle fracture surfaces seems plausible [7, 66, 216]. The lawn-like surface structure results from individually drawn fibrils, which fractured, relaxed and consigned such typical residues (Fig. 54 a to c). Due to the small size of fibril residues and their relaxation after failure, a macroscopically brittle fracture surface emerges. With increased local mechanical (true) stress during the FNCT, fracture is converted to ductile behavior and a central ligament is formed. Accordingly, fibril residues of the lawn-like structure are constantly growing in the transition region and merge into a sustained large fibril unit in the center of a fracture surface. A transition from macroscopically brittle to ductile behavior occurs (Fig. 54 b).

In biodiesel, diesel and NB (Fig. 54 d, e, f), no such typical lawn-like structure can be recognized. Macroscopically, a brittle fracture surface including a usual central ligament is noticed. However, the fracture surfaces microscopically exhibit platelet-like structures. Their individual components become smaller when the central ligament is approached. Due to the swelling and plasticizing effects of such fluids to PE-HD including the reduction of interchain bonding forces, fibrils are disentangling and relaxing differently compared to inert and surface-active fluids (air, water, detergent).

In inert and surface-active fluids, the remaining fibrils stand upright after failure and form the lawn-like features revealed by SEM (Fig. 54 a, b, c). In contrast, the swollen and plasticized material (pillow-like structure) leads to a premature failure of craze-fibrils (t_f* reduction, Fig. 48), which individually do not elongate to the same extent. Furthermore, the plasticized state results in a collapse of the remaining fibril fragments giving rise to the microscopically flat surface structures in figures 54 d, e, f. Hence, single fibril fragments are hardly noticeable on these fracture surfaces. Instead, fibril fragments cling together interconnected by secondary interactions with the sorptive fluid. The results of UV/Vis spectrophotometry confirm the presence of sorptive fluids on the FNCT fracture surfaces (section 4.3.5), which are partly saturated.

In sorptive bulk-active fluids, the occurrence of a craze-crack mechanism can be assumed since no complete characteristic ductile failure is noticeable on the fracture surfaces – only the central ligament represents the transition from brittle to ductile behavior as expected for all SCG/ESC fracture surfaces. Accordingly, FNCT is capable of providing information on SCG/ESC in bulk-active fluids.

Such a crack growth induced fracture behavior is confirmed in classic tensile tests applying notched specimens. On a sample basis, tensile tests were performed according to ISO 527-2 [123] at typical environmental conditions (23°C, 50% humidity, air) using biodiesel and diesel saturated FNCT specimens. Test speeds used were 1 mm/min in the region of tensile modulus up to a mechanical strain of $\varepsilon = 0.25\%$ and 50 mm/min thereafter [123, 170]. Macroscopically brittle fracture surfaces were obtained that typically indicate crack propagation (Fig. A1.85 in appendix A1). Hence, any mechanical loading leads to crack propagation in PE-HD independent of the sorption condition, provided that crack initiation is assured (e.g. in notched FNCT specimens). Resulting fracture surfaces macroscopically exhibit predominantly brittle character.

In NBA and NBL, a mixture of lawn-like and platelet-like structures can be perceived (Fig. 54 g, h). Macroscopically brittle fracture surface features with central ligaments are identified. Microscopically, the lawn-like, fibrillated structure starts from the notch area and is directed towards the central ligament. The platelet-like structure becomes dominant when the center of the fracture surface is approached. Hence, the impact of the surface-active detergent comes into effect first. After a certain exposure time, the bulk-active component becomes dominant. This was also already indicated by the different sizes of the crack growth areas on LSM fracture surfaces obtained from sorption-dependent FNCT (Fig. 51).

The fluid-dependent fracture surfaces are similar for all PE-HD types (Fig. B3.93, B3.94 and B3.95 in appendix B3). Especially, the fluid-dependent occurrence of lawn-like and platelet-like structures is equal in each case.

In terms of the assessment of the applicability of PE-HD types in a certain environment, the performance of an FNCT applying the respective fluid is reasonable and recommended based on the results in this study. However, NB can be considered as a reference (standard) liquid for sorptive, bulk-active fluids since it induces typical SCG/ESC effects (FNCT t_f* and fracture surfaces) similar to diesel and biodiesel. It has to be noted that genuine NB and mixtures with detergent solutions such as NBL are already established in practical tests of PE-HD packaging materials (section 4.2.1). However, it was not yet considered as test fluid in FNCT.

FNCT elongation

FNCT elongation data can be used to qualitatively estimate the crack propagation behavior in PE-HD induced by different fluids in terms of t_f* and fracture surface appearance. The results of the elongation measurements during FNCT in all fluids applied in this study are illustrated in figure 55.

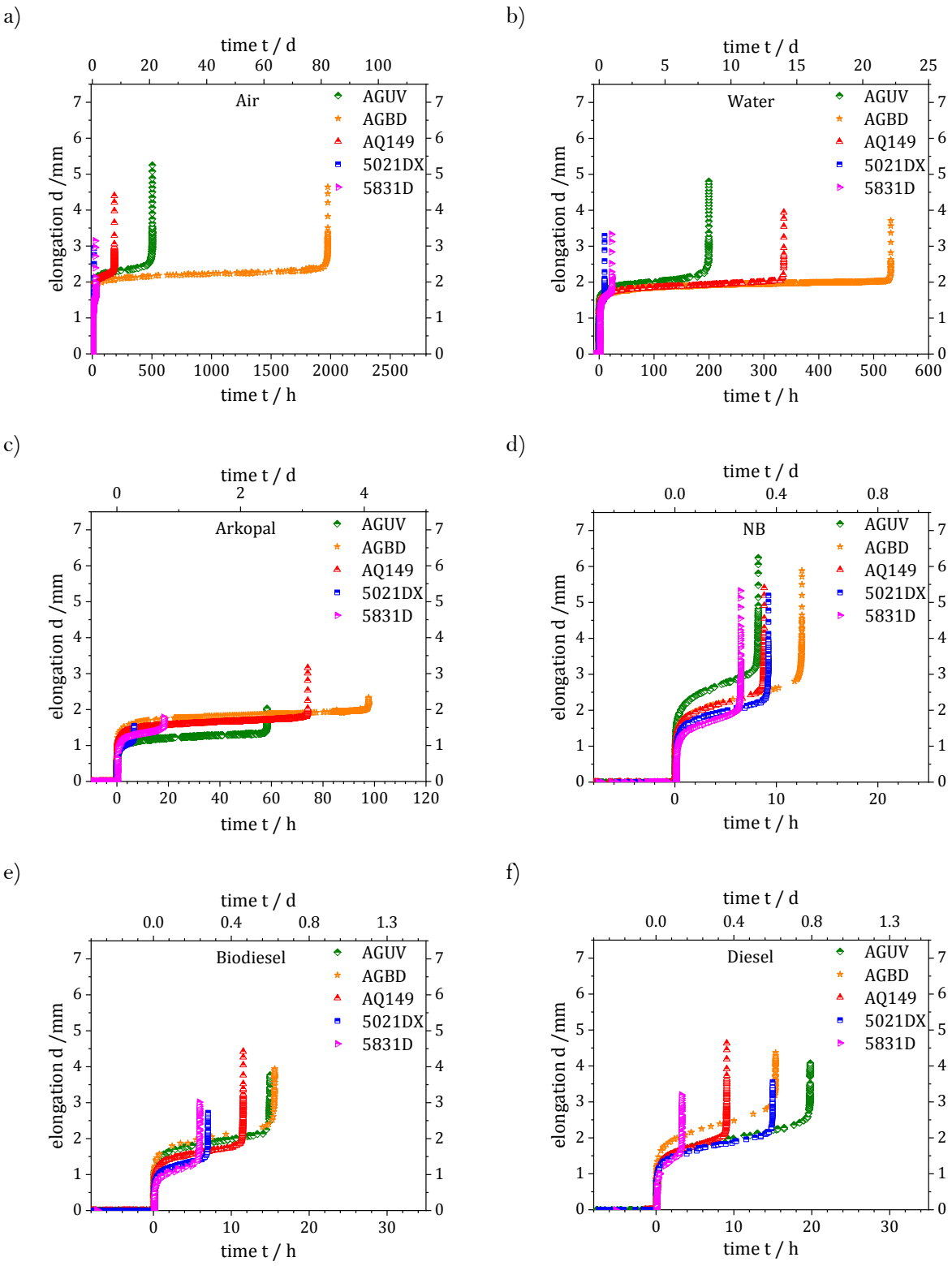

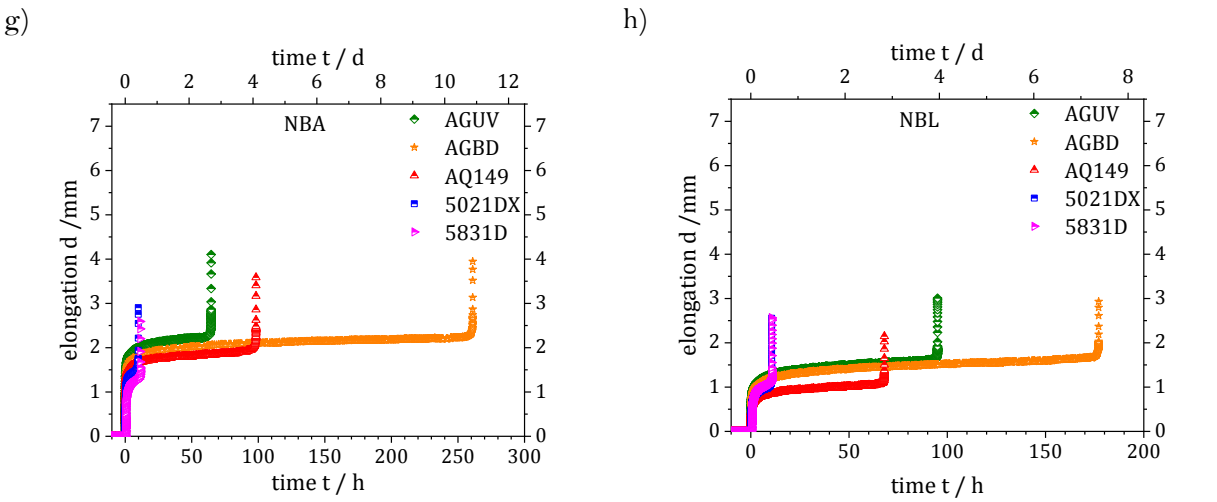

Figure 55: FNCT elongation data with $\sigma_L \approx \sigma_n = 9$ MPa and 50°C for each combination of PE-HD type and fluid.

The elongation data were obtained from FNCT performed at 50°C with an actual initial stress σ_L of approx. 9 MPa. They unveil that the maximum elongation d_{fail} (Fig. 26 c) differs in dependence on the test fluid (Fig. 55). The maximum elongations d_{fail} in air and water are similar and adopt values of approx. 3.5 mm to 5.0 mm (Fig. 55 a, b). In the detergent Arkopal, lower d_{fail} values of about 2.0 mm to 3.0 mm are obtained (Fig. 55 c), which are similar to d_{fail} reached in NBA and NBL (Fig. 55 g, h). d_{fail} obtained in biodiesel, diesel and NB (Fig. 55 e, f, d) exhibit higher values of approx. 5.0 mm up to 6.0 mm. Although no clear quantitative distinction between different fluids by d_{fail} can be established, qualitative trends are obvious. All elongation curves in figure 55 follow the general course and the three distinct regions of (I) the initial craze formation, (II) the constant crack growth and (III) the final failure depicted exemplary in figure 26 b, c can be identified.

Moreover, a distribution of d_{fail} values depending on the sorption becomes apparent: In the non-sorptive fluids air, water, detergent, NBA and NBL, the PE-HD types AGUV, AGBD as well as AQ149 show the highest and 5021DX as well as 5831D lower d_{fail} values. Since 5021DX and 5831D are assumed to have less tie molecules (section 4.3.1), there is a lower number of load bearing polymer chains during the craze-crack mechanism which is reflected by a lower maximum elongation and faster crack growth. In sorptive liquids biodiesel, diesel and NB (Fig. 42, 43), d_{fail} are similar for all PE-HD types. Similar to t_f*, sorptive liquids lead to an equalization in terms of d_{fail}. However, d_{fail} and t_f* are not directly correlated: A low t_f* does not inherently imply a high d_{fail}.

The FNCT elongation obtained in different fluids provides data for the qualitative assessment of fluid-dependent effects due to their correlation to t_f* and fracture surface appearance. Therefore, these data describe the crack growth and fracture during FNCT. As confirmed by typical elongation curves (Fig. 26 b, c, Fig. 55) and fracture surfaces (Fig. 49 a to c), a brittle to ductile transition is naturally passed during FNCT. Although the applied force is kept constant, the true stress taking effect locally at the crack tip is continuously increasing in the course of the test (sections 2.3.4 and 2.5.4). This results from the reduction of the cross-section due to crack growth (section 5.1.1). Despite initially selecting a stress low enough to ensure brittle behavior, the decreasing cross-sectional area always leads to ductile fracture behavior in the final stages of an FNCT (section 2.3.4). These final stages correspond to the formation of a central ligament (Fig. 47, section 5.1.1 and Fig. 55). Consequently, a balance of brittle and ductile/viscous behavior characterizes every FNCT and the corresponding fracture surface. Failure dominated by brittle behavior is referred to as 'brittle' fracture despite the presence of ductile portions, and vice versa. A correlation of the final ductile stages to region III in a typical FNCT elongation curve (Fig. 26 b, c) is evident.

5.1.4. Scheme of fluid-influenced stress crack damage mechanisms to PE-HD

Based on the results of the fluid-dependent assessment of stress cracking in this study (sections 5.1.1 to 5.1.3), a novel overview scheme of PE-HD damage mechanisms induced by mechanical stress and environmental fluids is proposed in figure 56.

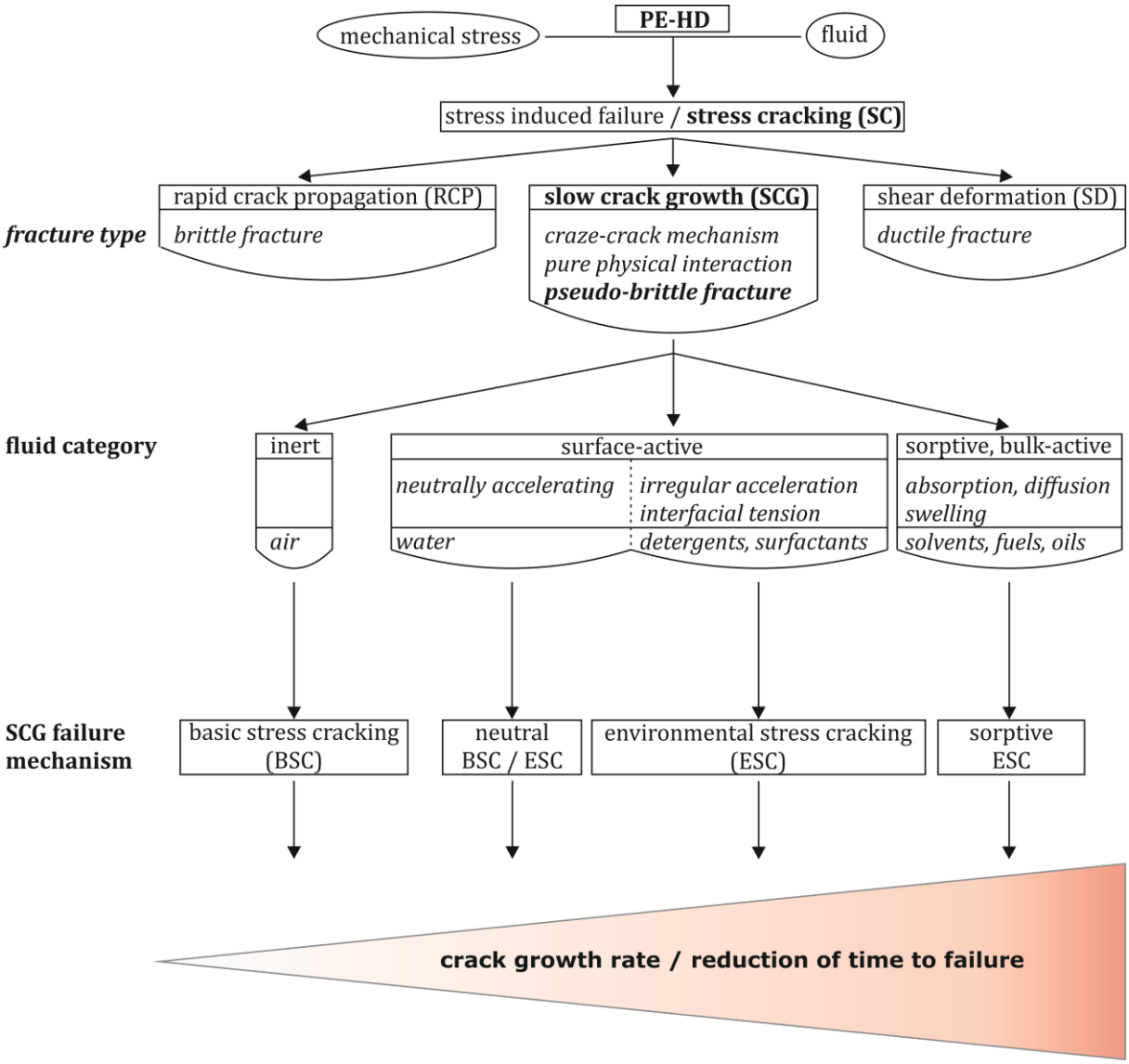

Figure 56: Schematic depiction of damage mechanisms to PE-HD induced by mechanical stresses and environmental fluids (inspired by [1]).

In this scheme (Fig. 56), a categorization of fluids according to their influence on crack propagation behavior in PE-HD is given. Therefore, the fluid categories inert, surface-active and sorptive, bulk-active are introduced (cf. Tab. 11). Moreover, the new term 'basic stress cracking' (BSC) is proposed to describe SCG in inert (air) and surface-active, neutrally accelerating fluids (water) to differentiate the distinct damage mechanism from the generic term of 'slow crack growth'. This term replacement is expedient since 'slow crack growth (SCG)' then only refers to the fundamental mechanism, especially in distinction to rapid crack propagation (RCP) phenomena that occur to PE-HD at high mechanical stresses (section 2.3). Low mechanical stresses (below yield strength) lead to pseudo-brittle failure induced by the long-term craze-crack mechanisms basic stress cracking (BSC),

environmental stress cracking (ESC), neutral BSC/ESC and sorptive ESC which are differentiated according to the fluid in effect and which are subordinated to SCG.

Although different fracture surfaces are obtained from tests in bulk-active fluids compared to purely surface-active fluids, the former fracture surfaces also indicate the occurrence of crack growth phenomena (sections 5.1.1 and 5.1.2): Pillow-like fracture surface features result from swelling effects, but no characteristic ductile failure induced by shear deformation occurs. This is an indicator for crack propagation. Therefore, damage effects of PE-HD in bulk-active fluids are also ascribed to an ESC mechanism. Since bulk-active fluids however result in a t_f* reduction compared to surface-active fluids (detergents), the underlying damage mechanism is suggested to be termed 'sorptive ESC'. The effects of bulk-active fluids that inherently contribute to such an accelerated crack growth are a reduction of surface energy (intermolecular / chain bonds), swelling and plasticization. These effects lead to the facilitated creation of new internal surfaces, the occurrence of secondary interactions of polymer chains with the molecules of the liquid (reduction of interchain Van der Waals forces) and enhanced disentanglements, especially of tie molecules (cf. section 5.1.3).

It has to be noted that the categorization of fluids and the respective classification of SCG failure mechanisms in the scheme (Fig. 56) is based on the evaluation of the 8 fluids and 5 PE-HD types tested in this study. The transition between fluid categories and the respective SCG failure mechanism classification might be smoother when a broader range of fluids is considered. The decision to assign a certain fluid to a distinct category and failure mechanism is determined by the surface activity (surface tension) and the sorptive character of the fluid with respect to PE-HD. Accordingly, a fluid can fit in two neighboring categories.

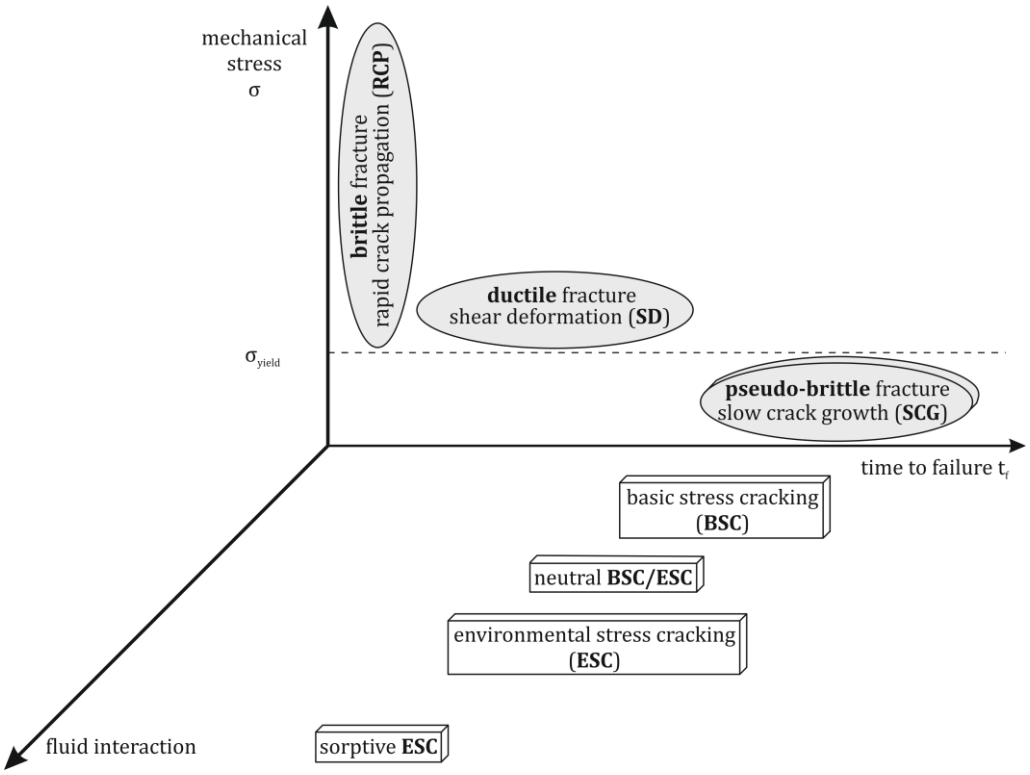

Figure 57: Three-dimensional matrix of failure mechanisms induced by mechanical stress in dependence on fluid interaction and the resulting time to failure with respective fracture types.

Furthermore, stress induced failure phenomena occurring to PE-HD can be categorized according to the mechanical stress in dependence on the interaction (surface energy, sorption) with the environmental fluid and the resulting time to failure t_f (3D matrix in Fig. 57). From this matrix, the

failure mechanism and the nature of fracture that are most likely to appear to PE-HD under the consideration of the mechanical stress applied, the environmental fluid in effect and the time to failure can be read at a glance:

Very high mechanical shock stresses (order of magnitude: ≈ 200 MPa, estimation from Charpy impact test values at temperatures of ≈ 40°C to 50°C in [217]) affecting PE-HD in very small time periods (order of magnitude: 10 ms) result in rapid crack propagation and in brittle failure (sections 2.3 and 2.3.4). Moderate mechanical stresses (> yield strength) and short-term loading lead to ductile fracture behavior induced by shear deformation (SD) in PE-HD (sections 2.3.3 and 2.3.4). Such phenomena were not explicitly considered in detail in this study. Low mechanical stresses (< yield strength) occurring over a long period of time result in slow crack growth (SCG) and in the appearance of typical pseudo-brittle fracture of PE-HD. This SCG mechanism can be subdivided into BSC and neutral BSC/ESC occurring at no and low interactions of the PE-HD with a fluid as well as ESC (significant reduction of surface energy) and sorptive ESC (additional bulk-effects) at severe interactions with a surrounding fluid.

5.2. Influence of physical and structural PE-HD properties on slow crack growth

Differences in the t_f* ranking of PE-HD types are obtained from FNCT in different test fluids. In this respect, two groups of PE-HD types are formed: (1) AGUV, AGBD and AQ149 and (2) 5021DX and 5831D. The first group of PE-HD types exhibits the highest t_f*. The FNCT t_f* of PE-HD types depend on the types of comonomers (1-butene, 1-hexene), their fraction and their distribution within the polymer chains (section 2.1.2). Therefore, the polymerization process (gas phase, loop or cascade reactor) and the applied catalysts (chromium-based, Ziegler-based) have significant influence on solid state polymer properties such as the crystallinity and crystalline morphology (sections 2.1.1 and 2.1.2). These properties determine the SCG behavior of PE-HD. Accordingly, differences in the FNCT t_f* of different PE-HD types are due to the types of comonomers and the polymerization processes.

For 5831D, t_f* barely depends on the surface activity (reduction of surface energy) of the test fluid. Significant t_f* differences are only obtained in sorptive, bulk-active liquids compared to solely surface-active or inert fluids (Fig. 46 and 48). This PE-HD type was the only one produced by an advanced cascade process and using 1-butene comonomers (section 4.1, Tab. 3). Therefrom, 5831D was obtained as a multimodal PE-HD with a high crystallinity and a density (section 4.3.2) of 0.958 g/cm³, which is higher than the density values of 5021DX (0.950 g/cm³), AGUV, AGBD and AQ149 (0.945 g/cm³ each). Since AGUV, AGBD, AQ149 and 5021DX were obtained using 1-hexene comonomers, a higher crystallinity and a higher density of 5831D (1-butene comonomers) seems plausible (cf. section 4.3.1). Concurrently, the amount of tie molecules might be low in 5831D due to a rather low molecular mass M_w. This might be assumed to lead to a faster crack growth induced by any fluid regardless of its surface activity as long as the surface tension of the PE-HD is reduced compared to air (which is the case for all fluids tested). Sorptive fluids are able to induce a further acceleration of crack growth in 5831D due to swelling effects (section 5.1.2). The results of the fluid-dependent sorption behavior of PE-HD types (section 4.3.4) reveal that AQ149 and 5831D show the highest mass uptakes of Arkopal solution (2 wt% aq.) and water. This is according to expectation since the overall mass uptake of water is known to be very low in PE-HD. However, even a small uptake of a fluid reducing the interfacial tension (section 4.3.3) is significant for the interaction between fibrils and fluids at the crack tip. A minimal increased swelling and plasticization effect in AQ149 and 5831D may be the reason for their reduced resistance to SCG. Since a stronger surface energy reduction is taking effect (section 5.1.3), FNCT t_f* are further decreased for AQ149 and 5831D in Arkopal compared to the other PE-HD types. Hence, the structural differences in 5831D and AQ149, such as the crystallinity, the crystalline morphology and a lower M_w that might indicate

a high amount of short chains and a lower number of tie molecules, accompanied by a slightly higher absorption of Arkopal and water cause the FNCT t_f* differences in the PE-HD type ranking.

In figure 58, the FNCT t_f* are correlated to the density ρ (Fig. 58 a), weight average molecular mass M_w (Fig. 58 b), crystallinity $X_{c,\,DSC}$ (Fig. 58 c) and α relaxation temperature T_α (Fig. 58 d) of the PE-HD types obtained from characterization (section 4.3).

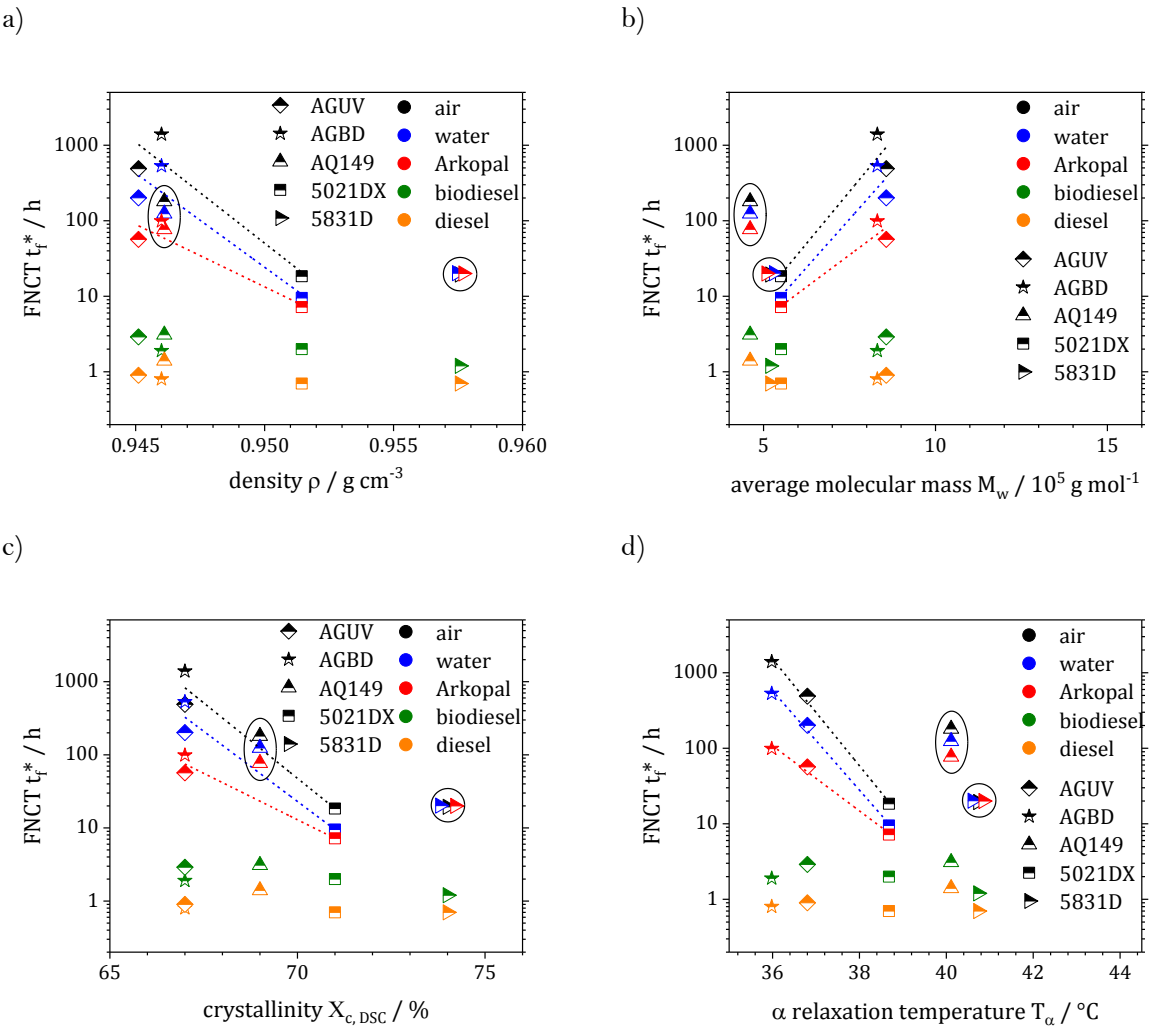

Figure 58: Correlations of a) density ρ, b) weight average molar mass M_w, c) crystallinity $X_{c,\,DSC}$ and d) α relaxation temperature T_α to FNCT t_f*; †x-axis values were spread over a short range to enhance the legibility of different markers.

The FNCT t_f* correlate in a similar way to the selected structural properties (Fig. 58). It has to be noted that multimodal distributions, short and long chain branching as well as fractions of comonomers are not considered within M_w (Fig. 58 b). For the recognition of these properties, more specific information on the formulation of the PE-HD types and the performance of multidimensional chronographic methods were required.

AGUV, AGBD and 5021DX show a similar tendency in all plots (Fig. 58 a to d) for FNCT t_f* in air, water and Arkopal with significantly reduced t_f* in the Arkopal solution. AQ149 has a similar relation of t_f* to crystallinity and density as AGUV, AGBD and 5021DX. However, linear trends are impossible to obtain due to the limited structural variation of the different PE-HD types. Since the crystallinity and the density of a PE-HD type are closely related to each other (sections 2.1.1 and 4.3.1), the similarity of their correlations to the FNCT t_f* is reasonable. 5831D shows a significant

difference to the other PE-HD types for all structural parameters. In the plots of molecular mass M_w and α relaxation temperature vs. FNCT t_f* (Fig. 58 d), the multimodal ACP PE-HD type 5831D with butene comonomers and AQ149 produced by a loop process with hexene comonomers also deviate from the gas phase polymerized types. Overall, according to the results obtained for air, water and detergent (Fig. 58), a lower density, crystallinity and α relaxation temperature but a higher molecular mass lead to higher t_f* in FNCT. This trend recurs but it is less prominent in sorptive bulk-active fluids. Due to similar swelling and plasticization induced by sorptive fluids to the different PE-HD types, they are effected similarly in terms of FNCT t_f*. Slight t_f* differences obtained from FNCT applying sorptive fluids only result from differences in the sorption behavior (liquid mass uptake) of the PE-HD types (section 5.1.3), which are assumed to be a consequence of the (small) differences in crystallinity. No correlation or distinct trend is found for t_f* with the ratio of amorphous and crystalline fractions in the PE-HD types (L_a/L_c and L_a/L_p, Tab. 9). The molecular mobility (mobility of polymer chains) within the amorphous phase as well as the ratio of amorphous and crystalline parts within a semi-crystalline polymer such as PE-HD are usually considered to influence crack propagation strongly (section 2.1.2) [28, 29, 30, 42]. Since no distinct trend of the amorphous and crystalline fractions with t_f* was found, a strong influence of the rigid amorphous phase and the number of tie-molecules is assumed. Hence, the rigid amorphous phase and the mobility of polymer chains therein strongly influence crack propagation.

The FNCT t_f* of AGUV, AGBD and 5021DX (all comprise hexene comonomers) show linear trends indicating a dependency on the selected structural properties. The t_f* of AQ149 (loop process, hexene comonomers) and 5831D (advanced cascade process, butene comonomers) exhibit no such trends. The superstructure of mono-, bi- or multimodal PE-HD types strongly depends on the polymerization process (gas phase, loop process, cascade process), the applied comonomers (butene, hexene) and their distribution (tie-molecules). Therefore, the identified trends are ascribed to the polymer production processes, which result in the occurrence of different fractions of rigid amorphous phases and superstructures.

5.3. Enhanced crack propagation analysis

To assess the processes underlying the crack propagation in SCG mechanisms in detail, specimens partially damaged in FNCT (Tab. 2) were analyzed by LM, LSM, SAM and CT. As part thereof, areas damaged by the craze-crack mechanism and corresponding time-resolved average crack lengths were determined (section 3.3, Fig. 28). Results of crack lengths and crack growth rates are illustrated in figure 64 (section 5.3.1) for AGUV tested in Arkopal, biodiesel and diesel at 50°C. Based on these results, a correlation of craze and crack length during the craze-crack mechanism (section 5.3.2) and their correlation with the FNCT elongation as well as the yield strength of PE-HD (section 5.3.3) was found.

5.3.1. Crack lengths and crack growth rates

A selection of AGUV light microscopy (LM) and laser scanning microscopy (LSM) fracture surface images is shown in figure 59. The images were obtained from specimens partly damaged by FNCT experiments in Arkopal. They are designated by the respective percentages of the total time to failure t_f*. To uncover the fracture surfaces and to enable an analysis by LM and LSM, specimens were broken manually at liquid nitrogen temperature ('cryo-fracture', section 3.3). The direction of the hammer impact is indicated by red arrows. Actual initial stresses σ_L applied are given (Fig. 59), which were obtained on the basis of LM A_L measurements after failure (Eq. 54 in section 3.2.2).

a) 0% t_f*, 0.0 h, σ_L = 0.0 MPa

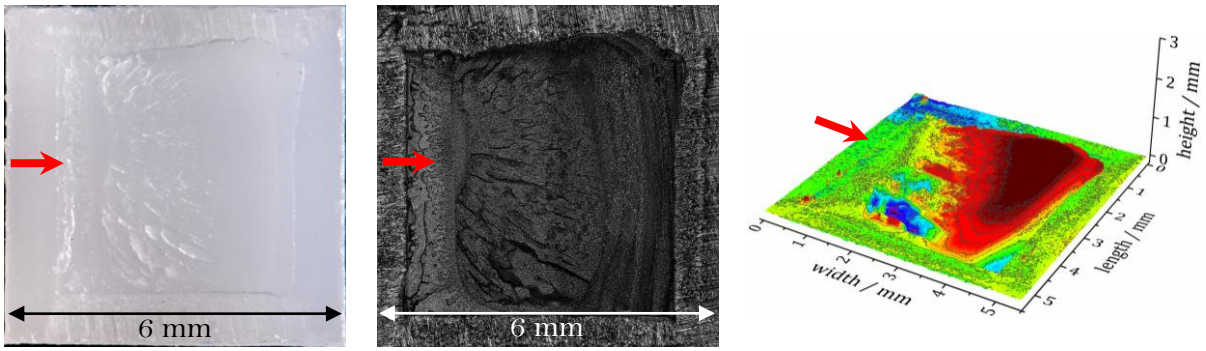

b) 33% t_f*, 18.7 h, σ_L = 8.5 MPa

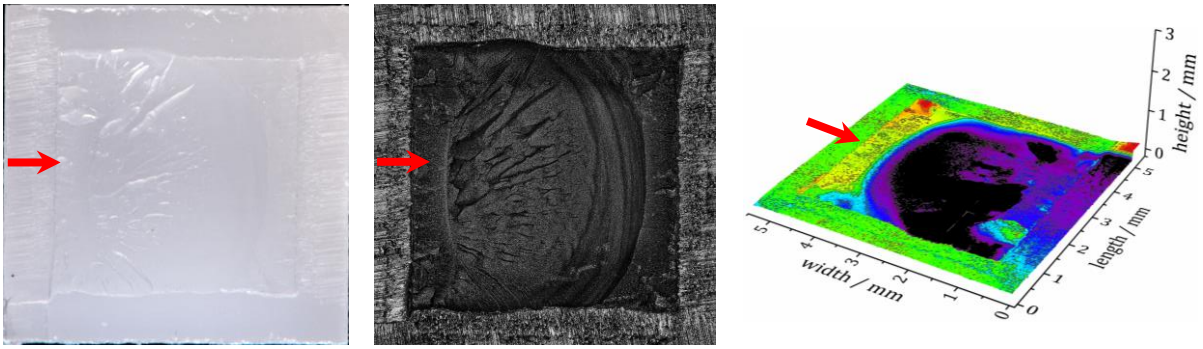

c) 66% t_f*, 37.4 h, σ_L = 8.7 MPa

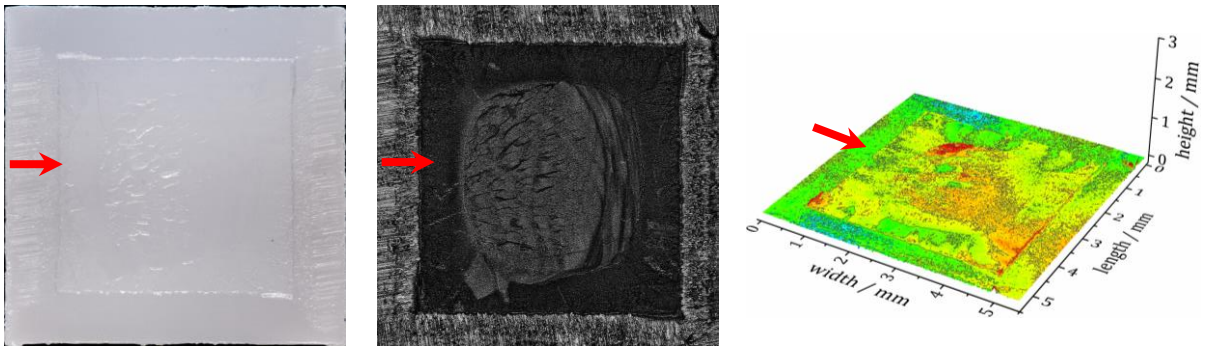

d) 97% t_f*, 55.0 h, σ_L = 8.7 MPa

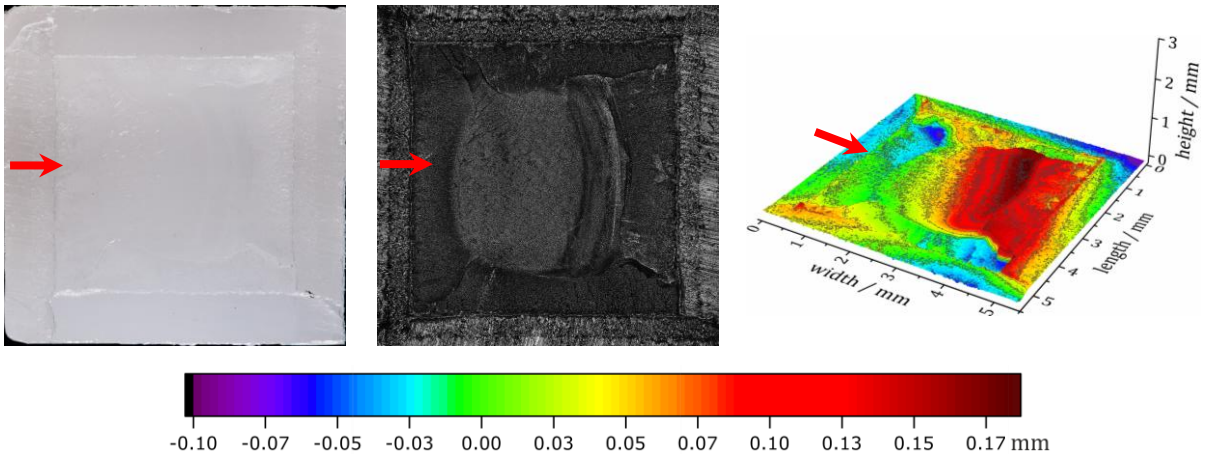

Figure 59: LM and LSM fracture surfaces of AGUV specimens partially damaged by FNCT in Arkopal; direction of hammer impact during cryo-fracture: ➔.

The LM and LSM micrographs of partially damaged specimens (Fig. 59) show typical brittle fracture surface profiles for areas damaged by craze-crack mechanism and by hammer impact (shock stress), respectively. The latter are reminiscent of typical truly brittle fracture surfaces obtained by Charpy impact tests (sections 2.3.4, [53, 67]). This is plausible since the manually exerted hammer impact is of similar nature as used in Charpy tests.

The differentiation of damaged and undamaged fracture surface areas with respect to the craze-crack mechanism is facilitated using LSM laser pictures. In LM micrographs, contrast is usually too low and there is no distinct sharp borderline on the fracture surface to divide damaged and undamaged areas. LSM height data show typical fracture surfaces. They give an impression of the shape of cryo-fractured surface areas, but they do not improve the distinction of damaged and undamaged parts with respect to the craze-crack mechanism.

The best possibility to differentiate these areas is given in LSM laser images. This results from the occurrence of different surface structures on a smaller length scale, that evolve according to the different fracture mechanisms (craze-crack and sudden impact). These surface structures lead to differences in the reflective properties which are best identified in the LSM laser greyscale images. The surface structures can be recognized in SEM micrographs as exemplified for the 97% t_f* AGUV specimen in Arkopal (Fig. 59 d) in figure 60 (also in Fig. 54).

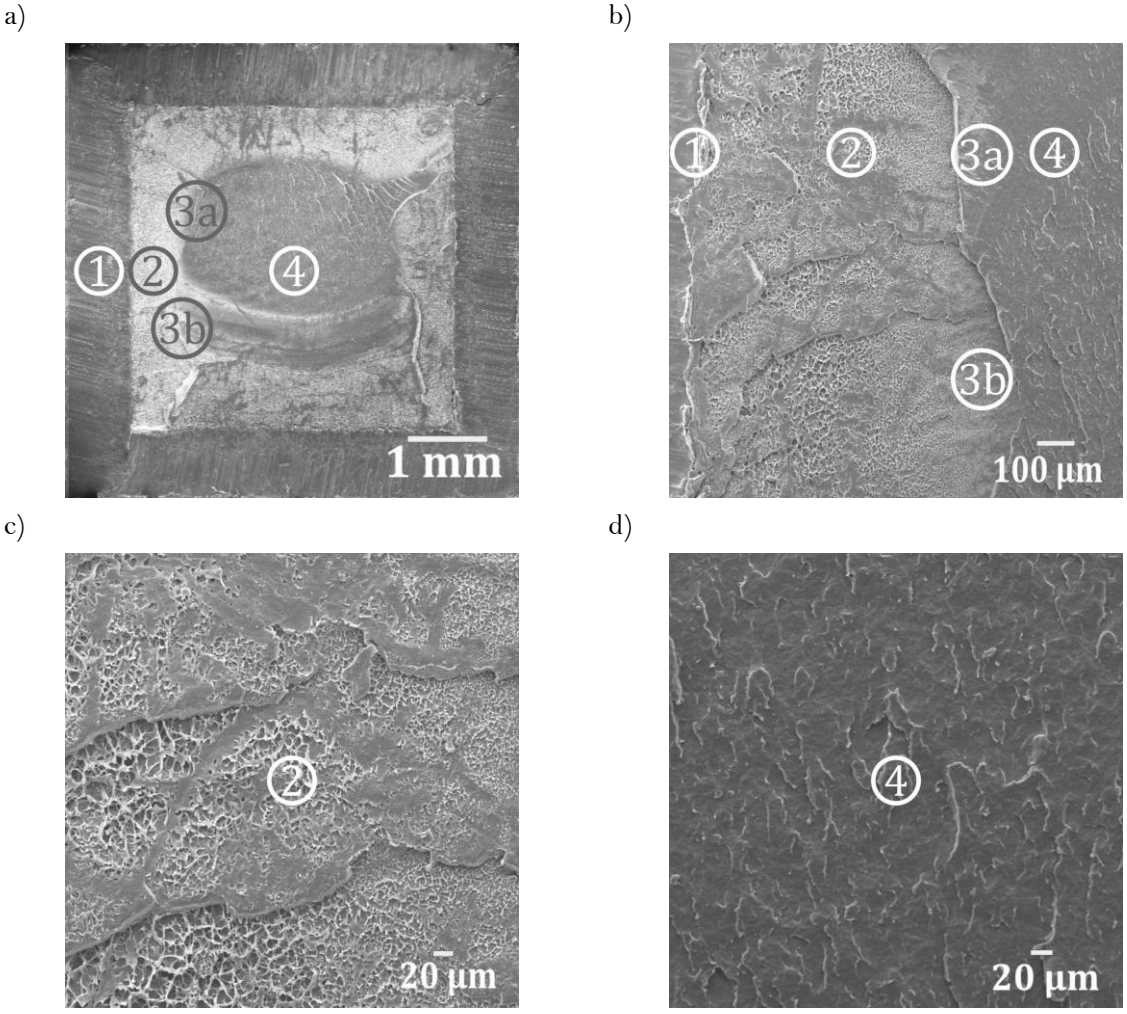

Figure 60: SEM images of partially damaged specimen, 97% t_f* of AGUV in Arkopal; a) overview, b) transition zone (3a, 3b) from notch (1) via ESC crack growth (2) to cryo-fractured area (4), c) surface structure induced by craze-crack mechanism, d) surface structure resulting from cryo-fracture.

The area of the notch, the area of the crack growth induced by the craze-crack mechanism and the cryo-fractured area show very different characteristics (Fig. 60 a, b). The notch area exhibits a flat surface traversed by striations resulting from the notching process using a razor blade (area 1 in Fig. 60 a, b). The crack growth area shows a globally (pseudo) brittle surface (area 2 in Fig. 60 c, Fig. 54). In contrast, the cryo-fractured area reveals a locally truly brittle and flat structure (area 4 in Fig. 60 d). A transition zone is revealed in between crack growth and cryo-fractured areas, which exhibits characteristics of both. Thus, this might be ascribed to either crack growth or cryo-fracture (3a and 3b in Fig. 60 a, b).

Using the non-destructive scanning acoustic microscopy (SAM), micrographs of partially damaged AGUV FNCT specimens in Arkopal were obtained 'quasi in-situ' from the plane of crack propagation (notch level, Fig. 61). For SAM analysis, areas damaged by the craze-crack mechanism were determined equally to LM and LSM analysis (sections 3.3 and 3.3.3, Eq. 59).

Figure 61 shows SAM depictions of (a) an undamaged specimen and (b - d) partially damaged specimens after 33 %, 66 % and 97 % of t_f* for AGUV in Arkopal. For (a), the colored area corresponds to the notched regions and the inner hollow area represents the undamaged part of the specimen. No crack can be seen. For (b - d), the predominantly black area corresponds to the notched region (larger opening distance), the colored area corresponds to crack propagation, and the hollow (white/transparent) area in the center represents the undamaged part.

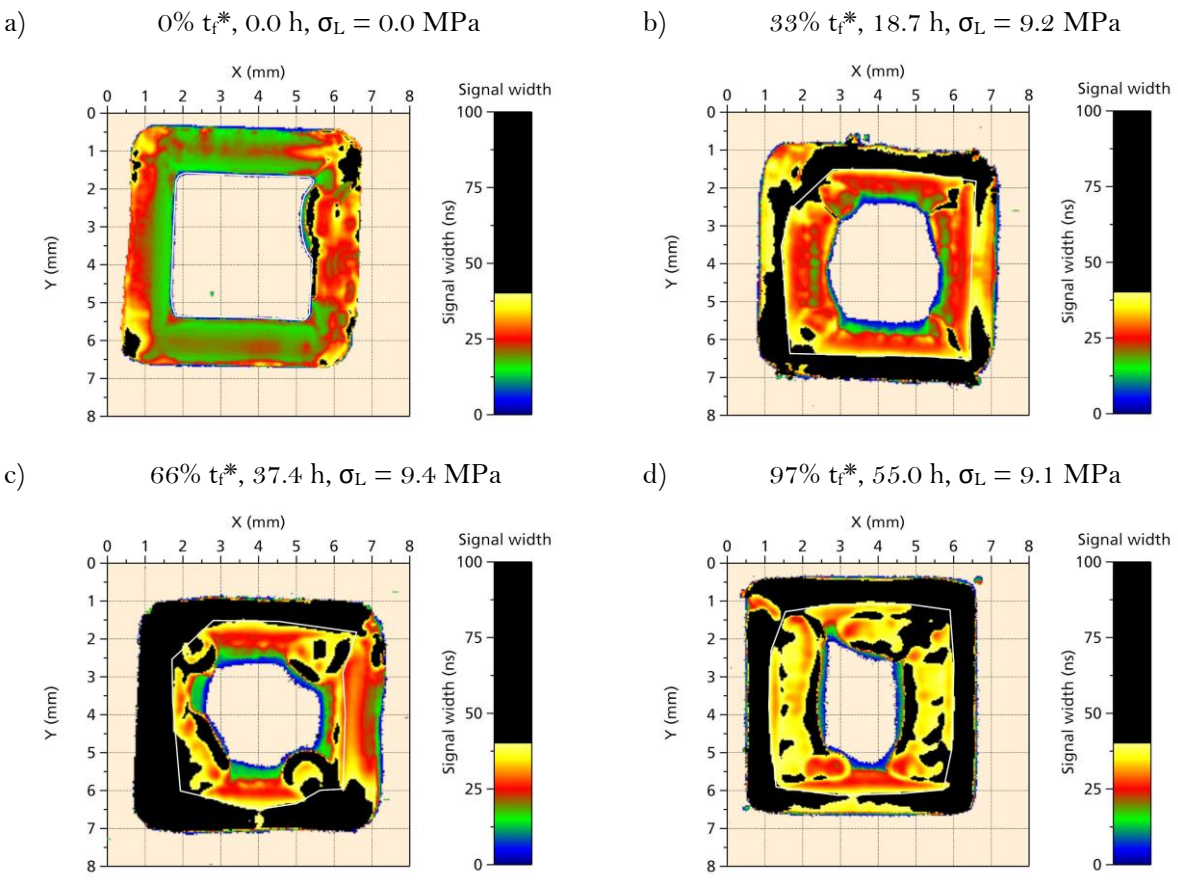

Figure 61: Areas of notch and crack propagation based on SAM data obtained for undamaged (a) and partially damaged (b - d) AGUV specimens loaded in Arkopal at 50°C.

From the time-of-flight (TOF) data, detailed information on the shape of the notch and cracked regions can be visualized. The crack is not propagating strictly in a plane area but reveals a more complex three-dimensional structure. However, a crack growth in the notch plane can be approximated since the differences in crack opening distance are small (signal widths, Fig. 61).

The central part of FNCT specimens was also captured as three-dimensional data sets obtained from X-ray micro computed tomography (CT) to analyze the fracture zone (section 3.3.4). The fracture planes and the crack lengths can be determined by the consideration of sectional planes in x-y- and x-z-orientation as sketched in figure 62. Although the entire FNCT specimen was measured, CT images show the decisive segments in which crack growth occurs in the lateral center of the specimen.

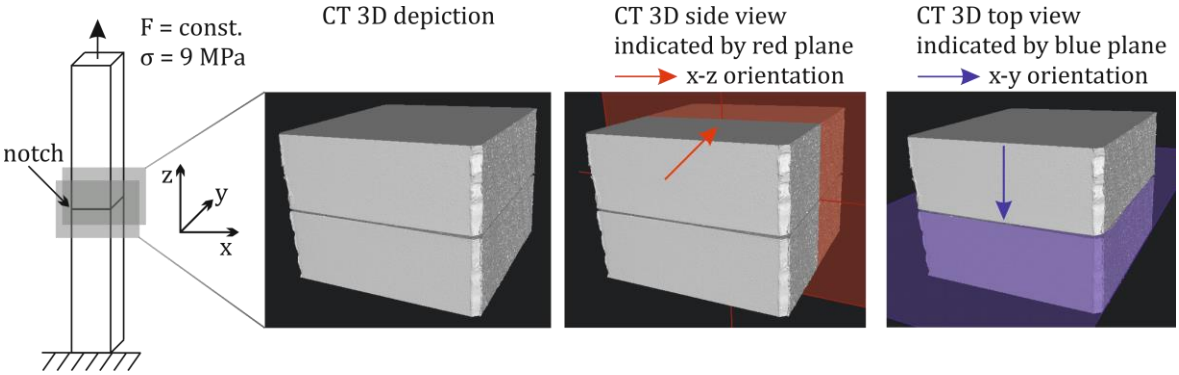

Figure 62: Scheme of an FNCT specimen as analyzed by X-ray computed tomography (CT).

Figure 63 exemplary shows the central sectional planes of the investigated area of AGUV FNCT specimens tested in Arkopal. CT images of AGUV in biodiesel and diesel can be found in figure B3.96 (Appendix B3, paragraph crack growth analysis). The sectional plane in x-z-orientation provides a side view of the crack. Therefrom, crack lengths can be measured directly. Individual voxels can be analyzed whether they belong to the crack or the bulk material. Furthermore, crazing structures can be identified which neither belong to the crack nor represent undamaged bulk material (especially in Fig. 63 c, d). As a result, the occurrence of crazes all over the entire specimen was revealed from CT images (Fig. 63 d). Thus, the entire specimen tested in Arkopal is unexpectedly completely damaged by either cracking or crazing after 97% t_f*.

The top view (x-y-sectional plane) represents the areas of notch, crack and central ligament. The similarity to the SAM fracture plane illustrations is obvious (Fig. 61). CT depictions were deliberately neither smoothed nor optically filtered to avoid loss of information on crack length and craze zone. Therefore, the occurrence of ring artefacts is accepted since they do not occur in the focused areas.

Crack propagation is not exactly symmetric but according to stress distribution, which is such that a cylindric residue of PE-HD material remains in the center of the specimen (undamaged area, Fig. 63 d). Therefore, the exterior shape of the sample is hardly reproduced interiorly due to crack propagation. Consequently, the crack length differs with respect to the measurement spot.

To determine the actual average crack length according to equation 55, distinct crack lengths were directly measured on both sides of sectional x-z- and y-z-planes in such a way that 25 values per side were obtained. Hence, 100 crack length values were obtained in total for every FNCT specimen (section 3.3.4).

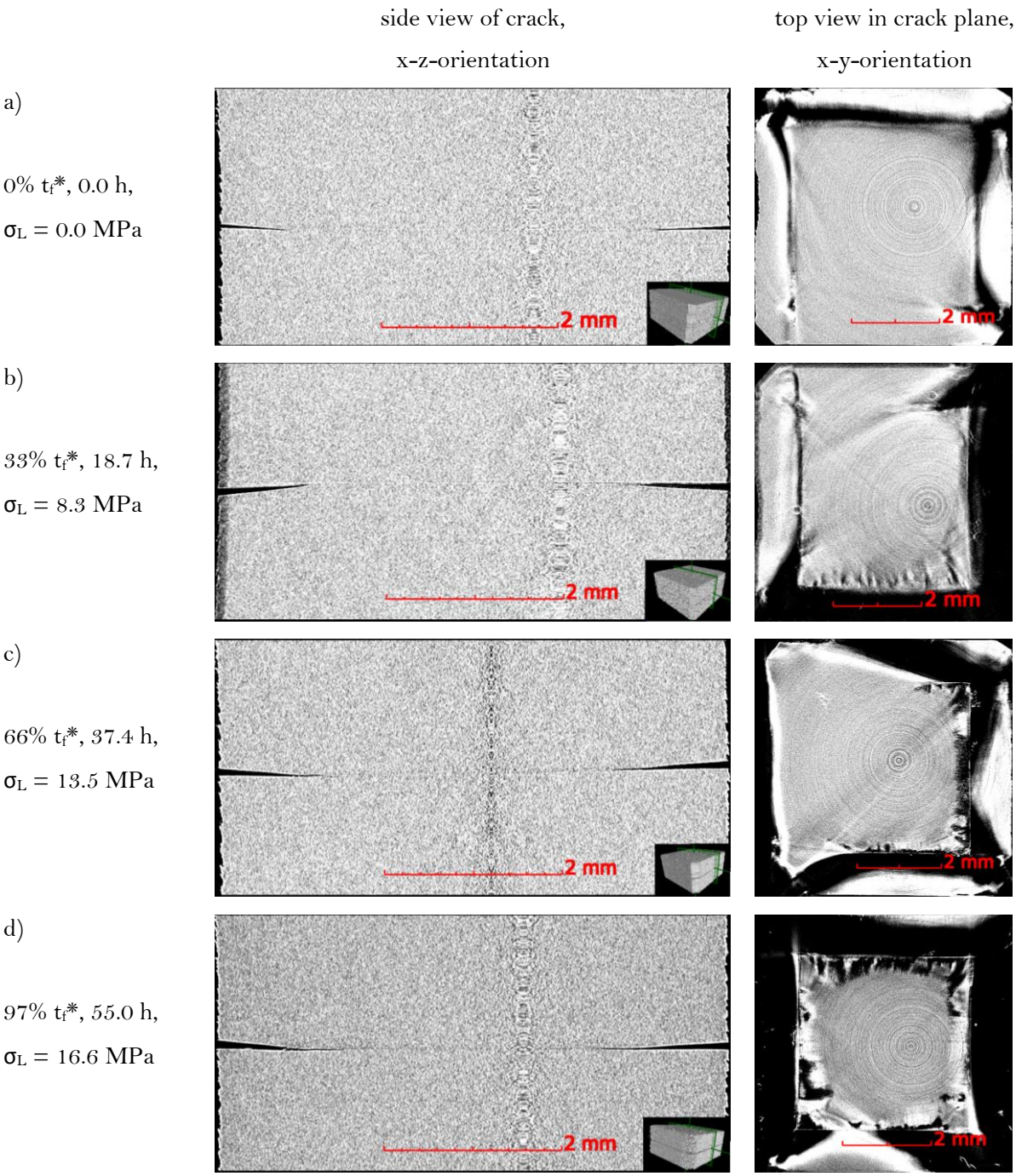

Figure 63: Partially damaged areas of AGUV FNCT specimens in Arkopal in the plane of crack propagation measured by CT, side view and top view.

The determined average crack lengths for the different techniques are shown as functions of fractional damage (FNCT exposure time) of AGUV in Arkopal (Fig. 64 a), biodiesel (Fig. 64 b) and diesel (Fig. 64 c). For biodiesel and diesel, all imaging techniques except the SAM were used. These data are compared to the specimen elongation directly measured during FNCT.

Crack growth rates were obtained from the slope of the central part of the average crack length curves (approx. region II, Fig. 26) indicated by a dashed line (Fig. 64). Crack growth rates are also given in table 12.

a)

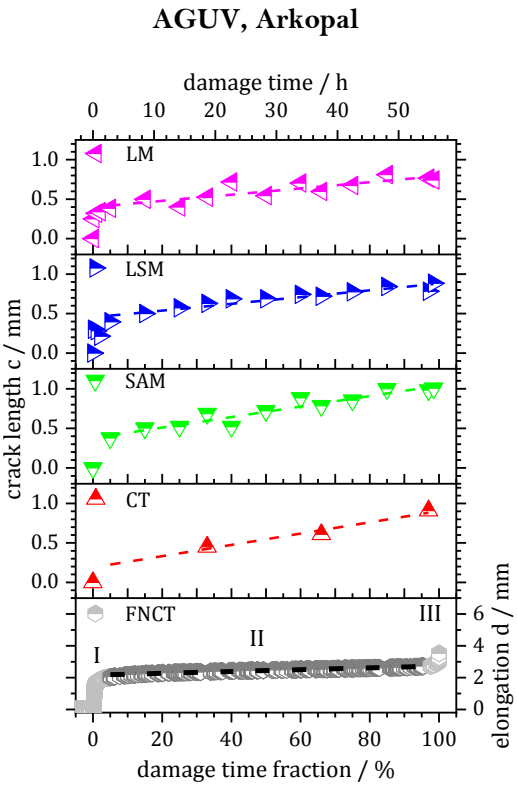

b)

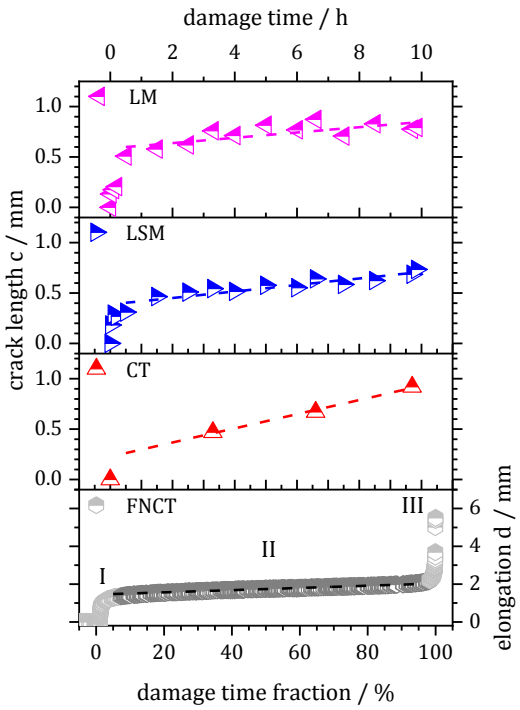

c)

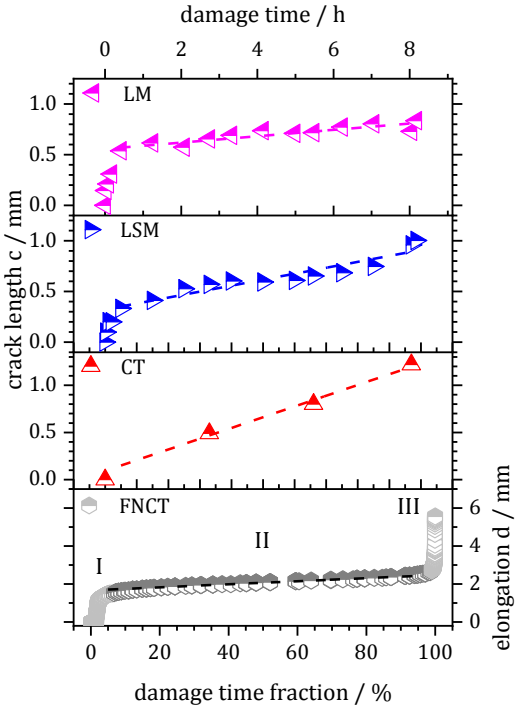

Figure 64: Average crack lengths and crack growth rates determined from the different imaging techniques compared to FNCT elongation data.

Table 12: Crack growth rates determined from different imaging techniques and FNCT elongation.

	crack growth rate $\dot{c}_{Arkopal}$ AGUV, Arkopal / µm h^{-1}	crack growth rate $\dot{c}_{BD}$ AGUV, biodiesel / µm h^{-1}	crack growth rate $\dot{c}_{D}$ AGUV, diesel / µm h^{-1}
LM	12.2 ± 2.0	26.3 ± 7.2	31.4 ± 4.6
LSM	13.5 ± 1.4	32.3 ± 4.5	70.8 ± 7.7
SAM	20.7 ± 2.0	-	-
CT	22.3 ± 4.3	70.2 ± 5.8	137.2 ± 14.4
FNCT (elongation d)	10.2 ± 0.1	59.0 ± 1.6	96.8 ± 1.1

The crack growth rates of the destructive optical techniques LM and LSM deviate significantly from the nondestructive methods SAM and CT (Fig. 64 a). Furthermore, the absolute crack lengths as detected by the nondestructive methods SAM and CT are larger than those detected by the destructive imaging methods LM and LSM.

Overall, crack lengths and crack growth rates are increased following the fluid-dependent ranking of diesel > biodiesel > Arkopal. Thus, the highest crack growth rate is obtained in diesel as already expected due to the t_f* values. Furthermore, a correlation between crack lengths and FNCT elongations d is noticeable. Crack growth rates obtained by imaging techniques are in the same order of magnitude and show the same fluid-dependent ranking as those obtained by FNCT elongation measurements (region II, Fig. 26).

Small crack length differences obtained by LM and by LSM result from the higher contrast of LSM laser images. Therefore, areas damaged by crack growth could be distinguished more exactly from areas damaged by cryo-fracture in LSM laser depictions. This is additionally indicated by a higher scatter of average crack lengths obtained by LM compared to LSM (Fig. 64). During the laser scanning procedure, the reflected laser intensity is utilized as a measure to determine the focus. Therefore, the confocal principal is used with a confocal aperture. As a consequence, laser images display distinct intensity values of reflected laser irradiation of each measuring point in focus. Since laser irradiation impinges perpendicularly to the fracture surface, flat surface structures lead to higher reflection (total reflection). In contrast, laser light is scattered on a rough surface and reflected intensity is lower. Hence, flat and truly brittle surfaces (cryo-fracture) appear bright, whereas rougher areas (crack growth) lead to darker greyscales on LSM laser images (Fig 59).

The occurrence of flat and brittle structures in cryo-fractured areas as well as rougher structures in crack growth areas is displayed in SEM micrographs (Fig. 60). Opposing to LSM, the contrast is reversed in SEM. Flat surfaces appear dark, whereas rough surfaces are depicted brighter. During SEM, the incident electron beam leads to an induction of secondary electrons which are extracted from the material, i.e. the sputtered FNCT specimen fracture surface. These secondary electrons are counted and used to create the micrograph depiction. The more secondary electrons are registered, the higher is the intensity. With a higher intensity, the micrograph appears brighter. Since rough surfaces exhibit a higher area than flat surfaces, a higher number of secondary electrons is extracted from rough surfaces, and they appear brighter (Fig. 60). In turn, the differences between flat and

rough surfaces is an indication of truly brittle surface areas resulting from rapid crack propagation (RCP) and brittle surface parts resulting from craze-crack / SCG phenomena (section 2.3).

The differences in average crack lengths obtained by destructive and nondestructive imaging methods result from a different detection of crack and craze zone. For the destructive imaging techniques, the distinction between crack and undamaged zone is based on differences in the reflective properties due to sub-micrometer surface structures. Due to craze-crack mechanism, the damaged zone consists of a craze zone, in which the bulk material is already damaged by elongated but still intact crazes (fibrils), and a crack zone with entirely fractured fibrils.

SAM and CT partly detect the craze zone as damaged, i.e. belonging to the crack. On the other hand, the destructive methods partially detect the craze zone as undamaged. This may be due to the relaxation of the less elongated fibrils at the craze tip after the release of the external load. After the subsequent cryo-fracture of an FNCT specimen, these areas do not exhibit the characteristic structures of the crack (the remaining fibrillar fragments as shown in Fig. 60 c). Therefore, they are identified by the destructive methods as undamaged.

This is illustrated by the SEM micrograph of a fracture surface at 97% t_f* shown in figure 60 a, b. The notch can be clearly identified (area 1). Additionally, the typical surface structure of the crack formed from the remains of highly elongated and fractured fibrils (area 2) as well as the smoother brittle surface of the cryo-fractured area (4) are revealed. Furthermore, smooth surfaces forming a transition zone between the two can be seen (3a, 3b). This transition zone may be attributed to the relaxed smaller crazes at the forefront of the growing crack. These parts of the fracture surface are detected as damaged, i.e. as part of the crack, by the non-destructive SAM and CT, whereas they are counted as undamaged by LM and LSM.

5.3.2. Correlation of craze and crack length

The systematic deviation alone does not explain the observed differences in crack growth rate (Tab. 12). This can be understood, when an increasing length of the craze zone with the growing crack is assumed. This is reasonable because the mechanical stress is significantly increased during FNCT (sections 2.3.4 and 5.1.1) promoting the formation of crazes. Therefore, the craze zone as well as the adjacent zone of plastic deformation is increased [10, 11] compared to the earlier stages of craze formation and crack growth.

Additionally, a linear correlation between the length of the craze zone and the crack length can be indicated based on fracture mechanic considerations. According to Irwin model, $K_{IC} = \sigma_B(\pi c)^{1/2}$ (Eq. 27 in section 2.4.2). Following the mathematical interpretation of the Dugdale plastic zone model (Fig. 8) by Rice, the length of the craze zone $R_{craze} = \frac{\pi}{8}\frac{K_{IC}^2}{\sigma_c^2}$ (Eq. 29 in section 2.4.3). At the moment of crack propagation, i.e. when the latest fibril of the craze zone fails, the craze stress σ_c and the fracture stress σ_B have to be equal ($\sigma_c = \sigma_B$). This includes the assumption that every fibril experiences a sort of tensile test, which is equal to a tensile test of the entire PE-HD material. Then, combining equations 27 and 29 leads to (Eq. 62):

$$R_{craze} = \frac{\pi}{8}\frac{\left[\sigma_B(\pi c)^{1/2}\right]^2}{\sigma_c^2} \Leftrightarrow R_{craze} = \frac{\pi}{8}\frac{\sigma_B^2}{\sigma_c^2}\pi c \overset{\sigma_B = \sigma_c}{\Longleftrightarrow} R_{craze} = \frac{\pi^2}{8}c \qquad (62)$$

with R_{craze}: length of craze zone, c: crack length. Hence, there is a linear correlation (Eq. 63) of:

$$R_{craze} \propto c \qquad (63).$$

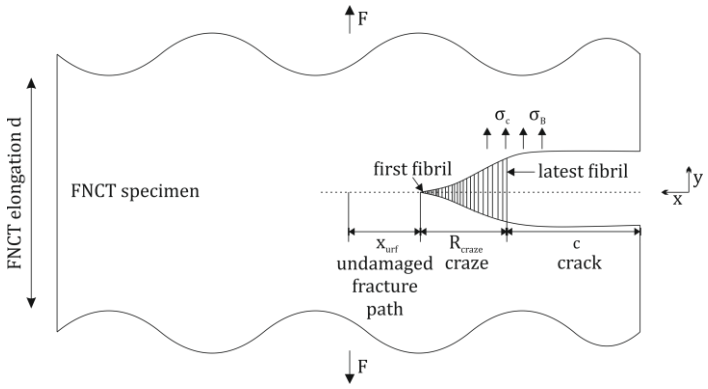

Figure 65: Schematic representation of craze and crack zone in an FNCT specimen, inspired by Fig. 8.

This linear correlation explains the (linear) increase of the craze zone with an increasing crack length (Fig. 65). Thus, the length of the craze zone R_{craze} is not constant during crack propagation but it increases with increasing crack length. The crack length c and the craze length R_{craze} are increased during crack growth and the undamaged residual fracture path x_{urf} decreases. x_{urf} is in plane and direction of crack growth and describes the zone which is neither damaged by a crack nor by a craze. After final failure of the entire FNCT specimen, x_{urf} is 0. Due to the relation of crack to craze length, PE-HD components which exhibit a certain crack length are already significantly further damaged by crazing. The fibrils of later crack propagation stages might be less elongated compared to earlier stages due to the limited internal deformation of the entire specimen above and below the crack plane, which is necessary to allow for a further crack opening. Therefore, they have a higher tendency to relax and appear undamaged to the destructive imaging methods after unloading of the FNCT specimen. Thus, the deviation between LM / LSM and SAM / CT is increasing with an increased length of crack and craze zone. Consequently, crack propagation rates are deviating substantially (Tab. 12 in section 5.3.1).

The appearance of a large craze-crack zone was indicated by SAM. From the signal width obtained from SAM time of flight differences, a certain crack (craze) opening distance could be estimated (Fig. 61). Furthermore, contrast differences between more (PE-HD) and less (craze, crack, air) X-ray optic dense material in the center of the specimens reveal the occurrence of a large craze zone in CT images (Fig. 63 c, d).

To verify the assumptions and the correlation of crack and craze length (Eq. 62), the measured crack lengths c and the calculated craze lengths R_{craze} were related to each other and to the undamaged residual fracture path x_{urf} (Fig. 66).

a) Arkopal (detergent)

b) biodiesel

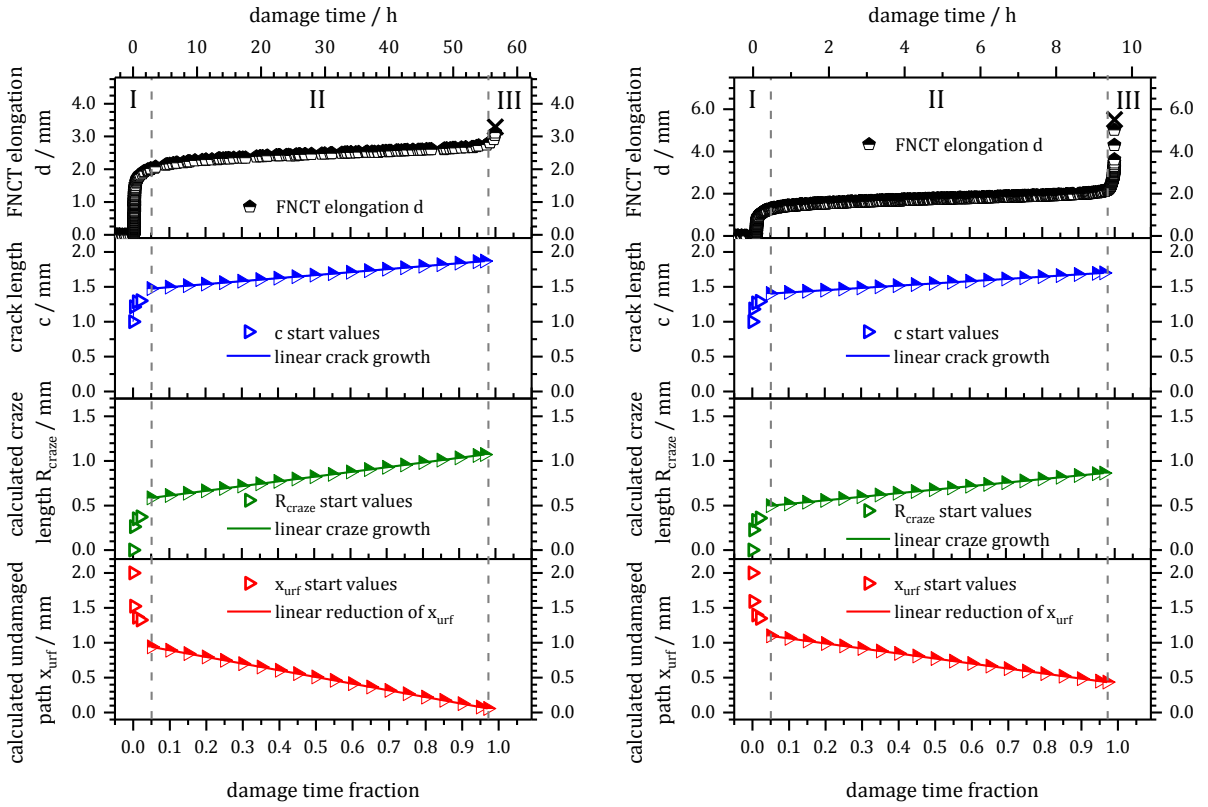

Figure 66: Correlations of FNCT elongation d and crack lengths c (including notch) to calculated craze lengths R_{craze} and undamaged residual fracture paths x_{urf} based on LSM crack length data.

The correlations of FNCT elongation d and crack lengths c with craze lengths R_{craze} and undamaged residual fracture paths x_{urf} in the detergent and in biodiesel are based on LSM crack length data (Fig. 64). Since the length data obtained by the nondestructive imaging methods SAM and CT represent the combined damage of crack and craze (section 5.3.1), LSM data were selected to consider the measured crack lengths only. Craze lengths were calculated using LSM crack length data and equation 62.

Craze lengths (Fig. 66) were calculated using crack length data without notch, because crazes occur after notching due to crack growth induced by the craze-crack mechanism under constant loading. The length of the calculated undamaged residual fracture path x_{urf} results from the starting x_{urf} value subtracted by the crack (excluding notch) and the craze length. One crack growing from the edge to the center of an FNCT specimen was regarded in these considerations (Fig. 65 and 67). Therefore, the x_{urf} start value is 2 mm, resulting from (Eq. 64):

$$x_{urf,start} = \frac{1}{2} FNCT\ specimen\ width - notch\ depth = \frac{1}{2} 6\ mm - 1\ mm \qquad (64).$$

In region I up to approx. 5% t_f*, the force applied is first taking effect. Thus, first crazes are formed and crack growth starts. The craze and the crack zones are increased distinctly. In the region of constant crack growth (region II), the crack and craze lengths increase linearly. Accordingly, x_{urf} decreases linearly (Fig. 66).

In the detergent Arkopal, $x_{urf} \approx 0$ at 97% t_f* (Fig. 66 a). Hence, the specimen is almost entirely damaged by either crack or craze after approx. 97% t_f*. Final specimen failure occurring in region III is inevitable at this point already. The reason for the sudden nonlinear increase in damage in region III is found in the high true mechanical stress which results from the decreased ligament area ($x_{urf} \rightarrow 0$). Remarkably, the true stress required to initiate final failure (transition of region II to region III) correlates to the yield strength of the material as determined by a classic tensile test. When the true stress reaches the value of the yield strength, the craze-crack mechanism merges into shear deformation. The latter results in the occurrence of a characteristic central ligament (section 5.1). This confirms the assumption that every fibril experiences a tensile test equal to the entire bulk material during craze-crack mechanism. Hence, the direct correlation of craze and crack zone lengths (Eq. 62) is also confirmed.

In the detergent Arkopal, the true stress reaches the yield strength (≈ 24 to 25 MPa [171], Fig. A1.84 in appendix A1) when almost the entire specimen is already damaged by craze or crack ($x_{urf} \approx 0$). In sorptive bulk-active fluids such as biodiesel, the yield strength is reduced (≈ 21 to 22 MPa, Fig. A1.84 in appendix A1) due to the effects of swelling and plasticization [193, 211]. Hence, the true stress required to initiate the transition from craze-crack mechanism to shear deformation is lower in biodiesel compared to the detergent Arkopal. Accordingly, a transition to shear deformation occurs, although the fracture path is not yet entirely damaged ($x_{urf} > 0$, Fig. 66). Therefore, fractions of cracked, crazed and undamaged regions are present in FNCT specimens affected by bulk-active fluids at the moment of the transition from craze-crack growth to shear deformation. This can directly be noticed on FNCT fracture surfaces (Fig. 67 and 70).

a) detergent (Arkopal) b) biodiesel

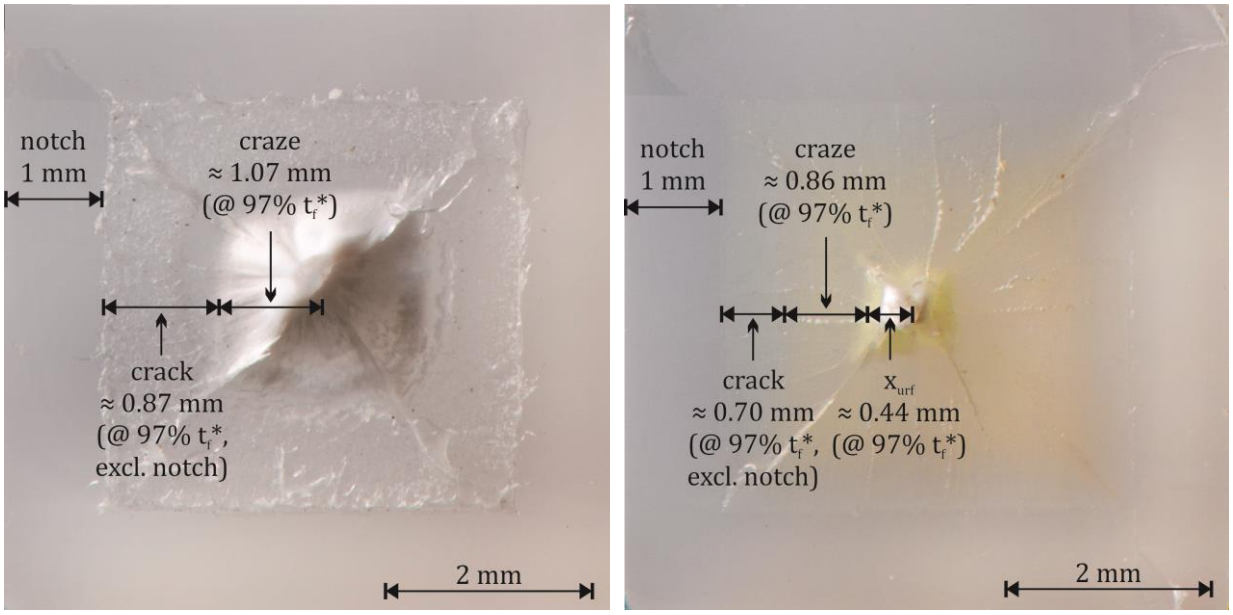

Figure 67: Correlations of crack lengths c, craze lengths R_{craze} and undamaged residual fracture paths x_{urf} with FNCT fracture surface features, exemplary depicted for AGUV in detergent (Arkopal) and biodiesel.

The occurrence of a craze zone that is already spread over the entire FNCT specimen cross section loaded for 97% t_f* in Arkopal was also revealed by the side view CT image (marked zone in Fig. 68 a and Fig. 63 d). Since the FNCT specimen loaded in biodiesel still comprises an undamaged fracture path ($x_{urf} > 0$, Fig. 67) after 97% t_f*, the craze zone does not yet cover the entire residual specimen cross section (Fig. 68 b and Fig. B3.96 in appendix B3). Furthermore, it has to be considered that the cavities of crazed regions might be filled with the sorptive fluid. As a result, present crazed regions

might not be identifiable in CT images of FNCT specimens tested in sorptive, bulk-active fluids since the difference in X-ray optic density between PE-HD and fluid is too low.

a) Arkopal b) biodiesel

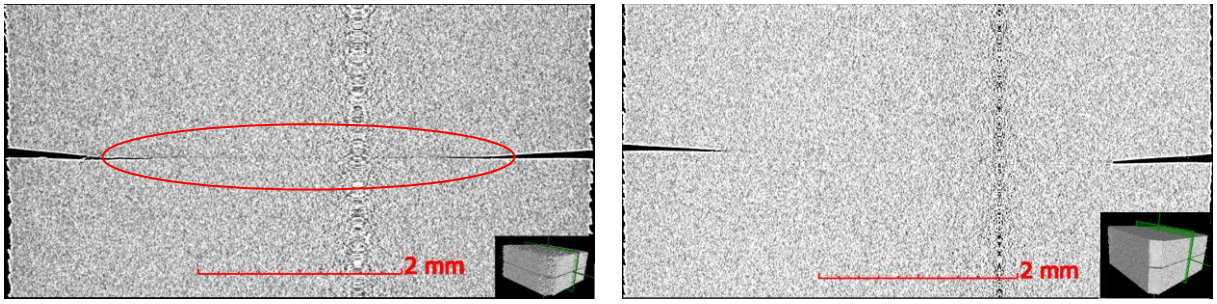

Figure 68: CT side view images of AGUV FNCT specimens loaded for 97% t_f* in a) Arkopal and b) biodiesel; cf. Fig. 63 d and Fig. B3.96.

The characteristic fracture surface features directly resulted from the conditions the certain regions were in at the start of shear deformation (transition from region II to III at ≈ 97% t_f*). Accordingly, regions that were entirely cracked at ≈ 97% t_f* show macroscopically pseudo-brittle failure. Craze regions result in the formation of elongated fibrils and higher features (e.g. plateau, pillow-like structures) on the resulting fracture surface (Fig. 67 a, b). Still undamaged bulk material parts (x_{urf}) are consequently drawn to even higher ligaments (Fig. 67 b). Differences between these fracture surface parts can be clearly distinguished. However, this fracture surface analysis also reveals that even crazed regions subjected to shear deformation may result in macroscopically ductile fracture behavior and can be considered as part of the central ligament (as especially in Fig. 67 a). This was unexpected, since a macroscopic ductile part on an FNCT fracture surface might intuitively have been ascribed to failure due to shear deformation of completely undamaged PE-HD parts.

In turn, the occurrence and the lengths of crack, craze and undamaged regions can be read from the fracture surfaces (especially in Fig. 67 b). The pillow-like structures occurring on fracture surfaces obtained from FNCT in bulk-active fluids result from elongated and saturated fibrils that were part of the crazed region prior to final failure. Hence, they finally failed due to shear deformation. However, the validity of an FNCT in bulk-active fluids is confirmed: since the craze and crack zones are still dominant on biodiesel and diesel fracture surfaces (Fig. 49 and 67 b), and both represent a sort of damage occurred to PE-HD, the FNCT is representative for the craze-crack damage mechanism.

5.3.3. Correlation of craze and crack length with FNCT elongation and yield strength

For AGUV tested in Arkopal, biodiesel and diesel, the average crack lengths show linear relations to time (Fig. 64) in a large range from approx. 5% t_f* to approx. 99% t_f* ('region II'). The slopes of the linear curves in this region are small. In region I below approx. 5% t_f*, an intense increase of crack length and elongation due to initial loading can be recognized. In region III at > 99% t_f*, the slope is also strongly increased until (rapid) final specimen failure due to shear deformation occurs, which results in macroscopically ductile fracture surface parts (central ligament). Such a progress of crack lengths (crack growth) is similar to the FNCT elongation behavior which is considered as typical for BSC/ESC (sections 3.2.2 and 5.1.3) because the overall time to failure t_f is determined by SCG in region II.

The ranking of crack growth rates (slopes in region II) for AGUV as determined by all imaging techniques congruently is $\dot{c}_{diesel} > \dot{c}_{biodiesel} > \dot{c}_{Arkopal}$ (Tab. 12 and Fig. 64). This ranking is in

accordance with the t_f* ranking obtained for AGUV. Even the quantitative differences between t_f* of AGUV tested in these fluids almost recur since the crack growth rates between Arkopal and biodiesel / diesel also differ by a factor of approx. 1/6 to 1/10 (Fig. 48 b and 64).

Moreover, a correlation between crack growth occurring in the notch plane and the FNCT elongation occurring in the direction of applied force is evident. The specimen elongation is related to the significant increase in true stress in the residual non-fractured central part of A_L during FNCT. Therefore, there is an indirect relation between elongation and crack growth. This is confirmed by the plot of actual stress applied σ_L versus FNCT elongation d (Fig. 69). σ_L was obtained by relating the force applied to the actual undamaged area measured by LSM from FNCT specimens obtained after preselected time periods (Tab. 2). Elongation d was obtained from the corresponding entire FNCT performed for the determination of t_f*.

a) b)

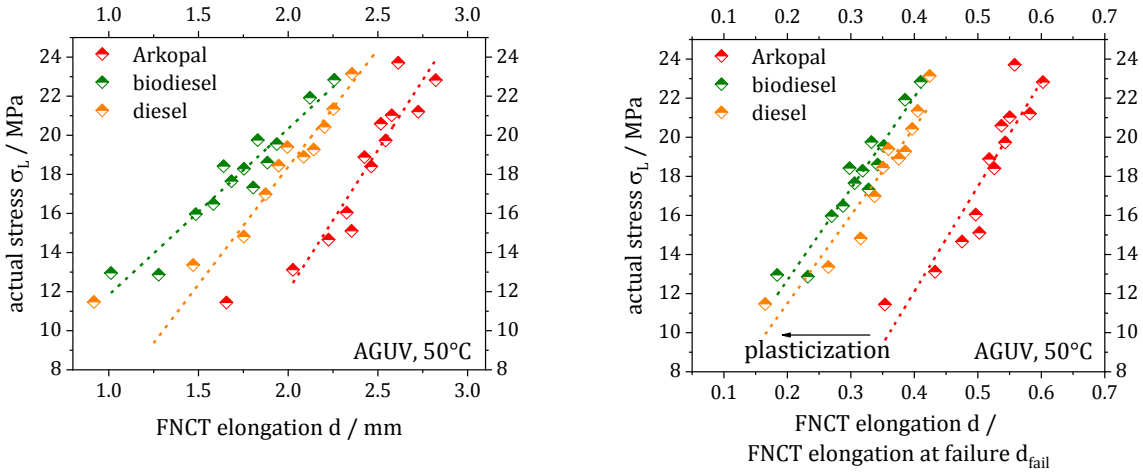

Figure 69: Actual stress applied σ_L in linear dependence on a) FNCT elongation d and b) FNCT elongation d normalized to d_{fail}.

In figure 69, a linear correlation between the actual stress applied and the FNCT elongation data in region II (crack growth region, Fig. 26 and 64) is revealed. The slopes of the linear regressions vary for different fluids (Fig. 69 a). Therefore, each system of PE-HD type and fluid exhibits a different characteristic correlation between crack growth and FNCT elongation. However, normalizing elongation values to d_{fail} (Fig. 26 c) for every system leads to similar slopes of linear regressions (Fig. 69 b). This confirms a linear correlation of FNCT elongation to crack growth.

This linear correlation can also be adapted to FNCT fracture surfaces (Fig. 70), additionally considering the assignment of cracked, crazed and undamaged zones to fracture surface features (section 5.3.2, Fig. 67). Furthermore, the effective actual stress can be calculated from the force applied and the residual fracture surface at each point in time. This can also be related to the fracture surface (Fig. 70). The correlation of actual stress to FNCT elongation is obvious. Moreover, it is confirmed that the actual stress has to adopt the yield strength value to initiate final failure (section 5.3.2) since a correlation to the characteristic fracture surface features is evident.

a) detergent (Arkopal)

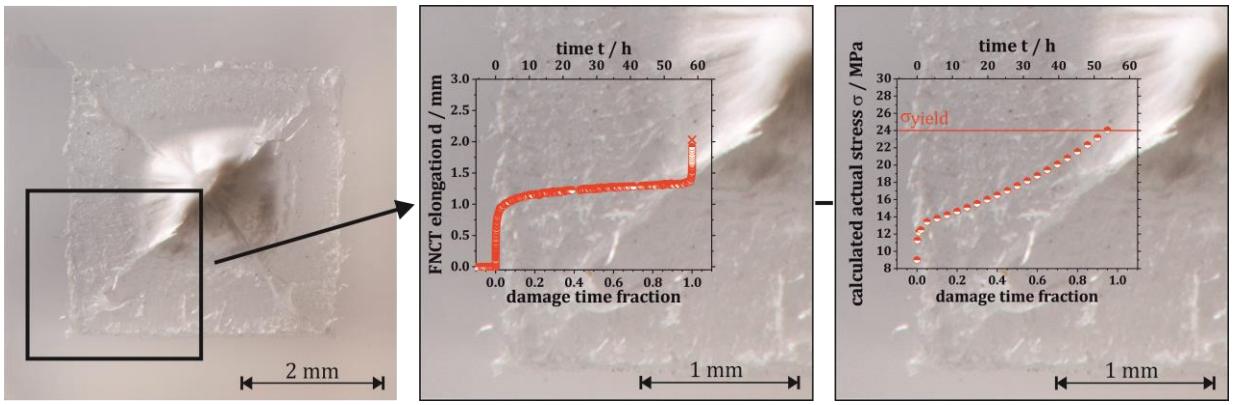

b) biodiesel

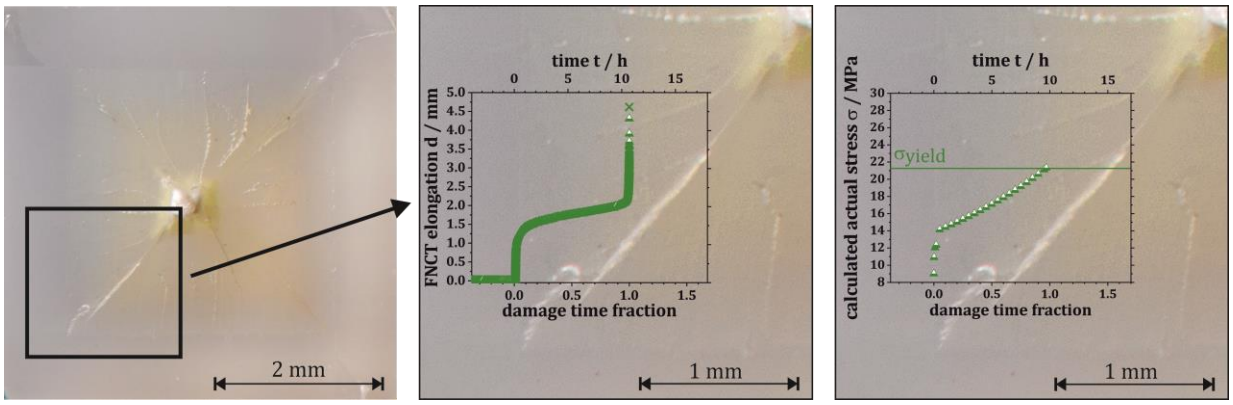

Figure 70: Relation of FNCT elongation d and the calculated actual stress σ to LM fracture surfaces, exemplary depicted for AGUV in a) detergent (Arkopal) and b) biodiesel.

Based on this correlation, FNCT elongation data are of high practical relevance since they can provide an indication of different crack growth rates. Furthermore, an early estimation of time to failure t_f is enabled, especially prior to actual final failure of a specimen. Such a premature estimation of t_f may be used as an additional tool to improve quality control processes, when specimens of PE-HD types are evaluated comparatively in a certain fluid in which the expected t_f* is known.

Furthermore, the direct comparison of the FNCT elongation d and the calculated actual stress σ_L of the Arkopal solution to biodiesel (Fig. 71 a, b) also reveals the swelling and plasticization effect of sorptive fluids: In biodiesel, a higher maximum elongation is obtained and the yield stress is lower which indicates that a lower stress is required to induce final failure. However, independent of the fluid used (surface active such as Arkopal vs. sorptive such as biodiesel), a kind of craze-crack mechanism is obtained during FNCT in both cases. This can be concluded from the general courses of the normalized curves (damage time fraction) of d and σ_L for Arkopal solution and biodiesel. Nevertheless, the crack propagation differs in rate and the resulting fracture surfaces (section 5.1.1 and 5.1.2) between these two. This substantiates the common idea of accepting a qualitative rating of different PE-HD types in terms of their SCG resistance as far as predominantly brittle fracture surfaces are obtained in FNCT [4, 9, 13] although different subordinated damage mechanisms (BSC, ESC, sorptive ESC) have occurred (section 5.1.1).

a) b)

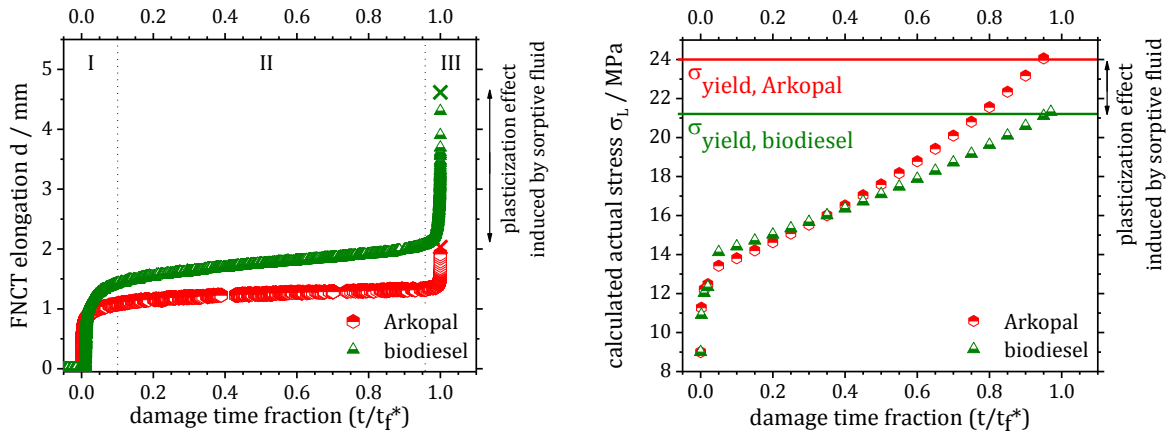

Figure 71: a) FNCT elongation d and b) calculated actual stress σ_L depending on the damage time fraction (t/t_f^*) of crack propagation analysis for Arkopal solution and biodiesel.

Since FNCT fracture surface features correlate to the yield strength, the latter can be used to pre-estimate the surface area of the central ligament. The higher the yield strength of a PE-HD type, a higher actual stress will be required to initiate final fracture (transition from region II to III) and the larger parts of the fracture surface are already damaged by constant craze and crack growth due to the craze-crack mechanism (section 5.3.2 and Fig. 70) when final failure occurs. Hence, the higher the yield strength of a PE-HD type, the smaller the central ligament area is supposed to be. Vice versa, from the occurrence of a small central ligament area on a fracture surface obtained from FNCT with the same test conditions, a PE-HD type with a higher yield strength can be concluded. This is confirmed by the yield strength values of PE-HD types used in this study and their FNCT fracture surfaces (Fig. 72).

a) AGUV
(σ_y = 24 MPa [171])

b) 5021DX
(σ_y = 25 MPa [174])

c) 5831D
(σ_y = 28 MPa [175])

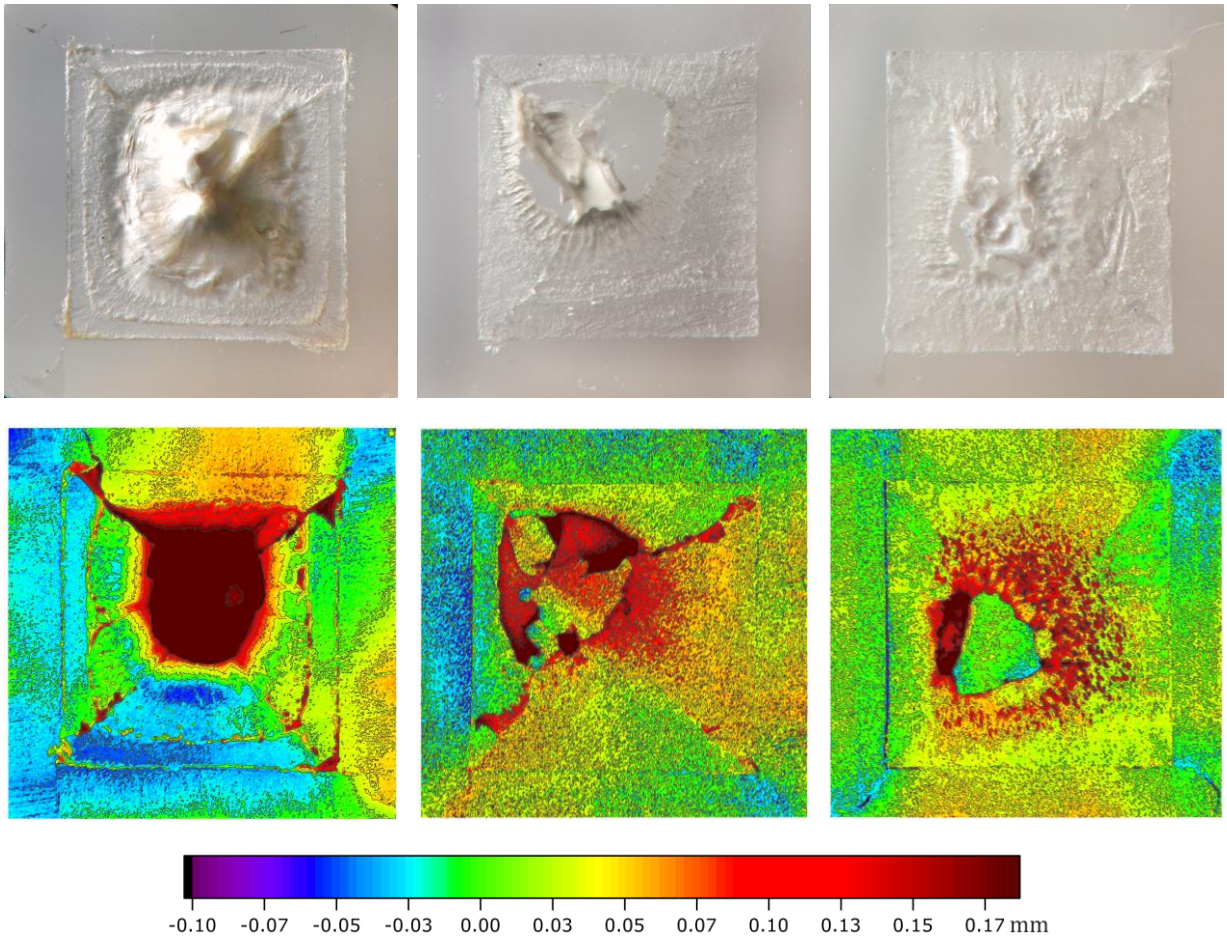

Figure 72: LM and LSM FNCT fracture surfaces of a) AGUV, b) 5021DX and c) 5831D tested in water at an initial stress of 9 MPa and a temperature of 50°C.

The base areas of the central ligaments on the fracture surfaces obtained for AGUV, 5021DX and 5831D from FNCT in water decrease with increasing yield strengths. Hence, a PE-HD type with a higher yield strength (5831D) exhibits smaller central ligament parts compared to a PE-HD type with a lower yield strength (AGUV).

5.4. Consequences for testing of slow crack growth in PE-HD

Due to the advent of new PE-HD types increasingly resistant to slow crack growth (SCG) and the associated mandatory demand for meaningful and practical relevant testing, methods such as the FNCT are scrutinized concerning their validity and significance. Furthermore, test methods are to be improved, especially in terms of time and cost efficiency. Therefore, the FNCT was evaluated in this study and the inclusion of additional data and analysis tools is proposed.

As a first approach to accelerate the FNCT, different test specimen geometries were evaluated (section 5.4.1). Furthermore, to ensure brittle fracture to occur but also to be as time efficient as possible, FNCT at lowest necessary but highest possible initial mechanical stresses and temperatures is desirable. In this respect, the brittle-ductile transition region was found at different initial stress and t_f values for different PE-HD types in different fluids (section 5.4.2). The influence of test temperature is considered in section 5.4.3. Additional data such as the specimen elongation can also

provide information concerning the brittle-ductile transition in FNCT and the damage processes (sections 5.1.3 and 5.3.3). The analysis of the corresponding fracture surfaces enables the identification of significant features which allow for a distinction of predominantly brittle or ductile behavior. By considering characteristic height data, a quantitative criterion for the differentiation of brittle and ductile fracture surfaces was derived (section 5.4.4).

5.4.1. FNCT geometry variation

The geometry of specimens and of notch configurations was varied to evaluate their influences on the FNCT (section 3.2.2). Time to failure t_f^* and elongation d data of FNCT geometry variation obtained for AGUV and 5021DX are depicted in figures 73 and 74.

a) b)

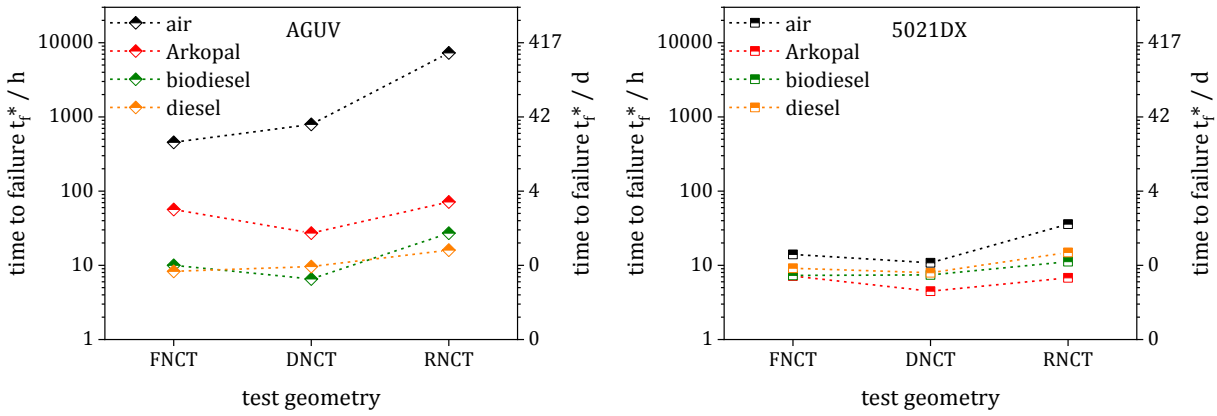

Figure 73: t_f^* of a) AGUV and b) 5021DX tested in air, Arkopal, biodiesel and diesel using FNCT, DNCT and RNCT geometry.

The geometry-dependent t_f^* values provide a ranking of $t_{f,\,DNCT}^* < t_{f,\,FNCT}^* < t_{f,\,RNCT}^*$. Thus, the RNCT led to the highest t_f^* in all fluids and did not provide any t_f^* reduction compared to the FNCT. In DNCT, t_f^* were slightly reduced compared to the FNCT. However, differences in the t_f^* ranking of PE-HD types are noticeable (Fig. 73 a and b). Although the t_f^* ranking with respect to the fluids is retained ($t_{f,\,air}^* > t_{f,\,detergent}^* > t_{f,\,biodiesel}^* > t_{f,\,diesel}^*$), the fluid influence leads to an unequal (irregular) reduction of t_f^* depending on the geometry for different PE-HD types (Fig. 73 a, b).

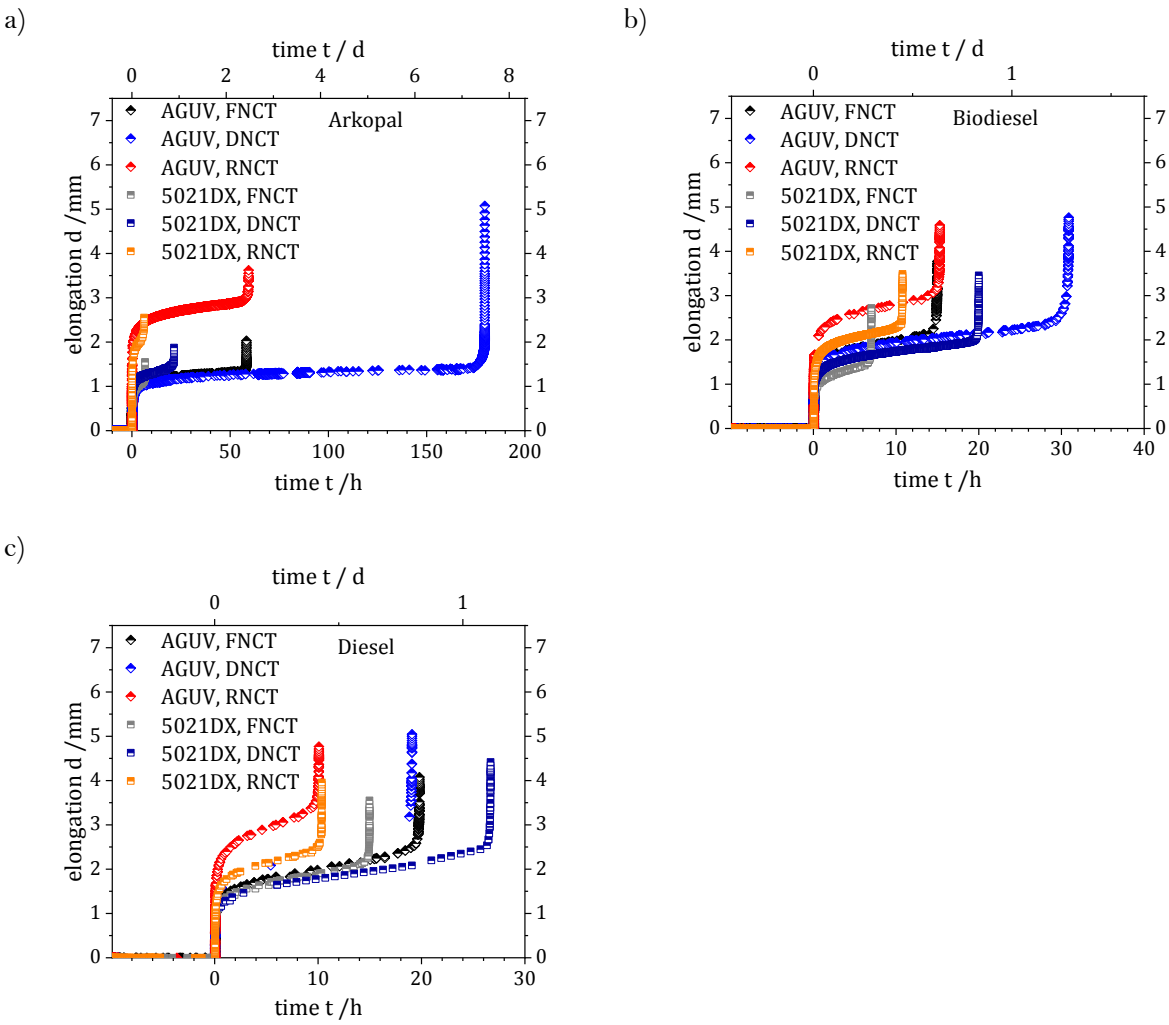

Figure 74: Elongation d data of AGUV and 5021DX using FNCT, DNCT and RNCT geometry, tested in a) Arkopal, b) biodiesel and c) diesel.

Differences from the influences of the different test geometries can also be noticed from FNCT elongation d (Fig. 74). d_{fail} (Fig. 26) tends to be higher for DNCT and RNCT. This indicates a higher central ligament and ductility. The geometry ranking concerning d_{fail} is $d_{fail,\ DNCT} > d_{fail,\ RNCT} > d_{fail,\ FNCT}$ (Fig. 74 a, b, c). Furthermore, $d_{II,start}$ is higher for RNCT independently from the fluid. In the detergent Arkopal, $d_{II,start}$ of DNCT and FNCT are similar (Fig. 74 a). In biodiesel and diesel, DNCT and FNCT show significant $d_{II,start}$ differences (Fig. 74 b, c).

Light microscopic (LM) and laser scanning microscopic (LSM) fracture surfaces for geometry variation of AGUV in Arkopal at 50°C are depicted exemplary in figure 75.

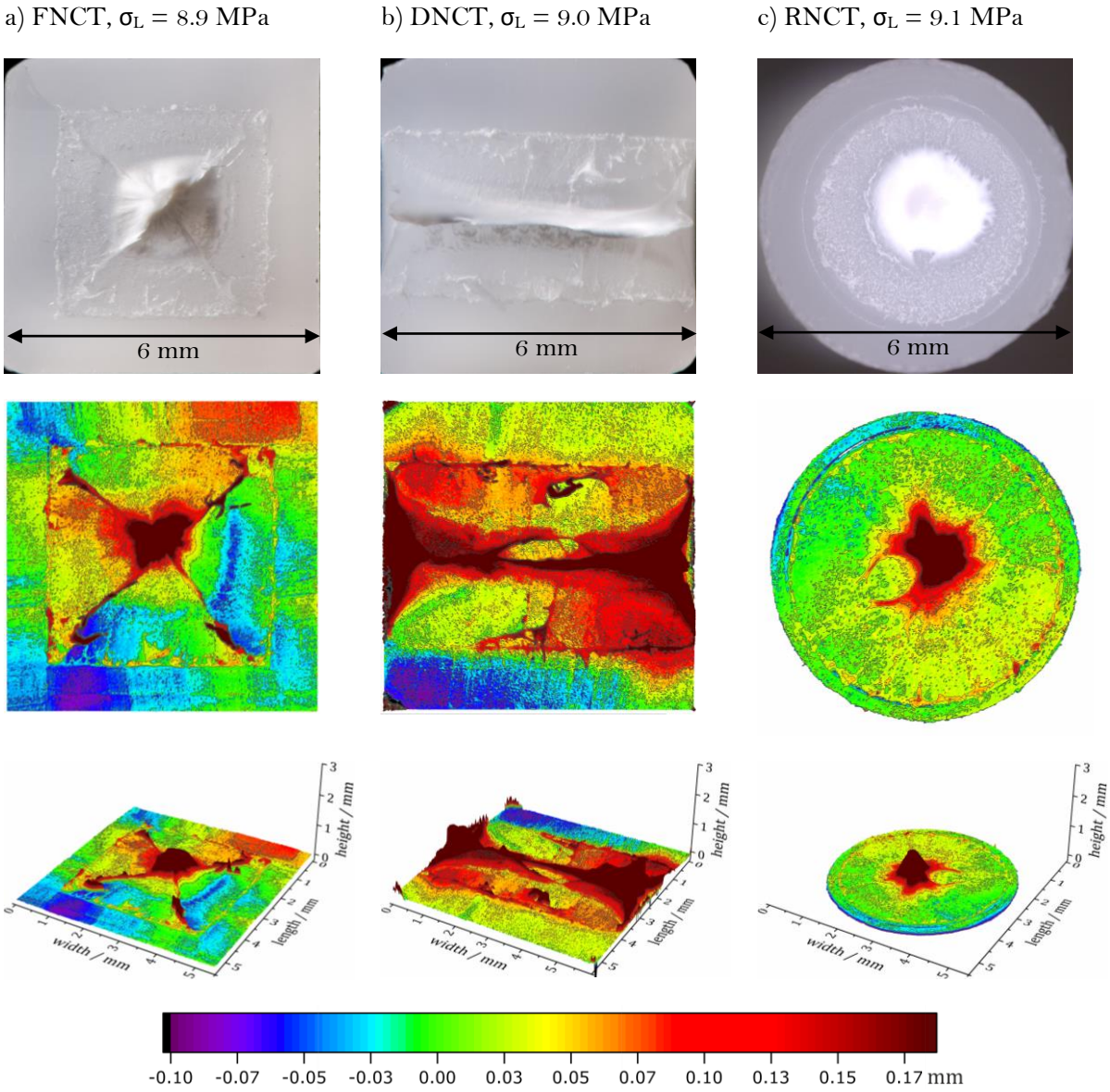

Figure 75: LM and LSM fracture surfaces for geometry variation of AGUV in Arkopal at 50°C.

Typical fracture surface areas with brittle and ductile parts were obtained for all geometries. Thus, DNCT and RNCT also show features on the fracture surface that are known from FNCT. In all geometries, a central ligament (ductile part) is surrounded by a smoother area (brittle part). Furthermore, the differently sized notch areas that depend on the geometries are distinguishable. In FNCT, the base area of the central ligament has a pyramidal shape (Fig. 75 a). In RNCT, the shape of the central ligament is similar to a cone with a circular base area (Fig. 75 c). The central ligament on DNCT fracture surfaces shows a base area approximating a trapezoid structure (Fig. 75 b). It is assumed that the distribution of ductile features on the fracture surfaces is according to the mechanical stress distribution in the specimen. This results in the formation of burrs and surface features typical for each geometry.

RNCT geometry is unfavorable in terms of test time efficiency since it results in longer t_f* than FNCT. This was expected, because circular test specimens inherently exhibit a homogeneous mechanical stress distribution in the plane of crack propagation without significant crack growth promoting stress peaks. This can be assumed from RNCT fracture surfaces (Fig. 75 c). They show a predominantly brittle fracture behavior with moderate surface roughness. Such results might be favorable for a precise description of the damage mechanism in effect (larger crack growth part).

However, this was accompanied by inconvenient longer test durations. Since RNCT fracture surfaces also exhibit a central ligament resulting from the high local (true) mechanical stress towards the end of the test, a fracture behavior typical for SCG is obtained similar to FNCT.

In DNCT, t_f* were partly reduced compared to FNCT. However, the t_f* reduction is accompanied by differences in the ranking of PE-HD types. Moreover, prominent features are unveiled on DNCT fracture surfaces (Fig. 75 c) that are attributed to ductile fracture behavior. Since large DNCT fracture surface parts exhibit ductile features, the t_f* reduction could be caused by an early change of the effective damage mechanism to shear deformation. Therefore, the applicability of DNCT to address SCG is questionable. DNCT results would have to be confirmed by FNCT, especially concerning the t_f* ranking of PE-HD types tested in a certain fluid. Hence, a change in test geometry from FNCT to DNCT is not expedient and should be avoided.

5.4.2. Brittle-ductile transition

The validity of an FNCT experiment has to be ensured in practical and routine SCG testing of PE-HD types. Therefore, the simple and fast differentiation between a predominantly brittle or ductile fracture surface on a macroscopic scale is usually used as a criterion (sections 2.3.4, 2.5.4 and 5.1). In this process, a predominantly brittle fracture surface is considered to be representative for both, BSC and ESC. Thus, its occurrence is a prerequisite for the validity of an FNCT. The naturally occurring ductile parts on a fracture surface might also result from the shear deformation of previously crazed and pre-damaged parts (sections 5.3.2 and 5.3.3). Nevertheless, a high portion of brittle fracture surface parts ensures the representativity for SCG with certainty since the tendency to yielding and the occurrence of predominantly ductile fracture behavior in non-damaged bulk material rises with increasing initial mechanical load. Precisely because by applying a higher initial mechanical stress, the yield strength (σ_y) is reached faster and ductile shear deformation is induced earlier. Therefore, a simple differentiation between predominantly brittle and ductile fracture surfaces is plausible to assess the validity of the FNCT in practical testing.

Predominantly brittle fracture is expected to occur in PE-HD at initial load levels below half of the yield strength as determined e.g. in a tensile test at the same temperature [11, 66, 68]. Furthermore, a clear distinction between brittle and ductile failure may simply be achieved by considering the relation of t_f to different load levels σ_L in the FNCT. From this, a plot can be obtained, in which two different regions of linear dependency can be identified. Therein, ductile behavior is ascribed to the region of higher and brittle behavior to the region of lower stresses (Fig. 6) [13, 62, 218]. Thus, the inflection point in this stress-t_f curve represents the transition region from brittle to ductile fracture behavior. Results of stress-dependent t_f and elongation d for AGUV and 5021DX are illustrated in figures 76 and 77.

a)

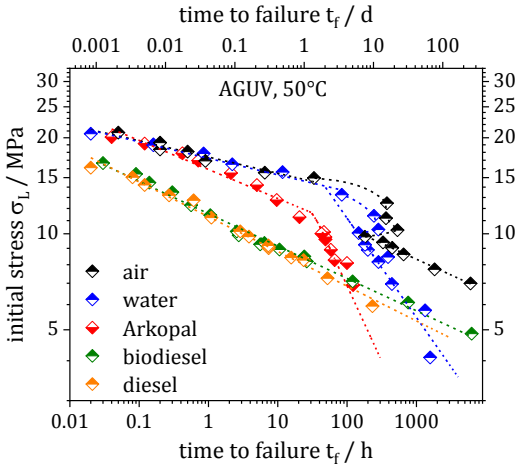

b)

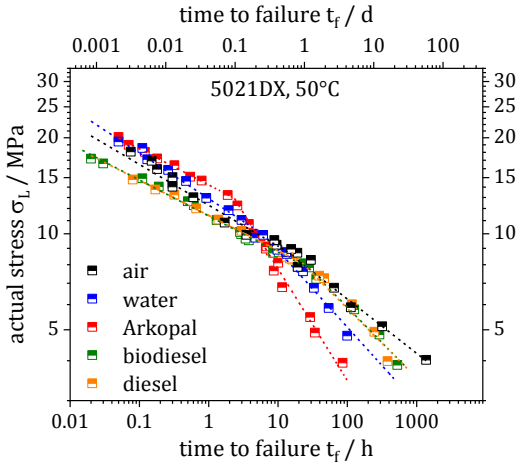

Figure 76: FNCT t_f of AGUV (a) and 5021DX (b) tested in air, water, Arkopal, biodiesel and diesel, each over a large range of actual initial stresses σ_L at 50°C (in accordance with ISO 16770 [13]).

For AGUV and 5021DX tested in air, water and detergent, the expected curves with a distinct transition from brittle to ductile fracture behavior are obtained (Fig. 76 a). Each curve consists of two different parts of linear dependency with different slopes as indicated by dashed lines. The σ_L values related to the transition regions are given in table 13.

Table 13: Stress values of brittle to ductile transition points of AGUV and 5021DX tested at 50°C in air, water, Arkopal, biodiesel and diesel.

fluid	**AGUV, 50°C / MPa**	**5021DX, 50°C / MPa**
air	15.5	9.1
water	13.9	10.0
Arkopal	11.6	12.9
biodiesel	-	7.8
diesel	-	8.3

For AGUV tested in water and air, the curve exhibits a 'nose' in the transition region. Such a special curve shape is known from literature [62, 105]. To ensure comparable and reproducible results, practical testing at stress levels within this region should be avoided. The onset of the 'nose' is found for AGUV tested in water (50 °C) at approx. 10.0 MPa. Excluding the 'nose', the brittle-ductile transition point is at 13.9 MPa for water. For AGUV tested in air, the 'nose' onset is located between 9 and 10 MPa and the brittle-ductile transition point is found at 15.5 MPa. The transition point for Arkopal can be identified at 11.6 MPa.

For 5021DX in water and air, the brittle-ductile transition points are located at 10.0 MPa and 9.1 MPa, respectively. They are lower than for Arkopal with a value of 12.9 MPa.

No distinct transition point can be determined for AGUV in biodiesel and diesel since only small t_f differences occur over a broad range of σ_L. Other criteria have to be considered to evaluate the

brittle-ductile transition of AGUV in biodiesel and diesel (section 5.4.4). The brittle-ductile transition regions of 5021DX tested at 50°C in biodiesel and diesel are identified at 7.8 MPa and 8.3 MPa, respectively. Hence, the transition from brittle to ductile fracture behavior differs depending on PE-HD type and fluid. To maintain comparability between several PE-HD types and fluids, a distinct stress value as universal as possible should be selected for FNCT to obtain brittle failure in all cases.

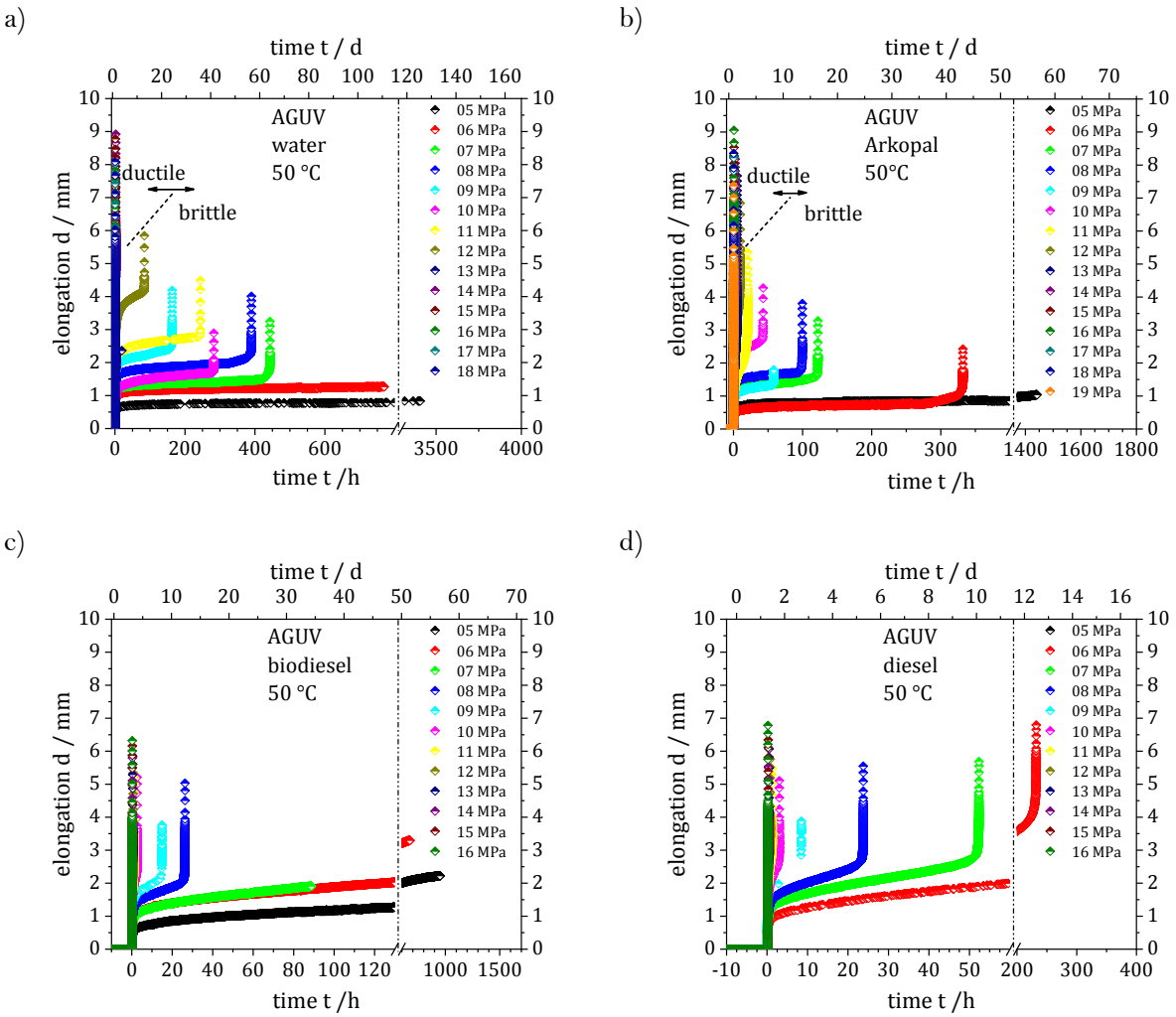

Figure 77: Time-dependent elongation curves of stress level-dependent FNCT of AGUV.

In figure 77, time-dependent elongation curves obtained from FNCT at different stress levels are depicted for AGUV in water, Arkopal, biodiesel and diesel. All results show that higher stress values σ_L lead to reduced t_f but a higher elongation d (Fig. 77). Although the general curvature is similar in all cases, d_{fail} is increased significantly with increasing stress above a certain σ_L value. Such a salient point of severe d_{fail} increase seems to be an indicator for the transition from brittle to ductile fracture behavior. d_{fail} follows the ranking $d_{fail,\,water} > d_{fail,\,Arkopal} > d_{fail,\,diesel} > d_{fail,\,biodiesel}$ at higher stresses (ductile region) but is reversed at lower stresses (brittle region). Bulk-active fluids (biodiesel, diesel) show reduced t_f but also decreased elongation values compared to inert and surface-active fluids at higher stresses (Fig. 77). In lower stress regions, especially below the brittle-ductile transition, biodiesel and diesel show increased d_{fail} compared to water and the detergent. Hence, bulk-active fluids exhibit a less stress dependency of d_{fail} (Fig. 77 b, d) than inert and surface-active fluids.

All elongation curves (Fig. 77) follow the course typical for FNCT (Fig. 26). For the high-stress curves above brittle-ductile transition, region II is no longer recognized in the graphs due to the

scaling of the time-axis. The slope of region II in the elongation curves additionally indicates whether a high or low portion of ductile fractions is present. With increased region II slopes, the fracture behavior tends to become predominantly ductile. Furthermore, the less the time-dependent portion of region II in the entire elongation curve, the more ductile behavior can be assumed (Fig. 77).

From LM and LSM micrographs of stress-dependent FNCT fracture surfaces of AGUV tested at 50°C in Arkopal, changes of the overall surface roughness and the development of the central ligament with increasing stress can be seen (Fig. 78). The color-code used in all LSM depictions covers a small height range from -0.10 to +0.17 mm (Fig. 81, also in Fig. 49) with the result that higher peaks are uniformly color-coded in brown. The micrographs were taken from specimens whose t_f were also considered in stress-t_f curves (Fig. 76).

a) σ_L = 8.9 MPa

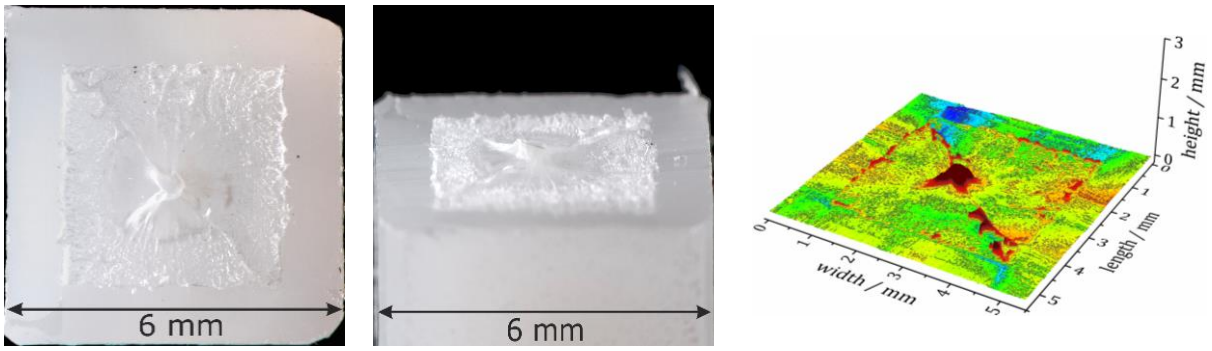

b) σ_L = 9.8 MPa

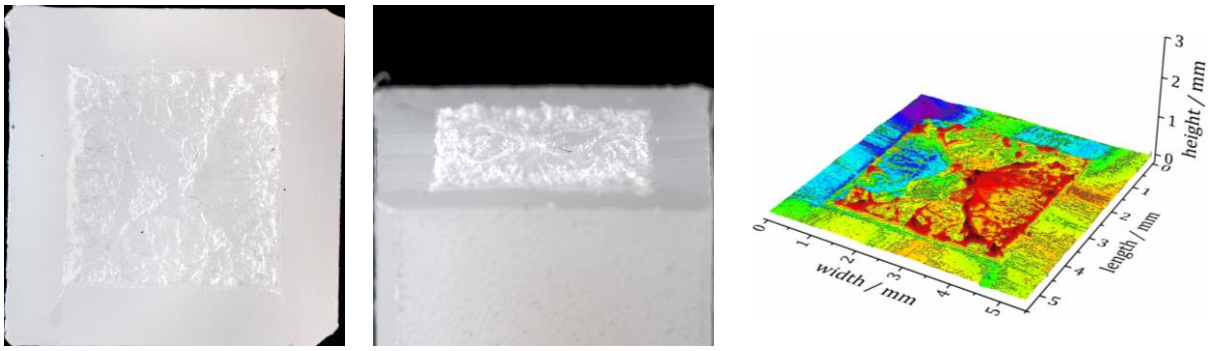

c) σ_L = 10.0 MPa

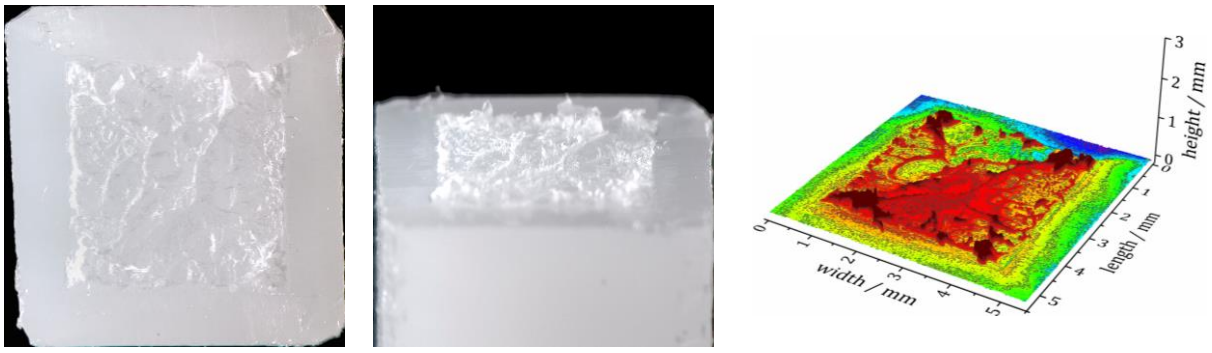

d) σ_L = 11.3 MPa

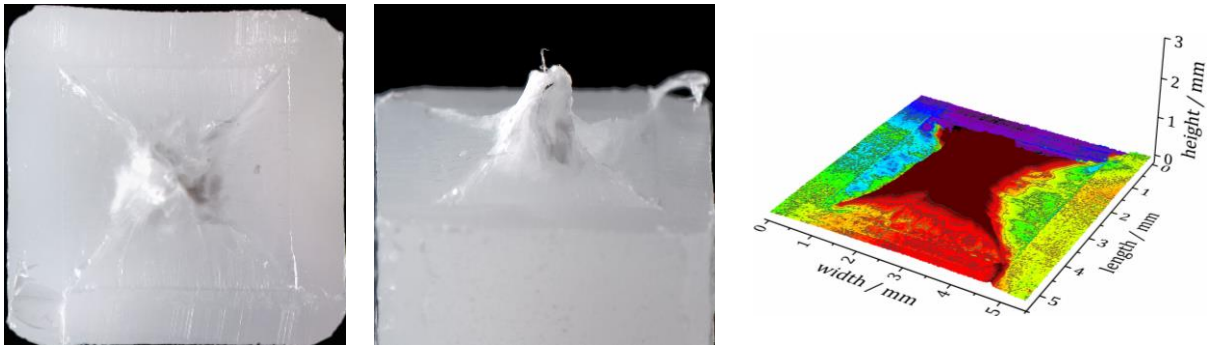

e) σ_L = 12.8 MPa

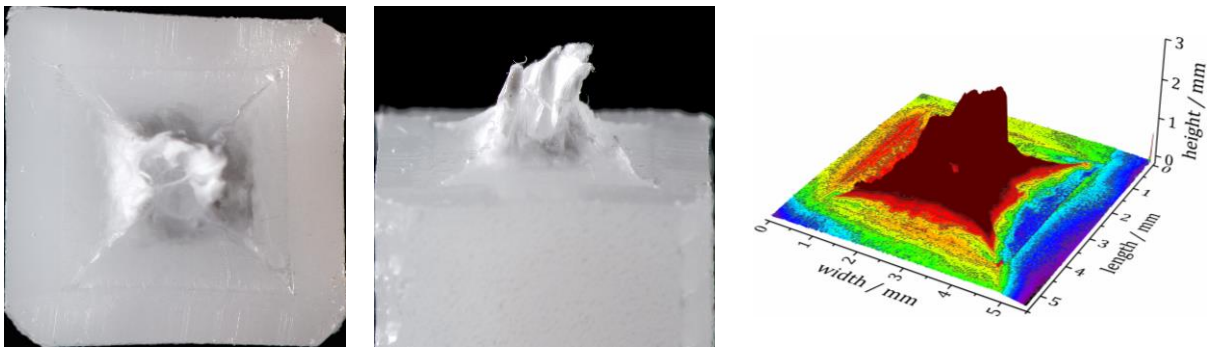

f) σ_L = 20.1 MPa

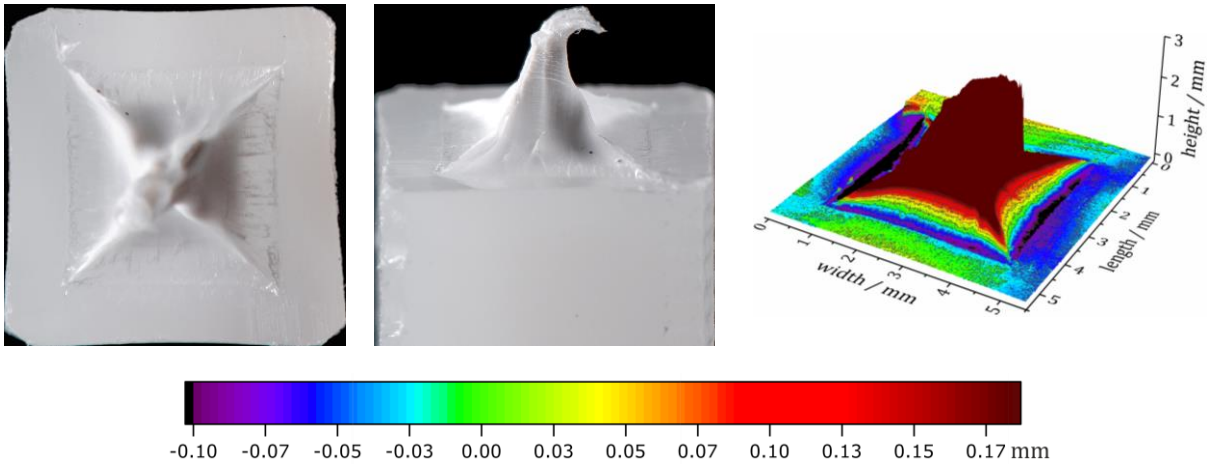

Figure 78: LM and LSM fracture surfaces for stress variation of AGUV tested at 50°C in Arkopal.

A transition from brittle to ductile behavior can be seen between (c, brittle) and (d, transition knee) to (e, ductile). In turn, the identified surface features can be used as criteria for the identification of brittle or ductile fracture behavior. The higher a central ligament overtops a certain average height value and the larger its base area, the more ductile failure behavior has to be supposed. Such a behavior can be seen for fracture surfaces resulting from FNCT applying stresses above the transition region derived from figure 76 (Fig. 78, d - f). The other surfaces (Fig. 78, a - c) show a higher portion of smooth parts with lower central ligament peaks. They are attributed to brittle failure.

Stress-dependent FNCT may be applied to determine the actual transition region from brittle to ductile fracture behavior. In all stress-dependent FNCT, higher stresses result in a reduction of t_f but

an increase in elongation d_{fail} independent of PE-HD type and fluid (Fig. 76, Fig. 77, Fig. B2.90). Hence, d_{fail} is an additional indicator for the transition from brittle to ductile fracture behavior. Furthermore, it correlates to the fracture surface appearance since increased elongation is associated with higher (predominantly central) ligaments characteristic for ductile behavior (Fig. 78). A tendency to either brittle or ductile fracture behavior is also appreciable from time-dependent elongation curves (Fig. 77), especially for inert and surface-active test fluids. However, a brittle-ductile transition region is not obtained from stress-dependent FNCT t_f for AGUV in sorptive fluids. Therefore, a detailed fracture surface analysis may alternatively be used to distinguish the two types of fracture.

A correlation between the fracture surfaces (Fig. 78) and elongation curves (Fig. 77 b) is evident. The shorter the constant crack growth region (region II) in the elongation curve, the more ductile features can be noticed on the fracture surface. Such features are an enhanced surface roughness and the formation of separate extended ligaments. The heights of such ligaments and the size of their base area are regarded as measures of ductile behavior. Furthermore, the outer rim of the central ligament base is related to the point in time of FNCT when ductile deformation starts after initial brittle crack propagation from the notch inwards (Fig. 70). Changes of the overall surface roughness as well as the development of the central ligament with increasing stress can be seen (Fig. 78). Additionally, characteristic fracture surface features suggest the occurrence of a transition region in contrast to a sharp transition point, as it might be indicated by the distinct 'knee' in stress-dependent t_f curves (Fig. 76).

Moreover, LM and LSM illustrations of a clearly brittle (a) and a clearly ductile (b) fracture surface obtained for 5021DX tested at 50°C in Arkopal are compared (Fig. B3.92 in appendix B3). The brittle and ductile nature of the fracture surfaces is determined by the location in the respective regions below and above the brittle-ductile transition of the stress-dependent FNCT (Fig. 76 b). Brittle and ductile failure result in different fracture surface appearances for the two different PE-HD types AGUV and 5021DX. For 5021DX, the visible surface features are less pronounced compared to AGUV. Consequently, criteria for the distinction of brittle and ductile behavior obtained from fracture surface properties have to take into account the differences in the general fracture behavior of different PE-HD types (section 5.4.4).

5.4.3. Temperature influence

Temperature-dependent FNCT were performed at constant nominal stresses σ_n of 9 MPa to evaluate the influence of temperature on the FNCT (Fig. 79, 80 and 81).

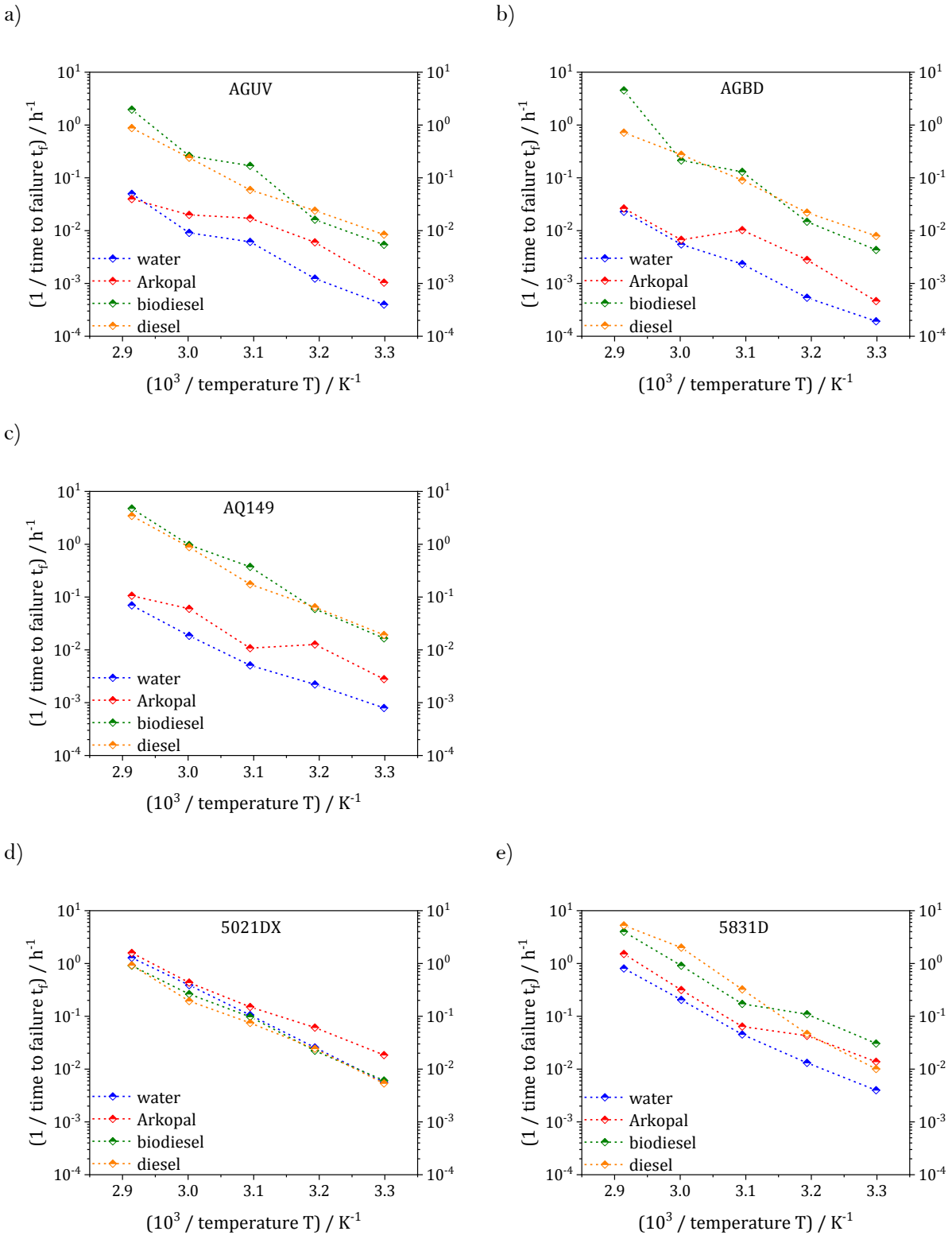

Figure 79: Arrhenius-like depiction of t_f (1 / t_f) vs. temperature (1 / absolute temperature in K).

An Arrhenius-like behavior is obtained from the relation of FNCT t_f to the test temperature (Fig. 79). Dashed lines in figure 79 are guides for the eye and no interpolations. In contrast to the standard FNCT procedure, only one specimen instead of five was tested at a preselected temperature and a nominal stress σ_n of 9 MPa. Therefore, marginal deviations in t_f might occur due to minor differences in the actual stresses applied σ_L.

Although a linear correlation between t_f and temperature is tendentially observed for all fluids and PE-HD types, a distinct step in curvature is found between 50°C and 60°C, e.g. for AGUV in water as well as Arkopal (Fig. 79 a) and AGBD in Arkopal (Fig. 79 b). It is speculated that this relates to an expected brittle-ductile transition. The slope above this transition point is similar to that below the step. This was unexpected since different failure mechanisms are presumed to be predominant (shear deformation vs. crack propagation), respectively.

The time-resolved FNCT elongation d curves depicted exemplary for AGUV in figure 80 show the tendency of obtaining higher maximum elongation values d_{fail} at higher temperatures. Therefore, similar changes towards higher test temperatures are obtained as for increasing stress levels at constant temperature (50°C, Fig. 77). However, the temperature-dependent changes in the elongation curves are more inconclusive compared to the observed changes in stress variation. Thus, the former are no additional indicator for a brittle-ductile transition. Due to the low t_f at higher temperatures, the constant crack growth region (region II) is barely noticeable in these curves. Nevertheless, all elongation curves follow the general course (Fig. 26 b, c).

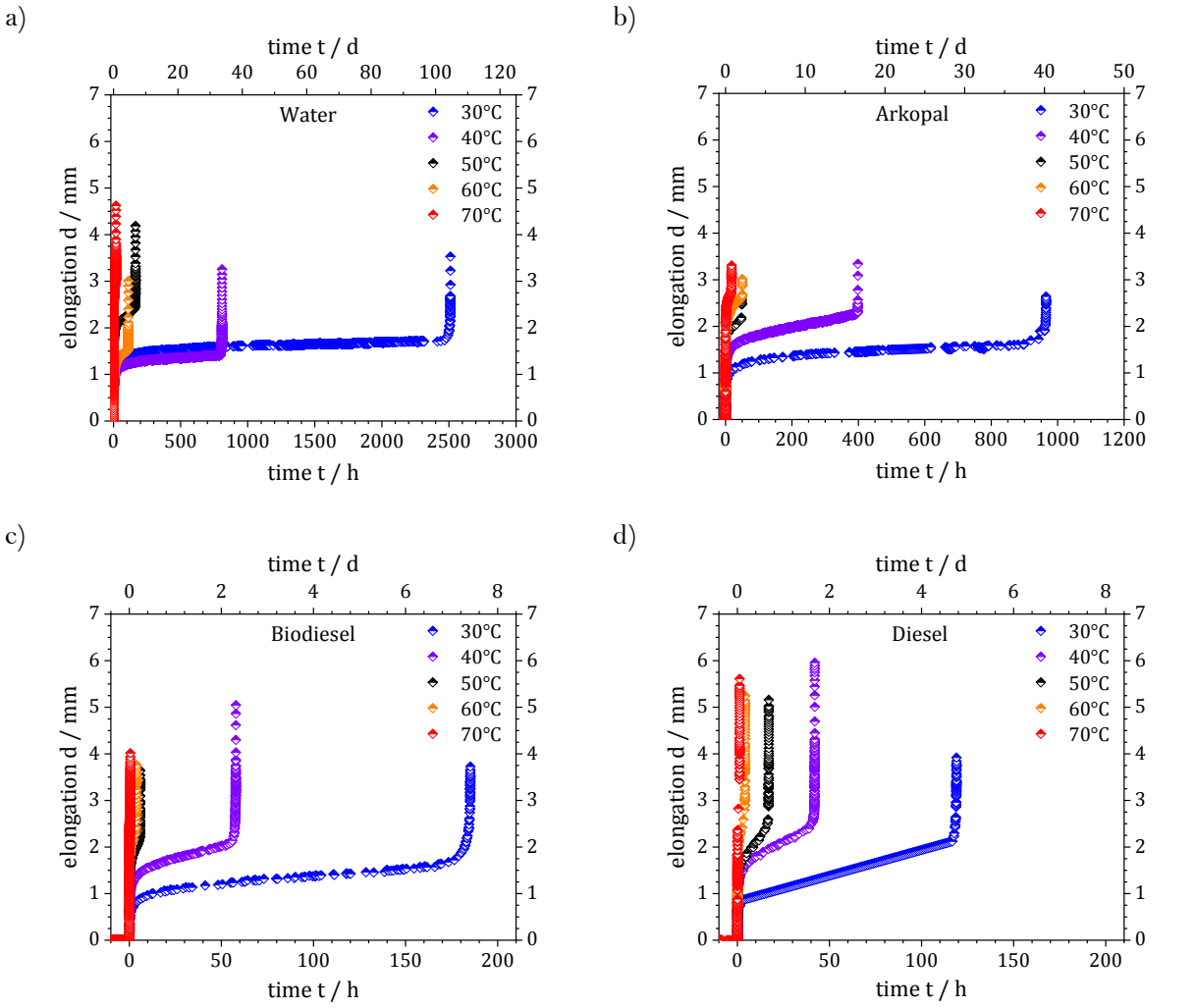

Figure 80: Elongation d data of temperature-dependent FNCT of AGUV tested in a) water, b) Arkopal, c) biodiesel, d) diesel.

An indication for a brittle-ductile transition can be identified in the LM and LSM micrographs of the temperature-dependent FNCT series of AGUV in Arkopal, which are exemplary illustrated in figure 81.

a) 30° C, σ_L = 8.9 MPa

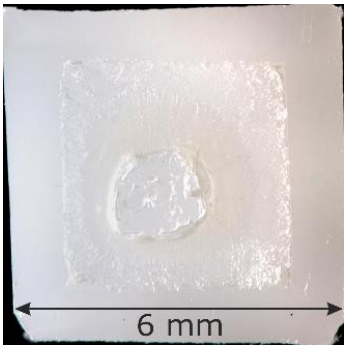

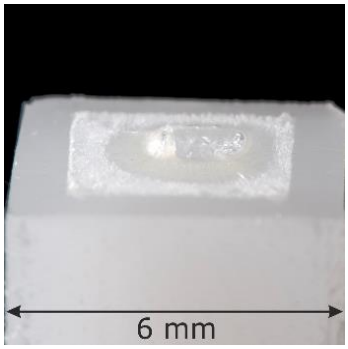

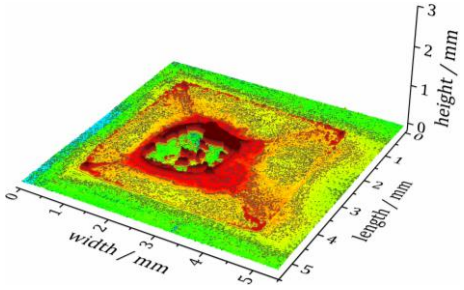

b) 40° C, σ_L = 9.2 MPa

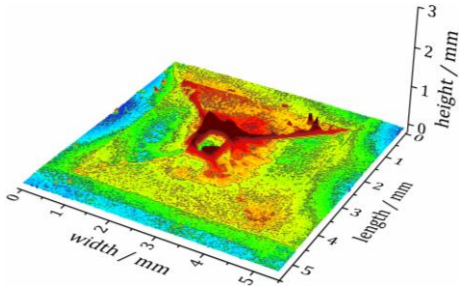

c) 50° C, σ_L = 8.9 MPa

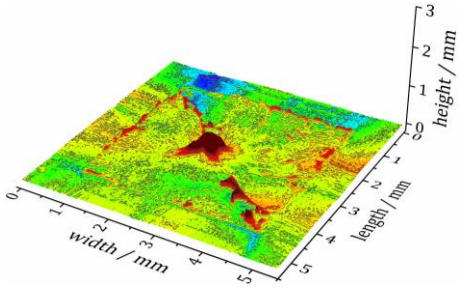

d) 60° C, σ_L = 9.3 MPa

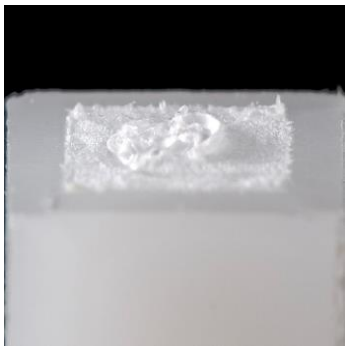

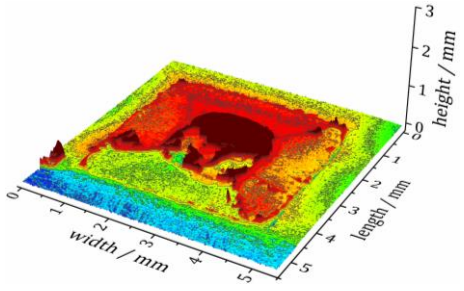

e) 70° C, σ_L = 8.9 MPa

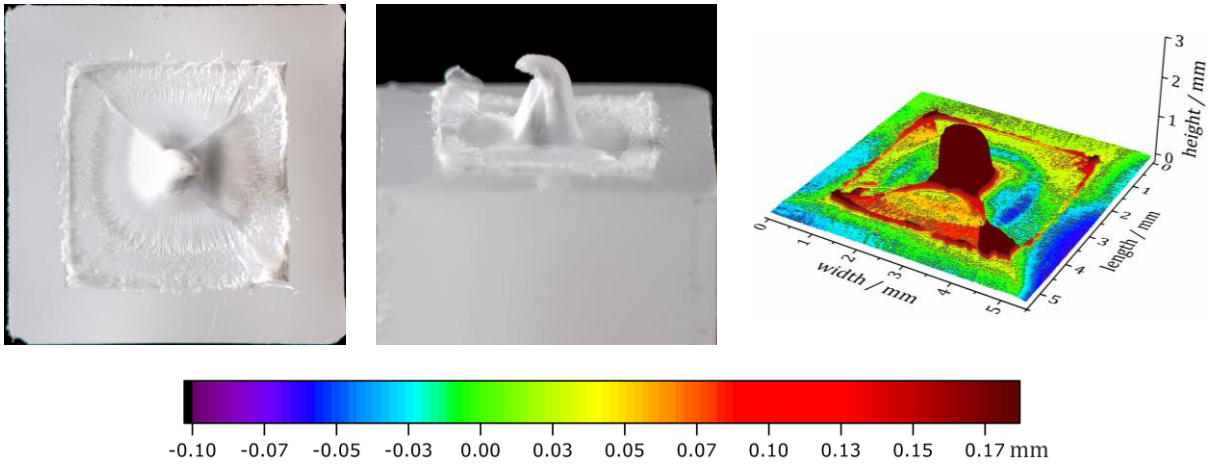

Figure 81: LM and LSM fracture surfaces of temperature-dependent FNCT of AGUV tested at σ_n = 9 MPa in Arkopal.

The fracture surfaces of FNCT specimens tested at 30 °C, 40 °C and 50 °C exhibit smooth surface features with low central ligaments, which are attributed to brittle fracture behavior (Fig. 81 a, b, c). The surfaces of specimens tested at 70 °C (and partially 60 °C) show pronounced features of a ductile fracture surface (Fig. 81 d, e). Hence, a step from a predominantly brittle to ductile fracture behavior is found for AGUV. This step may be related to the typical brittle-ductile transition. For other PE-HD types, similar results are obtained (Fig. B3.91 in appendix B3). However, the temperature-dependent 5021DX fracture surfaces reveal a significant difference in their overall appearance compared to AGUV. Especially, ductile features are less pronounced in 5021DX than in AGUV. This is similar to the appearance of fracture surfaces obtained for stress-dependent FNCT (Fig. 78 and Fig. B3.92 in appendix B3).

Thus, temperature-dependent fracture surfaces show a distinct increase of ductile features with increased temperatures such as stress-dependent fracture surfaces do with increased stresses. However, the development of changes with increasing temperatures (Fig. 81) is different from that observed for increasing stress (Fig. 78). It is concluded that a brittle-ductile transition region is clearly detectable in a series of stress-dependent FNCT but not unambiguously in a temperature-dependent series. A temperature-induced brittle-ductile transition would have to be practically assessed by stress-dependent FNCT series at different temperatures.

When temperatures are raised above a certain value, predominantly ductile instead of brittle fracture occurs. This was to be expected since the overall molecular mobility of the polymer matrix is enhanced at higher temperatures. Therefore, disentanglements and relaxation processes are facilitated, and ductile shear deformation becomes dominant. Crack propagation is diminished at the same time because stresses at the crack tip are reduced by local relaxation processes.

Although an Arrhenius-like behavior is found, results obtained from FNCT at higher temperatures (e.g. > 60°C) have to be considered with due care since they may reduce test times (t_f) but they also lead to predominantly ductile fracture behavior. Therefore, an interpolation of results to obtain t_f* by considering different temperatures should be avoided. Instead, t_f* values should be compared only when they were obtained at equal and low temperatures (< 60°C for the container materials in this study).

5.4.4. Criterion of brittleness

In the FNCT series of varying stresses and temperatures, a distinct change in fracture behavior, i.e. the balance of brittle and ductile fracture portions, was found. The fracture surface analysis is a powerful tool to differentiate between ductile and brittle fracture behavior. Typically, the occurrence of brittle fracture in FNCT is considered as a prerequisite to assess SCG in PE-HD (sections 2.3.4). Hence, an FNCT experiment might be regarded as 'valid', if it represents the craze-crack damage mechanism. As revealed by the results in this study, a fracture surface part appearing ductile on a macroscopic scale finally failed due to shear deformation but it might have been pre-damaged by crazing (sections 5.3.2 and 5.3.3). Both, crack as well as craze zones, are considered to represent damage by the craze-crack mechanism that occurred to PE-HD. Therefore, crazed parts such as the pillow-like structures on biodiesel and diesel fracture surfaces have to be classified as 'valid' in the consideration of the FNCT evaluability (section 5.3.2). Hence, the pillow-like structures are regarded as 'brittle' in terms of the FNCT validity.

In practical testing, an objective criterion is desirable to decide whether a specific fracture surface is to be regarded as predominantly brittle or ductile, i.e. whether the FNCT is valid or invalid concerning its evaluability with respect to the craze-crack mechanism. Such a criterion has to take into account the characteristics of specific systems of PE-HD type and fluid in terms of fracture surfaces since the corresponding brittle and ductile features differ (sections 5.4.2 and 5.4.3).

Referring to the usual distinction between brittle and ductile fracture surfaces to address the validity of an FNCT, a criterion of brittleness B is proposed which is based on the results obtained from LSM fracture surface analysis. Surface roughness parameters, heights of distinct surface features and proportions of surface areas are considered therein.

Two parameters are here considered to be decisive for the assessment of a fracture surface in terms of brittleness: the overall height of the highest peak (typically the central ligament) and the average height of the entire fracture surface related to the height of the notch plane (zero level) determined as surface roughness. If the values of these parameters are high, the fracture surface will be regarded as ductile. Since the values of the highest peaks differ significantly between several PE-HD types and fracture surfaces, they have to be related to the overall maximum height of the highest ligament in a stress-dependent FNCT series of a certain system of PE-HD type and fluid. Values of surface roughness areas have to be related to the actual initial fracture surface A_L (Fig. 25). Altogether, the highest peak on a distinct fracture surface (profile) R_p [219], the highest peak of all fracture surfaces in a stress-dependent FNCT series R_{max} and the arithmetic average of the fracture profile (surface roughness) R_a [219] are considered for the criterion of brittleness B (Fig. 82). R_a is determined according to (Eq. 65 and Eq. 66) [219]:

$$R_a = \frac{1}{MN}\sum_{m=1}^{M}\sum_{n=1}^{N}|Z(x_m, y_n) - \langle Z\rangle| \tag{65}$$

$$\text{with } \langle Z\rangle = \frac{1}{MN}\sum_{m=1}^{M}\sum_{n=1}^{N} Z(x_m, y_n) \tag{66}$$

and $Z(x_m, y_n)$: height value of a pixel on the fracture surface and $\langle Z\rangle$: mean of height values of all pixels on the fracture surface.

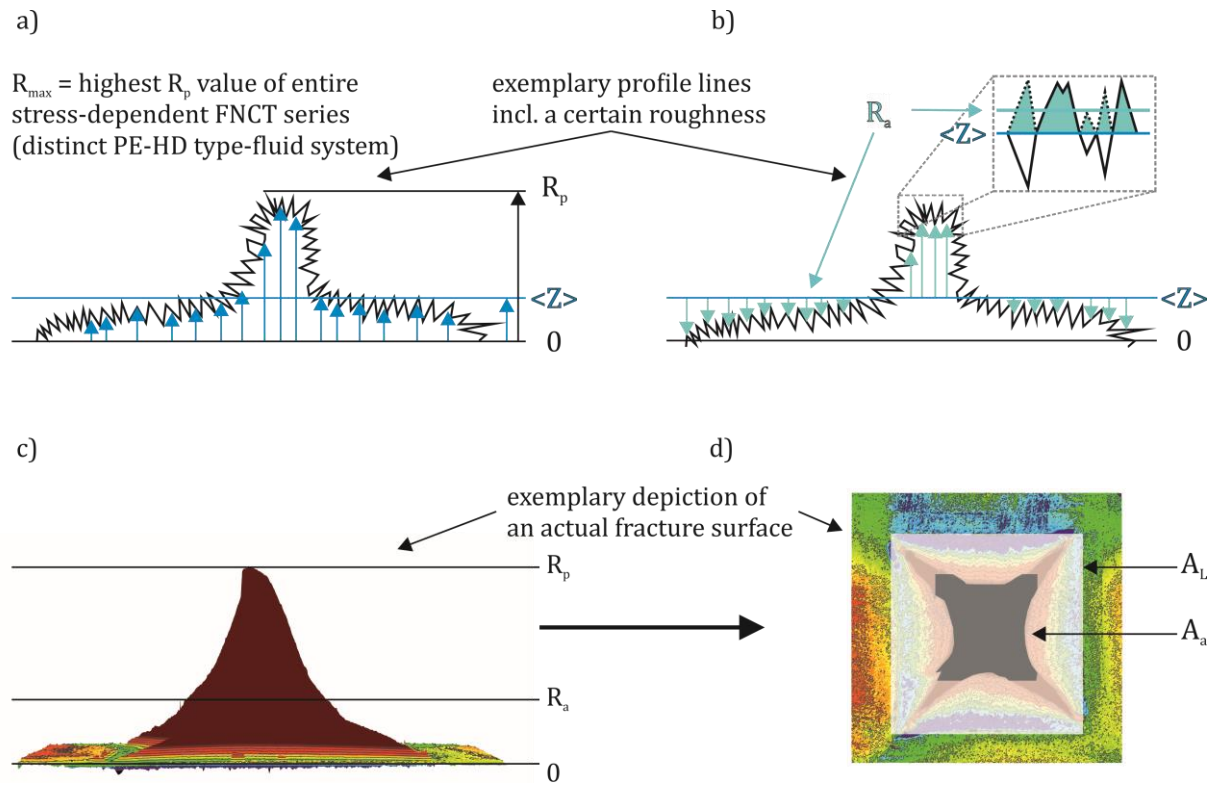

Figure 82: Schematic depiction of parameters used in the criterion of brittleness B, a) exemplary profile line describing R_p, R_{max} and $\langle Z \rangle$, b) exemplary profile line showing R_a, c), d) exemplary depiction of an actual fracture surface (ductile) with R_p, R_a, A_L and A_a.

To evaluate the surface roughness that contributes to the brittleness of an FNCT fracture surface, the portion of surface area A_a that overtops the value of R_a has to be regarded (Fig. 82 a, b, c). Hence, the criterion of brittleness B comprises the two parameters:

$$\frac{R_p}{R_{max}} \quad \text{and} \quad \frac{A_a}{A_L},$$

with R_p: maximum height of fracture surface (profile), R_{max}: maximum height of all fracture surfaces in a stress-dependent FNCT series of the distinct system of PE-HD type and fluid, A_L: actual initial cross-section after notching (Fig. 82 d, Fig. 25), A_a: area on the fracture surface that overtops R_a (number of pixels exhibiting height values > R_a, Fig. 82 d).

An FNCT fracture surface is thus considered as predominantly brittle and 'valid', when the (central) ligament is small and the surface roughness is low. Based on experience, such conditions are represented by $\frac{R_p}{R_{max}} < 0.5$ and $\frac{A_a}{A_L} > 0.5$. Accordingly, the criterion of brittleness B is based on empirical fracture surface data and is defined as (Eq. 67):

$$B = \frac{1}{2}\left[\frac{R_p}{R_{max}} + \left(1 - \frac{A_a}{A_L}\right)\right] \tag{67}$$

with $B < 0.5$ characterizing a brittle, valid and $B > 0.5$ denominating a ductile, invalid fracture surface. The limiting case of $B = 0.5$ only occurs for unfractured FNCT specimens since the parameters $\frac{A_a}{A_L}$ and $\frac{R_p}{R_{max}}$ would have to adopt the same values. This was only possible when R_p equals R_{max} and the entire fracture surface area is simultaneously higher than R_a. In such cases, there was no

crack propagation and the fracture surface was naturally non-evaluable. Moreover, $\frac{A_a}{A_L}$ and $\frac{R_p}{R_{max}}$ influence each other since the value of R_p is included in R_a. Therefore, these parameters are self-regulating and contradictions that might result from their individual consideration are prevented. Furthermore, differences in the appearance of fracture surfaces between several PE-HD types (e.g. AGUV and 5021DX) are accounted for. Either an increased overall height of the characteristic surface features (R_p) or a high surface roughness (R_a, A_a) preferably contributes to the criterion of brittleness.

The brittle-ductile transition is considered as a region rather than being a sharp point (section 5.4.2), which is confirmed by fracture surface analysis (Fig. 78). Therefore, B also has a tolerance region. Based on empirical experience, the range of $0.45 < B < 0.55$ is considered as transition region. Fracture surfaces that lead to B values within this range may be regarded with due care since they might be part of the brittle-ductile transition region. An evaluation of such FNCT fracture surfaces should be avoided.

In this study, LSM data and an analysis procedure applying Origin software (section 3.3.2) were used to obtain B values. Principally, a variety of methods arbitrarily selected and easy to perform may be applied, as long as the required parameters (R_p, R_a, R_{max}) are obtained. The determination of R_{max} requires the performance of an entire stress-dependent FNCT series of a certain system of PE-HD type and fluid. Since the maximum height of fracture surface features usually correlates to the stress applied in FNCT (Fig. 78), a measurement of fracture surface features from a single test at high initial stress might alternatively be sufficient (e.g. FNCT at 18 MPa for AGUV in Arkopal). Determined once, R_{max} is valid for the regarded system of PE-HD type and fluid. In quality control processes, R_{max} could be used for all upcoming measurements and would not have to be determined repeatedly. If fracture surface features do not correlate to applied stresses in FNCT, R_{max} would have to be determined differently and B should be considered with due care. However, this seems very unlikely according to all results obtained in this study.

Since R_{max} indicates differences in the fracture behavior of several PE-HD types, it might correlate to their MFR. Both, MFR and characteristic fracture surface features, differ decisively between AGUV, AGBD and AQ149 on the one hand and 5021DX and 5831D on the other (Tab. 3). Since the MFR correlates to the toughness determined by Charpy impact tests [220], it might also represent an indicator of pronounced fracture surface features resulting from FNCT. A high MFR represents a low viscosity and a low (Charpy) toughness. Accordingly, a low MFR indicates a high ductility and prominent FNCT fracture surface features, such as in AGUV compared to 5021DX. This is plausible since MFR is a technical parameter which is determined by viscosity. The viscosity of a polymer is a measure of its flowability and it is affected by structural properties (sections 2.1.2 and 5.2) such as MM, MMD, crystallinity, short and long chain branches and tie molecules (number and lengths). Furthermore, the ability of polymer chains to disentangle is governed by these properties and might be the main contribution to the occurrence of characteristic fracture surface features. This leads to the correlation of MFR with characteristic FNCT fracture surface features.

In table 14, a selection of fracture surfaces of brittle and ductile character, corresponding B values and an optical assessment in terms of FNCT validity is given exemplary.

Table 14: Examples of enhanced fracture surface analysis applying the criterion of brittleness B.

PE-HD type	fluid (T = 50°C)	σ_L / MPa	criterion of brittleness B	FNCT validity	LSM fracture surface (3D)
AGUV	air	9.0	0.42	valid, predominantly brittle	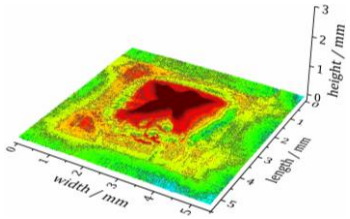
AGUV	air	16.9	0.76	invalid, predominantly ductile	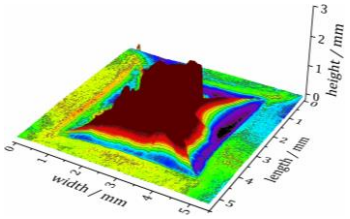
AGUV	Arkopal	9.8	0.26	valid, predominantly brittle	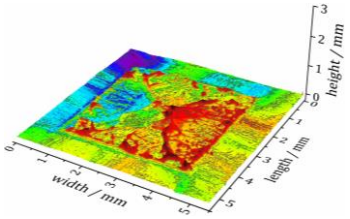
AGUV	Arkopal	17.9	0.88	invalid, predominantly ductile	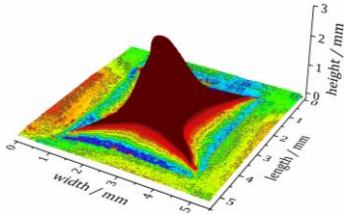
AGUV	Arkopal	11.3	0.55	tendentially invalid, predominantly ductile, transition region	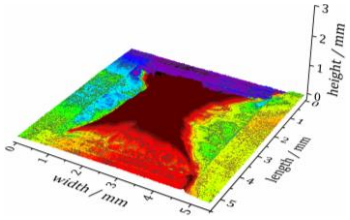
AGUV	diesel	12.7	0.94	invalid, predominantly ductile	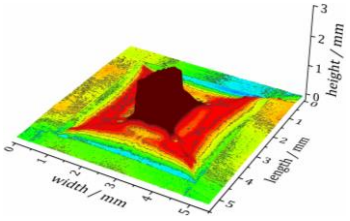
AGUV	diesel	8.3	0.36	valid, predominantly brittle	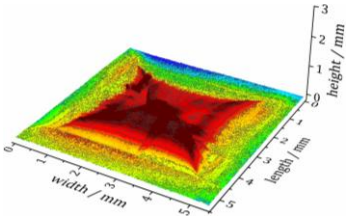

PE-HD type	fluid (T = 50°C)	σ_L / MPa	criterion of brittleness B	FNCT validity	LSM fracture surface (3D)
AGUV	biodiesel	10.2	0.73	invalid, predominantly ductile	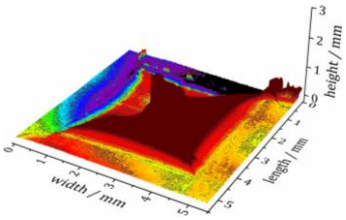
AGUV	biodiesel	8.2	0.41	valid, predominantly brittle	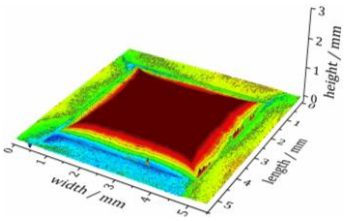
5021DX	Arkopal	14.7	0.62	invalid, predominantly ductile	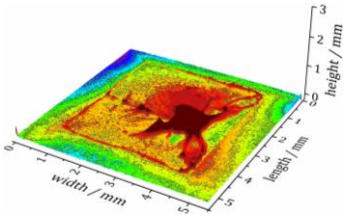
5021DX	Arkopal	8.1	0.38	valid, predominantly brittle	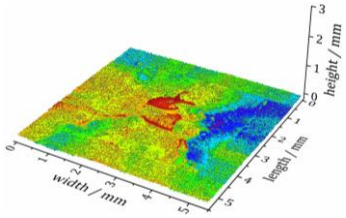
5021DX	water	11.1	0.51	tendentially invalid, predominantly ductile, transition region	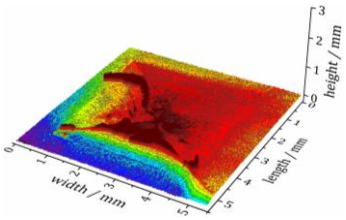
5021DX	water	9.3	0.38	valid, predominantly brittle	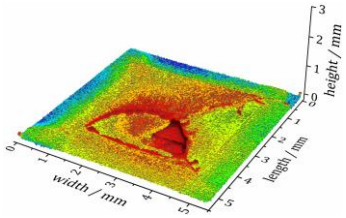

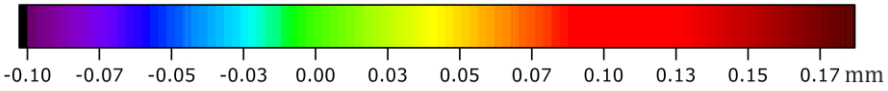

By applying B, the transition regions from a valid to an invalid FNCT (predominantly brittle to ductile fracture behavior) of AGUV tested in biodiesel and diesel could be estimated, which was not feasible by the usual stress-t_f curves (Fig. 76 and Tab. 13). These transition regions can be assumed to be in the stress ranges of 9.3 MPa to 11.5 MPa for biodiesel and 8.4 MPa to 9.8 MPa for diesel. Hence, B is a valuable tool to estimate the brittle-ductile transition region and FNCT validity, especially if this is impossible from stress-dependent t_f curves in a distinct system of PE-HD type and fluid such as for AGUV in biodiesel and diesel.

The criterion of brittleness B presented in this study is a first proposal for the assessment of fracture surfaces to ensure the evaluability of an FNCT with respect to the craze-crack mechanism (SCG, i.e. BSC/ESC). The development of B is based on empirical FNCT and imaging data obtained for five PE-HD types tested in a limited number of fluids. To establish a general validity of B, a larger amount of data for a representative variety of PE-HD materials as well as for alternative test conditions (e.g. those usually applied for pipe materials) is required than obtained in this study.

6. Conclusion

The influences of environmental fluids on the slow crack growth (SCG) behavior of five commercially available PE-HD container materials for the transport and packaging of dangerous goods were assessed in this study. The SCG mechanism was studied by applying the full-notch creep test (FNCT).

In the FNCT, the time to failure t_f^* of specimens is used as a measure for the resistance of PE-HD against crack propagation induced by a craze-crack mechanism. FNCT specimens are notched prior to testing to avoid the influence of crack initiation. Therefore, the FNCT is the method of choice to address SCG phenomena that result from low mechanical stresses. SCG is influenced by the physico-chemical characteristics of external fluids, which can also be addressed in FNCT. In this study, a multi-station FNCT device was used which allowed for separate control of stress and temperature. The device is designed for the application of different test fluids including organic and dangerous liquids. Furthermore, the elongation of specimens was continuously recorded during FNCT. To assess the influences of environmental fluids including air, water, surfactant (detergent) solutions and organic liquids (sorbents) on the SCG induced by the craze-crack mechanism in more detail, an enhanced FNCT fracture surface analysis was performed. Therefore, light microscopy (LM), laser scanning microscopy (LSM) and scanning electron microscopy (SEM) were used. Moreover, the FNCT was evaluated critically as test method for SCG.

The FNCT results show significant differences of the crack propagation in PE-HD container materials that depend on the different external fluids. The ranking of FNCT t_f^* with respect to the fluids tested was:

$$t_{f,\,air}^* > t_{f,\,water}^* > t_{f,\,detergents}^* > t_{f,\,biodiesel}^* > t_{f,\,diesel}^*.$$

The reduction of t_f^* depends on both, (i) the surface tension of the fluids and (ii) their sorption behavior. Consequently, the effect of t_f^* reduction of environmental fluids in contact with PE-HD results from the reduction of energy required to create new internal surfaces during the craze formation in the craze-crack mechanism. This is based on the reduction of interfacial energy and surface tension (detergents) and the additional reduction of the forces between polymer chains (sorptive fluids). Based thereon, the fluids are categorized according to their effect on PE-HD in (i) inert (air), (ii) surface-active (water, detergents) and (iii) sorptive bulk-active (biodiesel, diesel). In addition to the reduction of interfacial energy, plasticization effects lead to a facilitated disentanglement of polymer chains which results in the premature failure of fibrils in bulk-active fluids and an accelerated crack propagation. This effect depends on the amount of fluid absorbed by PE-HD (equilibrium sorption behavior of PE-HD). Considering partly saturated FNCT specimens and the results of Bell telephone testing (BTT), a temporary blunting effect was unveiled that occurs to PE-HD in sorptive bulk-active fluids. According to that, the crack tip is blunted due to the incorporation of a small amount of bulk-active liquid within the zone of plastic deformation which reduces the effective stress at the crack tip. Only after a certain sorption degree is reached, bulk-active fluids plasticize the PE-HD to an extent which leads to facilitated crazing and crack growth. In terms of practical testing, n-butyl acetate (NB) was identified to be a suitable standard fluid to simulate the effects of bulk-active fluids to PE-HD since it evoked a crack propagation and sorption behavior similar to biodiesel and diesel.

Differences in crack propagation and fracture behavior of the PE-HD types that depend on the fluids were confirmed by FNCT fracture surfaces analysis performed by LM, LSM and SEM. From LM and LSM, globally brittle fracture surfaces were obtained in all fluids with differences in the characteristic of their fracture surface features. In this respect, fracture surfaces obtained by FNCT in (1) air/water, (2) detergent and (3) biodiesel/diesel/NB could be differentiated. Based on SEM micrographs, periodic characteristic structures in the order of magnitude of 50 µm were identified

which indicate locally ductile fracture. However, these structures are related to 'macroscopic brittle fracture' in the order of magnitude of approx. 500 µm. This is regarded as 'pseudo-brittle' in distinction to 'truly brittle' fracture surfaces typically resulting from rapid crack propagation (RCP). Since it can be assumed that every fibril experiences a sort of tensile test during craze-crack mechanism, the appearance of locally ductile fracture structures can be expected. Due to the small size of relaxed fibrils after fracture, the resulting surfaces exhibit macroscopically (LM, LSM length scale) brittle character but a microscopically (SEM length scale) lawn-like structure. These microscopic lawn-like surface structures are directly related to crack growth and can be used as an indicator for the craze-crack damage mechanism. In contrast, macroscopically ductile fracture behavior represents the damage mechanism of shear deformation. Since the progressive reduction of residual area during FNCT leads to a continuous increase in local mechanical stress, a transition from SCG (pseudo-brittle) to shear deformation (ductile) has to be expected from the rim to the center of the specimen. Therefore, the innermost part of an FNCT fracture surfaces is always ductile in nature. Since FNCT results are only justified by definition when craze-crack (SCG) is the dominating damage mechanism, fracture surfaces have to be predominantly pseudo-brittle in order to follow the specifications in the test standard. Due to the swelling and plasticizing effect of sorptive bulk-active fluids, the corresponding fracture surfaces show distinct differences in LM/LSM and SEM compared to non-sorptive fluids: A pillow-like structure occurs in LM/LSM and instead of lawn-like, platelet-like surface structures are observed in SEM. This is attributed to fractured fibrils that collapse and lie flat on the resulting fracture surface. In consequence of the sorption behavior of PE-HD, fracture surface areas are submerged by the fluid and appear as platelet-like structures. These appear as pillow-like superstructures on a higher length scale in LM and LSM. Since macroscopically pseudo-brittle fracture surfaces are obtained, the craze-crack mechanism is assumed to be the dominating damage effect for bulk-active fluids.

Moreover, the effects of different fluids concerning t_f* and fracture surface appearances could be related to the FNCT elongation (e.g. the maximum elongation d_{fail}). Thus, the elongation is identified to be an additional indicator of crack propagation during FNCT. Accordingly, the fracture behavior of FNCT specimens can be estimated from elongation data.

Based on the FNCT results, a novel scheme of damage mechanisms that occur to PE-HD due to both, mechanical stress levels and the influence of environmental fluids, is proposed. This comprises the categorization of fluids according to their damage effects to PE-HD. The scheme involves a clarification of terminology for the description of damage mechanisms. In this respect, the term 'basic stress cracking (BSC)' is introduced, which refers to crack growth induced by inert (air) and surface-active (water) fluids that accelerate the FNCT without a change in the t_f* ranking of PE-HD types (called 'neutrally accelerating'). This term is especially intended to allow for a differentiation to the 'environmental stress cracking (ESC)', which occurs to PE-HD in surface-active, irregular accelerating (detergents) and bulk-active (oils, solvents) fluids. Therefore, BSC behavior can be regarded as an intrinsic property of a polymer, whereas the fluid in contact is necessary for the occurrence of ESC. A change in crack growth induced by a surrounding fluid can be a pure surface (detergent, surfactant solutions) or an additional bulk (sorptive fluids) effect. Hence, BSC and ESC refer to the superordinate category slow crack growth (SCG) and the fluid taking effect on PE-HD.

Besides differences in FNCT depending on the environmental fluids, variations in SCG behavior that depend on the PE-HD type were found. A lower density, crystallinity and α relaxation temperature as well as a higher molecular mass lead to higher FNCT t_f*. This trend is less prominent in sorptive bulk-active fluids. Since no distinct correlation of the amorphous and crystalline fractions in PE-HD to t_f* was found, an influence of the rigid amorphous phase and the number of tie-molecules is assumed. Therefore, the rigid amorphous phase and the mobility of

polymer chains strongly influence crack propagation. Furthermore, the superstructure of mono-, bi- or multimodal PE-HD types depends on the polymerization process (gas phase, loop process, cascade process), the applied comonomers (butene, hexene) and their distribution (tie-molecules). Therefore, differences in crack growth and fracture behavior that depend on the PE-HD type are ascribed to the technical polymerization processes and the resulting crystalline superstructures.

From an enhanced FNCT fracture surface analysis using LM, LSM, SEM, scanning acoustic microscopy (SAM) and computed X-ray tomography (CT), crack lengths and crack growth rates during FNCT were obtained in more detail. The differences in crack growth induced by different fluids were confirmed. Furthermore, a significant difference was found between damaged and undamaged areas obtained from the optical methods applied on the free fracture surfaces (LM, LSM) and the non-destructive imaging techniques (SAM, CT). Therefrom, an increasing length of craze zone R_{craze} with a progressively propagating crack (length c) was revealed. This was confirmed by fracture mechanic considerations which resulted in: $R_{craze} \propto c$.

Hence, a PE-HD specimen which shows a propagating crack, is also damaged by crazing of the uncracked region (pseudo-intact) to an equivalent extent. This assumption is supported by fracture surface features. The actual mechanical stress taking effect on the residual ligament area of the specimen was related to the resulting fracture surface features and to the course of the FNCT. In this respect, the yield strength of the PE-HD type as measured in a tensile test at the specific temperature was identified as the value of actual stress required to induce final specimen failure during FNCT. Hence, when an actual stress as high as the yield strength is reached due to the decrease of the residual ligament area induced by the craze-crack mechanism, the residual bulk material will fail entirely by shear deformation. The latter results in the occurrence of an extended central ligament on the fracture surface.

Moreover, crack and craze lengths can be related to FNCT elongation. This confirms the FNCT elongation to be a feasible additional indicator for an early damage estimation of PE-HD. The FNCT elongation can also be regarded as an additional indicator of the crack growth rate. This is especially advantageous in FNCT quality control processes. Nevertheless, the FNCT is supposed to be performed until entire specimen failure. The indicator might especially be helpful for testing of high-performance PE-HD types, for which conventional conditions result in test durations longer than 1000 h.

As a major result obtained from this study, the course of crack growth and failure during an individual FNCT experiment is described for the first time: At the beginning of the FNCT, a low mechanical stress is subjected to the entire cross section of the specimen (low global stress). However, a higher stress is induced locally at the notch tip due to its geometry. At this point, the voiding mechanism starts, i.e. cavities and fibrils ('crazes') are formed. After this, the local stress that acts on the single fibrils in the craze zone is further increased. As a result, the fibrils become constantly smaller due to necking and furthermore, cavities grow and coalesce. Subsequently, the local stress subjected to the first fibrils becomes too high, they fail, and crack growth starts. Consistently, these fibrils fail locally ductile as detectable in SEM since they individually passed a sort of tensile test. When crack growth started, the global stress is increased due to the associated reduction of the residual cross section of the entire specimen. In further consequence, this process of craze formation, cracking and the increase of the global stress is constantly advancing. During the constant craze-crack growth, the craze and crack zones grow simultaneously and in a linear relation to each other. When the global stress reaches the yield strength of the PE-HD material, the craze-crack growth is stopped, and it is transitioned into global shear deformation. Since crazed zones are

already present in the 'pseudo-intact' region of the specimen, these zones are subjected to shear deformation in the bulk just in the same way as residual undamaged cross-sectional parts. The fibrils in the previously crazed zones also fail due to shear deformation, which results in the occurrence of ductile fracture surface parts (central ligament). Furthermore, ductile fracture surface parts that resulted from bulk shear deformation of crazed regions can even be distinguished from those of previously undamaged zones.

In sorptive bulk-active fluids, an unexpected type of fracture surface features occurs: although the bulk of previously crazed regions is also affected by shear deformation, crazed regions can optically not be assigned to the central ligament after final failure. In contrast, their failure results in the occurrence of a macroscopically pillow-like plateau structure on the fracture surface. Based on these results, the fibrils might hypothetically finally fail almost simultaneously due to their plasticization. Furthermore, the yield strength of the PE-HD material is decreased as a result of plasticization in sorptive bulk-active fluids. Therefore, the global stress required to induce final failure (transition from region II to III in time-resolved elongation curve) is reached faster during such an FNCT. Accordingly, the lengths of the cracked and crazed zones that were formed until the transition into shear deformation are smaller in sorptive compared to non-sorptive fluids under the same initial loading conditions (e.g. a typical initial global stress of 9 MPa). Besides, a classic central ligament also occurs from shear deformed previously undamaged bulk material. Since crazed and cracked regions are still dominant on the fracture surface, the significance of the FNCT with respect to the craze-crack mechanism is confirmed for sorptive bulk-active fluids. However, an FNCT in sorptive bulk-active fluids might not be directly comparable to a conventional FNCT (e.g. performed in surfactant solutions). The initial global stress might have to be adjusted appropriately to ensure the predominant occurrence of crazing and cracking instead of shear deformation of undamaged bulk material.

An approach to an enhanced analysis of the FNCT in sorptive bulk-active fluids can be deduced from the previous considerations: if the time to failure was related to the actual crack length (obtained by measuring the corresponding parts on the fracture surface), a specific actual crack growth rate could be derived. Such specific crack growth rates can be compared for a sophisticated assessment of the SCG behavior of different PE-HD types in different fluids. The incorporation of such an analysis procedure into routine testing remains to be done.

Based on the understanding of damage mechanisms in PE-HD, the FNCT was evaluated in terms of time efficiency and significance for the assessment of SCG. Furthermore, it was sought to be improved within practically relevant limits which are easily realizable. Therefore, stress-dependent, temperature-dependent and specimen geometry-dependent FNCT series were performed. A variation of FNCT specimen geometry led to longer test durations (RNCT increased t_f* by a factor of approx. 3.6 compared to FNCT) or a higher portion of ductile fracture surfaces features (DNCT compared to FNCT) indicating the predominant occurrence of shear deformation instead of SCG. Thus, different specimen geometries are not adequate to improve the FNCT. Higher test temperatures reduce t_f* but also result in a change of damage mechanism, which is confirmed by fracture surface analysis. Hence, test temperatures have to be selected with due care. Especially, FNCT t_f* results should be compared only when they were obtained by using equal test temperatures (no interpolation). From stress-dependent FNCT series, distinct differences in fracture behavior and fracture surface features of PE-HD were revealed. The higher the initial mechanical stress applied to FNCT specimens, the more ductile fracture surface features are obtained.

Since the occurrence of predominantly pseudo-brittle fracture is the typical prerequisite to consider the FNCT as representative for SCG, a distinct FNCT is only regarded as evaluable ('valid') in practical testing if a predominantly pseudo-brittle fracture surface is obtained. Therefore, an easy-to-

operate criterion was developed to assess fracture surfaces with respect to their brittleness. This is based on LSM roughness data. Such a criterion is a practical tool usable in test routines to verify FNCT results according to their significance with respect to the craze-crack mechanism, especially if the brittle-ductile transition is not determinable by classic methods (e.g. by considering the 'knee' in the stress-t_f curve). Since the criterion developed in this study is based on a small number of PE-HD types, this is a first proposal and its validation is required for a broader variety of materials and test fluids. However, the enhanced fracture surface analysis developed in this study is a valuable tool for a detailed evaluation of the FNCT and further methodological improvements, especially addressing sorptive bulk-active fluids such as biodiesel and diesel.

7. Literature

[1] W. Schatt, Einführung in die Werkstoffwissenschaft, 5. Auflage, Deutscher Verlag für Grundstoffindustrie, Leipzig, 1984.

[2] A. Ghanbari-Siahkali, P. Kingshott, D.W. Breiby, L. Arleth, C.K. Kjellander, K. Almdal, Investigating the role of anionic surfactant and polymer morphology on the environmental stress cracking (ESC) of high-density polyethylene, Polym. Degrad. Stab., 89 (2005) 442-453.

[3] R.A.C. Deblieck, D.J.M. van Beek, K. Remerie, I.M. Ward, Failure mechanisms in polyolefines: The role of crazing, shear yielding and the entanglement network, Polymer, 52 (2011) 2979-2990.

[4] J.M. Lagarón, J.M. Pastor, B.J. Kip, Role of an active environment of use in an environmental stress crack resistance (ESCR) test in stretched polyethylene: A vibrational spectroscopy and a SEM study, Polymer, 40 (1999) 1629-1636.

[5] A. Lustiger, R.L. Markham, Importance of tie molecules in preventing polyethylene fracture under long-term loading conditions, Polymer, 24 (1983) 1647-1654.

[6] N. Pons, A. Bergeret, J.C. Benezet, L. Ferry, F. Fesquet, An Environmental Stress Cracking (ESC) test to study the ageing of biopolymers and biocomposites, Polym. Test., 30 (2011) 310-317.

[7] A.L. Ward, X. Lu, Y. Huang, N. Brown, The mechanism of slow crack growth in polyethylene by an environmental stress cracking agent, Polymer, 32 (1991) 2172-2178.

[8] J.J. Cheng, M.A. Polak, A. Penlidis, Influence of micromolecular structure on environmental stress cracking resistance of high density polyethylene, Tunn. Undergr. Space Tec., 26 (2011) 582-593.

[9] D.C. Wright, Environmental stress cracking of plastics, Rapra Techology Ltd., Shawbury (UK), 1996.

[10] G. Menges, Das Verhalten von Kunststoffen unter Dehnung, Kunststoffe, 63 (1973) 95-100.

[11] N. Brown, X. Lu, A fundamental theory for slow crack growth in polyethylene, Polymer, 36 (1995) 543-548.

[12] M.K.V. Chan, J.G. Williams, Slow stable crack growth in high density polyethylenes, Polymer, 24 (1983) 234-244.

[13] ISO 16770:2004 - Plastics - Determination of environmental stress cracking (ESC) of polyethylene - Full-notch creep test (FNCT), 2004.

[14] L.M. Robeson, Environmental stress cracking: A review, Polym. Eng. Sci., 53 (2013) 453-467.

[15] J.-W. Wee, Y. Zhao, B.-H. Choi, Observation and modeling of environmental stress cracking behaviors of high crystalline polypropylene due to scent oils, Polym. Test., 48 (2015) 206-214.

[16] P.C. Paris, M.P. Gomez, W.E. Anderson, A rational analytic theory of fatigue, The trend in engineering, 13 (1961) 9-14.

[17] M. Fleissner, Experience with a full notch creep test in determining the stress crack performance of polyethylenes, Polym. Eng. Sci., 38 (1998) 330-340.

[18] W.D. Callister, Fundamentals of materials science and engineering, interactive e-text, Wiley Print, New York (2001).

[19] W.B. Jensen, The origin of the polymer concept, J. Chem. Educ., 85 (2008) 624-625.

[20] H. Staudinger, Über Polymerisation, Berichte der deutschen chemischen Gesellschaft (A and B Series), 53 (1920) 1073-1085.

[21] A.D. Jenkins, Contemporary polymer chemistry (3rd edition), HR Allcock, FW Lampe and JE Mark. Pearson Education, Inc (Pearson/Prentice Hall), Upper Saddle River, NJ, USA, 2003, ISBN 0-13-065056-0 pp 18 + 814, Polym. Int., 53 (2004) 1395-1395.

[22] Consultic Marketing, Produktion, Verarbeitung und Verwertung von Kunststoffen in Deutschland 2015, ed.: BKV GmbH, PlasticsEurope, IK Industrievereinigung, VDMA, bvse-Bundesverband Sekundärrohstoffe, Alzenau (2016).

[23] R. Geyer, J.R. Jambeck, K.L. Law, Production, use, and fate of all plastics ever made, Sci. Adv., 3 (2017) 5.

[24] PlasticsEurope Market Research Group (PEMRG), Conversio Market & Strategy GmbH, Plastics – the facts 2017, PlasticsEurope, Brussels, Belgium (2017).

[25] G. Natta, G. Allegra, P. Corradini, Different crystalline modifications of TiCl3, a catalyst component for polymerization of alpha-olefins .1. alpha-, beta-, gamma- TiCl3 .2. delta- TiCl3, J. Polym. Sci., 51 (1961) 399.

[26] G. Natta, A. Zambelli, I. Pasquon, Stereospecific catalysts for head-to-tail polymerization of propylene to a crystalline syndiotactic polymer, J. Am. Chem. Soc., 84 (1962) 1488.

[27] T.E. Nowlin, R.I. Mink, Y.V. Kissin, Supported Magnesium/Titanium-Based Ziegler Catalysts for Production of Polyethylene, in: R. Hoff, R.T. Mathers (Eds.) Handbook of Transition Metal Polymerization Catalysts, 2010.

[28] I.M. Ward, J. Sweeney, Mechanical properties of solid polymers, 3rd edition, John Wiley & Sons Ltd., Chichester (2013), ISBN: 978-1-4443-1950-7.

[29] M. Rubinstein, R.H. Colby, Polymer Physics, Oxford University Press Inc., New York (2003), ISBN: 978-0-19-852059-7.

[30] H. Beerbaum, Ermittlung strukturbezogener bruchmechanischer Werkstoffkenngrößen an Polyethylen-Werkstoffen, Mathematisch-Naturwissenschaftlich-Technische Fakultät, Martin-Luther-Universität Halle-Wittenberg (1999) pp. 193.

[31] J.M.B. Sanders, Techniques to Determine the Remaining In-Service Life of Polymer Pipes for the Water Industry, Mechanical Engineering, Imperial College London (2010).

[32] W. Keim, Kunststoffe: Synthese, Herstellungsverfahren, Apparaturen, Wiley-VCH, Weinheim (2012), ISBN: 978-3-527-66039-1.

[33] J. Lehotay, J. Danecek, O. Liska, J. Lesko, E. Brandsteterova, Analytical study of the additives system in polyethylene, J. Appl. Polym. Sci., 25 (1980) 1943-1950.

[34] J.M. Howard, Gel permeation chromatography and polymer additive systems, J. Chromatogr., 55 (1971) 15 et seqq.

[35] A.M. Wims, S.J. Swarin, Determination of antioxidants in polypropylene by liquid-chromatography, J. Appl. Polym. Sci., 19 (1975) 1243-1256.

[36] I. Chodak, A. Romanov, M. Ratzsch, G. Haudel, influence of the additives on polyethylene crosslinking initiated by peroxides, Acta Polym., 38 (1987) 672-674.

[37] C.W. Bunn, The crystal structure of long-chain normal paraffin hydrocarbons - The "shape" of the CH_2 group, Trans. Faraday Soc., 35 (1939) 0482-0490.

[38] J.I. Lauritzen, J.D. Hoffman, Theory of formation of polymer crystals with folded chains in dilute solution, Journal of Research of the National Bureau of Standards Section a-Physics and Chemistry, 64 (1960) 73-102.

[39] D.M. Sadler, G.H. Gilmer, A model for chain folding in polymer crystals - rough growth faces are consistent with the observed growth-rates, Polymer, 25 (1984) 1446-1452.

[40] J.J. Cheng, M.A. Polak, A. Penlidis, Phase Interconnectivity and Environmental Stress Cracking Resistance of Polyethylene: A Crystalline Phase Investigation, J. Macromol. Sci., Part A: Pure Appl. Chem., 46 (2009) 572-583.

[41] G.H. Michler, Electron Microscopy of Polymers, Springer, Berlin, Heidelberg (2008), ISBN: 978-3-540-36350-7.

[42] N. Brown, X.C. Lu, Y.L. Huang, R.Z. Qian, Slow crack-growth in polyethylene - a review, Makromolekulare Chemie-Macromolecular Symposia, 41 (1991) 55-67.

[43] N. Alberola, J.Y. Cavaille, J. Perez, Mechanical-gamma and beta-relaxations in polyethylene .1. glass transitions of polyethylene, Eur. Polym. J., 28 (1992) 935-948.

[44] UBA – Umweltbundesamt, Untersuchungen der Umweltwirkungen von Verpackungen aus biologisch abbaubaren Kunststoffen, Umweltforschungsplan des Bundesministeriums für Umwelt, Naturschutz und Reaktorsicherheit Deutschland, Texte, 52 (2012).

[45] Consultic Marketing, Produktion, Verarbeitung und Verwertung von Kunststoffen in Deutschland 2015, ed.: BKV GmbH, PlasticsEurope, IK Industrievereinigung, VDMA, bvse-Bundesverband Sekundärrohstoffe, Alzenau (2016).

[46] Solubility, IUPAC Compendium of Chemical Terminology, 2nd ed. (the 'Gold Book'), compiled by A. D. McNaught, A. Wilkinson, Blackwell Scientific Publications, Oxford (1997), DOI: 10.1351/goldbook.S05740.

[47] C. Reichardt, Pyridinium N-phenolate betaine dyes as empirical indicators of solvent polarity: Some new findings, Pure and Applied Chemistry 76 ,10 (2004) 1903-1919.

[48] J. Crank, The mathematics of diffusion, 2nd edition, Clarendon Press, Oxford, England, 1975.

[49] W. Henry, III. Experiments on the quantity of gases absorbed by water, at different temperatures, and under different pressures, Philos. Trans. R. Soc. Lon., 93 (1803) 29-274.

[50] T.C. Merkel, V.I. Bondar, K. Nagai, B.D. Freeman, I. Pinnau, Gas sorption, diffusion, and permeation in poly(dimethylsiloxane), J. Polym. Sci., Part B: Polym. Phys., 38 (2000) 415-434.

[51] K. Ghosal, B.D. Freeman, Gas separation using polymer membranes: an overview, Polym. Adv. Technol., 5 (1994) 673-697.

[52] R. Sander, Compilation of Henry's law constants (version 4.0) for water as solvent, Atmos. Chem. Phys., 15 (2015) 4399-4981.

[53] M. Böhning, U. Niebergall, A. Adam, W. Stark, Impact of biodiesel sorption on mechanical properties of polyethylene, Polym. Test., 34 (2014) 17-24.

[54] T. Alfrey, E.F. Gurnee, W.G. Lloyd, Diffusion in glassy polymers, J. Polym. Sci., Part C: Polym. Sym. 12PC, (1966) pp. 249 et seqq.

[55] W. Grellmann, S. Seidler, Deformation and fracture behaviour of polymers, Springer series engineering materials, Berlin, Heidelberg, Springer-Verlag, New York (2001), ISBN: 3-540-41247-6.

[56] H-H. Kausch, Polymer fracture, 2nd Ed., Springer-Verlag, Berlin (1987), ISBN: 978-3-642-96460-2.

[57] R.P. Kambour, A Review of Crazing and Fracture in Thermoplastics, J. Pol. Sci. Macrom. Rev., 7 (1973) 1-154.

[58] A.M. Donald, E.J. Kramer, The mechanism for craze-tip advance in glassy-polymers, Philos. Mag. A-Phys. Condens. Matter Struct. Defect Mech. Prop., 43 (1981) 857-870.

[59] A.M. Donald, E.J. Kramer, R.A. Bubeck, The entanglement network and craze micromechanics in glassy-polymers, J. Polym. Sci., Part B: Polym. Phys., 20 (1982) 1129-1141.

[60] E.J. Kramer, Microscopic and molecular fundamentals of crazing, Adv. Polym. Sci., 52-3 (1983) 1-56.

[61] H.G.H. van Melick, L.E. Govaert, H.E.H. Meijer, On the origin of strain hardening in glassy polymers, Polymer, 44 (2003) 2493-2502.

[62] W.W. Müller, HDPE Geomembranes in Geotechnics, Springer, Berlin 2007, ch.3.2 and ch. 5.7.

[63] A.S. Argon, Physical basis of distortional and dilatational plastic-flow in glassy polymers, J. Macromol. Sci.-Phys., B 8 (1973) 573-596.

[64] A.S. Argon, Theory for low-temperature plastic-deformation of glassy polymers, Philos. Mag., 28 (1973) 839-865.

[65] C. Thomas, V. Ferreiro, G. Coulon, R. Seguela, In situ AFM investigation of crazing in polybutene spherulites under tensile drawing, Polymer, 48 (2007) 6041-6048.

[66] R. Qian, X. Lu, N. Brown, Investigating the existence of a threshold stress intensity for slow crack-growth in high-density polyethylene, J. Mater. Sci., 24 (1989) 2467-2472.

[67] M. Böhning, U. Niebergall, A. Adam, W. Stark, Influence of biodiesel sorption on temperature-dependent impact properties of polyethylene, Polym. Test., 40 (2014) 133-142.

[68] E. Nezbedova, P. Hutar, M. Zouhar, Z. Knesl, J. Sadilek, L. Nahlik, The applicability of the Pennsylvania Notch Test for a new generation of PE pipe grades, Polym. Test., 32 (2013) 106-114.

[69] J.J. Cheng, M.A. Polak, A. Penlidis, Phase Interconnectivity and Environmental Stress Cracking Resistance of Polyethylene: A Crystalline Phase Investigation, J. Macromol. Sci., Part A: Pure Appl. Chem., 46 (2009) 572-583.

[70] Y.L. Huang, N. Brown, Dependence of slow crack-growth in polyethylene on butyl branch density - morphology and theory, J. Polym. Sci., Part B: Polym. Phys., 29 (1991) 129-137.

[71] Y.L. Huang, N. Brown, The dependence of butyl branch density on slow crack-growth in polyethylene - kinetics, J. Polym. Sci., Part B: Polym. Phys., 28 (1990) 2007-2021.

[72] Y.L. Huang, N. Brown, The effect of molecular-weight on slow crack-growth in linear polyethylene homopolymers, J. Mater. Sci., 23 (1988) 3648-3655.

[73] X.C. Lu, N. Ishikawa, N. Brown, The critical molecular weight for resisting slow crack growth in a polyethylene, J. Polym. Sci., Part B: Polym. Phys., 34 (1996) 1809-1813.

[74] ISO 1167-1:2006 - Thermoplastics pipes, fittings and assemblies for the conveyance of fluids - Determination of the resistance to internal pressure - Part 1: General method; German version, 2006.

[75] ISO 1167-2:2006 - Thermoplastics pipes, fittings and assemblies for the conveyance of fluids - Determination of the resistance to internal pressure - Part 2: Preparation of pipe test pieces; German version, 2006.

[76] ISO 9080:2012 - Plastics piping and ducting systems - Determination of the long-term hydrostatic strength of thermoplastics materials in pipe form by extrapolation; German version, 2012.

[77] R.P. Brown, Testing plastics for resistance to environmental-stress cracking, Polym. Test., 1 (1980) 267-282.

[78] R. Ayyer, A. Hiltner, E. Baer, Effect of an environmental stress cracking agent on the mechanism of fatigue and creep in polyethylene, J. Mater. Sci., 43 (2008) 6238-6253.

[79] H.R. Brown, A theory of the environmental stress cracking of polyethylene, Polymer, 19 (1978) 1186-1188.

[80] A.A. Griffith, The phenomena of rupture and flow in solids, Philos. Trans. R. Soc., 221, 163 (1921).

[81] J.J. Benbow, F.C. Roesler, Experiments on controlled fractures, Proc. Phys. Soc. Lon., Sec. B, 70 (1957) pp. 201 et seqq.

[82] J.P. Berry, Determination of fracture surface energies by cleavage technique, J. Appl. Phys., 34 (1963) 62 et seqq.

[83] J.J. Benbow, Stable crack propagation in plastics, Proc. Phys. Soc. Lon., 78 (1961) pp. 970 et seqq.

[84] G. R. Irwin, Analysis of Stresses and Strains near the End of a Crack Traversing a Plate, J. Appl. Mech. Tran. ASME, 24 (1957) pp. 351-369.

[85] E. Orowan, Surface energy and surface tension in solids and liquids, Proc. R. Soc. Lon., Ser. A: Math. Phys. Sci., 316 (1970) 473 et seqq.

[86] N.H. Macmillan, A. Kelly, Relationship between ideal tensile-strength and surface-energy, Mat. Sci. Eng., 10 (1972) 139 et seqq.

[87] E.H. Andrews, Fracture mechanics approach to corrosion stress cracking in plastics, Proc. Conf. Phys. Yield Fract., Institute of Physics & The Physical Society London, Oxford (1966) pp. 127 et seqq.

[88] R.P. Kambour, Structure and properties of crazes in polycarbonate and other glassy polymers, Polym., 5 (1964) 143-155.

[89] R.P. Kambour, Mechanism of fracture in glassy polymers .3. Direct observation of craze ahead of propagating crack in poly(methyl methacrylate) and polystyrene, J. Polym. Sci., Part A-2: Polym. Phys., 4 (1966) pp. 349 et seqq.

[90] D.S. Dugdale, Yielding of steel sheets containing slits, J. Mech. Phys. Solids, 8 (1960) 100-104.

[91] J.R. Rice, Fracture - An Advanced Treatise, Academic Press, New York, 1968.

[92] J.R. Rice, A path independent integral and approximate analysis of strain concentration by notches and cracks, J. Appl. Mech., 35 (1968) 379 et seqq.

[93] M.K.V. Chan, J.G. Williams, J-integral studies of crack initiation of a tough high-density polyethylene, Int. J. Fract., 23 (1983) 145-159.

[94] Y.W. Mai, B. Cotterell, On the essential work of ductile fracture in polymers, Int. J. Fract., 32 (1986) 105-125.

[95] J.S. Wu, Y.W. Mai, The essential fracture work concept for toughness measurement of ductile polymers, Polym. Eng. Sci., 36 (1996) 2275-2288.

[96] J.G. Williams, M. Rink, The standardisation of the EWF test, Eng. Fract. Mech., 74 (2007) 1009-1017.

[97] J.B. DeCoste, F.S. Malm, V.T. Wallder, Cracking of Stressed Polyethylene, Ind. Eng. Chem., 43 (1951) 117-121.

[98] R.P. Brown, Testing plastics for resistance to environmental-stress cracking, Polym. Test., 1 (1980) 267-282.

[99] ASTM D1693:2012 – Standard test method for environmental stress-cracking of ethylene plastics, 2012.

[100] ISO 13274:2014 – Packaging – Transport packaging for dangerous goods – Plastics compatibility testing for packaging and IBCs; German version, 2014.

[101] H. Zanziger, I.D. Peggs, Stress cracking resistance of HDPE geomembranes with very high densities, Conference Paper GhlGS GeoAfr., (2013) 1-11.

[102] ISO 22088-3:2006 – Plastics – Determination of resistance to encvironmental stress cracking (ESC) – Part 3: Bent strip method; German version, 2006.

[103] ISO 22088-4:2006 – Plastics – Determination of resistance to encvironmental stress cracking (ESC) – Part 4: Ball or pin impression method; German version, 2006.

[104] ISO 16241:2005 – Notch tensile test to measure the resistance to slow crack growth of polyethylene materials for pipe and fitting products (PENT), 2005.

[105] ASTM F1473:2016 – Standard test method for notch tensile test to measure the resistance to slow crack growth of polyethylene pipes and resins, 2016.

[106] ASTM D5397:2007 – Standard test method for evaluation of stress crack resistance of polyolefin geomembranes using notched constant tensile load test (NCTL), 2007.

[107] N. Nishio, S. Iimura, M. Yasuhara, F. Nagatani, 9th Plastic Gas Pipe Symposium, (1985) 29.

[108] M. Fleissner, Experience with a full notch creep test in determining the stress crack performance of polyethylenes, Polym. Eng. Sci., 38 (1998) 330-340.

[109] H.R. Brown, A theory of the environmental stress cracking of polyethylene, Polymer, 19 (1978) 1186-1188.

[110] X.C. Lu, X.Q. Wang, N. Brown, Slow fracture in a homopolymer and copolymer of polyethylene, J. Mater. Sci., 23 (1988) 643-648.

[111] ISO 1872-2:2007 – Plastics – Polyethylene (PE) molding and extrusion materials – Part 2: Preparation of test specimens and determination of properties; German version, 2007.

[112] ISO 293:2005 – Plastics – Compression molding of test specimens of thermoplastic materials; German version, 2005.

[113] ISO 17855-2:2014 – Plastics – Polyethylene (PE) molding and extrusion materials – Part 2: Preparation of test specimens and determination of properties; German version, 2015.

[114] G. Pinter, M. Haager, W. Balika, R.W. Lang, Cyclic crack growth tests with CRB specimens for the evaluation of the long-term performance of PE pipe grades, Polym. Test., 26 (2007) 180-188.

[115] ISO 18489:2016 – Polyethylene (PE) materials for piping systems – Determination of resistance to slow crack growth under cyclic loading – Cracked round bar test method, 2016.

[116] T.R. Kratochvilla, A. Frank, G. Pinter, Determination of slow crack growth behaviour of polyethylene pressure pipes with cracked round bar test, Polym. Test., 40 (2014) 299-303.

[117] ISO 13479:2009 – Polyolefin Pipes for the Conveyance of Fluids – Determination of Resistance to Crack Propagation – Test Method for Slow Crack Growth on Notched Pipes, 2009.

[118] ISO 179-1:2010 – Plastics – Determination of Charpy impact properties – Part 1: Non-instrumented impact test; German version, 2010.

[119] ISO 179-2:2012 – Plastics – Determination of Charpy impact properties – Part 2: Instrumented impact test; German version, 2012.

[120] A. Frank, G. Pinter, Evaluation of the applicability of the cracked round bar test as standardized PE-pipe ranking tool, Polym. Test., 33 (2014) 161-171.

[121] L. Kurelec, M. Teeuwen, H. Schoffeleers, R. Deblieck, Strain hardening modulus as a measure of environmental stress crack resistance of high density polyethylene, Polymer, 46 (2005) 6369-6379.

[122] ISO 18488:2015 – Polyethylene (PE) materials for piping systems – Determination of Strain Hardening Modulus in relation to slow crack growth – Test method, 2015.

[123] ISO 527-2:2012 – Plastics – Determination of tensile properties – Part 2: Test conditions for molding and extrusion plastics; German version, 2012.

[124] D.J.M. Van Beek, R. Deblieck, Strain hardening: An elegant and fast method to predict the slow crack growth behavior of HDPE pipe materials, Soc. Plast. Eng. - EUROTEC 2011 Conference Proceedings (2011).

[125] R.N. Haward, G. Thackray, Use of a mathematical model to describe isothermal stress-strain curves in glassy thermoplastics, Proc. R. Soc. Lon., Ser A: Math. Phys. Sci., 302 (1968) pp. 453 et seqq.

[126] R.N. Haward, Strain hardening of high density polyethylene, J. Polym. Sci., Part B: Polym. Phys., 45 (2007) 1090-1099.

[127] M.O. Robbins, R.S. Hoy, Scaling of the Strain Hardening Modulus of Glassy Polymers with the Flow Stress, J. Polym. Sci., Part B: Polym. Phys., 47 (2009) 1406-1411.

[128] L.E. Govaert, T.A.P. Engels, M. Wendlandt, T.A. Tervoort, U.W. Suter, Does the Strain Hardening Modulus of Glassy Polymers Scale with the Flow Stress, J. Polym. Sci., Part B: Polym. Phys., 46 (2008) 2475-2481.

[129] P. Duffo, B. Monasse, J.M. Haudin, C. Gsell, A. Dahoun, Rheology of polypropylene in the solid-state, J. Mater. Sci., 30 (1995) 701-711.

[130] J. Fawaz, S. Deveci, V. Mittal, Molecular and morphological studies to understand slow crack growth (SCG) of polyethylene, Colloid Polym. Sci., 294 (2016) 1269-1280.

[131] P. Sardashti, C. Tzoganakis, M.A. Polak, A. Penlidis, Improvement of Hardening Stiffness Test as an Indicator of Environmental Stress Cracking Resistance of Polyethylene, J. Macromol. Sci., Part A: Pure Appl. Chem., 49 (2012) 689-698.

[132] R.E. Robertson, Polymer order and polymer density, J. Phys. Chem., 69 (1965) pp. 1575 et seqq.

[133] ASTM D971:2012 – Standard test method for interfacial tension of oil against water by the ring method, 2012.

[134] P. Lecomte du Noüy, An interfacial tensiometer for universal use, J. Gen. Physiol., 7 (1925) 625-653.

[135] C. Huh, S.G. Mason, A rigorous theory of ring tensiometry, Colloid Polym. Sci., 253 (1975) 566-580.

[136] G. Lu, X.-D. Wang, Y.-Y. Duan, A Critical Review of Dynamic Wetting by Complex Fluids: From Newtonian Fluids to Non-Newtonian Fluids and Nanofluids, Adv. Colloid Interface Sci., 236 (2016) 43-62.

[137] W. Schmidt, Optische Spektroskopie, 2. Ed., Wiley-VCH, Weinheim (2014), ISBN: 978-3-527-29828-0.

[138] Lange's Handbook of Chemistry, 14th Edition, Ed. J.A. Dean, McGraw-Hill, Inc., New York (1992), ISBN: 978-0-070-16194-8.

[139] Handbook of Chemistry and Physics, 56th Edition, Ed. R.C. Weast, CRC Press, US (1975), ISBN: 978-0-878-19455-1.

[140] P. Kubelka, F. Munk, Ein Beitrag zur Optik der Farbanstriche, Z. Tech. Phys. (Leipzig), 12 (1931) 593–601.

[141] P. Kubelka, New Contributions to the Optics of Intensely Light-Scattering Materials. Part I, J. Opt. Soc. Am., 38 (1948) 448-457.

[142] P. Kubelka, New Contributions to the Optics of Intensely Light-Scattering Materials. Part II: Nonhomogeneous Layers*, J. Opt. Soc. Am., 44 (1954) 330-335.

[143] H.G. Völz, Practical pigment testing with the aid of the Kubelka-Munk theory, Prog. Org. Coat., 13 (1985) 153-169.

[144] M. Scorah, Experimental and Modelling Investigation of a Novel Tetrafunctional Initiator in Free Radical Polymerization, PhD thesis, UWSpace, Waterloo, CN (2005), URI: http://hdl.handle.net/10012/887.

[145] J.J. Cheng, Mechanical and Chemical Properties of High Density Polyethylene: Effects of Microstructure on Creep Characteristics, PhD thesis, UWSpace, Waterloo, CN (2008), URI: http://hdl.handle.net/10012/4121.

[146] P. Pip, Physical concepts and ultrasonic measurements on fracture mechanics of semi-crystalline polymers, Master thesis, TU Darmstadt, Darmstadt, Germany, date: 23rd of February 2017, 42-59.

[147] W. Callister, Fundamentals of Materials Science and Engineering, John Wiley & Sons, New York (2001), ISBN: 0-471-39551-1.

[148] B. Fahlman, Materials Chemistry, Springer, Dordrecht, Netherlands, 2007.

[149] N. Casiez, S. Deschanel, T. Monnier, O. Lame, Acoustic emission from the initiation of plastic deformation of Polyethylenes during tensile tests, Polym., 55 (2014) 6561-6568.

[150] K.P. Menard, Dynamic mechanical analysis, CRC Press LLC, Boca Raton, US (1999).

[151] X.M. Jiang, Z.Q. Wu, Bragg's law with refractive correction of low-angle x-ray-diffraction for periodic multilayers, Chin. Phys. Lett., 8 (1991) 356-359.

[152] H.F. Brinson – Polymer Engineering Science and Viscoelasticity, Springer, New York (2008), ISBN: 978-0-387-73860-4.

[153] D.G. Legrand, R.P. Kambour, W.R. Haaf, Low-angle x-ray scattering from crazes and fracture surfaces in polystyrene, J. Polym. Sci., Part A-2: Polym. Phys., 10 (1972) pp. 1565 et seqq.

[154] H.R. Brown, E.J. Kramer, Craze microstructure from small-angle x-ray-scattering (SAXS), J. Macromol. Sci.-Phys., B19 (1981) 487-522.

[155] T.R. Steger, L.E. Nielsen, Microvoid formation during deformation of high-impact polystyrene, J. Polym. Sci., Part B: Polym. Phys., 16 (1978) 613-625.

[156] ISO 11542:2010 – Plastics – Ultra-high-molecular-weight polyethylene (PE-UHMW) molding and extrusion materials – Part 2: Preparation of test specimens and determination of properties; German version, 2010.

[157] M. Schilling, M. Böhning, H. Oehler, I. Alig, U. Niebergall, Environmental stress cracking of polyethylene high density (PE-HD) induced by liquid media - Validation and verification of the full-notch creep test (FNCT), Mat. Sci. Eng. Tec., 48 (2017) 846-854.

[158] M. Schilling, U. Niebergall, I. Alig, H. Oehler, D. Lellinger, D. Meinel, M. Böhning, Crack propagation in PE-HD induced by environmental stress cracking (ESC) analyzed by several imaging techniques, Polym. Test., 70 (2018) 544-555.

[159] N. Ogata, T. Yanagwa, K. Yoshida, Environmental stress cracking of low-density polyethylene in normal alcohols, J. Polym. Sci., Part B: Polym. Phys., 24 (1986) 89-97.

[160] R.J. Renka, A.K. Cline, A triangle-based C-1 interpolation method, Rocky Mt. J. Math., 14 (1984) 223-237.

[161] I. Alig, S. Tadjbach, P. Krüger, H. Oehler, D. Lellinger, Prog. Org. Coat., 64 (2009) 112-119.

[162] A. Levene, W.J. Pullen, J. Roberts, Sound velocity in polyethylene at ultrasonic frequencies, J. Polym. Sci., Part A: Gen. Pap., 3 (1965) pp. 697 et seqq.

[163] M.D. Lechner, K. Gehrke, E.H. Nordmeier, Makromolekulare Chemie, 3rd ed., Birkhäuser Verlag, Basel (2003), ISBN: 978-3-7643-6952-1.

[164] I. Alig, M. Bargmann, H. Oehler, D. Lellinger, M. Wanner, D. Koch, J. Phys. D: Appl. Phys., 44 (2011) 034009.

[165] H. Oehler, I. Alig, D. Lellinger, M. Bargmann, Prog. Org. Coat., 74 (2012) 719-725.

[166] L.A. Feldkamp, L.C. Davis, J.W. Kress, Practical cone-beam algorithm, J. Opt. Soc. Am., Part A: Opt. Image Sci. Vis., 1 (1984) 612-619.

[167] ISO 1183-1:2013 – Plastics – Methods for determining the density of non-cellular plastics – Part 1: Immersion method, liquid pycnometer method and titration method; German version, 2013.

[168] ISO 1133-1:2012 – Plastics – Determination of the melt mass-flow rate (MFR) and melt volume-flow rate (MVR) of thermoplastics – Part 1: standard method; German version, 2012.

[169] ISO 3146:2000 – Plastics – Determination of melting behavior (melting temperature or melting range) of semi-crystalline polymers by capillary tube and polarizing-microscope methods, 2000.

[170] ISO 527-1:2012 – Plastics – Determination of tensile properties – Part 1: general principles; German version, 2012.

[171] Datasheet – Lupolen 4261 AG UV 60005, polyethylene, high density, Basell Polyolefine GmbH, Frankfurt, Germany, Release date: 26th of July 2004.

[172] Datasheet – Lupolen 4261 AG BD, polyethylene, high density, Basell Polyolefine GmbH, Frankfurt, Germany, Release date: 15th of March 2012.

[173] Datasheet – Lupolen 4261 A Q149, polyethylene, high density, Basell Polyolefine GmbH, Frankfurt, Germany, Release date: 08th of June 2015.

[174] Datasheet – Lupolen 5021 DX, polyethylene, high density, Basell Polyolefine GmbH, Frankfurt, Germany, Release date: 29th of February 2012.

[175] Datasheet – Hostalen ACP 5831 D, polyethylene, high density, Basell Polyolefine GmbH, Frankfurt, Germany, Release date: 18th of February 2013.

[176] ISO 17855-1:2015 – Plastics – Polyethylene (PE) molding and extrusion materials – Part 1: Designation system and basis for specifications; German version, 2015.

[177] Datasheet – EU-safety sheet – Arkopal N 100, CAS-No.: 9016-45-9, Sigma-Aldrich Chemie GmbH, Steinheim, Germany, Release date: 9th of September 2015.

[178] Datasheet – EU-safety sheet – n-butyl acetate, CAS-No.: 123-86-4, datasheet version: 12.3, Merck KGaA, Darmstadt, Germany, Release date: 31st of July 2018.

[179] BAM Gefahrgutregel GGR 015: Nachweis der ausreichenden chemischen Verträglichkeit von Verpackungen zur Beförderung gefährlicher Güter aus Polyethylen (PE) und aus koextrudiertem Kunststoff (Coex-PE/PA bzw. Coex-PE/EVOH) gegenüber flüssigen Stoffen; German version, 21.05.2013.

[180] Datasheet – EU-safety sheet – water (demineralized), CAS No.: 7732-18-5, Bernd Kraft GmbH, Duisburg, Germany, Release date: 21st of November 2017.

[181] M. Schilling, U. Niebergall, M. Böhning, Full notch creep test (FNCT) of PE-HD – Characterization and differentiation of brittle and ductile fracture behavior during environmental stress cracking (ESC), Polym. Test., 64 (2017) 156-166.

[182] G. Knothe, C.A. Sharp, T.W. Ryan, Exhaust emissions of biodiesel, petrodiesel, neat methyl esters, and alkanes in a new technology engine, Energy Fuels, 20 (2006) 403-408.

[183] ISO 3679:2015 – Determination of flash / no-flash and flash point – Rapid equilibrium closed cup method; German version, 2015.

[184] Datasheet – EU-safety sheet – diesel fuel, CAS-No.: 68334-30-5, Eni / Eni oil products, Rome, Italy, Release date: 30th of May 2012.

[185] Datasheet – EU-safety sheet – biodiesel fuel in FAME quality, CAS-No.: 870530-78-2, EINECS No.: 273-606-8, UCY business services & trading GmbH, Alfter, Germany, Release date: 8th of August 2011.

[186] DIN EN 590:2004 – Automotive fuels – Diesel – Requirements and test methods; German version, 2004.

[187] DIN EN 14214:2003 – Automotive fuels – Fatty acid methyl esters (FAME) for diesel engines – Requirements and test methods; German version, 2003.

[188] Datasheet – safety sheet – n-dodecane, CAS-No.: 112-40-3, version 5.8, Sigma-Aldrich Chemie GmbH, Steinheim, Germany, Release date: 19th of October 2015.

[189] Datasheet – safety sheet – 1-nonanol, CAS-No.: 143-08-8, version 5.1, Sigma-Aldrich Chemie GmbH, Steinheim, Germany, Release date: 28th of August 2014.

[190] Datasheet – safety sheet – 2-nonanone, CAS-No.: 821-55-6, version 5.4, Sigma-Aldrich Chemie GmbH, Steinheim, Germany, Release date: 27th of October 2015.

[191] Datasheet – safety sheet – nonanal, CAS-No.: 124-19-6, version 5.2, Sigma-Aldrich Chemie GmbH, Steinheim, Germany, Release date: 17th of January 2014.

[192] Datasheet – safety sheet – nonyl acetate, CAS-No.: 143-13-5, version 5.2, Sigma-Aldrich Chemie GmbH, Steinheim, Germany, Release date: 25th of March 2014.

[193] Validierung und Weiterentwicklung des „Full Notch Creep Tests“ zur Bewertung von Kunststoffen für Gefahrgutbehälter, final report of AiF/IGF/FGK joint project 18606N elaborated by BAM, Berlin and Fraunhofer LBF, Darmstadt from 1st July 2015 to 30th August 2018, IGF Schlussbericht, 2018.

[194] W. Meng, H. Li, J. Li, B. Chen, The Effect of Comonomer Type and Content on the Properties of Ziegler-Natta Bimodal High-Density Polyethylene, J. Korean Chem. Soc., 55 (2011) 673-679.

[195] M.M.D. Forte, F.O.V. da Cunha, J.H.Z. dos Santos, J.J. Zacca, Ethylene and 1-butene copolymerization catalyzed by a Ziegler-Natta/Metallocene hybrid catalyst through a 2^3 factorial experimental design, Polymer, 44 (2003) 1377-1384.

[196] A.E. Hamielec, J.B.P. Soares, Polymerization reaction engineering - Metallocene catalysts, Prog. Polym. Sci., 21 (1996) 651-706.

[197] J. Minick, A. Moet, A. Hiltner, E. Baer, S.P. Chum, Crystallization of very-low-density copolymers of ethylene with alpha-olefins, J. Appl. Polym. Sci., 58 (1995) 1371-1384.

[198] G. Strobl, The Physics of Polymers, 2nd ed., Springer, Berlin (1997), ISBN: 3-540-63203-4.

[199] F.J. Stadler, Dynamic-mechanical behavior of polyethylenes and ethene-/α-olefin-copolymers: Part III. γ-relaxation, Korean J. Chem. Eng., 28 (2011) 2057.

[200] F.J. Stadler, Dynamic-mechanical behavior of polyethylenes and ethene/α-olefin-copolymers: Part II. α- and β-relaxation, Korean J. Chem. Eng., 28 (2011) 954-963.

[201] K.H. Nitta, A. Tanaka, Dynamic mechanical properties of metallocene catalyzed linear polyethylenes, Polymer, 42 (2001) 1219-1226.

[202] F.J. Stadler, J. Kaschta, H. Munstedt, Dynamic-mechanical behavior of polyethylenes and ethene-/alpha-olefin-co-polymers. Part I. alpha '-relaxation, Polymer, 46 (2005) 10311-10320.

[203] F.M. Mirabella, A. Bafna, Determination of the crystallinity of polyethylene/α-olefin copolymers by thermal analysis: Relationship of the heat of fusion of 100% polyethylene crystal and the density, J. Polym. Sci. B: Polym. Phys., 40 (2002) 1637-1643.

[204] E. Foldes, G. Keresztury, M. Iring, F. Tudos, Crystallinity of polyethylene measured by density, DSC and Raman-spectroscopy - a comparison, Angew. Makromol. Chem., 187 (1991) 87-99.

[205] J.H. Snoeijer, B. Andreotti, A microscopic view on contact angle selection, Phys. Fluids, 20 (2008) 057101.

[206] T. Young, III. An essay on the cohesion of fluids, R. Soc. Pub., 95 (1805) 65-87.

[207] W.A. Zisman, in Contact Angle, Wettability, and Adhesion: Advances in Chemistry Series, in: F. Gould Robert (Ed.) Contact Angle, Wettability and Adhesion, Am. Chem. Soc., Washington, D.C. (1964), ISBN: 978-0-841-20044-9.

[208] A.W. Neumann, R.J. Good, C.J. Hope, M. Sejpal, An equation-of-state approach to determine surface tensions of low-energy solids from contact angles, J. Colloid Interface Sci., 49 (1974) 291-304.

[209] D.Y. Kwok, A.W. Neumann, Contact angle measurement and contact angle interpretation, Adv. Colloid Interface Sci., 81 (1999) 167-249.

[210] S. Mondal, M. Phukan, A. Ghatak, Estimation of solid–liquid interfacial tension using curved surface of a soft solid, Proc. Nat. Acad. Sci USA, 112 (2015) 12563-12568.

[211] M. Böhning, U. Niebergall, M. Zanotto, V. Wachtendorf, Impact of biodiesel sorption on tensile properties of PE-HD for container applications, Polym. Test., 50 (2016) 315-324.

[212] X.C. Lu, N. Brown, Abnormal slow crack growth in polyethylene, Polymer, 38 (1997) 5749-5753.

[213] ISO 16101:2004 – Packaging – Transport packaging for dangerous goods – Plastics compatibility testing, 2004.

[214] M. Weltschev, F. Heming, M. Haufe, M. Heyer, The influence of the age of biodiesel and heating oil with 10 % biodiesel on the resistance of sealing materials at different temperatures, Mat. Sci. Eng. Tec., 48 (2017) 837-845.

[215] A. Munack, M. Petchatnikov, L. Schmidt, J. Krahl, Final report of research project "Spektroskopische Untersuchungen zur Ergründung der Wechselwirkungen zwischen Biodiesel und Dieselkraftstoff bei Blends", Inst. Agrartech. Biosystemt., Johann Heinrich von Thünen-Instituts, Bundesforschungsinstitut Ländliche Räume, Wald und Fischerei, Braunschweig / Coburg, Germany (2009).

[216] X.C. Lu, Z.Q. Zhou, N. Brown, A sensitive mechanical test for slow crack growth in polyethylene, Polym. Eng. Sci., 37 (1997) 1896-1900.

[217] R.A.C. Deblieck, D.J.M. van Beek, M. McCarthy, P. Mindermann, K. Remerie, B. Langer, R. Lach, W. Grellmann, A simple intrinsic measure for rapid crack propagation in bimodal polyethylene pipe grades validated by elastic-plastic fracture mechanics analysis of data from instrumented Charpy impact test, Polym. Eng. Sci., 57 (2017) 13-21.

[218] E. Nezbedova, P. Hutar, M. Zouhar, Z. Knesl, J. Sadilek, L. Nahlik, The applicability of the Pennsylvania Notch Test for a new generation of PE pipe grades, Polymer Testing, 32 (2013) 106-114.

[219] ISO 4287:2010 – Geometrical product specifications (GPS) – Surface texture: Profile method – Terms, definitions and surface texture parameters; German version, 2010.

[220] C. Grein, K. Bernreitner, A. Hauer, M. Gahleitner, W. Neissl, Impact modified isotatic polypropylene with controlled rubber intrinsic viscosities: Some new aspects about morphology and fracture, J. Appl. Polym. Sci., 87 (2003) 1702-1712.

[221] F. Saghir, Z. Khan, A. Bazoune, Effect of temperature on tensile properties of HDPE pipe materials, Plast. Rub. Compos., 35 (2006) 226-230.

[222] M. Mahl, C. Jelich, H. Baier, Thermo-mechanical behavior of polyethylene under mechanical loads at cryogenic and elevated temperatures, Int. J. Press. Vess. Piping, 150 (2017) 11-18.

[223] S. Hobeika, Y. Men, G. Strobl, Temperature and strain rate independence of critical strains in polyethylene and poly(ethylene-co-vinyl acetate), Macromolecules, 33 (2000) 1827-1833.

– This page is intentionally blank. –

Symbols

Symbol	dimension	Description
A	mm^2	(cross-sectional) area
a	mm	(edge) length (mainly in x-direction)
A_{cal}	-	absorbance
A_d	mm	damaged area
A_L	mm^2	actual residual cross-section (ligament area)
A_n	mm^2	notch area
A_{tfs}	mm^2	area of total fracture surface
A_{ud}	mm^2	undamaged area
b	mm	(edge) length, width (mainly in y-direction)
B	-	criterion of brittleness
γ	J/m^2	surface energy (free energy per unit area of surface)
C	g/g	concentration
c	mm	crack length
$\dot{c}$	µm/h	crack growth rate
C_a	g/g	concentration of a species in the aqueous phase
c_i	m/s	sound velocity
δ	mm	crack tip opening displacement (CTOD)
δ_0	mm	initial value of crack tip opening displacement
$\dot{\delta}$	mm/s	crack tip opening displacement rate
D	cm^2/s	diffusion coefficient
d	mm	(time-dependent) elongation (value), obtained by FNCT elongation measurement
D_0	cm^2/s	temperature-independent preexponential (initial value of diffusion coefficient)
d_{end}	mm	end-to-end distance between effective entanglements
d_{fail}	mm	(maximum) elongation at failure (in FNCT)
D_{fibril}	mm	fibril diameter
$d_{II,end}$	mm	elongation at end of region II in entire elongation curve (FNCT)
$d_{II,start}$	mm	elongation at onset of region II in entire elongation curve (FNCT)
d_{notch}	mm	notch depth
D_{pol}	-	polydispersity (ratio of Mw and Mn)
du_i	mm	displacements in LEFM
Δa	mm	amount of crack extension
ΔG	J	free energy of dissolution ('Gibbs energy')
ΔH	J	activation enthalpy (enthalpy of dissolution)
ΔS	J/K	entropy of mixture
ΔH_a	J	enthalpy of melting for amorphous standard

ΔH_c	J	enthalpy of melting for crystalline standard
ΔH_f	J	enthalpy of melting
$\boldsymbol{\Delta H_f^0}$	J	melting enthalpy of a mono crystal
$\boldsymbol{\epsilon}$	°	Bragg angle of intensity maximum
ε	mm	mechanical strain
$\boldsymbol{\dot{\varepsilon}}$	mm/s	strain rate
$\boldsymbol{\dot{\varepsilon}_0}$	mm/s	start value of strain rate
e	C	electron charge
E	MPa	tensile modulus / Young's modulus
E*	MPa	'reduced modulus' (cf. E, Young's modulus)
E_{is}	J/m²	energy required to create new internal surfaces
F	N	force
$F(R_{coeff})$	-	Kubelka-Munk function
G	J	energy (value) available for unit increase in crack length, also termed 'strain energy release rate'
G*	MPa	complex modulus (DMA), shear modulus
G'	MPa	real part of complex modulus (DMA), 'store modulus', shearing mode
G"	MPa	imaginary part of complex modulus (DMA), 'loss modulus', shearing mode
G_c	J	critical value of G
$<G_p>$	MPa	strain hardening modulus
h	mm	specimen thickness
H^{cp}	mol/(m³·Pa)	constant of Henry's law (Henry solubility)
I	W/m²	measured irradiation intensity
I_0	W/m²	incident irradiation intensity
J	J	(surface) work parameter
J*	1/Pa	complex compliance
J_{df}	mol/(m²·s)	diffusion flux
J_{IC}	J	critical value of J at which true crack growth starts
J_p, P	mol/ (cm·s·Pa)	rate of transfer of diffusing/permeating substance, permeability (constant)
K	1/cm	absorption coefficient
K(z)	1/m	correlation function
k_f	1/m	wave number of scattered wave
K_H / $\boldsymbol{K_H^{pc}}$	Pa	Henry's law volatility constant
K_I	MPa· $\sqrt{m}$	stress intensity factor
k_i	1/m	wave number of incident wave
K_{IC}	MPa· $\sqrt{m}$	critical value of KI
λ	nm	wavelength
λ_d	-	true strain (value), dimensionless ratio
L	mm	length, gauge length

L_0	mm	initial (gauge) length, distance between gauge marks
L_a	nm	thickness of amorphous region
L_c	nm	thickness of crystalline region
L_p	nm	long period of lamellar structure (in polymer chain regions)
l_p	nm	thickness of thin plane sheet
L_t	nm	minimal length of a tie molecule
μ_0	$m \cdot kg/(A^2 s^2)$	vacuum permeability ('magnetic constant')
M_∞	g	equilibrium mass
m_e	kg	electron mass
M_i	g	mean molecular weight of size range i
M_n, $\overline{\mathbf{M_n}}$	g/mol	number average (value) of molecular mass
M_t	g	time-dependent mass
M_w, $\overline{\mathbf{M_w}}$	g/mol	weight average (value) of molecular mass
ν	cm^3	activation volume for shear flow
η	Pa·s	viscosity
η^*	Pa·s	complex viscosity
n	-	degree of polymerization (average number of mer units in a polymer chain)
N	-	total number (integer)
N_i	-	number of chains per size i
n_{mer}	-	number of subunits in a polymer
n_n	-	number-average degree of polymerization
n_w	-	weight-average degree of polymerization
p	Pa	(partial) pressure
P_0	mol/ (cm·s·Pa)	temperature-independent permeability preexponential (initial value of permeability)
Q	J/mol	(activation) energy
q	-	scattering vector
Q_d	J/mol	activation energy for diffusion
Q_p	J/mol	activation energy for permeation
ρ	g/cm^3	density
R	J/(mol·K)	universal gas constant
R_0	mm	average height related to the zero level (notch plane) of the fracture surface
R_a	mm	arithmetic average of fracture surface profile
$r_{acoustic}$	-	acoustic reflection coefficient
R_{coeff}	-	reflection (reflectance), reflection coefficient
R_{craze}	mm	length of craze zone
r_e	m	electron radius
R_{max}	mm	maximum height of highest embossment of all fracture surfaces in a stress-dependent FNCT series
R_p	mm	the maximum height of the highest embossment on the distinct fracture surface (profile)

$\sum_e$	-	number of load bearing (polymer) chains in polymeric network
σ	MPa	mechanical stress, load
σ_B	MPa	fracture stress (of a material)
σ_c	MPa	craze stress
σ_L	MPa	actual mechanical stress (value) obtained by recalculation after (LM based) measurement of actual residual cross-section AL
σ_n	MPa	nominal mechanical stress (value) subjected to specimens
σ_y	MPa	yield stress (shear stress)
S	-	solubility coefficient
S_{coeff}	$1/cm^3$	scattering coefficient
θ	°	(contact, scattering) angle
T	°C, K	(absolute) temperature
t	s, h	time
T_α	°C, K	α relaxation temperature
tan δ	-	damping (DMA), dissipation factor
t_f	h	time to failure (value) of a single FNCT measurement
t_f*	h	time to failure (value) of a set of FNCT measurements (usually 5 single measurements) and subsequent regression; referred to actual stress values
T_g	°C, K	glass-rubber transition temperature (usually simply denoted as glass transition temperature)
T_m	°C, K	melting temperature
T_{meas}	$1/cm^3$	transmittance
t_n	mm	nominal thickness of NCTL specimen
U	J	required energy to fracture covalent chain bonds (internal energy)
$\boldsymbol{\nu}_e$	-	effective entanglement density
W / dW	J	(physical) work / amount of work
w_i	-	weight fraction of molecules within the same size interval
X_c	-	polymer crystallinity
x	mm	distance (one-dimensional), e.g. specimen thickness
x_i	-	fraction of the total number of chains within a corresponding size rage
x_{urf}	mm	undamaged residual fracture path of a growing crack
Z(x, y)	mm	height value of a pixel regarded on the fracture surface
Z_i	$(Pa \cdot s)/m^3$	acoustic impedance

Abbreviations

Abbreviation	Description
π bond	specific chemical bond
ACP	advanced cascade process
µm	micrometer (length unit)
AGBD	PE-HD material Lupolen 4261 AG BD
AGUV	PE-HD material Lupolen 4261 AG UV 60005
AQ149	PE-HD material Lupolen 4261 A Q149
Arkopal	2 wt% aqueous solution of detergent Arkopal N 100
ASTM	American Society for Testing and Materials (standard methods)
BHT	butylated hydroxytoluene
BSC	basic stress cracking
BTT	Bell telephone test
C_2H_4	chemical formula of ethylene
C_2H_6	chemical formula of ethane
C_3H_8	chemical formula of propane
C_4H_{10}	chemical formula of butane
CAS No.	CAS (Chemical Abstracts Service) registry number
C-C	representation of two bonded carbon atoms
CH_3	methyl group
CH_4	chemical formula of methane
Cl	chlorine, chlorine atom
CO_2	carbon dioxide (molecule)
COD	crack opening displacement
CRB	cracked round bar test
CT	X-ray (industrial) computed tomography
CTOD	crack tip opening displacement
DIN	Deutsche Industrie Norm (German Industrial Standard) (DIN + [number] refers to distinct standard indicated by [number])
DMA	dynamic mechanical analysis
DMTA	dynamic mechanical thermal analysis
DNCT	Double-notch creep test
DSC	differential scanning calorimetry
EINECS No.	EINECS (European Inventory of Existing Commercial Chemical Substances) registry number
EN	European Norm (European Standard) (EN + [number] refers to distinct standard indicated by [number])
ESC	environmental stress cracking
ESCR	environmental stress cracking resistance
FAME	fatty acid methyl ester(s)

FNCT	full-notch creep test, full-notch creep testing
GBR-P	polymeric geosynthetic barriers (geomembranes)
GPa	gigapascal
GPC	gel permeation chromatography
H_2O	water (molecule)
HD	high density (e.g. in PE-HD)
HPLC	high-pressure liquid chromatography
IBC	intermediate bulk container
Ir	iridium (element)
ISO	International Organization for Standardization (ISO + [number] refers to distinct standard indicated by [number])
IUPAC	International Union of Pure and Applied Chemistry
LC	liquid chromatography
LCB	long chain branches
LD	low density (e.g. in PE-LD)
LEFM	linear elastic fracture mechanics
LM	light microscopy
LSM	laser scanning microscopy
Lutensol	specific fatty alcohol polyglycol ether
NB	n-butyl acetate
NBA	2 wt-% solution of n-butyl acetate in a 2 wt-% aqueous solution of Arkopal N 100
NBL	2 wt-% solution of n-butyl acetate in a 5 wt-% aqueous solution of Lutensol
NCTL	notched constant tensile load test
NDR	natural draw ratio
M	mass
MFR	melt flow rate
mm	millimeter (length unit)
MM	molecular mass
MMD	molecular mass distribution
MPa	megapascal
NPEO	nonylphenol polyglycol ether
NPT	notch pipe test
O_2	oxygen (molecule)
PA	polyamide
PC	polycarbonate
PE	polyethylene
PE-HD	polyethylene, high density
PE-LD	polyethylene, low density
PE-LLD	polyethylene, linear low-denstiy
PE-MD	polyethylene, medium density

PE-MHW	polyethylene, high molecular weight
PENT	Pennsylvania edge notched tensile test
PET	polyethylene terephthalate
PE-UHMW	polyethylene, ultra-high molecular weight
PMMA	polymethyl methacrylate
PP	polypropylene
PPO	poly(phenylene oxide)
PS	polystyrene
PSF	polysulfone
Pt	platinum (element)
PTFE	polytetrafluoroethylene (best-known brand name of PTFE-based formulas is 'Teflon')
PVC	polyvinylchloride
R·	chemical radical, catalyst species in terms of polymerization
RCP	rapid crack propagation (distinction to slow crack propagation phenomena)
RME	rapeseed methyl ester
RNCT	round-notch creep test
SAM	scanning acoustic microscopy
SAXS	small angle X-ray scattering
SCB	small chain branches
SCE	spectral reflection data excluding specular component (gloss)
SCG	slow crack growth
SCGR	slow crack growth resistance
SCI	spectral reflection data including specular component (gloss)
SEC	size exclusion chromatography
SEM	scanning electron microscopy
SENT / SNCT	single (edge) notch creep test
SHT	strain hardening test
TCB	1,2,4-trichlorobenzene
TEM	transmission electron microscopy
TOF	time of flight
TT	Tensile testing
UV/Vis	ultraviolet and visible part of eletromagnetic spectrum (special wavelength region)
WAXS	wide angle X-ray scattering
$X_{c,\ DSC}$	polymer crystallinity, determined by DSC
$X_{c,\ XRD}$	polymer crystallinity, determined by XRD
$X_{c,SAXS}$	polymer crystallinity, determined by SAXS
XRD	X-ray diffraction
2D	two-dimensional (2 dimensions)

3D	three-dimensional (3 dimensions)
5021DX	PE-HD material Lupolen 5021 DX
5831D	PE-HD material Hostalen ACP 5831 D

List of tables & figures

Appendix

Appendix A1

Strain Hardening Test (SHT), Experimental Data

As the SHT was performed in another part of the study presented, experimental as well as fundamental data with respect to its analysis are given in this section.

A heatable tensile testing machine (Z020/TH2A of Zwick Roell, Zwick GmbH & Co. KG, Ulm, Germany; temperature chamber type W91255) was employed for strain hardening tests referring to ISO 18488 [122] (section 2.5.5). Standard SHT procedure was conducted at a temperature of 50°C (to enhance comparability to classic BSC/ESC testing methods such as FNCT) with a strain rate of 20 mm/min. The strain was measured by digital image correlation from optical markers attached closely to the narrow parallel sides of the specimen (gauge length).

The (technical) strain ε is defined by the actual specimen length L divided by the original specimen length L_0 according to (68):

$$\varepsilon = \frac{L-L_0}{L_0} = \frac{\Delta L}{L_0} \tag{68}$$

The draw ratio λ_d describes the factor by which the specimen is elongated and is calculated using (Eq. 69):

$$\lambda_d = \frac{L}{L_0} = 1 + \varepsilon \tag{69}$$

The (technical) stress σ is calculated by the value of force F acting on the cross-section A of the specimen (Eq. 70):

$$\sigma = \frac{F}{A} \tag{70}$$

The average slope of an obtained curve section is calculated by fitting an analytical equation to the section according to (Eq. 71):

$$\overline{f'(a,b)} = \frac{1}{b-a}\int_a^b f'(x)\,dx = \frac{f(b)-f(a)}{b-a} \tag{71}$$

f is the fitting function for the curve section within limits a (lower section limit) and b (upper section limit).

The stress-strain curve obtained by SHT is fitted by a function following Neo-Hookean constitutive model as it is proposed in [122] and [124]. Thereafter, the strain hardening modulus $\langle G_p \rangle$ as the average difference quotient (section 2.5.5) is derived from (Eq. 72) and (Eq. 73):

$$\sigma = G_p\left(\lambda_d^2 - \frac{1}{\lambda_d}\right) + C \tag{72}$$

with σ: (technical) stress, λ_d: draw ratio, C: constant and G_p: strain hardening modulus (proportionality constant), leading to

$$\langle G_p \rangle = \overline{\sigma'(\lambda_{d1},\lambda_{d2})} = \frac{1}{\lambda_{d2}-\lambda_{d1}}\int_{\lambda_{d1}}^{\lambda_{d2}} \sigma'(\lambda_d)\; d\lambda_d = \frac{1}{\lambda_{d2}-\lambda_{d1}} G_p\left[\left(\lambda_{d2}^2 - \frac{1}{\lambda_{d2}}\right) - \left(\lambda_{d1}^2 - \frac{1}{\lambda_{d1}}\right)\right] \tag{73}$$

In ISO 18488, the application of fixed integration limits of $\lambda_{d1} = 8$ and $\lambda_{d2} = 12$ is suggested [122]. Since the PE-HD resins investigated in this study exhibit draw ratios at failure lower than $\lambda_d = 12$,

alternative analysis methods were examined. An extrapolation of data to an upper integration limit of $\lambda_d = 12$ although the test specimen failed at a lower λ_d value is possible. However, this might lead to an erroneous value. Therefore, to demonstrate the strong influence of the selection of integration limits, data of a typical stress-strain curve obtained by SHT was analyzed and the resulting strain dependent $<G_p>$ is given (Fig. A1.83).

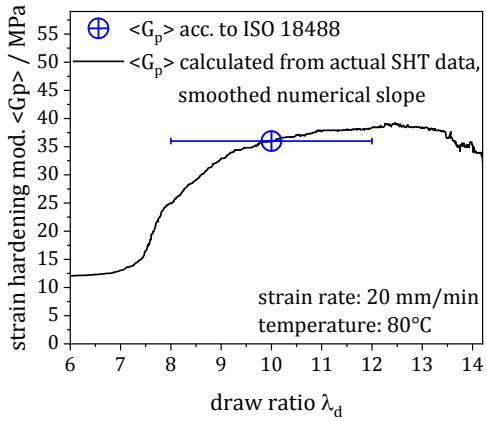

Figure A1.83: Strain hardening modulus $<G_p>$ of a typical stress-strain curve in dependence on the draw ratio λ_d; comparatively, $<G_p>$ derived by ISO 18488 and calculated using fixed limits.

$<G_p>$ results obtained by an analysis applying fixed integration limits have to be considered with due care since the selection of integration limits is crucial and might influence the $<G_p>$ value (Fig. A1.83). This is especially significant, if the material properties change strongly during the test. An alternative to select and define integration limits is to use inherent values derived from characteristic properties of the stress-strain curve, such as the natural draw ratio (NDR, section 2.5.5) and the draw ratio at break.

Furthermore, testing below the α'-transition temperature of PE-HD (approx. 80°C to 100°C, Fig. 38 b), leads to an incorporation of enthalpic energy parts in the stress-strain curve, which might result in different $<G_p>$. Therefore, SHT should be performed in the temperature range of the α'-transition temperature (not at low temperatures such as 50°C, which is usually applied in FNCT).

Tensile test experimental data

As part of the basic characterization of the PE-HD types used in this study and additionally addressing other aspects of the joint project, classic tensile tests were performed employing a Z020/TH2A tensile test machine of Zwick Roell, Zwick GmbH & Co. KG, Ulm, Germany. The tests were conducted in accordance with ISO 527-2 [123]. Therefore, test speeds of 1 mm/min in the region of Young's modulus and 50 mm/min thereafter and typical environmental conditions (23°C, 50% humidity, air) were used. In addition to non-saturated, specimens previously saturated in biodiesel and diesel were applied to address the influence of sorptive bulk-active fluids on PE-HD concerning its tensile test behavior. The results of tensile tests applying non-saturated and biodiesel saturated AGUV specimens are depicted exemplary in figure A1.84.

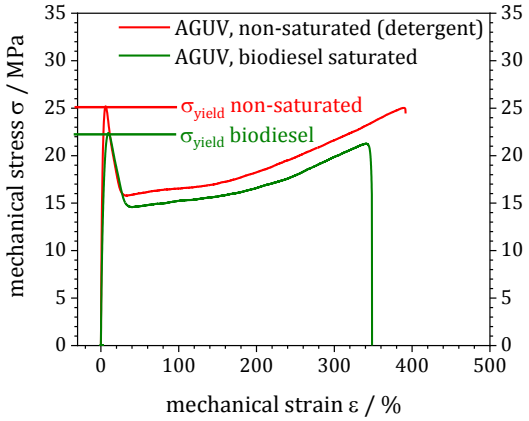

Figure A1.84: Tensile test results of non-saturated and biodiesel saturated AGUV specimens.

Especially, the values of yield strengths corresponding to the fluid influence can be noticed from the results of tensile tests of non-saturated and biodiesel saturated AGUV specimens (Fig. A1.84). Evidently, the influence of a bulk-active fluid leads to a reduction of the yield strength of a PE-HD material. Furthermore, it has to be noticed that a test temperature increase also leads to a decrease of yield strength, independent of sorption (saturation) conditions [221, 222, 223]. This explains slight differences in the values of yield strength measured at 23°C (Fig. A1.84) and calculated values of the actual mechanical stress that initiates final failure (transition from region II to III) in a specimen during FNCT (Fig. 70).

Tensile tests of FNCT specimens – fracture surface analysis

In this section, LSM fracture surfaces of tensile tested AGUV FNCT specimens pre-saturated in biodiesel and diesel, respectively, are presented exemplary. Tensile tests were performed to saturated FNCT specimens in accordance with ISO 527-2 [123] at 23°C and 50% humidity.

a) biodiesel, pre-saturated FNCT specimen (AGUV)

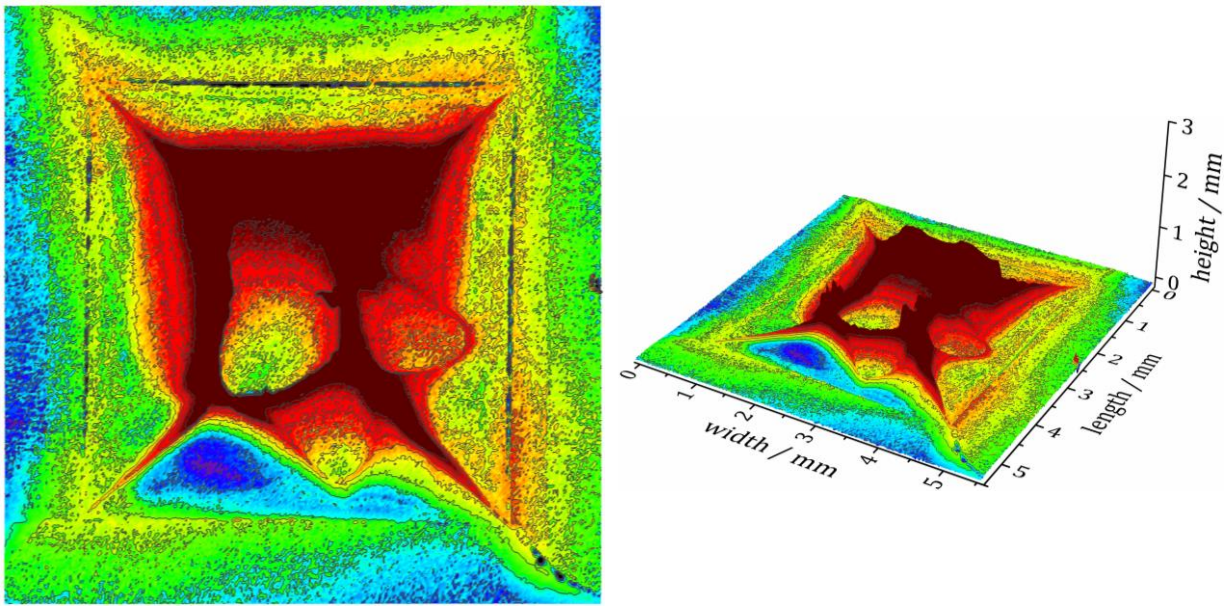

b) diesel, pre-saturated FNCT specimen (AGUV)

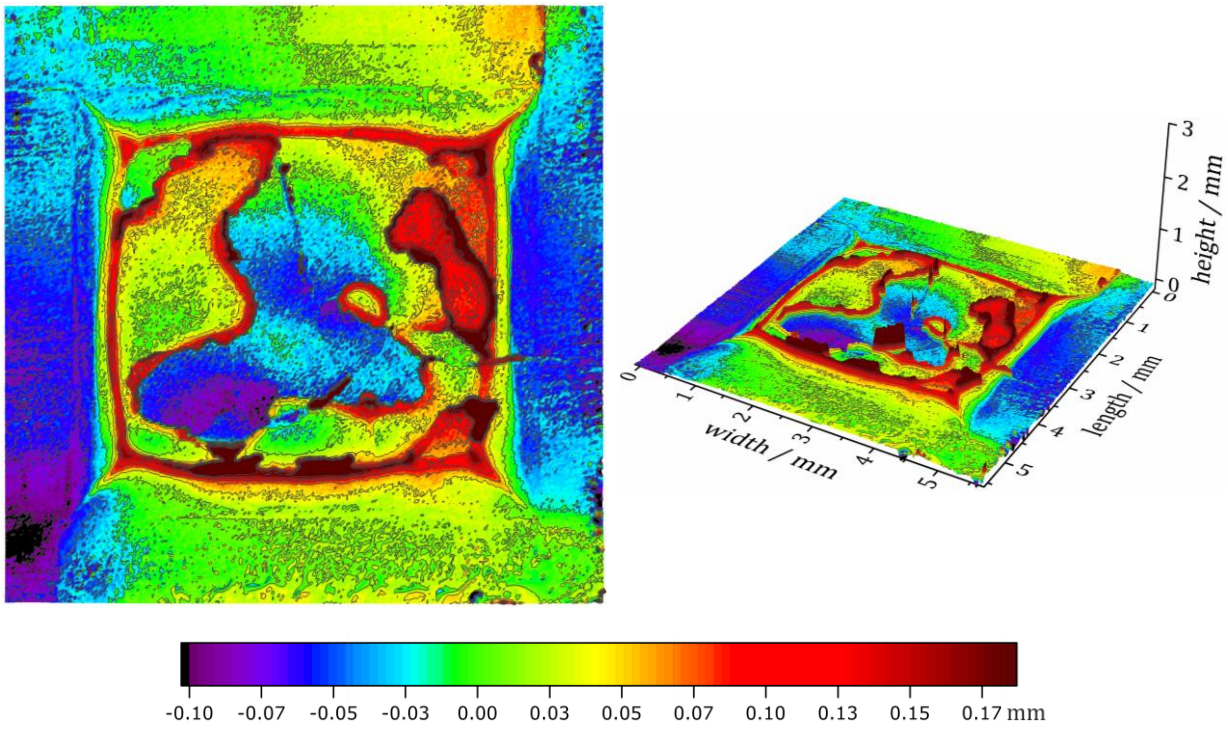

Figure A1.85: 2D and 3D LSM fracture surfaces of tensile tested AGUV FNCT specimens pre-saturated in biodiesel (a) and diesel (b).

Appendix A2

Design / constructional drawings

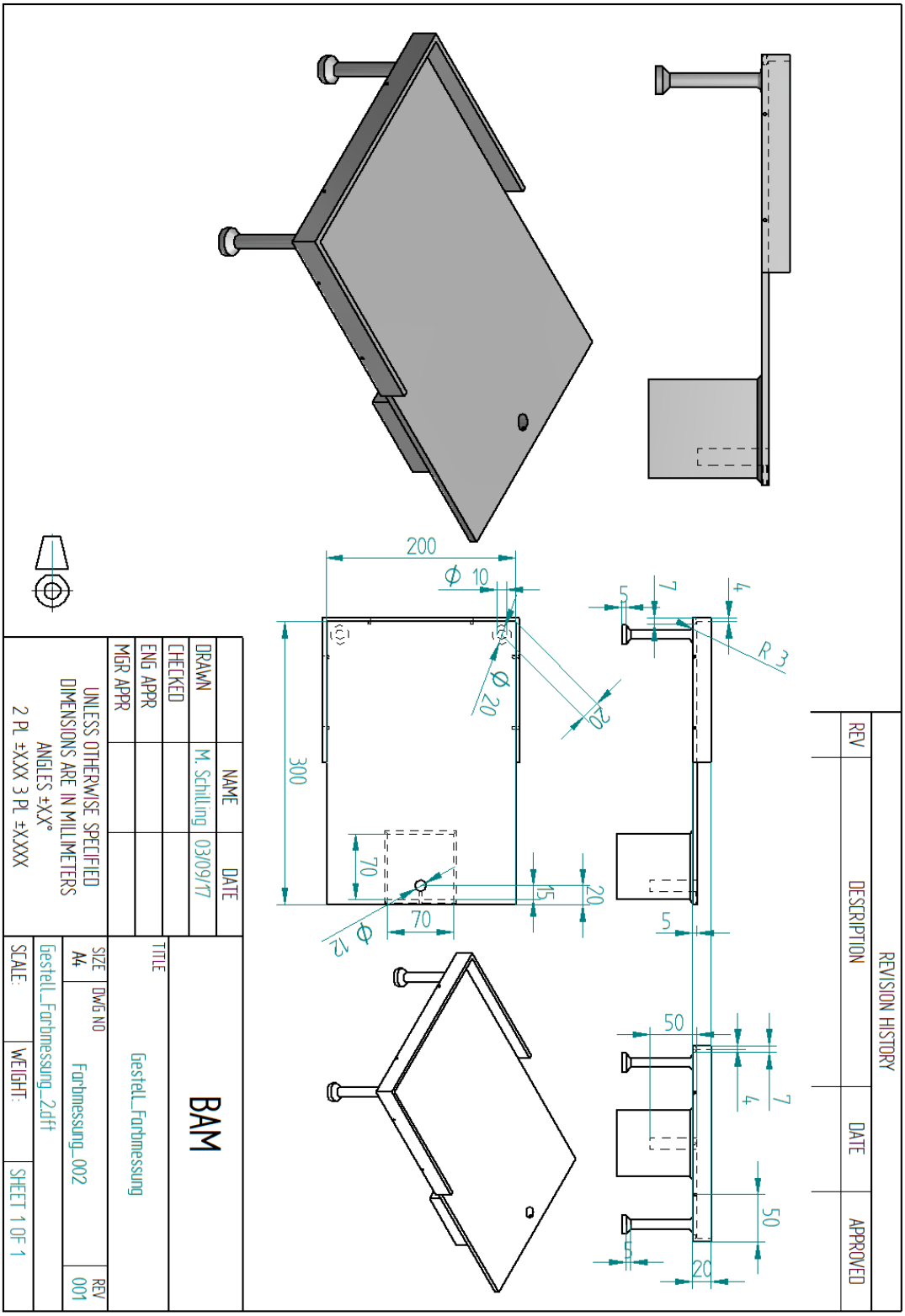

Figure A2.86: Constructional drawing of special jig designed for UV/Vis spectrophotometric measurements of FNCT specimens.

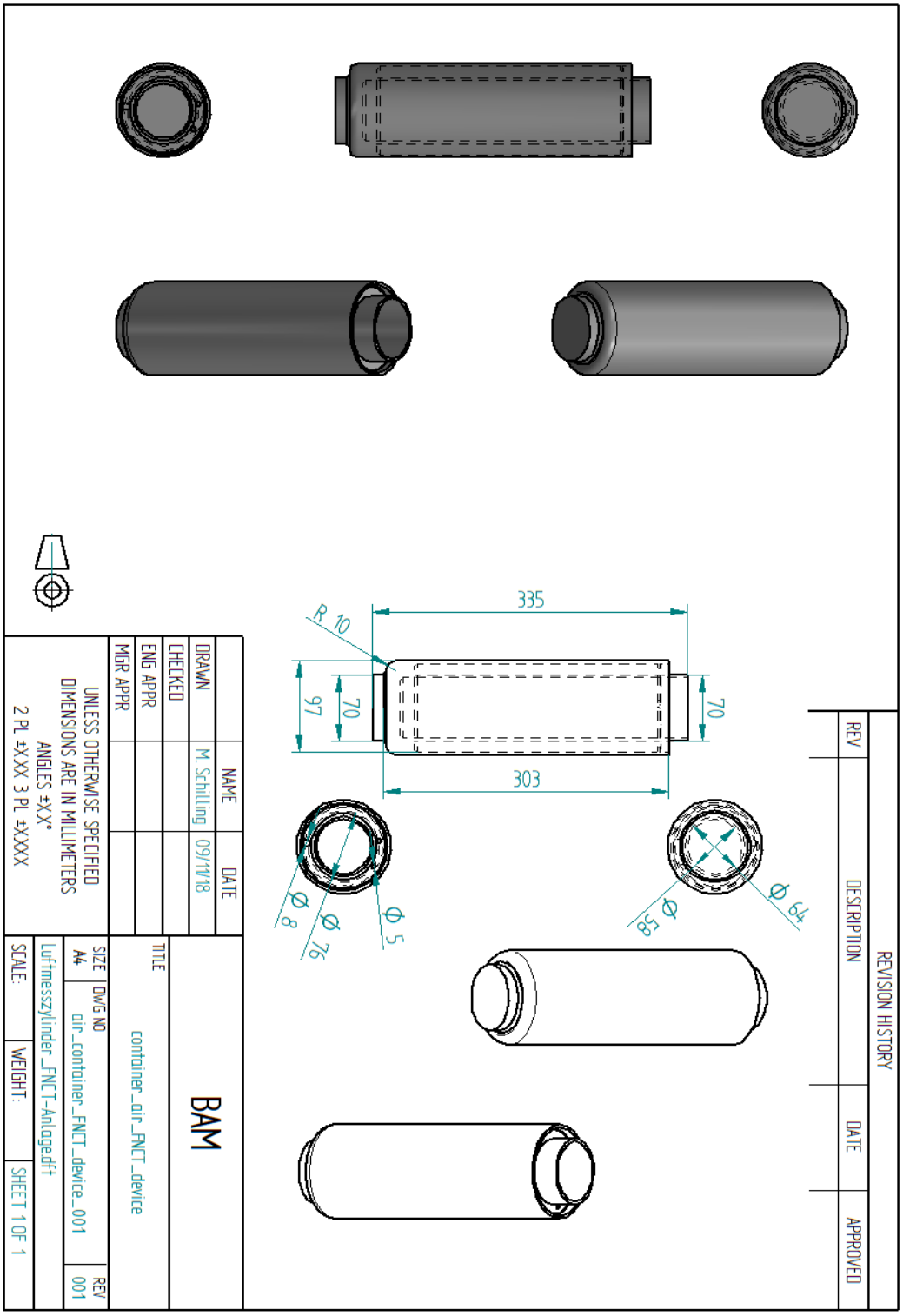

Figure A2.87: Constructional drawing of fluid container for FNCT measurements in air.

Appendix A3

Pictures of FNCT fluid containers for FNCT in air

a) b)

c)

Figure A3.88: Fluid containers for FNCT measurements in air, a) frame container, b) inlay of air container, c) two air containers attached to FNCT device during measurement.

Appendix B1

Sorption behavior

Additional sorption data are presented in this section. Figure B1.89 comprises information on biodiesel and diesel sorption obtained for AGUV FNCT specimens at 50°C. Figure B1.89 a represents an overview and in figure B1.89 b, data are depicted in a smaller time range to especially allow a facilitated consideration of the sorption process start including the conditioning time of specimens during FNCT (10 h).

a) b)

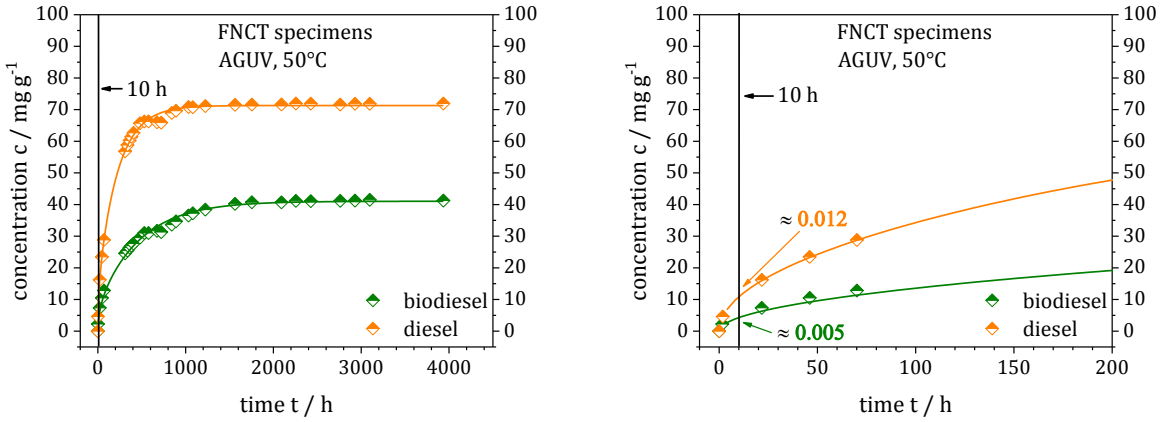

Figure B1.89: Sorption behavior of AGUV FNCT specimens immersed in biodiesel and diesel at 50°C; a) sorption data overview, b) sorption data in smaller time range.

Appendix B2

Full-notch creep test (FNCT), results

a) AGBD, 50°C

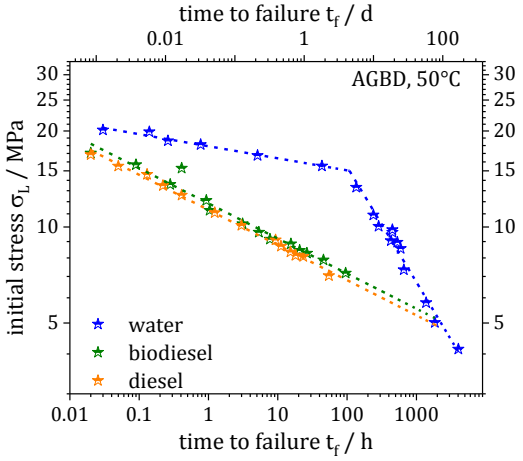

b) 5831D, 50°C

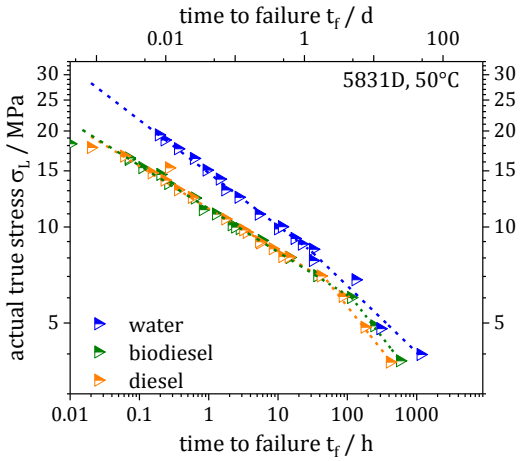

Figure B2.90: FNCT time to failure values t_f of AGBD (a) and 5831D (b) in water, biodiesel and diesel, each over a large range of actual applied stresses at 50°C (depiction in accordance with ISO 16770 [13]).

Appendix B3

Fracture surface analysis

Temperature variation

a) 30° C, σ_L = 9.0 MPa

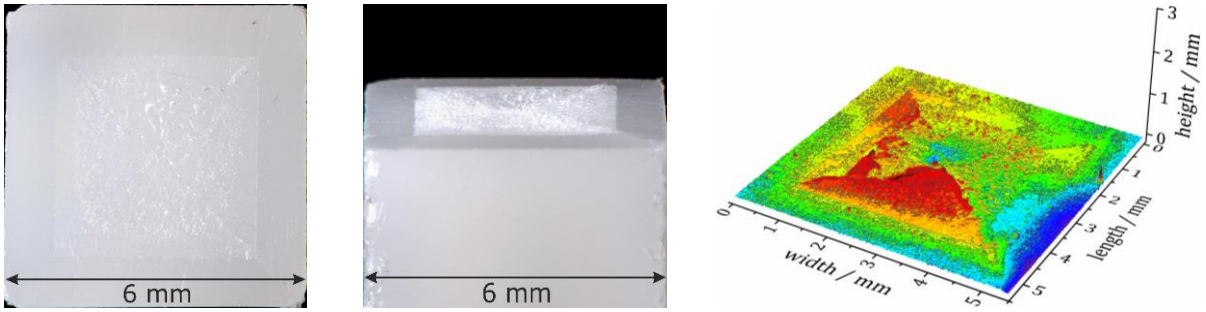

b) 70° C, σ_L = 8.8 MPa

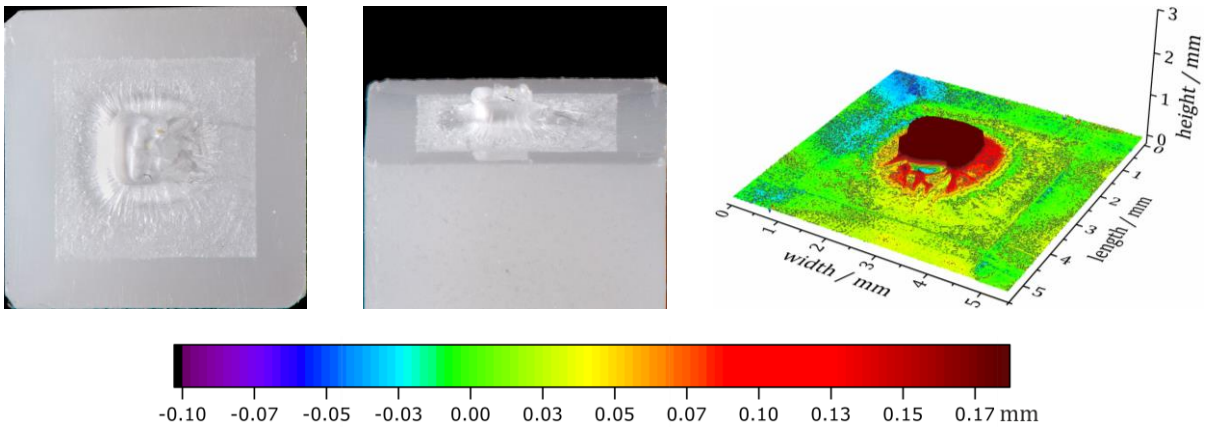

Figure B3.91: LM and LSM fracture surfaces for temperature variation of 5021DX in Arkopal N 100.

Stress variation

a) σ_L = 8.1 MPa

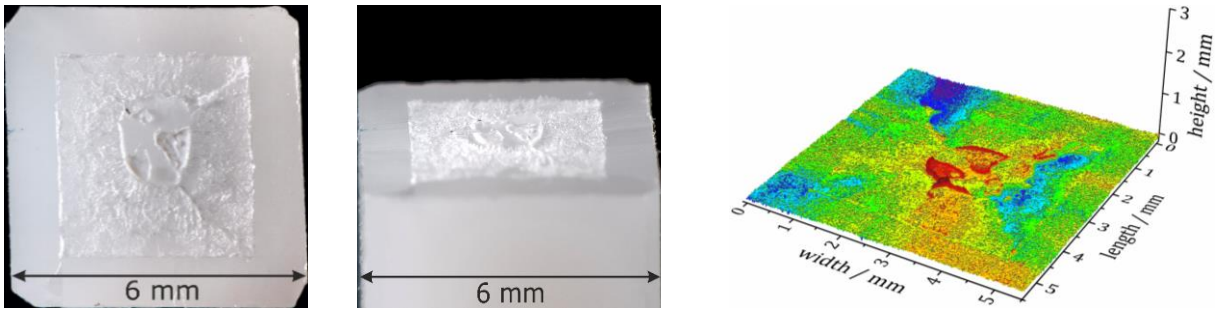

b) σ_L = 14.7 MPa

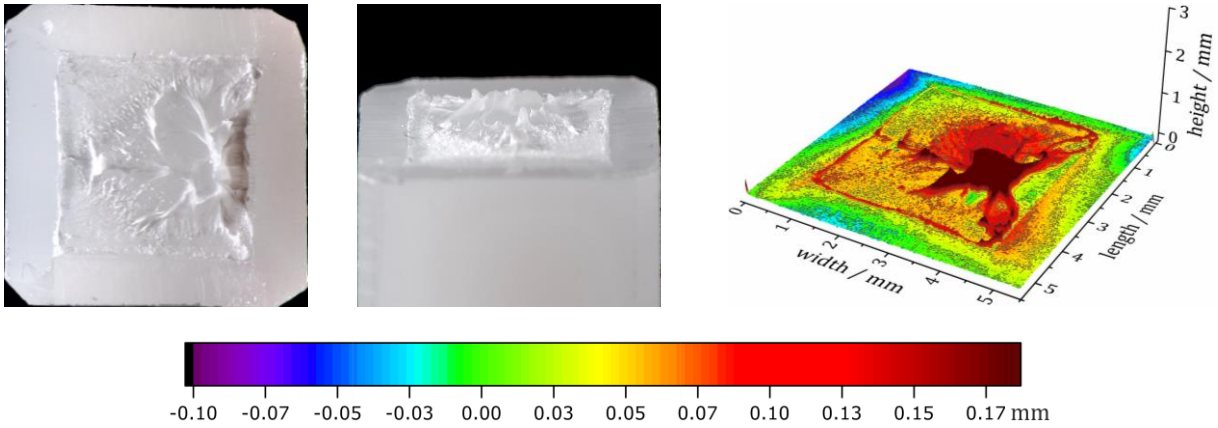

Figure B3.92: LM and LSM fracture surfaces for stress variation of 5021DX in Arkopal N 100 at 50°C.

a) air, σ_L = 8.8 MPa

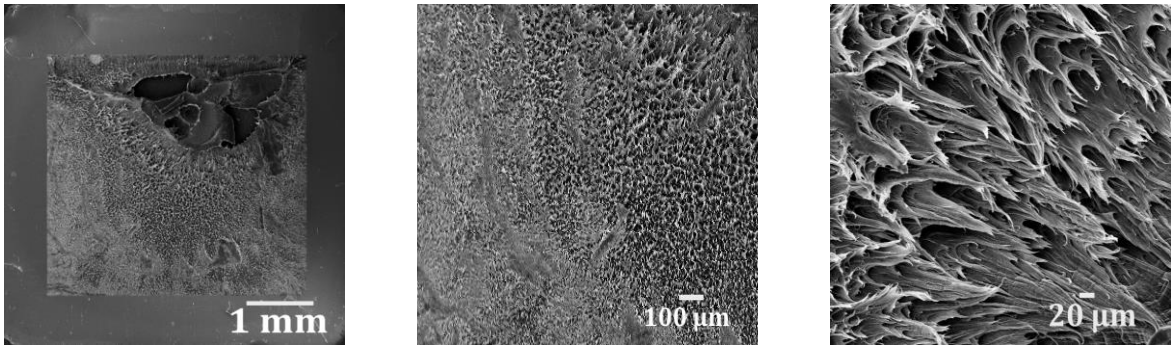

b) water, σ_L = 8.8 MPa

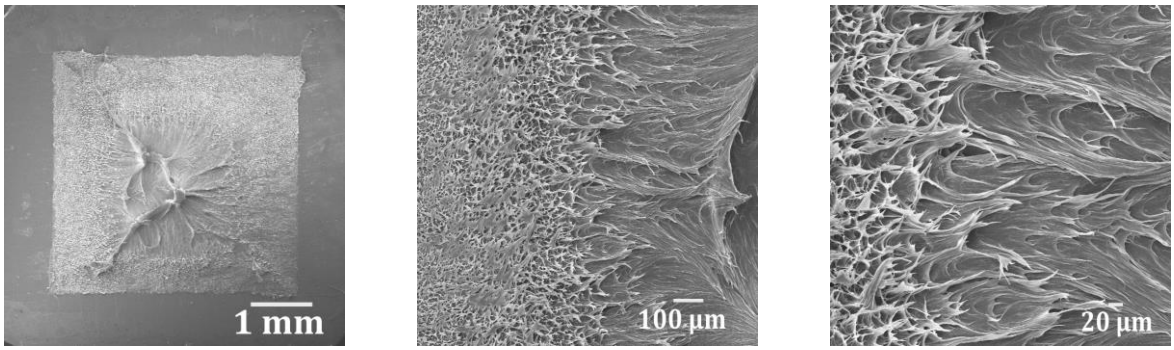

c) Arkopal, σ_L = 8.1 MPa

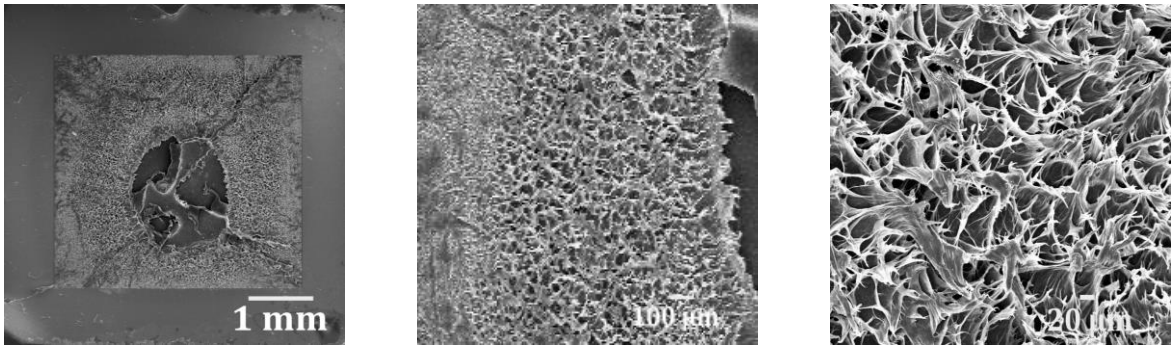

d) biodiesel, σ_L = 9.0 MPa

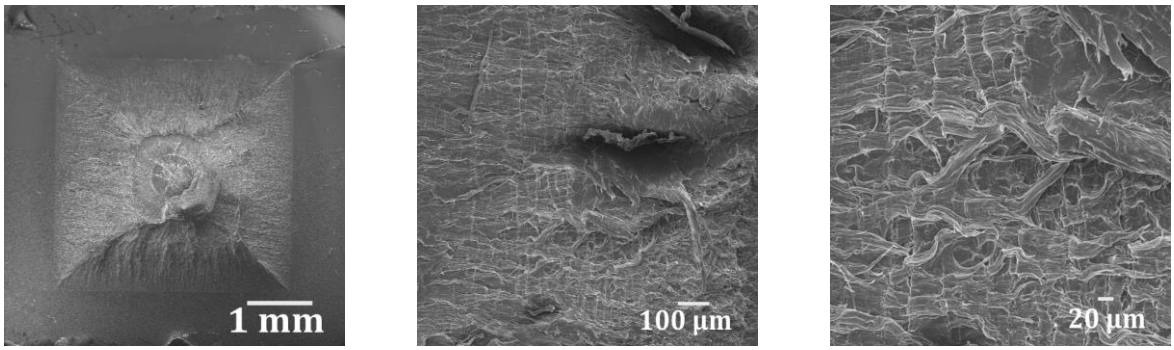

e) diesel, σ_L = 8.8 MPa

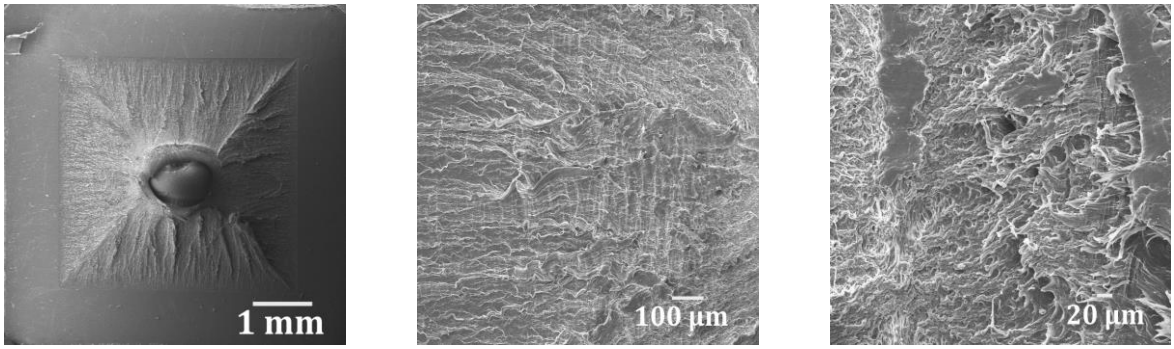

f) NB, σ_L = 8.9 MPa

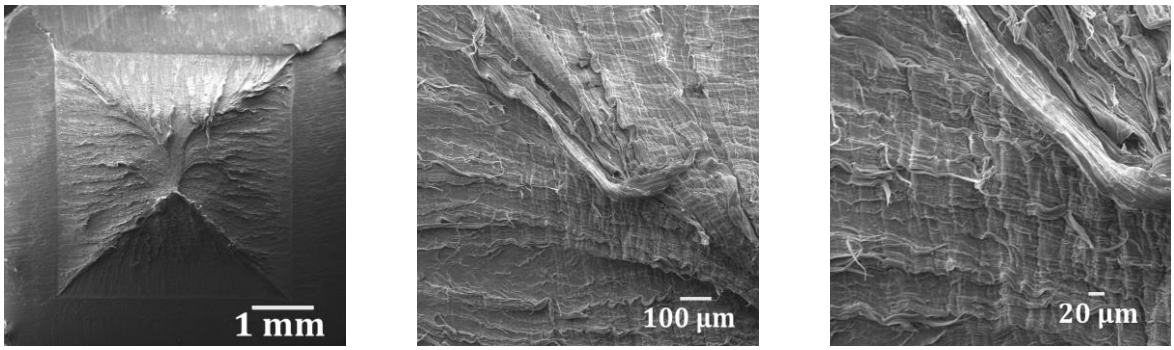

g) NBA, σ_L = 8.7 MPa

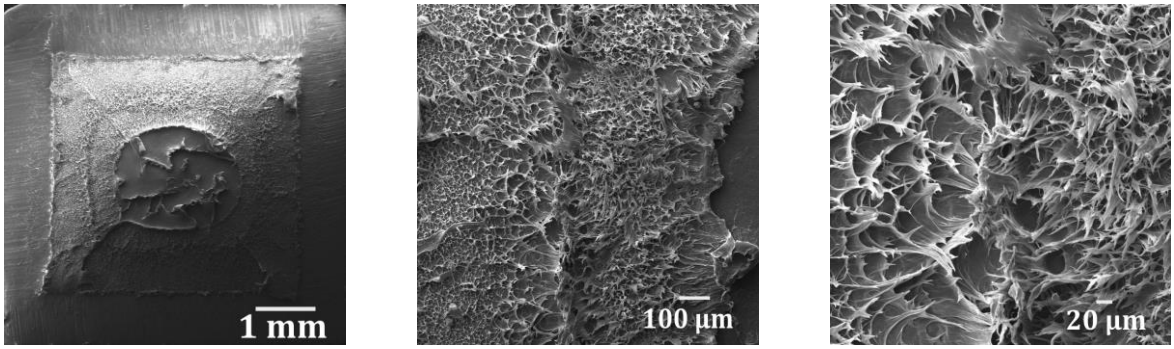

h) NBL, σ_L = 8.7 MPa

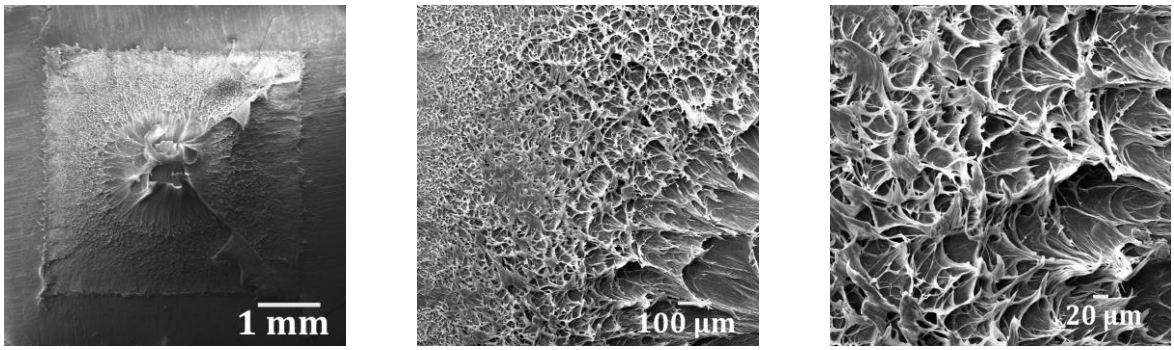

Figure B3.93: SEM fracture surfaces for fluid variation of 5021DX, FNCT specimens measured at 50°C, magnifications 30x, 200x and 500x (left to right), respectively.

a) air, σ_L = 9.0 MPa

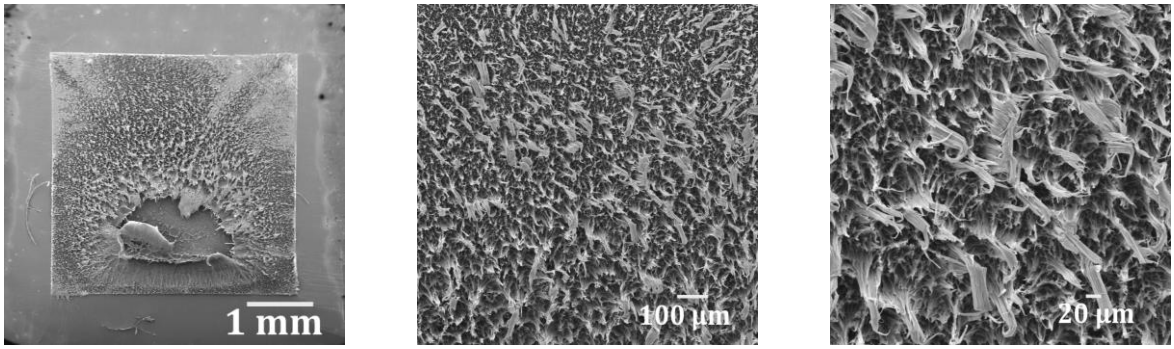

b) Arkopal, σ_L = 9.0 MPa

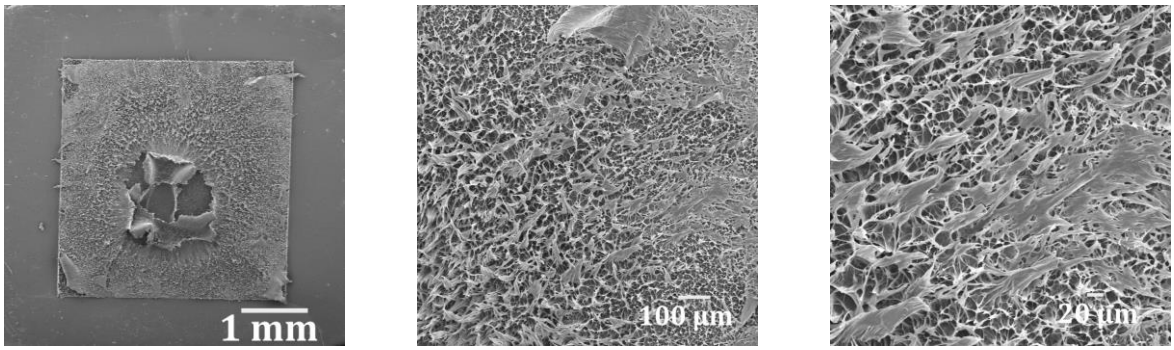

c) diesel, σ_L = 8.9 MPa

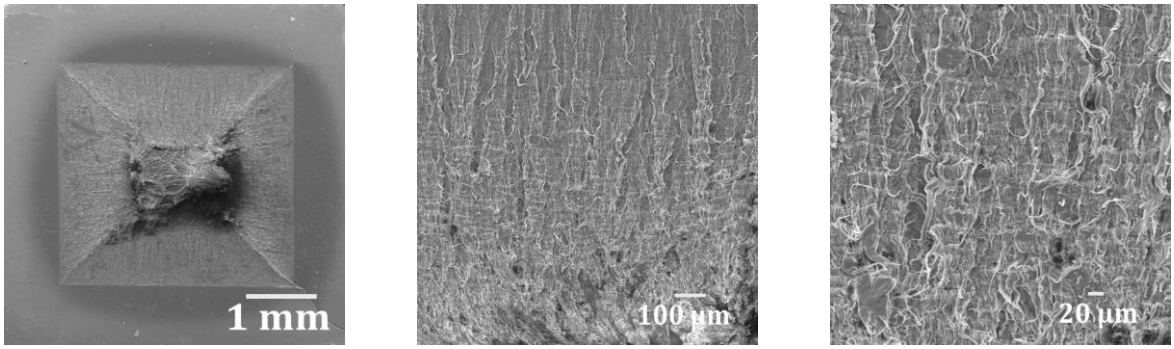

Figure B3.94: SEM fracture surfaces for fluid variation of 5831D (air, Arkopal, diesel), FNCT specimens measured at 50°C, magnifications 30x, 200x and 500x (left to right), respectively.

a) air, σ_L = 9.0 MPa

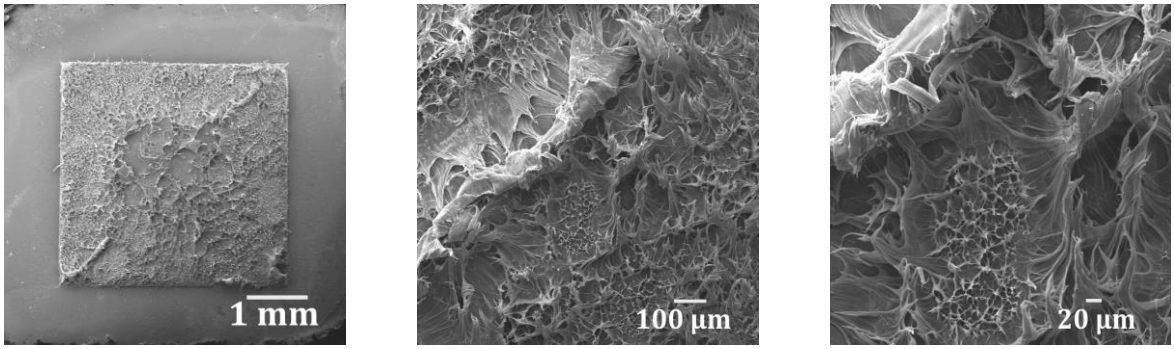

b) Arkopal, σ_L = 9.0 MPa

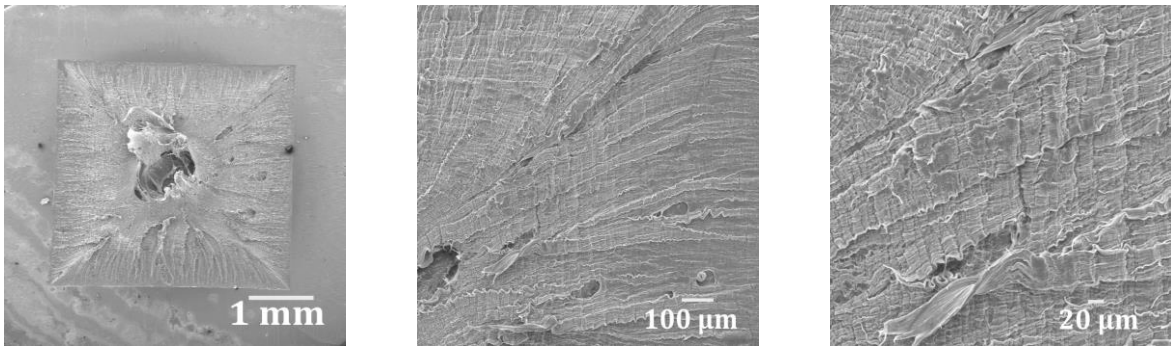

c) diesel, σ_L = 8.9 MPa

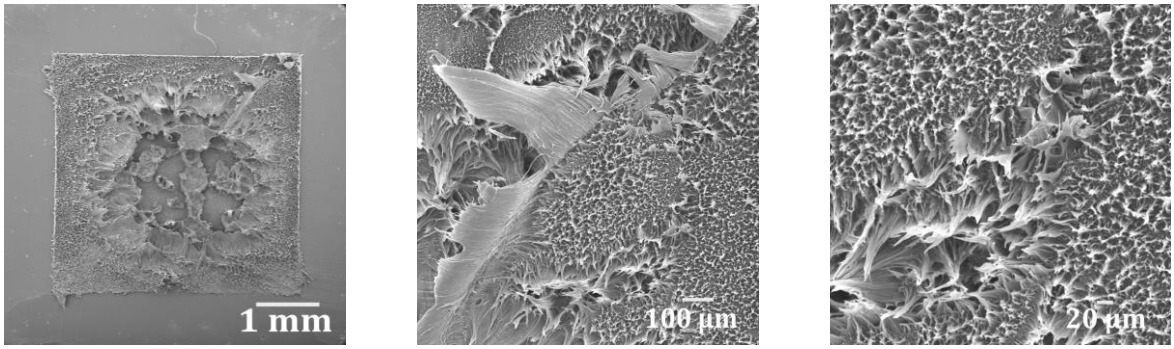

Figure B3.95: SEM fracture surfaces for fluid variation of AQ149 (air, Arkopal, diesel), FNCT specimens measured at 50°C, magnifications 30x, 200x and 500x (left to right), respectively.

Crack growth analysis

AGUV, biodiesel,

side view of crack, x-z-orientation

a) 0% t_f*, 0.0 h, σ_L = 0.0 MPa

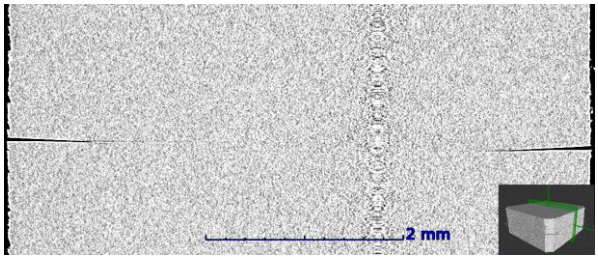

b) 33% t_f*, 3.3 h, σ_L = 8.8 MPa

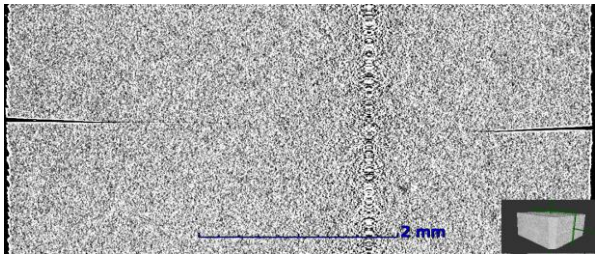

c) 66% t_f*, 6.6 h, σ_L = 14.9 MPa

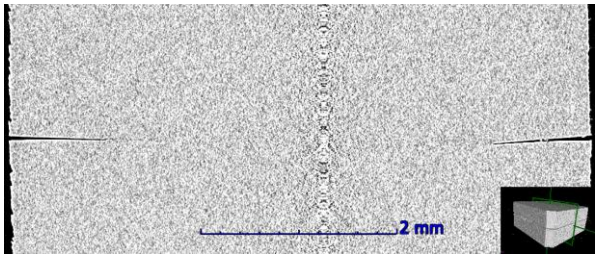

d) 97% t_f*, 9.7 h, σ_L = 19.6 MPa

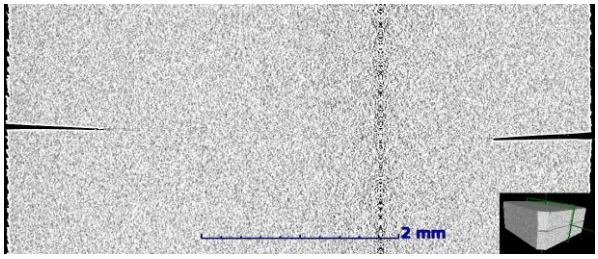

AGUV, diesel,

side view of crack, x-z-orientation

e) 0% t_f*, 0.0 h, σ_L = 0.0 MPa

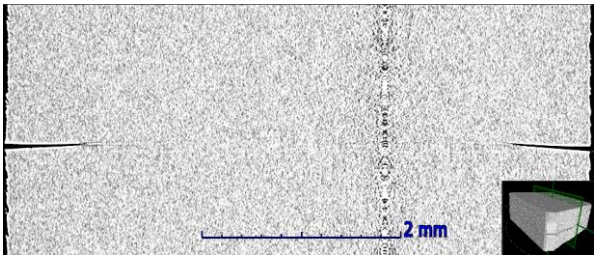

f) 33% t_f*, 2.7 h, σ_L = 8.2 MPa

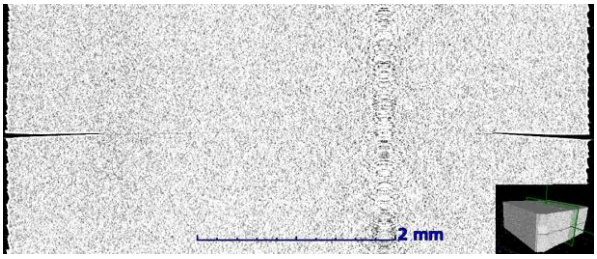

g) 66% t_f*, 5.5 h, σ_L = 13.9 MPa

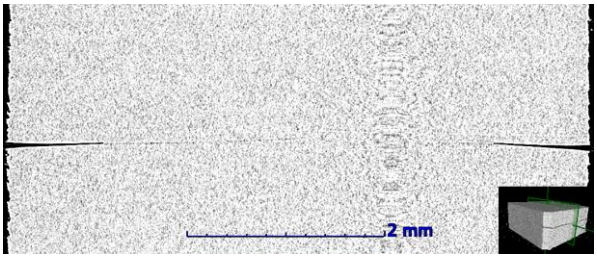

h) 97% t_f*, 8.1 h, σ_L = 21.4 MPa

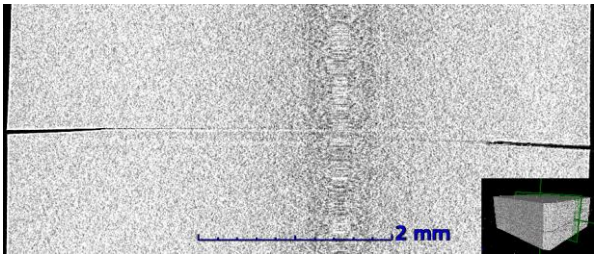

Figure B3.96: Partially damaged areas of AGUV tested in biodiesel (a-d) and diesel (e-h) in the plane of crack propagation and growing crack measured by CT, side view in x-z orientation.